A Feasibility Study of a Hybrid Power Generation System using Offshore-wind and Tidal Turbines in New Zealand

A thesis

submitted in fulfilment

of the requirements for the degree

of

Doctor of Philosophy in Engineering

at

Auckland University of Technology

by

Navid Majdi Nasab

2022

Abstract

In New Zealand, the government aims for 100% of electricity production to be from renewable sources and reduce greenhouse gas emissions by 30% from 2005 levels by 2030. Despite increasing energy demands, depleting fossil fuel resources, and pressure to reduce Greenhouse Gas emissions, reducing the cost electricity is still not fully utilised.

This thesis presents methods to target, optimise and design more practical hybrid systems of wind and tidal energies in large scale for connecting to national grid and in small scale for offgrid design, and overcome technical limitations of current methods.

Original contributions of this thesis to literature include novel developments and applications in six areas:

i) a new off-grid design: define a method for using tidal energy for off-grid design and how to apply wind and tidal data into a microgrid system in an optimized offshore site;

ii) a new on-grid design: define a method for using tidal energy for on-grid design and how to apply wind and tidal data into a microgrid system in an optimized offshore site;

iii) Define a method that could be used to optimize wind generation using climate models for precise forecast of wind generation in different directions;

iv) Define a method that could be used to optimize tidal generation using climate models for precise forecast of tidal generation in different directions;

v) Define a method of foundation design of integrated wind and tidal structures in shallow water depths using monopile and spar buoy floating

respectively in order to investigate acceptability of microgrid design in terms of structural modelling; and

vi) Compare how off-grid and on-grid designs can reduce the amount of emissions as an alternative of using fossil fuels.

The developed methods have been applied to two optimized sites after ensuring getting same coordinates from both python codes of moana project of MetOcean company and Goring model of NIWA.

Offgrid results confirms that using two wind and four tidal turbines (2W+4T) is the optimized design to produce higher electricity with lower cost. The model reduced the COE from 23 cent to 21 cent for Oban and is a clean replacement to current diesel station has pollution. In comparison to other scenarios, the proposed system can generate higher power, higher renewable fraction, lower pollutants and more economic. To ensure about results, a sensitivity analysis about efficiency of inverter and economical viability performed validated 2W+4T is the optimized scenario.
For Ongrid design, Cook Strait is selected for providing electricity demand of node CPK0331 (Central Park) using EMI data and then proved using 36 wind turbines (36W) is the optimized design to produce higher electricity with lower cost. In comparison to other scenarios, the proposed system results higher renewable fraction in lower COE. To ensure about results, a sensitivity analysis about efficiency of inverter and economic viability was performed and validated that 36W is the optimized scenario.
Depending on water height less and over 30m, two types of foundation in Cook Strait (monopile and spar buoy floating) evaluated after contacting NIWA and getting long/lat. Different load scenarios of wind and wave according to imposed to structures to find ULS (ultimate limit state) and calculating the required sizes for each foundation to tolerate against loads. Based on monopile design, diameter, thickness, and length of monopile can be 6, 0.083, and 60 meter respectively. In spar buoy floating foundation, the minimum diameter of the caisson and the embedment depth can be 6.9 and 22.07 meter respectively. The maximum load for both type of foundations occurs in extreme wind load scenario when wind and wave act in same direction.

Acknowledgements

This thesis is dedicated to *my father who passed away on 30 July 2021 and I could not attend in his funeral for covid-19 pandemic restrictions*. The last time I saw him before leaving my country is always in my mind.

I wish to express my gratitude to my supervisors, Dr Jeff Kilby from Auckland University of Technology and Dr Leila Bakhtiaryfard from National Taiwan University for their patience, support, guidance and advice throughout this research. I also greatly appreciate the assistance given by Dr Craig Stewart from the National Institute of Water and Atmospheric Research Institute (NIWA), at Wellington and Dr. Julie Jakoboski from MetOcean, at Raglan, for. imparting professional knowledge and information.

Sincere thanks are also extended to helpful proofreader Dr Douglas Hicks, and the administration staff, specially postgraduate coordinator Josephine Prasad, for their kindness and encouragement during my studying period at the Auckland University of Technology. Without their supports, passing PGR9 was impossible.

Special thanks to my landlady, Dawn Mullins, who her supports during post-PGR9 were wonderful.

Last but not least, thanks to my beloved wife, Masoumeh, for providing me with her pure love and unwavering support. This work would not have been possible without her support, understanding, patience and help.

Contributing Publications

The majority of the proposed methods and results in this thesis have been published in the international journal and peer-reviewed conference papers. Chapter 1 used the materials taken published in fluids [1]. Chapter 2 and 3 and 7 is comprised of an article which is accepted to the PRES22 Conference and will be published in Chemical Engineering Transactions Journal. Part of Chapter 4 is published in Energies and Sustainability [2, 3]. Chapter 5 is comprised of the articles published in Energies and fluids [1, 2].

The research comprising this thesis has been presented at several local and international conferences, namely, Renewable Transformation Challenge 2019, AUT Postgraduate Research Symposium 2019 and 2020, the PRES'19, PRES'20, PRES'21, and PRES'22 Conferences [4-6], IEEE abstract competition 2019, International Conference on Sustainable Energy and Green Technology (SEGT) 2019 [7], 29th Australasian Universities Power Engineering Conference 2019 (AUPEC) [8].

Research Publications

[1] **Nasab, N.M**., et al., Optimization of a Grid-Connected Microgrid Using Tidal and Wind Energy in Cook Strait. Fluids, 2021. 6(12): p. 426.

[2] **Nasab, N.M.**, J. Kilby, and L. Bakhtiaryfard, Case Study of a Hybrid Wind and Tidal Turbines System with a Microgrid for Power Supply to a Remote Off-Grid Community in New Zealand. Energies, 2021. 14(12): p. 3636.

[3] **Nasab, N.M.**, J. Kilby, and L. Bakhtiaryfard, The Potential for Integration of Wind and Tidal Power in New Zealand. Sustainability, 2020. 12(5): p. 1-21.

[4] **Nasab, N.M.**, J. Kilby, and L. Bakhtiaryfard, Comparative Critique on Power Generation in Wind Turbines. Chemical Engineering Transactions, 2019. 76: p. 883-888.

[5] **Nasab, N.M.**, J. Kilby, and L. Bakhtiaryfard, Wind Power Potential Assessment for Three Locations in New Zealand. Chemical Engineering Transactions, 2020. 81: p. 73-78.

[6] **Nasab, N.M.** and J. Kilby, Feasibility Study: Effect of Tidal Turbines Cut-in Speed for Power Generation in New Zealand. Chemical Engineering Transactions, 2021. 88: p. 13-18.

[7] **Nasab, N.M.**, J. Kilby, and L. Bakhtiaryfard. Effect of rotor length on generating power in horizontal axis wind turbines. in IOP Conference Series: Earth and Environmental Science. 2020. IOP Publishing.

[8] **Nasab, N.M.**, J. Kilby, and L. Bakhtiaryfard. Effect of Number of Blades on Generating Power In Wind Turbines. in 2019 29th Australasian Universities Power Engineering Conference (AUPEC). 2019. IEEE.

There are three other journal papers to be published with below titles:

[9] **Nasab, N.M.**, Jeff Kilby, Recognizing the Sites with Maximum Power Generation According to Typical Wind Patterns of New Zealand, accepted to PRES 22 and will be published in Vol. 94 2022 of Chemical Engineering Transactions Journal.

[10] Integration of wind and Tidal Turbines using Floating Foundations

[11] Analysis and Design of Monopile Foundations for Offshore Wind and Tidal Turbine Structures

Presentations

[12] **Nasab, N.M.** Integrating wind and hydropower. Renewable Transformation Challenge 2019; Elsevier.

[13] **Nasab, N.M.** Parameters in Choosing a Wind Turbine and Increasing Their Performance. AUT IEEE Abstract Competition 2019; Auckland, New Zealand.

[14] **Nasab, N.M.** Integrating wind and hydropower. AUT Postgraduate Research Symposium 16 August 2019: Auckland, New Zealand.

[15] **Nasab, N.M.** A feasibility study of a hybrid power generation system using offshore-wind turbine and tidal turbine. AUT Postgraduate Research Symposium 17 August 2020: Auckland, New Zealand.

[16] **Nasab, N.M.** Integrating offshore sources to reduce electricity cost. Falling Wall Lab 1 October 2021: Mongolia.

Table of Contents

List of Figures

List of Tables

Nomenclature

COE	Levelized Cost of Energy
DC	Direct Current
DER	Distributed Energy Resource
EOG	Extreme Operating Gust
ESS	Extreme Sea State
ETM	Extreme Turbulence Model
EWH	Extreme Wave Height
FLS	Fatigue Limit State
HAWT	Horizontal axis wind turbine
IEA	International Energy Agency
IEC	International Electrotechnical Commission
LF	Load Following
LHV	Lower Heating Value
MP	Monopile
MSL	Mean Sea Level
NPC	Net Present Cost
NTM	Normal Turbulence Model
O&M	Operation and Maintenance
RNA	Rotor-Nacelle Assembly
SLS	Serviceability Limit State
TSA	Turbine Swept Area
TSR	Tip Speed Ratio
TP	Transition Piece
TT	Tidal Turbine
ULS	Ultimate Limit State
VAWT	Vertical axis wind turbine

Attestation of Authorship

I hereby declare that this submission is my own work and that, to the best of my knowledge and belief, it contains no material previously published or written by another person except where explicitly defined in the acknowledgements, nor material which to a substantial extent has been submitted for the award of any other degree or diploma of a university or other institution of higher learning.

Navid Majdi Nasab

June 2022

Chapter 1

Introduction

The research presented in this thesis investigates modelling the integration of two offshore renewable energy types, wind and tidal, using a microgrid to remove the detrimental effects of diesel on the environment along with showing a decrease in the cost of electricity generation in New Zealand.

1.1 Background

The World Energy Outlook 2019 clarifies the effect of current decisions on energy systems in the future. If no policy actions are taken, then the current trend of energy demand is anticipated to increase by 1.30% per year until 2040, leading to an increase in emissions [9]. Nowadays with the increasing global energy demand and global climate change, two important solutions have been considered to tackle this issue: (i) reducing the cost of energy and (ii) finding new sources of energy that are environment-friendly [10]. With the negative climate impact of fossil fuel power generation and the requirement of global policy to shift towards a green mix of energy production, the investment in renewable energy is an opportunity in developing countries. However, a poor economy associated with limited income, funds availability, and regulations governing project funding and development are key factors that challenge investors in the energy sector [11].

The New Zealand government has set the country's goal to reduce greenhouse gas emissions by 30% from 2005 levels by 2030 and 80% and more by 2050 [12]. Between 1990 and 2019, Green House Gases (GHG) emissions increased from 41,114-kilo tonnes carbon of dioxide equivalent (kt CO2-e[1]) to 82,318-kt CO2-e [13].

[1] CO2 and other greenhouse gases. Carbon dioxide, or CO_2, is a natural, colorless, and odorless greenhouse gas that is emitted when fossil fuels (i.e. natural gas, oil, coal, etc.) are burnt.

In New Zealand, the government aims for 90% of electricity production to be from renewable sources by 2025 [14], and 100% by 2035 [15]. Currently, 11,349 kilometres of transmission lines distribute electricity from remote areas, where generators are located, all over New Zealand. New Zealand consumes about 38,800 gigawatt-hours (GWh) of electricity per year. In 2017, renewable sources (hydro, geothermal, wind, and solar) supplied 59%, 17%, 5%, and 0.2% of the country's electricity needs, respectively, and thermal sources (coal, diesel, and gas) supplied the other 18.8% [15].

Wind power systems are a cost-effective technology for harnessing renewable energy and have expanded annually at a dramatic rate of 25–35% globally over the last decade [16, 17].

In more recent studies, the advantages of offshore wind generation against onshore wind generation have been highlighted through Life Cycle Analysis (LCA), showing a 48% improvement in the sustainability of the project [18]. Offshore wind farms have increasingly attracted massive investment since 2015 [19, 20]. However, the cost of electricity using offshore wind is have increased significantly since the mid-2000s with capital costs (capex) currently around £3 m/Megawatt (MW) installed, compared to around half that five years ago [21]. Installing tidal turbines in New Zealand, as another good source of renewable energy, is usually considered to be not cost-effective because the turbines can be exposed to harsh currents that can reduce their life. In addition, the foundation design can be complicated when the water depth is more than 30 m [22].

Wind power systems, as a form of renewable energy source, are often integrated with other forms of power-generating systems to form a small power grid, known as a microgrid. Integrating both wind and tidal turbines using the same foundation reduces the cost of electricity [23] and enables a more predictable power generation from two different energy sources.

1.2 Research Aim

The research aims to investigate the feasibility of integrating of two available offshore renewable energies, wind and tidal, using a microgrid with the aim to avoid the detrimental effects of fossil fuels on the environment and decrease the cost of electricity. The methodology will be demonstrated and explained by being applied to two sites:

i. Foveaux for supplying electricity to isolated area of Stewart Island.
ii. Terawhiti in Cook Strait for connecting to node node CPK0331 (Central Park) in national grid.

To achieve to overall aim, first coordinates of Foveaux and Terawhiti identified from both python codes of moana project of MetOcean company and Goring model of NIWA. In case of offgrid design in Foveaux, optimization software is used to simulate electricity consumption from a set of hourly operating loads, then simulate reductions in the percentage of diesel power output dependent on the percentages of wind and tidal power available each hour in Stewart Island. The novelty of research, with respect to the state of the art, is the use of tidal energy in order to enhance the overall efficiency of the microgrid while preserving its stability. This issue is of particular interest for diesel-based island microgrids that face, constantly, the issues of reducing their dependency from fossil fuels and of enhancing the quality of their supply, by reducing voltage drops and power losses. For ongrid design, the research investigates the best scenario in Cook Strait for a microgrid using wind and tidal energy as Cook Strait has the greatest potential for tidal energy in New Zealand. Three different scenarios of electricity generation are analyzed (i) using tidal turbines only, (ii) using wind turbines only, and (iii) using both wind and tidal turbines.

The second aim of thesis is to develop a unique method for structural design of microgrid systems in both shallow and deep waters using monopile and spar buoy floating respectively. The method enables to find required dimensions tolerating against wind and wave loads. Finally, the third aim would explorer how to use climate models for precise forecast of wind and tidal power generation in different patterns. Based on it, it is expected to find superior directions with maximum power generation.

As a result of the above aims, the research method focuses on simulation modelling a hybrid system for electrical power generation using wind and tidal sources. The hybrid renewable energy system is to be electrically connected to a microgrid system [24]. IEA Wind TCP[2] Task 37-May 2019 is used for offshore design as the reference [25]. Having developed supplementary codes to cover analysis (data collection considering power consumptions in optimized sites and available wind and tidal sources, propose a way of microgrid design for wind and tidal sources and selection of microgrid components based on mentioned elements), Table 1-1 addressed the list of software in this research.

Table 1-1: List of softwares

Software	Comments	Used in
SIMULINK [26]	A MATLAB-based block diagram environment for multidomain simulation and Model-Based Design.	Chapter 4
QBlade [27]	An open source wind turbine calculation software; The prefix of Q relies to this concept that QBlade comes with a user-friendly graphical user interface (GUI) based on Qt which means that software runs on hardware platforms such- as Linux, Windows, macOS, Android or embedded systems.	Appendix B
RETScreen [28]	Clean energy management software; The prefix of RE (renewable energy) is used to determine if a renewable energy project makes a financial sense with an analysis capable of covering an entire project life cycle.	Chapter 5
Homer Pro [29]	Homer stands for "Hybrid Optimization of Multiple Energy Resources" is a global standard for optimizing microgrid design. The HOMER Pro® microgrid software has become a recognized global standard for optimizing microgrid design in all sectors, from off-grid village power and island utilities to grid-connected campuses and military bases.	Chapter 3,4,5
WRPLOT View [30]	Wind Rose Plot View is a fully operational wind rose program for meteorological data.	Chapter 3,5,6

[2] IEA Wind TCP: The International Energy Agency Wind Technology Collaboration Programme

TOPEX/POSEIDON [31]	Stands for "Topography Experiment/Poseidon" used to provide high-accuracy global sea level (ocean height) measurements	Chapter 5
Python [32]	A programming language designed by Guido van Rossum for data analysis.	Chapter 5, Appendix D

These simulations enable the following:

- To propose designs to generate electricity at a lower cost and recognise optimised sites for power generation, based on the resource capacity (wind, tidal or both).
- To identify the directions of turbines for maximum power based on wind or tidal direction, strength and frequency.
- To recognise the optimum height where speed is maximum based on wind or tidal velocity profile.
- Calculate the electricity demand and propose a microgrid design that enables electricity generation for that location at a lower cost. The site is off-grid (isolated) or on-grid (connected to the national grid).
- Propose an optimised design for necessary components such as turbines, generators, converters, controllers, and batteries.

1.2.1 Research Questions

This research aims to answer the following questions:

1. Which parameters affect the generated power output from a hybrid system?
2. What type of foundation, platform and tower structure could be available to support the whole system?
3. Can a microgrid be designed to optimise the power output from a hybrid system?
4. Does the extra power output justify constructing the hybrid system?
5. If built, will the economic return be better than separate wind or tidal turbine installations?

1.3 Thesis Outline

Chapter 1 covers the general background of the research carried out and presented in this thesis, and the following chapters are structured according to the objectives.

Chapter 2 reviews literature relevant to elements of the hybrid system (wind turbines, tidal turbines, supporting structures, supply links, including microgrids), recent developments in this field and then status of wind, tidal and hybrid offshore generation will be addressed.

Chapter 3 reviews the potential of offshore energy in New Zealand. For wind, Global Wind Atlas and for tidal MetOcean model is used for several sites to find optimized sited for generating hybrid power from both sources.

Chapter 4 introduces several parameters that contributed to the selection of wind and tidal turbines. However, the first parameter is site potential in terms of wind and tidal sources. After recognizing the sites capable of integrating wind and tidal, the next question that needs to be answered is where this power will be supplied and whether it is off-grid or on-grid. For both cases, the amount of load or power consumption is necessary. And finally, based on on-site location and the area of electricity supplied, suitable turbines will be chosen.

Chapter 5 propose two microgrid designs to evaluate the feasibility of using a hybrid system consisting of wind and tidal turbines: i) The off-grid case study is Stewart Island, where the cost of electricity, provided by a central diesel power station, is higher than the grid network in New Zealand. Local residents believe that reducing the consumption of diesel and having a renewable source of electricity generation is one of the island ’s highest priorities. ii) The grid-connected design was evaluated based on facility location in Cook Strait. The closest node is selected to Terawhiti in Cook Strait and several calculations are carried to reach an optimized design compatible with this node.

Chapter 6 uses resource data and site location of the previous chapter to find suitable foundations and calculate required dimensions. The monopile has been found to be a suitable foundation type for less than 30 m water depth; Also, the possibility of using foundation for water depths more than 60 m was examined by proposing a

floating system in Cook Strait after finding a 110 m site from the national institute of Water and Atmospheric Research (NIWA).

Chapter 7 presents analysis for the wind and tidal rose in the proposed sites and how it affects power generation. Global Wind Atlas used to find wind rose of Foveaux and Terawhiti as optimized sites for Stewart Island and node CPK0331 (Central Park). For plotting tidal roses, the flow speeds provided by the National Institute of Water and Atmospheric Research (NIWA) used.

Finally, Chapter 8, Discussion and Conclusion, discusses the pros and cons of the results and techniques from other chapters and the conclusions and recommendations for future work in this field of research.

Chapter 2

Literature Review

2.1 Introduction

The main energy sources include coal, oil, natural gas, nuclear energy, and renewable energy. Among these, coal, oil, and natural gas are fossil fuels. Fossil fuels are responsible for more than 90 percent of global combustion-related CO_2 emissions with 37 gigatons (37,000 million tons) in 2017. The shares of fossil fuels to the global CO_2 emissions are 45 percent for coal, 35 percent for oil, and 20 percent for natural gas.

The main renewable energy sources include solar, wind, hydro, biomass, and geothermal. Energy sources from the ocean, including ocean thermal energy conversion (OTEC), wave, and tidal, are also renewable sources, but they are currently not economical and the technologies are still in the experimental and developmental stage. An energy source is called renewable if it can be renewed and sustained without any depletion and any significant effect on the environment. It is also called an alternative, sustainable, or green energy source. The best-known renewable source is solar energy. Although solar energy is sufficient to meet the entire energy needs of the world, currently it is not used as extensively as fossil fuels because of the low concentration of solar energy on earth and the relatively high capital cost of harnessing it. The conversion of kinetic energy of wind into electricity via wind turbines represents wind energy, and it is one of the fastest-growing renewables as wind turbines are being installed all over the world. The collection of river water in large dams at some elevation and then directing the collected water into a hydraulic turbine is the common method of converting water energy into electricity. Hydro or water energy represents the greatest amount of renewable electricity production, and it supplies most of the electricity needs of some countries.

Geothermal energy refers to the heat of the earth. High-temperature underground geothermal fluid found in some locations is extracted, and the energy of the geothermal fluid is converted to electricity or heat. Geothermal energy conversion is one of the most mature renewable energy technologies. Geothermal energy is mostly used for electricity generation and district heating. Organic renewable energy is referred to as biomass, and a variety of sources (agriculture, forest, residues, crops, etc.) can be used to produce biomass energy. Biomass is becoming more popular with the help of the variety of available sources.

Wave and tidal energies are renewable energy sources, and they are usually considered as part of ocean energy since they are available mostly in oceans. Thermal energy of oceans due to absorption of solar energy by ocean surfaces is also considered as part of ocean energy, and this energy can be utilized using the OTEC system. Wave and tidal energies are mechanical forms of ocean energy since they represent potential and kinetic energies of ocean water.

Hydrogen is an energy carrier that can be used to store renewable electricity. It is still a developing technology, and many research activities are under way to make it viable.

Fuel cells convert chemical energy of fuels (e.g., hydrogen) into electricity directly without a highly irreversible combustion process, and it is more efficient than combustion-based conversion to electricity.

All renewable energy sources can be used to produce useful energy in the form of electricity and some renewables can also produce thermal energy for heating and cooling applications. Wind and water energies are converted to electricity only while solar, biomass, and geothermal can be converted to both electricity and thermal energy (i.e., heat).

We should point out that what we call renewable energy is usually nothing more than the manifestation of solar energy in different forms. Such energy sources include wind energy, hydroelectric power, ocean thermal energy, ocean wave energy, and wood. For example, no hydroelectric power plant can generate

electricity year after year unless the water evaporates by absorbing solar energy and comes back as rainfall to replenish the water source (Figure 2-1) [33].

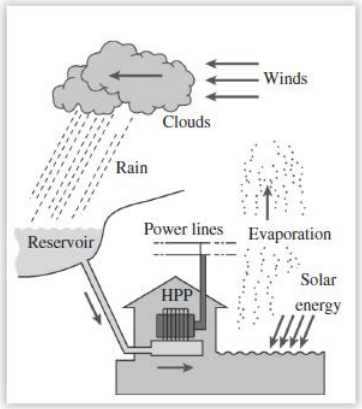

Figure 2-1: The cycle that water undergoes in a hydroelectric power plant (HPP)[33].

A brief history of innovation in New Zealand 's electricity sector is shown in Figure 2-2.

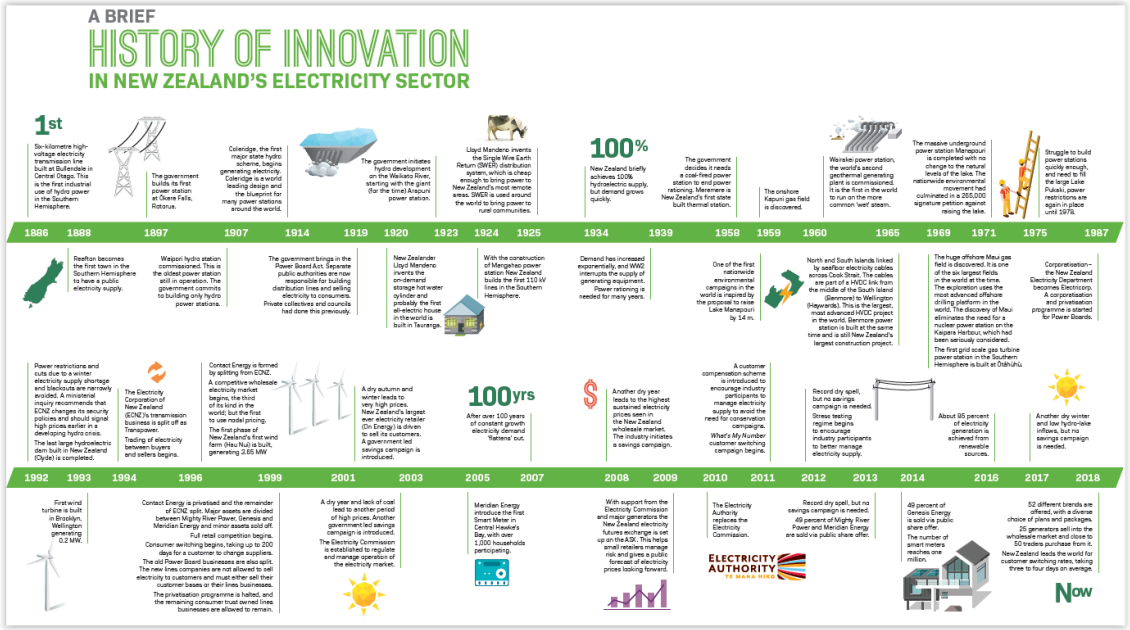

Figure 2-2: The history of electricity in New Zealand [15].

The literature relevant to the thesis aim broadly falls into generation electricity from two offshore sources of wind and tidal and recent developments on how to hybrid

them. The microgrid field is enormous and, as a result, the scope of this literature review chapter is limited to those areas of research that are mostly relevant to thesis aim. In the first section, a comprehensive definition of renewable sources has presented. Subsequently, based on the thesis aim, development of offshore wind and tidal power generation and their hybrid technology have been reviewed. Microgrid design provides the opportunity of comparing the possibility of more electricity generation with lower cost rather than using solely wind or tidal turbines. Both microgrid design using only wind or tidal energy can be compared with hybrid design. The goal is to evaluate feasibility of hybrid power generation system using offshore-wind and tidal turbines in New Zealand. As New Zealand has shown a good potential of offshore energy and this has not been used in electricity sector, the methods used in literature review can be improved to investigate the possibility of offshore generation in New Zealand.

2.2 Literature Review on Offshore Wind Turbines

Wind turbines produce electricity by converting the wind's kinetic energy into mechanical energy, and then electrical energy, shown in Figure 2-3.

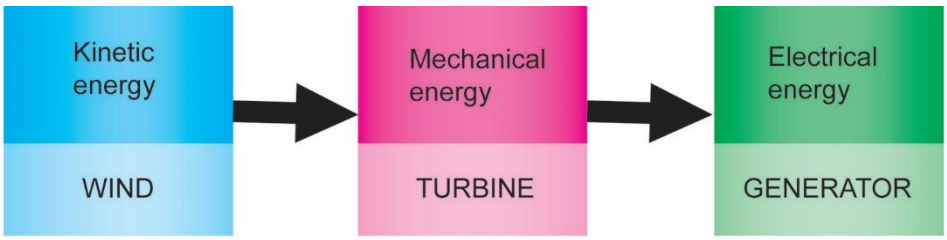

Figure 2-3: Block Diagram of a Wind turbine

Wind turbines are an essential source of renewable energy and are used by many countries as part of their strategy to reduce their reliance on fossil fuels [34]. A research assessment carried out by Evans et al. [35] claims that wind energy has the *'lowest relative greenhouse gas emissions, the least water consumption demands, and the most favourable social impacts'* compared to photovoltaic, tidal, geothermal, coal and gas energy.

2.2.1 History of Offshore Wind Turbine Generation

A literature review by Martínez et al. [36] found studies on electricity production from wind energy account for 3,730, and of these, 1,736 focus on offshore deployments. In 2016, 16% of global electricity produced from offshore and onshore wind as an increasingly efficient and price-competitive renewable energy source [37]. It is estimated that onshore and offshore wind power will generate more than a third of the total electricity needed in the medium term, becoming the primary generation source by 2050 [38]. In 2015, only 5% of New Zealand electricity generation was supplied from wind [39], which is expected to be 20% of NZ generation by 2035 [40].

Compared with onshore wind energy resources, offshore wind fields have many advantages, such as persistent wind, faster-flowing speed, higher uniformity, and longer available time per year, flat sea surface, low turbulence intensity, which promotes the vigorous development of the offshore wind power industry [41, 42]. More importantly, installing wind turbines in the ocean can protect the environment [43] and save land resources [44]. The ocean area is vast, providing good conditions for developing large-scale wind farms and large-scale turbines [45]. The power generation by the identical turbines in the offshore area is 50%– 100% higher than that in the onshore area [46].

Offshore wind power turbine manufacture is currently dominated by few companies [47]. The main ones are Siemens, Vestas, and Repower, and in recent years several other manufacturers are developing such as Areva Multibird, Sinovel, and General-Electric [47].

In 1991, Wind World installed the first offshore wind turbine at Nogersund in Sweden using a 220-kW turbine. One year later, Denmark was the first country to establish an offshore wind farm using 11 turbines at 450 kW capacity, each with a water depth of between 2 to 4 meters. Until 2001, several offshore farms developed in the capacity of less than 1 MW. From 2001 to 2003, several large offshore wind farms were installed in Denmark using turbines with more than 2 MW rated power.

Since 2003, the major countries that developed larger offshore wind farms were the United Kingdom (UK), Germany, and Belgium, and since 2008, UK has dominated [48].

While most wind farms are onshore, some European countries have a significant investment in the offshore industry. United Kingdom, Germany, and Denmark are the three top countries with 35, 20, and 12 offshore wind farms, respectively [49]. The development of offshore wind farms in Europe is more than other continents; 95 offshore wind farms in Europe with 21 GW capacity all installed from 1991 till 2020. However, this capacity will be 68 GW by 2030 [50]. Rapid development is forecast in Asia and America, from 0.5 and 0.1 GW in 2006 to 27 and 4.8 GW by 2030, respectively [51].

Offshore wind energy kept growing in the past decade (from 3 GW in 2010 to 29.5 GW in 2019) [52]. According to the Global Wind Energy Council report in 2020, this capacity doubled in just five years, and it is predictable to develop faster [53].(See Figure 2-4)[54]. Offshore wind will become a dominant source of electricity beyond the year 2040 in the EU [55].

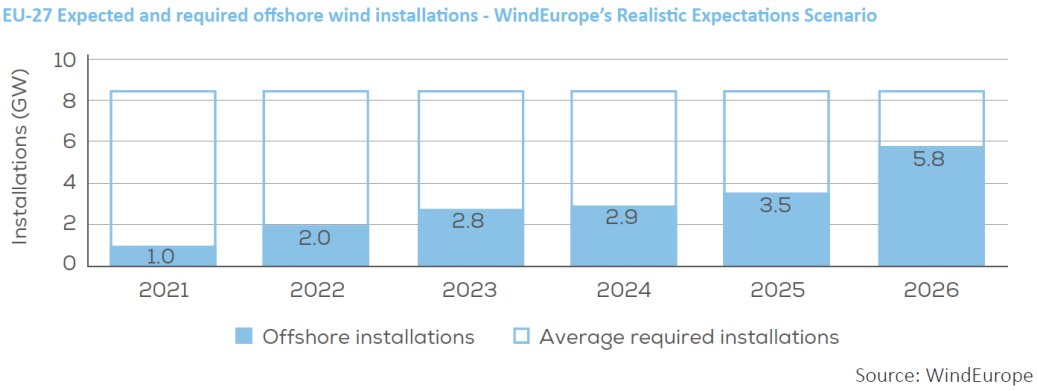

Figure 2-4: Expected and required offshore installations in Europe, 2021 -2026 [54].

Figure 2-5 shows that there would be a rising trend for global offshore market. While in 2018 the global market held an installed capacity of more than 23 GW, it is expected to reach 94 GW by the end of 2026 [56].

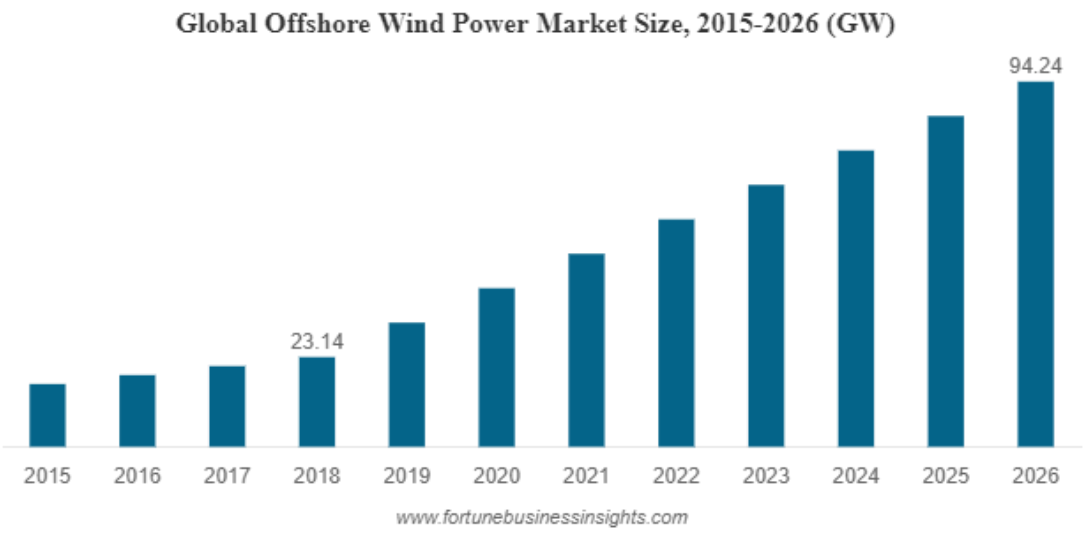

Figure 2-5:Global offshore wind power market size, 2015-2026 [56].

2.2.2 Recent Developments in Offshore Wind Turbine Technology Worldwide

The limitations and resistance of many societies against onshore wind installation have attracted several researchers and designers to recently consider how to increase offshore wind turbines' capacity. Wang et al. investigate the dynamic response of offshore wind turbine supported on monopile foundation in clay subjected to wind, wave and earthquake actions. They use an open-source software platform OpenSees, based on a kriging model, to approximate the system's response [57]. Morato et al. propose a computationally efficient reliability framework for offshore wind turbine support structures to capture the structure's dynamic behaviour. This framework considers uncertainties related to the soil-pile interaction through the flexural rigidity and the equivalent length, but it could be interesting to see the relationship between these parameters and actual parameters such as friction angle [58]. Kavari et al. designed a wind turbine blade by blade element momentum theory in order to reducing the effects of wind shear on the blade [59]. Ke et al. discuss structural responses, buckling stability, and ultimate bearing capacity of the large-scale wind turbine system, considering different yaw angles under wind and rain conditions. While additional rain load influences the

buckling stability of wind turbine system slightly, its effects on ultimate bearing capacity should not be neglected [60]. To design performance-scaled rotors, Wen et al. propose maximum lift tracking and load distribution matching algorithms to assign the chord lengths and twist angles. Both approaches can generate desired rotor thrusts in a range of tip speed ratios [61]. Li et al. established an aeroelastic model of flexible wind turbine blades based on the geometrically exact beam theory and blade element momentum method. They verified the aeroelastic coupling model based on several previous studies [62]. Afsharian et al. simulate a wind farm with 432 offshore wind turbines in Lake Erie. The results show that wind turbines impact water circulation in the central basin. This occurs because the reduced wind speed and stress leads to less mixing, lower current speeds and higher surface water temperature [63]. Allan et al. explore the potential economic and environmental impact of UK offshore wind capacity developments between 2019 and 2029 and identified that the further investment in offshore wind capacity associated with the more optimistic Brexit (the UK's departure from the European Union) scenario involves some additional emissions, but this effect is swamped by the savings in emissions that result from substituting wind for coal in the generation of electricity [64]. Balasubramanian et al. address the new approaches used in wind farm modelling for wind farm layout optimization [65]. Barter et al. propose a design methodology that may push floating wind plants toward a lower Levelized Cost of energy than fixed-bottom offshore wind [66]. Dabachi et al. propose a new design of Floating H-Darrieus Vertical Axis Wind Turbine with three-stage rotors. This design solves the problem of starting a large turbine and facilitates maintenance by adopting three mechanisms Bearing Swivel Rollers at each stage [67]. Peng et al. summarize the existing research results for the related technologies of multiphase wind power generation, including the design of multiphase wind turbines, multiphase converters, and multiphase generators [68]. Peng et al.'s another study systematically compiles the investigations of the wake flow fields and vortical structures of VAWTs to reduce mutual interference, and thereby maximize the total power output. The results of these studies suggest that the wakes of VAWTs are characterized by distinctive features, such as strong asymmetry and counter-rotating vortical motion [69]. Another study by Peng et al. proposes an improved Gaussian process (GP) fault detection algorithm to boost power production and reduce maintenance costs [70]. The latest research in

leading-edge erosion (LEE) from different viewpoints is discussed by Mishnaevsky et al. to predict blade erosion to set the frequency of maintenance events [71]. Liu et al. undertake a systematic literature review of methodologies and theories commonly used in offshore wind power investment decision-making [72]. Khan et al. provide an in-depth review of the frequency support strategies for offshore wind power plants and the voltage source converter stations in a multi-terminal HVDC system, including a comparison of the related approaches and the gaps present in the existing literature [73]. Karanikas et al. evaluates the possible health-related hazards relevant to wind farms (noise, electromagnetic fields, shadow flicker, epoxy and styrene and physical stress) during their various lifecycle stages [74]. Kaldelis et al. carries out a systematic analysis and comparison of nine commonly utilized analytical and semi-empirical wake models, deployed in order to represent the wind speed downstream the wind turbine's rotor [75]. Jiang Z. provides a comprehensive review of the installation technologies for offshore wind turbines [76]. P.Huynh shows the feasibility of Maximum power point tracking (MPPT) based on a finding that the active-rectifier d-axis current can control the total system output power [77].

Out of 20 Journal papers summarised [57-77] , 14 [59, 61-63, 65-70, 72, 73, 76, 77] propose or review proposals for new technical developments which claim the potential for improving offshore wind turbines' design and performance. They are:

* reducing wind shear effects on turbine blades Kavari[59].
* designing performance-scaled rotors Wen et al. [61]
* more flexible wind turbine blades Li [62].
* predicting blade erosion and setting the frequency of blade maintenance Mishnaevsky [72].
* better blade/rotor fault detection to reduce downtime Peng c [70].
* multi-phase technology for low-voltage high-power operation Peng a [68].
* use of voltage source converter stations Khan [73].
* maximum power point tracking for rotors Huynh [77].
* better techniques for offshore installation, includes floating wind turbines Jiang, Barter, Dabchi [66, 67, 76].
* Optimizing wind farm layout, includes reducing array density to decrease

wind flow interference Afsharian, Balasubramanian, Peng b [63, 65, 69].

Of the 14 [59, 61-63, 65-70, 72, 73, 76, 77] which propose specific technical developments, all rely on (or review other authors' use of) computer design algorithms and performance simulation models.

Five authors [63, 65-67, 76] definitely and another four authors [68, 69, 72, 73] may verify their simulations by comparing results with measured outputs from offshore turbine arrays (Jiang, Barter, Dabchi, Afsharian, Balasubramanian, Peng a, Peng b, Mishnaevsky, Khan and a 10^{th} verifies by comparing with output from a lab-scale emulator Huynh [77].

Six report performance improvements in terms of greater annual power output, through multiphase turbine designs Peng a [68], control of system output through maximum power tracking Huynh [77], better turbine array layouts Afsharian, Balasubramanian, Peng b [63, 65, 69], and improved blade or rotor designs Dabchi [67], and just one another report making operation more economical by improved installation techniques, specifically floating turbine platforms Barter [66]. Another reports it through improved maintenance techniques, specifically maintenance opportunity prediction Mishnaevsky [72].

Finally, three of the 20 Journal papers mention unresolved technical issues which need further research. These are solutions to cope with challenging technical problems in multiphase turbine design Peng a [68], ways to reduce within-grid turbulence and atmospheric boundary layer turbulence in turbine arrays Peng b [69], and providing a complete overview/forecast of opportunities for applying blade erosion control safely Mishnaevsky [72].

2.2.3 The Status of Offshore Wind Energy in New Zealand

Historically in New Zealand the main renewable energy sources have been geothermal and hydro power. However in the future most incremental growth in renewable energy are forecasted to come from wind energy and geothermal energy

capacity additions, which can be seen in the electricity generation projection chart shown in Figure 2-6 [78].

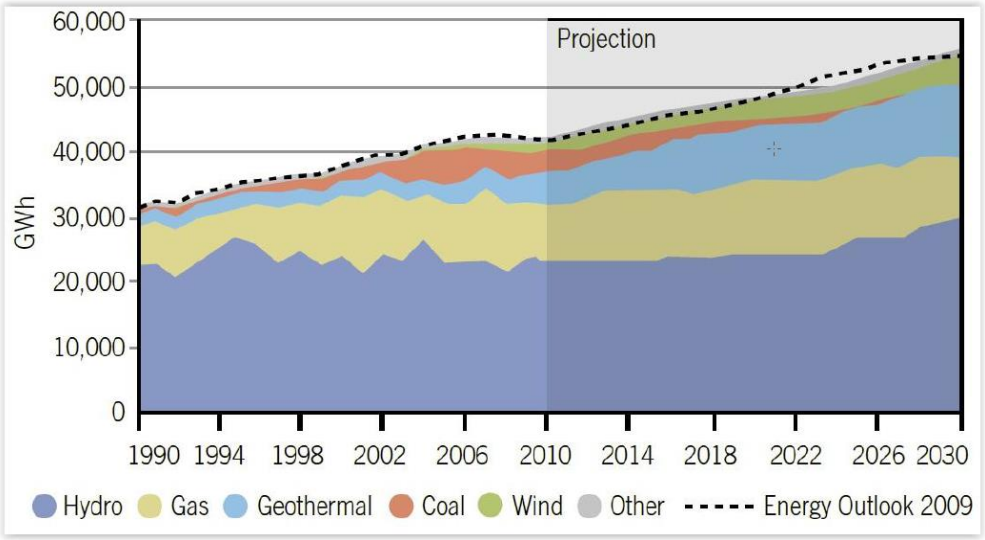

Figure 2-6: Forecast of electricity generation by fuel in New Zealand [78].

Wind provided 2,232 GWh of electricity, or 5.1 per cent, of total electricity supply in 2019 which was 37 per cent of the capacity factor (Capacity factor for wind is the amount of electricity generated in relation to the maximum output capable of being generated by installed wind turbines over a period of time assuming no downtime for maintenance) [79].

By 2030 it is predicted that wind generation in New Zealand will increase six-fold, producing as much as 20% of all electricity. Wind farm capacity can be built as it is essentially the most cost effective form of electricity generation, being predictable, dependable and the costs of fuel are known (wind is free) [78]. The Ministry of Business, Innovation and Employment (MBIE) report issued on June 2020 describes the desired wind generation growth stack on a decadal basis between 2020 and 2060 as tabulated in Table 2-1.

Table 2-1: Minimum cumulative MW of new wind generation till 2060 [80].

Year	2030	2040	2050	2060
MW (Cumulative)	2500	4000	6000	8000

It shows that 2500 MW of new wind generation is required between 2020 – 2030, 1500 MW between 2030-2040, 2000 MW between 2040-2050, and 2000 MW between 2050-2060. To put this in context, there is currently only 690 MW of wind generation in NZ – and the majority of this total has taken the previous 20 years to develop and construct [80].

Most existing wind generation is located in the Waikato, Manawatu, Wellington and Southland. Future growth areas include Northland, west coast Waikato, South Taranaki, Hawkes Bay, Canterbury, Otago and Southland [81].

2.3 Literature Review on Offshore Tidal Turbines

Tidal energy is a predictable energy source, relying only on the gravitational pull of the moon and the sun and the centrifugal force created via the rotation of the earth (See Appendix C). Hydrokinetic energy generated in the oceans Marine Renewable Energy (MRE), harvested from tides, currents, waves, thermal and salinity gradients, is projected to increase noticeably in the coming decades. A literature search by Martínez et al. [36] has found 2,484 ocean energy studies, 904 of them dealing with tidal. Figure 2-7 shows the locations of global tidal resources [82]. The potential of the global tidal range energy resource is distributed among Canada (23%), Australia (30%), UK (13%), France (13%), US (11%), Brazil (5%), South Korea (2%), Argentina (1%), Russia (<1%), India (<1%) and China (<1%) [83]. Overall, the tidal potential resource energy with current technologies is estimated to be about 75 GW in the world [84].

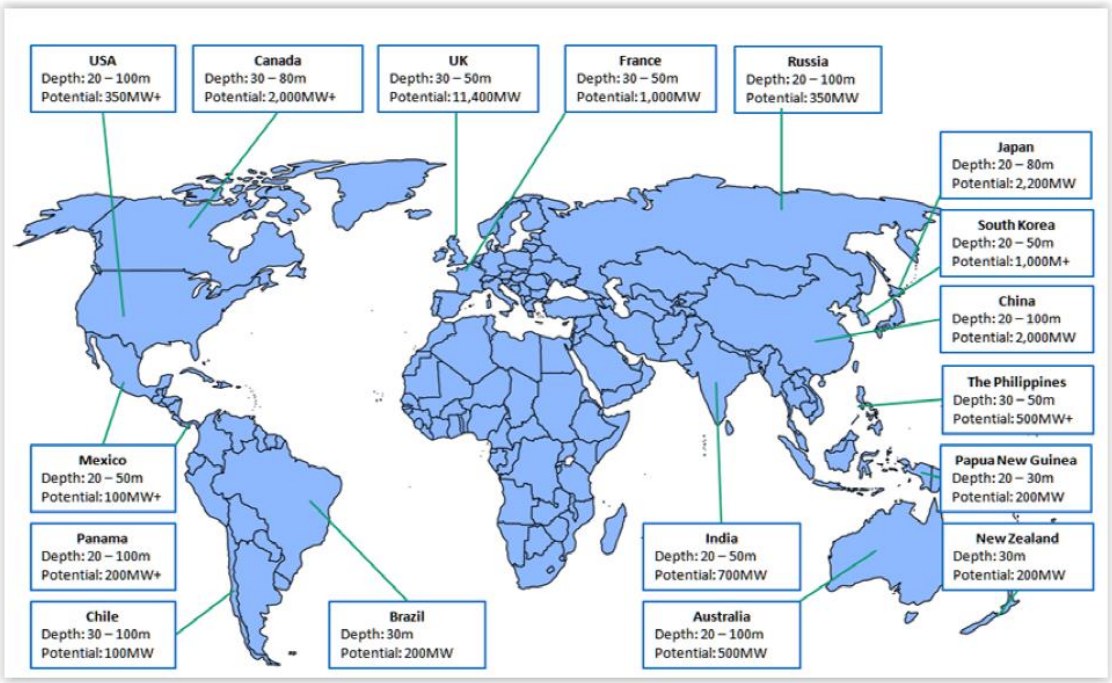

Figure 2-7: Global Tidal resources [82].

Tidal energy projects utilize the kinetic energy available in water currents to turn turbines. Because the blades are turned by water rather than wind, they have to be shorter and stronger to withstand higher hydrodynamic forces [85]. So, instead of an airfoil working with wind, a hydrofoil is selected to design a tidal turbine. The Tidal energy sector has much higher device reliability requirements than the wind industry because of the inaccessibility of the turbines [86]. Tidal turbines can produce an enormous amount of energy, more than four times per square metre of the rotor than wind turbines [87]. However, they face some problems: complex operation and maintenance due to harsh environment, corrosion of parts by saltwater, high stress of the turbine shaft due to the density of water, cavitation of turbine blades, changing frequency due to generation and load imbalances. Tidal turbines also have extra design issues such as the importance of synchronizing the tidal current power generator, the need of reinforcing switchgear and cable thermal ratings and fault protection mechanisms in weak electrical networks, the other fault for connecting tidal generator and flicker in network interactions [88].

2.3.1 History of Tidal Turbine Generation

Few tidal power stations have been constructed. Why just eight of them are operating, which is explained by Aguayo et al. [89]. These tidal power stations built between 1967-2016 are described by Rourke et al. [90]:

- **Barrage de la Rance-France, 1967:** Capacity: 240 MW contains 24 turbines with a yearly production of 500 GWh. The generator runs in reverse mode and pumps seawater to raise the level behind the barrage further before slack water is reached (the short period when there is no movement either way in the tidal stream). It maximizes output power decreasing the start-up period [91].
- **Kislaya-Russia-1968:** It was built near the Barents Sea with 0.4MW capacity, which upgraded later to 1.2 MW later in 2006 [92].
- **Jiangxia-China-1980:** The Jiangxia Tidal Power Station is the fourth biggest tidal power station globally, with an installed capacity of 3.2 MW and annual energy output of 10,000 MWh [93].
- **Annapolis Royal -Canada-1984:** The grid-connected power plant with 20 MW capacity and annual generation capacity of 30 GWh takes four years to build in the Bay of Fundy as the second-largest commercial tidal power plant in the world [92].
- **Strangford Lough-UK-2008**: Capacity: 1.2 MW. It includes a twin axial-flow turbine supported on a structure with the potential to lift the moving components out of the water for maintenance [94].
- **Uldolmok-South Korea-2009**: The capacity of this tidal power plant is 1.5 MW, and the annual energy output is 2.4 GWh per year [92].
- **Sihwa Lake-South Korea-2011**: K-water company built the largest tidal power plant with an installed capacity of 254 MW and is an annual output generating of 552 GWh [92].
- **Eastern Scheldt-Netherlands-2015**: The capacity of this tidal power plant is 1.25 MW, estimated to provide electricity for 1000 households [92].

The principal manufactures of tidal turbines for new tidal power plants under construction since 2016 are listed in Table 2-2Table 2-2: Tidal Turbine Manufacturers [95].

Table 2-2: Tidal Turbine Manufacturers [95].

Companies	*Where Installed*	*Turbine Name*	*Operational Year*
MeyGen	Pentland Firth (Scotland, UK)	AHH[3] turbine, AR[4]1500	2016
AR, AHH	Sound of Islay (Scotland, UK)	AR1500 or AHH turbine	2016
MCT[5] Atlantis Resources	Kyle Rhea (Scotland, UK), Anglesey (Wales, UK)	SeaGen S	>2016 >2016
DCNS[6] EDF[7]	Paimpol-Brehat (France), Nova Scotia (Canada)	OpenHydro	2016/2017 2016
GE[8]&Alstom Energy DCNS, EDF	Raz Blanchard (France)	GE-Alstom turbine	2017/2018 2018
Sabella	Fromveur (France)	Sabella	2019

Figure 2-8, sourced from Soede [96], shows the development of tidal turbines with colour coding from light to dark. The below figure shows for individual companies the technology development in terms of maturity (colour coding, light to dark) and demonstration projects (text). Technology readiness level (TRL) estimates the maturity of technologies based on a scale from 1 to 9 with 9 being the most mature technology. The arrows represent staff transfer, acquisition and technology / component transfer (dashed lines indicate a planned transfer), and together with the status of technology development this gives an indication of the extent of knowledge and experience transfer and collaboration in the technology development activities.

[3] Andritz Hydro Hammerfest
[4] Atlantic Resources
[5] Marin Current Turbines
[6] Direction des Constructions Navales
[7] Electricitie de France
[8] General Electric

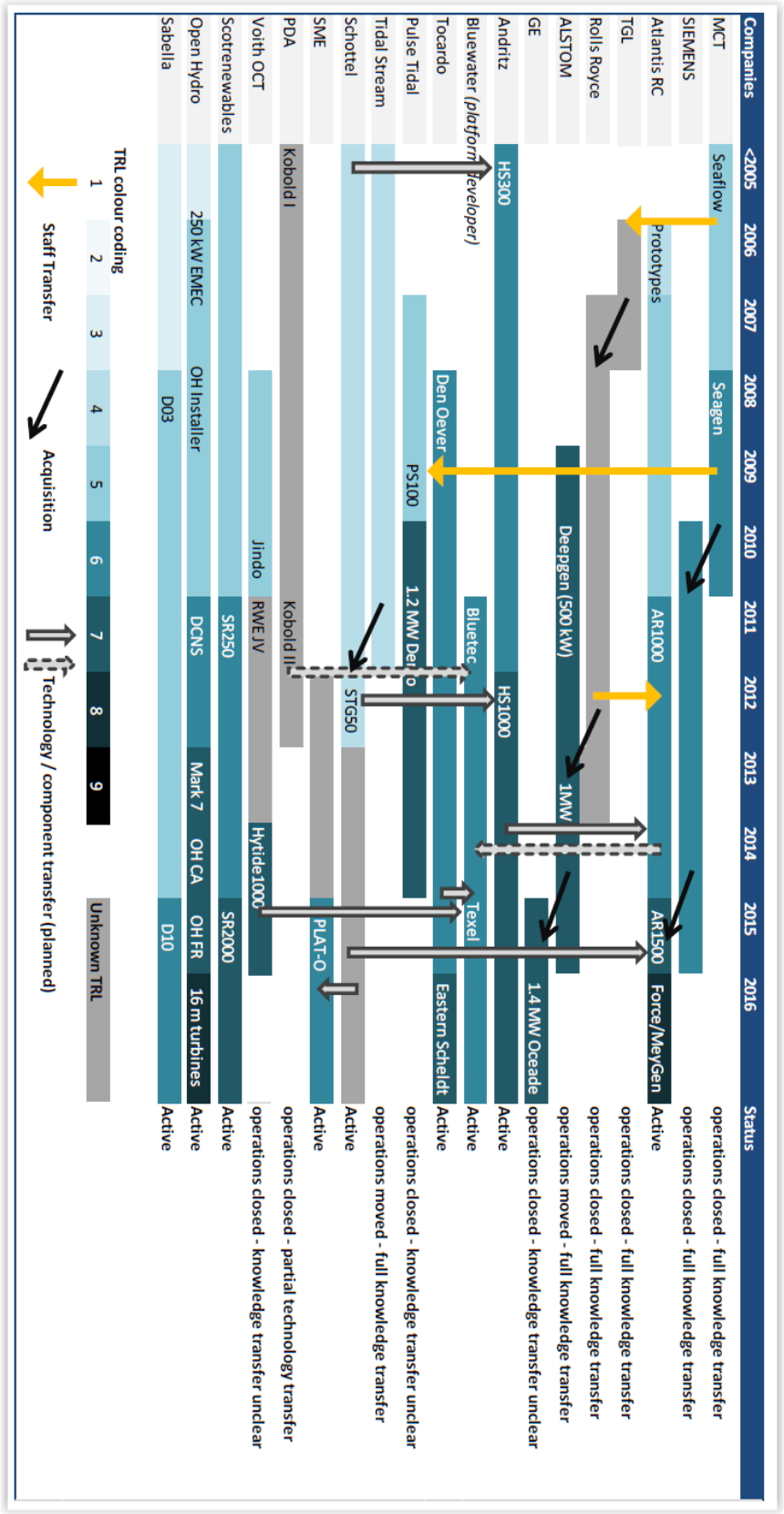

Figure 2-8: Schematic overview of tidal turbine development [96].

2.3.2 Recent Developments in Tidal Turbine Technology Worldwide

Meanwhile, with this development, several research have conducted to boost the energy production of tidal turbines. M.G. Borg et al. investigate the hydrodynamic performance of a ducted high-solidity tidal turbine and validate the experimental results [97, 98]. Brockhaus et al. describe the analysis and validation of six different blockage correction methods for tidal turbines [99]. M.G. Borg et al. again analyse fibre composite designs for high-solidity ducted tidal turbine blades [100, 101]. Alvarez et al. explore the potential effects caused by dredging operations, energy production and efficiency of tidal turbines [102]. Baker et al. examine the impact of a proposed Severn tidal barrage linking hydrodynamic modelling to marine species distribution models and conclude that a large-scale tidal barrage may impact species distribution by altering food web dynamics and altering food availability [103]. Brown et al. developed a coupled turbine thrust methodology for floating tidal stream turbines [104]. Chen et al. propose the wake model integrated with the RSS (root sum of squares) model to predict the velocity shape of the resultant wakes of turbine arrays and exhibit agreement with experimental measurements [105]. Nachtane et al. review the recent advancements in designing a hydrofoil for the horizontal axis tidal current turbine [106]. Djebarri et al. propose a design methodology of permanent magnets (PM) generators used for fixed-pitch tidal turbines to reduce maintenance [107]. Liu et al. propose a new individual pitch control (IPC) method based on vector analysis to calculate the fatigue loads of a two-bladed 600-kW horizontal-axis tidal current turbine (TCT) around the Zhoushan Sea [108]. Lopez et al. propose a cost model and tool for calculating the Levelized cost based on a tidal energy farm [109]. Dong et al. designed an active variable-pitch and direct drive permanent magnet synchronous generator (PMSG) to harness the bidirectional flow direction [110]. Delafin et al. consider using variable pitch to control the angle of attack of the blades and improve the performance of Darrieus tidal turbines [111]. Aguayo et al. propose a mixed-integer programming method to design tidal-current farms in Chile by computing the number, locations, submarine cable connections of tidal turbines, and the tidal current farm's overall capacity [89].

Out of 16 papers summarised in the previous paragraph [89, 97-111], ten of them [97, 98, 100-102, 104, 106, 107, 110, 111] propose or review proposals for new technical developments which claim the potential for improving tidal turbines' design and performance. They are:

* a ditched high solidity tidal turbine to improve power & torque coefficient, thrust coefficient, and wake velocity profiles for a ditched, high solidity tidal turbine M.G. Borg et al. a [97, 98].

* better material for ditched, high solidity tidal rotors to reduce deformation M.G. Borg et al. [100, 101].

* improving the power output of tidal turbines by dredging Alvarez et al. [102].

* a new floating tidal turbine Brown et al. b [104].

* hydrofoil design using composite materials Nachtane et al. [106].

* method to optimize the generator design for tidal generation Djebarri et al. [107].

***** a tidal turbine with symmetrical airfoils and backwards swept blades to follow

* the bidirectional flow Dong et al. [110].

* reducing the angle of attack of the blades in the upstream half of the turbine to increase the flow speed Delafin et al. [111].

Of the ten [97, 98, 100-102, 104, 106, 107, 110, 111] which propose specific technical developments, all rely on (or review other authors' use of) computer design algorithms and performance simulation models.

Seven authors verify their simulations by comparing results with measured outputs from tidal turbine arrays M.G. Borg et al.[97, 98], Dong et al. [110], Alvarez et al. [102], Brown et al. [104], Djebarri et al. [107], Delafin et al [111]. 8 report performance improvements in terms of greater annual power output through using ducted rotors M.G. Borg et al. a, increasing flow speed of a novel floating model Brown et al., re-designing generator Djebarri et al. [107], reducing the angle of

attack (Delafin et al. [111]), using corded blade rather than the solid blade M.G. Borg et al. b [97, 98] and design bidirectional flow turbine Dong et al. [110].

Just one author reports making operation more economical by improved installation techniques (Alvarez et al. [102]). None report achieving it through improved maintenance techniques.

Finally, four authors of the 16 mention unresolved technical issues which need further research. These are considering turbulence and scour when dredging Alvarez et al. [102], improving the performance of the ducted, high-solidity tidal turbine using the optimised shell and webbing thickness M.G. Borg et al. b [97, 98], coupling the upstream and downstream halves of a turbine to improve power coefficient Delafin et al. [111], and introducing the use of composite materials in tidal current turbines because of their excellent mass/durability relations Nachtane et al.

2.3.3 The Status of Offshore Tidal Energy in New Zealand

Bellve, Austin and Woods [73] cited Hicks and Hume's data in a 2007 report proposing the Kaipara harbour as most suitable for tidal energy generation. In 2011 Crest Energy, based on this evaluation, proposed installing 200 marine turbines in the Kaipara Harbour. It was anticipated, given the available currents, that each turbine will generate ~1.2 MW peak with expected power capacity of 1.750 GWh per annum. The Crest Energy proposal didn't go ahead, and project had been put in hold. Intellectual property (designs, models, economic analyses) and development rights were sold to another company Todd Energy in 2013.

Tidal and wave power are examples of emerging technologies that may become viable forms of electricity generation for New Zealand in the future [15].

2.4 Literature Review on Offshore Hybrid Systems

Deployed on floating bodies or along with cables, offshore energy harvesters can convert wave, solar, tidal, ocean current, and other renewable energy sources to stable electrical energy [112]. Hybrid them with wind electricity generation would reduce the currently significant operations & maintenance (O&M) of a wind turbine (WT) which are around 10-25% of the total cost of the electricity, and a lower transmission cost [113, 114].

Combining two systems in the area generally required for one can realise the potential for a higher energy density [23]. Energy service will be available even in the absence of one type of energy [114].

A trend in recent years towards installing distributed generation resources (DER) alters the traditional operating principle of electricity supply. Parts of a network can now operate in isolation from the main supply grid [115]. A distributed network consists of one or more microgrids with a couple of points to provide electricity demand and increase the reliability of the power supply [116].

The terms microgrid and mini-grid are often mixed. To understand the difference, first, the term "grid" needs to be defined clearly: The main grid is a network of large generation stations collectively with a GW power rating to carry power through transmission lines that connect from sub-stations to multiple supply networks at different locations [117]. A mini-grid has small generation sources with a collective MW power rating, is disconnected from the larger main grid, and connects to one local supply network [118]. A microgrid is a group of loads and energy resources that are individually controllable, in the range of kilowatts to megawatts [119]. A microgrid can be operated in a grid-connected or disconnected mode [120]. In remote areas isolated from main or mini-grids, electricity is already being supplied in a relatively expensive and quick way through off-grid (or island-mode) microgrids [2].

2.4.1 History of Offshore Hybrid Energy Generation

By bringing together two marine renewable technologies with considerable synergies, the combined harnessing of offshore energies presents excellent potential for development. This is corroborated by some recent European Union (EU) funded projects: MARINA[9], ORECCA[10], TROPOS[11], MERMAID[12] and H2OCEAN[13] [121]. MARINA classifies combined wave–wind systems according to the technology, water depth (shallow, transition or deep water), or location relative to the shoreline (shoreline, nearshore, offshore). ORECCA analyses the offshore renewable energies (ORE) combined resources in Europe. Looking particularly at the combined wave–wind resource in Europe, this can be divided into three main sea basins: the Mediterranean Sea, North and Baltic Seas and the Atlantic Ocean. TROPOS is aimed at developing a floating multi-purpose platform system for deepwater [121]. The MERMAID project seeks to develop concepts for the next generation of offshore activities for multi-use of ocean space. It proposes new design concepts for combining offshore activities, like energy extraction, aquaculture, and platform-related transport at various ocean areas [122]. H2OCEAN is developing a wind-wave power open-sea platform equipped for hydrogen generation with support for multiple energy users [123].

The main projects installed in the previous decade 2010-2019 were 2.3 MW Hywind in Norway year 2009, 2 MW Principle Power in Portugal year 2011, MOE project in Japan with capacities of 100-kW half-scale model in 2012 and 2 MW full scale in 2013 [124].

[9] Maritime industry authority
[10] Offshore renewable energy conversation platform coordination action
[11] Modular multi-use deep water offshore platform harnessing and servicing Mediterranean, Subtropical and Tropical marine and maritime resources
[12] Metrication and resource modelling aid
[13] H2 refers to hydrogen and ocean refers to wind-wave power

2.4.2 Recent Developments in Offshore Hybrid System Technology Worldwide

Da et al. propose a control scheme for a hybrid system. Adjusting the generator's rotation speed, can maximize the system's output power under fluctuating wind or tidal current [125]. Li et al. show integration of floating wind turbines with a wave energy converter and tidal turbines increase the power production by 22% - 45% [126]. Lande et al. model co-location of a wind turbine with an array of tidal stream turbines in MeyGen site located in the Pentland Firth, UK. It will increase energy yield by around 11% and decrease Levelized cost by 10% [127]. Nichita et al. present the "accelerated simulation time" method and its experimental validation; Wind/tidal turbine characteristics are obtained using the simulation approach developed at GREAH lab and are validated with an actual ocean turbine installed in the Circulating Water Channel at Inha University Ocean Engineering Laboratory, South Korea [128]. Phurailatpam et al. [129] present a DC microgrid for rural applications in India using wind turbine (WT) and photovoltaic panels (PV). Azaza et al. give some insight and techno-economic analysis of microgrid deployment in different Swedish regions using PV/WT/DG, a battery bank, and an energy management system to identify the optimal system size and configuration [130]. Thakur et al. design, construct, and test a new physical simulator in a real microgrid environment under different operating conditions. The simulator replicates the behaviours of a designed wind turbine. The experiments have also shown that the designed wind turbine can work in harmony with PV power modules and battery storage in response to weather and load variations in an island microgrid environment [131].Wang et al. analyse the stability of a microgrid system containing an offshore wind farm (OWF), an offshore tidal farm (OTF), and a seashore wave farm (SWF) fed to an onshore power grid through a high-voltage direct current (HVDC) link based on a voltage-source converter (VSC) [24]. Adetunji et al. propose an optimized grid-connected microgrid for South Africa using photovoltaic panels (PV) and a supporting lead-acid battery for downtime [132]. Kitson et al. present a DC microgrid system, interfacing wind and solar using a power electronic interface with droop functions. A case study site in Nepal is simulated to demonstrate the system's performance to variable generation and

loads [133]. Oulis Rousis et al. designed an off-grid system in Greece relying on PV, diesel generators, and batteries for energy storage [134]. Phurailatpam et al. compare different scenarios of DC microgrids for Indian context using wind and photovoltaic panels for rural and urban power supply in India [135]. Faridnia et al. designed a grid-connected microgrid for a tidal farm near Darwin, in the north of Australia, including tidal power as the main supply, a pumped hydro system (PHS) with 1000kWh capacity as the long-term storage system and a micro-turbine (MT) with the objective of minimizing the operating cost [136]. Colombo et al. added Photovoltaic (PV) to power-to-gas (P2G) to reduce emissions [137].

All 13 papers reviewed in this section [23, 24, 125-130, 132-135, 137], propose or review proposals for new technical developments which claim the potential for enabling hybrid generation from offshore renewable sources. They are:

* Dynamic model of controlling the speed of a gearless generator using PWM rectifiers to harvest more power Da et al. [125].
* Proposing a new concept of floating system adding wind to tidal turbines at sea site with a water depth of 320 m Li et al. [126].
* Adding a wind turbine with an array of tidal turbines in the UK Lande et al. [127].
* Emulator of wind/tidal system in GREAH lab of France Nichita et al. [128].
* Offgrid design combining wind and PV in India Phurailatpam et al. a [129].
* Offgrid design combining battery, wind and PV in Sweden Azaza et al. [130].
* on grid design combining battery and PV in South Africa Adetunji et al. [132].
* Offgrid community in Nepal combining wind and PV Kitson et al. [133].
* Offgrid design combining battery, diesel generator and PV in Greece Oulis Rousis et al.[134].
* Offgrid and ongrid design of wind and PV in India Phurailatpam et al. b [135].

Adding PV to P2G in the campus microgrid of the University of California Colombo et al. [137].

* Feasibility design of co-location of offshore turbines in Isle of Islay (Gruszczynski A et al.[23].
* Microgrid design of an OWF, an OTF, and an SWF fed to grid through VSC-based HVDC link Wang et al. [24].

Five of these verify their simulations, and another five may, by comparing results with measured outputs from offshore hybrid systems that are installed or under construction:

* compared with a wave energy converter developed under the collaboration between the National Renewable Energy Laboratory (NREL) and the Sandia National Laboratories Li et al. [126].
* validated with real ocean turbine installed in Circulating Water Channel of Inha University Ocean Engineering Laboratory Nichita et al. [128].
* Offgrid design combining wind and PV in India Phurailatpam et al. a [129].
* comparison with current grid measured in India Phurailatpam et al. b [135].
* co-located offshore turbines in the Isle of Islay Gruszczynski A, et [23].
* Co-location of a wind turbine with an array of tidal stream turbines in the Pentland Firth, UK Lande et al. [127].
* A lab-scale microgrid including PV, wind turbine and battery storage in Canada Thakur et al. [131].
* Increasing the share of renewable energy and accelerating decarbonization with the integration of PV and P2G Colombo et al. [137].
* Grid-connected design of a tidal farm with a micro-turbine (MT) in Australia Faridnia et al. [136].

At least four reports that the operation of hybrid systems is feasible (Gruszczynski A et al.[23], Nichita et al. [128], Phurailatpam et al. b [135], Colombo et al. [137]. Another five reports that their hybrid systems are under construction or about to be constructed (Li et al. [126], Lande et al. [127], Phurailatpam et al. a [129], Wang et al. [24], Faridnia et al. [136]). So, it can not evaluate feasibility yet. As yet, none report on whether installing and operating a hybrid system is economical. Two of the designs (Thakur et al. [131] and Colombo et al. [136] constructed & under construction rely on microgrids for electrical linkage.

Finally, three of the 13 mention unresolved technical issues which need further research. These are power management of the proposed hybrid system Da et al. [125], the structural dynamics of turbine control Li et al. [126], vessel capability impact on overall Levelized cost[14] Lande et al. [127].

2.4.3 The Status of Offshore Hybrid Energy in New Zealand

In New Zealand offshore wind and tidal energies has not been used for providing electricity demand. Thus, it worth to investigate the idea of hybrid offshore energy as two predictable sources of energy which integrating them with a same foundation can generate more electricity in lower cost.

2.5 Conclusions

Compared with on-shore wind energy resources, off-shore wind fields have many advantages, such as persistent wind, faster-flowing speed, higher uniformity, and longer available time per year. Flat sea surface and low turbulence intensity promote the vigorous development of the offshore wind power industry. More importantly, installing wind turbines in the ocean can protect the environment and save land resources. The vast ocean area provides suitable conditions for developing large-scale wind farms and turbines. The power generation by the identical turbines in the off-shore area is 50%– 100% higher than in the on-shore area.

The high-capacity factor of 45% of NZ in terms of wind generation makes it a favourable place for investment in wind energy when it compared to global average of 24%, and 16% in Germany. Increasing the capacity factor from 30% to 40 % can reduce the cost of generation from 115 to 85 $NZ/MWh. Also, New Zealand is an ideal candidate for tidal energy production with strong tidal currents in certain areas, such as Cook Strait, French Pass and Foveaux Strait. Having this potential in offshore wind and tidal energy and the aim of government to reach

[14] The average cost of production of 1kWh of electricity

100% electricity production from renewable sources by 2030, integrating both offshore sources for reducing the cost of electricity and increasing power generation worths investigation.

Chapter 3

Potential Offshore Renewable Energy Sources in New Zealand

3.1 Introduction

The future of the New Zealand (NZ) electricity system has been the focus of a number of studies in recent years with reports undertaken by Transpower, the Interim Climate Change Committee, MBIE (Ministry of Business, Innovation and Employment) and the Productivity Commission being the most noteworthy. These reports address the growth of NZ's electricity market suggesting a total annual demand of between 49-57 TWh by 2035 and estimating total demand of up to approximately 70 TWh by 2050. NZ's current demand is ~40 TWh/annum [80]. So, it is essential to look for new sources of power generation. While New Zealand is surrounded by water and there is a good potential of offshore energy, it has not been used for power generation yet.

This chapter gives a brief explanation of wind and tidal sources as two good sources of offshore around New Zealand coast.

3.2 Wind Potential of New Zealand

In this section typical wind patterns in New Zealand recorded by NIWA introduced to evaluate the optimized sites among them with higher amount of power generation. A comprehensive simulation model has been set up, using several available commercial software packages to test the performance, capacity and efficiency of the results. Available wind records have been used from NASA to conduct simulation model runs of them. Homer Pro software used to propose a microgrid design for each site and calculate power. Generation of electricity with wind

turbines depends on the wind speeds and cut-in speed of the wind turbines. In other words, to reach maximum efficiency from wind power, the first step is to analyse the wind speeds of the site where turbine will be located and then estimate the generated power from that turbine. To do it, it is necessary to find the range of wind speeds and the wind directions with demonstrating wind rose and the percentage of year a turbine is working in more than cut-in speed.

Wind energy is one of the renewable energy sources already being used to meet the world's massive demand for electricity and reduce use of its fossil fuels. Historically in New Zealand the main renewable energy sources have been geothermal and hydro power. However, in the future most incremental growth in renewable energy are forecasted to come from wind energy and geothermal energy capacity [78].
The percentage of generation electricity from wind in the decade 2011-2020 in comparison to total renewable sources used shown in Figure 3-1[138].

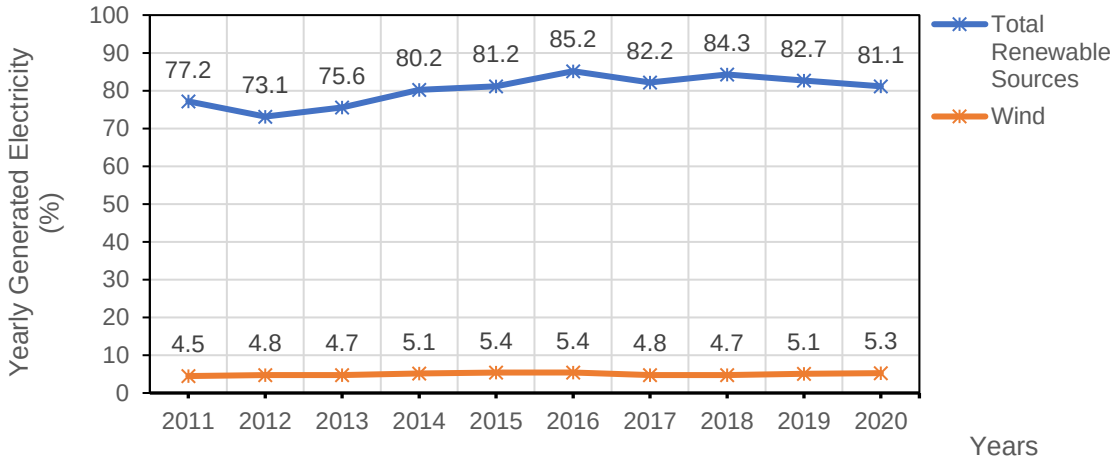

Figure 3-1: Percentage of electricity generation in New Zealand 2011-2020 [138].

Wind provided 2,232 GWh of electricity, or 5.1 %, of total electricity supply in 2019 which was 37 % of the capacity factor. Capacity factor for wind is the amount of electricity generated in relation to the maximum output capable of being generated by installed wind turbines over a period of time assuming no downtime for maintenance [79].

By 2030 it is predicted that wind generation in New Zealand will increase six-fold, producing as much as 20 % of all electricity. Wind farm capacity can be built as it

is essentially the most cost-effective form of electricity generation, being predictable, dependable and the costs of fuel are known (wind is free) [78]. The Ministry of Business, Innovation and Employment (MBIE) report issued on June 2020 [80] describes the desired wind generation growth between 2020 and 2060. It shows that 2,500 MW of new wind generation is required between 2020 – 2030, 1,500 MW between 2030-2040, 2,000 MW between 2040-2050, and 2,000 MW between 2050-2060 [80].

To reach the targeted wind generation growth, wind energy needs to be investigated from different aspects. The effects of configuration parameters on the performance of wind turbines have been thoroughly investigated [139]. RETScreen software was used to identify which of the harbour/estuary sites in New Zealand appear to have potential for wind power generation [3]. However, to ensure their better operation in an environment, some technical challenges remain to be resolved.

Historically, wind directions have been determined from eolian sandstones [140]. In modern wind turbines, control mechanisms and operation of yaw systems maximize wind power extraction from different wind directions [141]. But no one has used climate models for predicting generated wind power in different wind patterns. To do this, Global Wind Atlas [142] is used to plot wind rose of current wind patterns in New Zealand and in the next step, wind speeds data from each site imported from NASA database [143] to WRPLOT view software [30] and Homer Pro [29] to find wind frequency distribution and output power in each site.

What is novel about the project described in this section is that it investigates the technical feasibility of wind generation directional-wise. The results will be enable to propose the sites with better efficiency.

Westerly wind patterns prevail in most parts of New Zealand. National Institute of Water and Atmospheric Research (NIWA) recording sites in 2014 summarize every hourly measurement, illustrating patterns of turbulence and calm in different places shown in Figure 3-2.

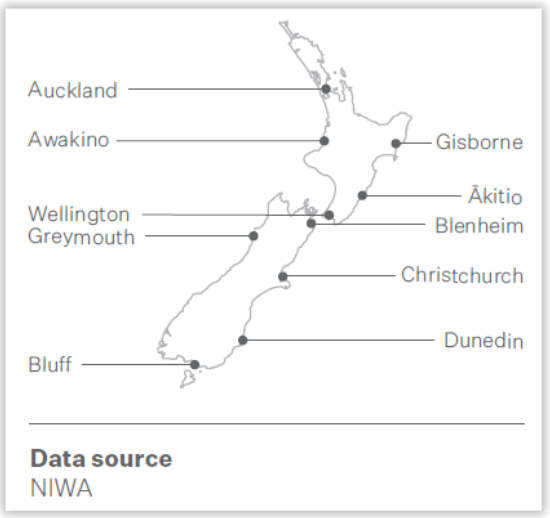

Figure 3-2: NIWA recording sites, selected to show typical wind patterns in 2014 [144].

Global Wind Atlas [142] is used to update wind patterns of New Zealand during 2021 as shown in left sides of Figure 3-3. For each site selected, scatter charts show how often and how strongly winds blow from different directions during 2021. The centre of each plot represents calm conditions. Wind strength is shown by the distance from the chart centre, in 1 metre-per-second steps. The further a tick is from the calm centre, the stronger the wind. Wind direction is determined by angle from the centre. Northerly winds are at a 12 o'clock position; easterlies at 3 o'clock. The duration for which wind blew from a particular direction at a certain strength is shown defining wind class frequency distribution graphs. WRPLOT view software [30] was used to plot wind frequency distribution downloaded from NASA Surface Meteorology and Solar Energy database [143]. Totally 8,760 wind speeds for 12 months in 1 h interval imported to software to introduce wind class of sites. Assuming a typical cut-in speed of 4 ms^{-1}, WRPLOT[30] enables the percentage of power generation for each sites when wind blows over cut-in speed as presented on right sides of Figure 3-3 [142].

(a)

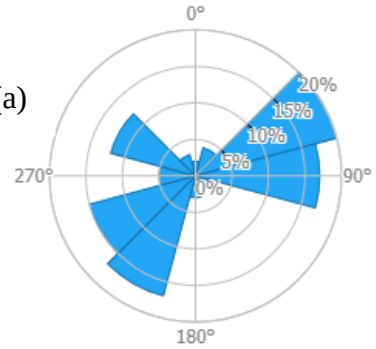
0°
90°
180°
270°
20%
15%
10%
5%
0%

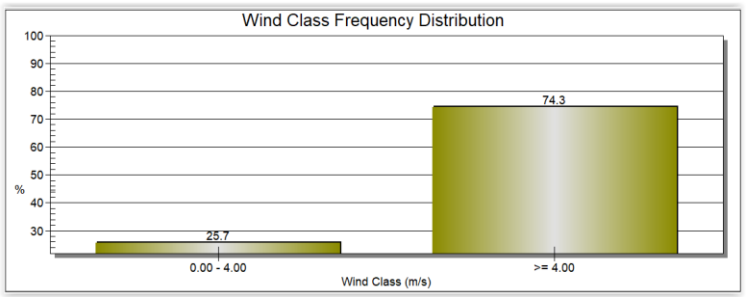
Wind Class Frequency Distribution
100
90
80
70
60
50
40
30
%
74.3
25.7
0.00 - 4.00
>= 4.00
Wind Class (m/s)

(b)

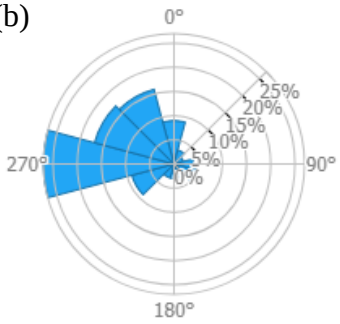
0°
90°
180°
270°
25%
20%
15%
10%
5%
0%

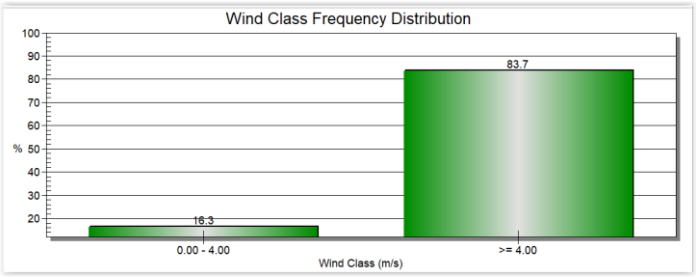
Wind Class Frequency Distribution
100
90
80
70
60
50
40
30
20
%
83.7
16.3
0.00 - 4.00
>= 4.00
Wind Class (m/s)

(c)

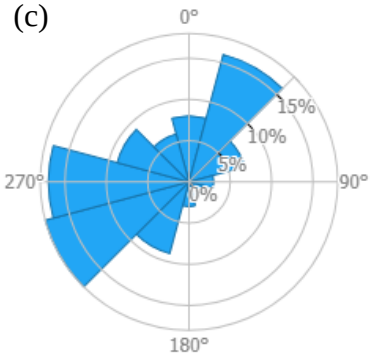
0°
15%
10%
5%
270°
90°
0%
180°

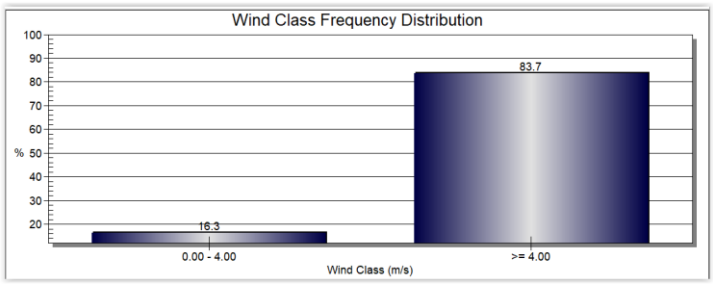
Wind Class Frequency Distribution
100
90
80
70
60
% 50
40
30
20
83.7
16.3
0.00 - 4.00
>= 4.00
Wind Class (m/s)

(d)

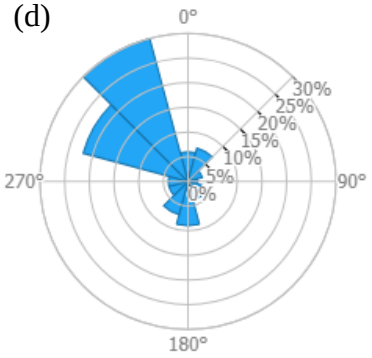
0°
30%
25%
20%
15%
10%
5%
270°
90°
0%
180°

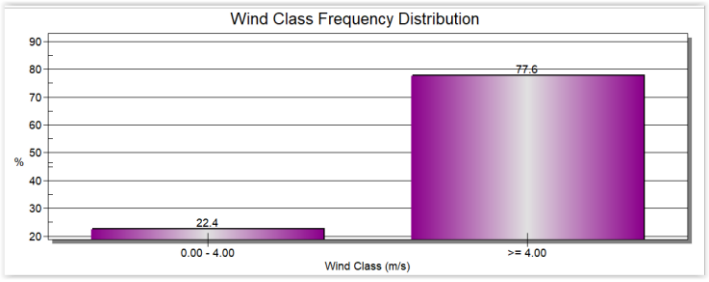
Wind Class Frequency Distribution
90
80
70
60
50
%
40
30
20
77.6
22.4
0.00 - 4.00
>= 4.00
Wind Class (m/s)

(e)

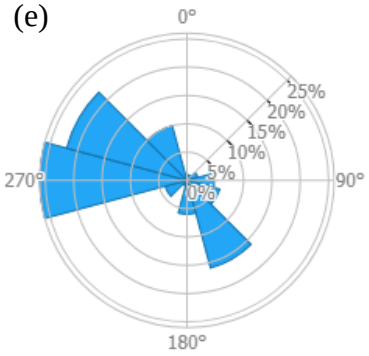
0°
25%
20%
15%
10%
5%
0%
270°
90°
180°

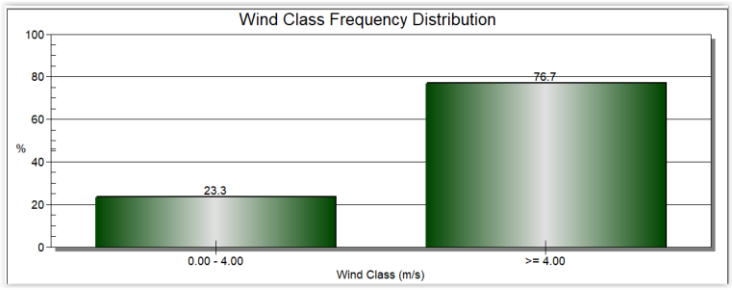
Wind Class Frequency Distribution
100
80
60
40
20
0
%
76.7
23.3
0.00 - 4.00
>= 4.00
Wind Class (m/s)

(f)

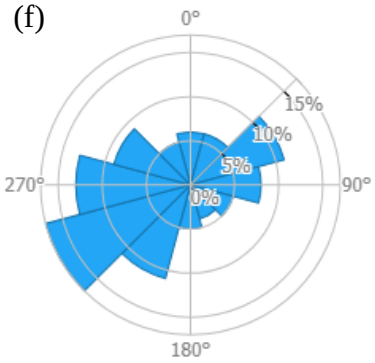
0°
15%
10%
5%
0%
270°
90°
180°

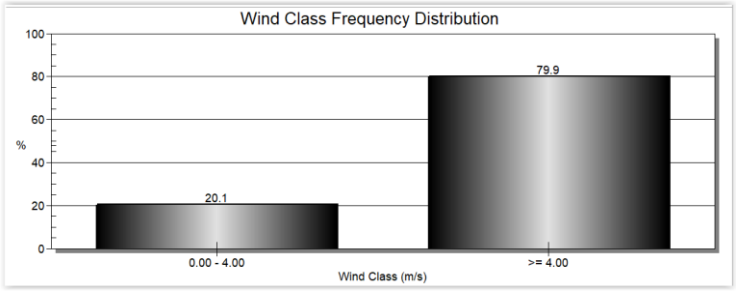
Wind Class Frequency Distribution
100
80
60
40
20
0
%
79.9
20.1
0.00 - 4.00
>= 4.00
Wind Class (m/s)

(g)

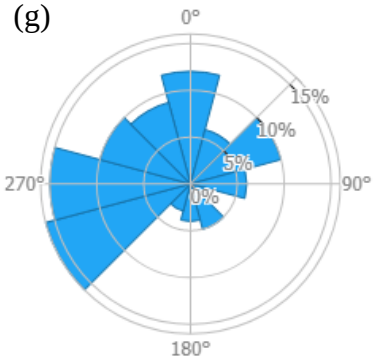
0°
15%
10%
5%
0%
270°
90°
180°

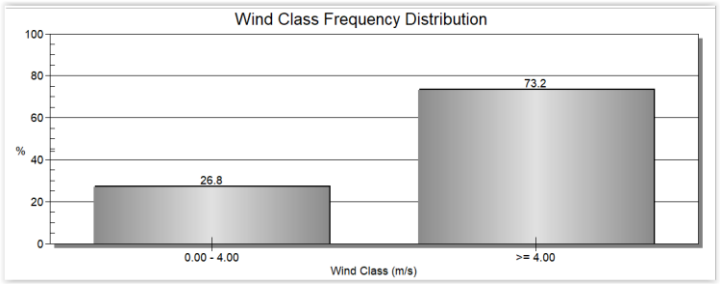
Wind Class Frequency Distribution
100
80
60
40
20
0
%
73.2
26.8
0.00 - 4.00
>= 4.00
Wind Class (m/s)

(h)

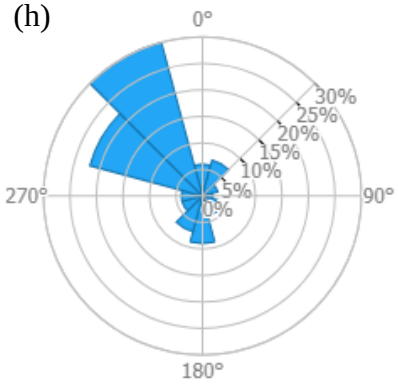
0°
30%
25%
20%
15%
10%
5%
0%
270°
90°
180°

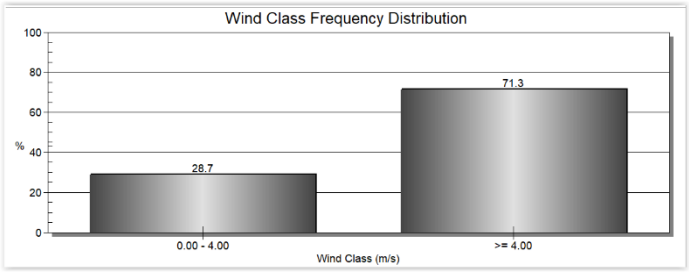
Wind Class Frequency Distribution
100
80
60
40
20
0
%
71.3
28.7
0.00 - 4.00
>= 4.00
Wind Class (m/s)

(i)

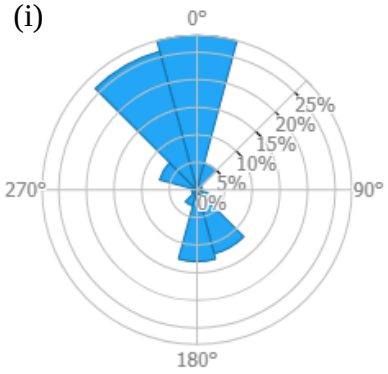

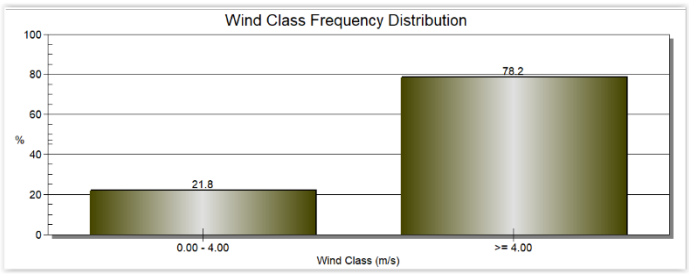

(j)

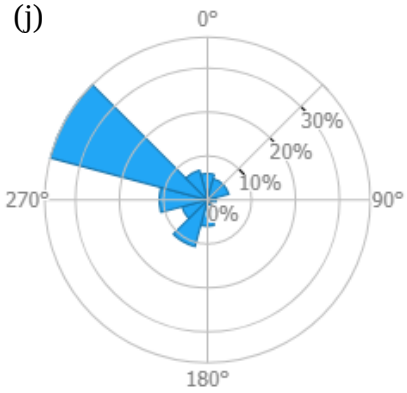

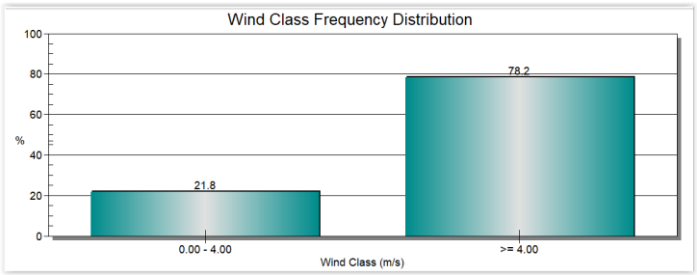

Figure 3-3: Wind patterns of New Zealand; (a) Christchurch: gentle winds from most directions, (b) Bluff: strong westerlies, moderate easterlies and southerlies, (c) Dunedin: wind from most directions except the north-east and south, (d) Greymouth: strong south-westerlies and easterlies, (e) Blenheim: moderate westerlies and north westerlies, (f) Auckland: dominated by westerlies, south westerlies, and north easterlies, (g) Awakino: strong westerlies and moderate south-easterlies, (h) Gisborne: a calm year of mostly

gentle winds, (i) Wellington: strong northerlies and southerlies, (j) Akitio: wind from all directions, with especially strong north-westerlies.

The sites in Figure 3-3 show typical wind speeds and directions on different New Zealand coastlines:

* West coast of the South Island (Greymouth site) has strong south-westerlies (from sea), also strong easterlies (from mountains). However, this coast is stormy (frequent big waves), so cost of building and maintaining offshore turbine towers may be too high. In order to understand the economics of offshore wind energy projects, the following key parameters need to be taken into account:

- foundations are considerably more expensive. Costs depend on both the water depth and the chosen construction principle. For a conventional turbine sited on land, the share of the total cost for the foundations is around 4–6%. In the two largest Danish offshore wind farms (Horns Rev and Nysted) this percentage is 21%, and may be even higher in deeper water or with less favourable soil conditions;
- the construction and installation techniques are less developed than for onshore projects. This has an impact both in terms of cost and of reliability. The visible efforts that are being made in R&D are expected to bring these costs down;
- O&M costs are substantially higher than for onshore projects. The higher cost of transport, as well as reduced site access, due to wave and weather conditions are the main causes. Having an efficient O&M strategy is extremely important for keeping costs down. O&M costs can constitute up to 30% of overall costs for offshore wind farms;
- electrical connections between the turbines, and between the farm and the onshore grid, generate substantial additional costs compared to onshore wind projects. Going back to the example of Horns Rev and Nysted, they accounted for another 21% of the total investment costs. Again, this percentage will rise in deeper or more distant waters;
- environmental analyses tend to be more stringent, sometimes including R&D programs to monitor impact on mammals and other sea communities. With the generalization of offshore wind energy projects, these are expected to decrease in cost and complexity; and

- the investor faces higher risks, which translate into higher interest rates and premiums [145].

Sheltered sites on this coast are the fiords at the south end, e.g., Dusky Sound. However, fiord sides are mountains which cause turbulent changes in wind direction and velocity. Another sheltered site is a big tidal estuary, Whanganui Inlet at the north end near Farewell Spit. Here mountains are not so high, so turbulent wind changes are not so great.

* West coast of the North Island (Awakino site) has strong westerlies and moderate south-easterlies. This coast is also stormy, so cost of building and maintaining offshore turbine towers may also be too high here. Sheltered sites on this coast are several large harbours e.g. Manukau. Shores are hilly to flat, so local turbulence may not be a problem when operating wind turbines.

* East coast of the North Island. North-east part from North Cape to East Cape is represented by the Auckland site. This coast is dominated by south-westerlies, but also has strong north-easterlies. Sea bottom is shallow creating opportunity for offshore tower installation in absence of big waves, (except during north-easterly storms, when wave damage might be a risk). Here are many harbours with deep channels, also many tidal estuaries.

The east part—from East Cape to Cape Kidnappers—is represented by the Gisborne site. Here, winds from all directions are mostly gentle. So, this coast may be unsuitable for wind turbines (although north-west winds blow from inland ranges towards coast—and may be stronger in some years, than the wind rose diagram indicates). The east part's harbours and estuaries are few, small, and shallow.

The south-east part from Cape Kidnappers to Cook Strait is represented by the Akitio and Wellington sites. Winds blow from all directions, and especially strong north-westerlies and northerlies blow from inland ranges towards coast. This coast may have potential for installing wind turbines offshore (but just close to coast where sea bottom is shallow—Hikurangi Trench farther out is too deep). There are no harbors, just a few estuaries (miniscule).

* North coast of South Island (Blenheim site). Between Farewell Spit and Cape Campbell, dominant winds are moderate westerlies and north-westerlies. The offshore sea bottom is shallow in the bays (Golden Bay, Tasman Bay, Cloudy Bay). Marlborough Sounds are narrow harbors with deep channels. Additionally, there are some estuaries, e.g. Collingwood, Waimea, Nelson, and Wairau. However,

because this coast does not have a strong wind prevailing from one direction, it may not be as good for wind energy.

* East coast of South Island (Christchurch and Dunedin sites). Winds from most directions are gentle to moderate. Along the Canterbury coast, north-west winds blow from the mountains across the plains (and may be stronger in some years, than the wind rose diagram indicates). On the Otago coast (Dunedin), south-west winds have greater frequency and strength. However, overall, this coast may not be good for finding suitable sites.

* South coast of South Island (Bluff site) has very strong prevailing westerlies, plus moderate easterlies and southerlies. Offshore sea bottom is shallow in Foveaux Strait. Here, wave attack is frequent, but waves are moderately sized. There is only one large harbor (Bluff), and several large shallow estuaries (Mataura, Oreti, Aparima). The south coast of Stewart Island is stormier, with very large waves. It has two large harbors (Paterson and Pegasus) [3].

Homer Pro is used to calculate annual generated power [29]. To do so, Homer needs at least 8,760 value for 12 months. So, if there be a value for 1 h, a total of 8,761 (total number of hours in a year) values of wind speed can be gathered and imported to software to help Homer calculate the annual average water speed. Based on the geographical coordinates of above sites, their annual power is summarised in Table 3-1.The maximum efficiency can be seen in Dunedin and Bluff sites respectively. In both sites, wind blows over 4 ms^{-1} in 83.7% of year. The minimum wind power is in Gisborne and Awakino shows east of north island is not a good area for investment at all. While percentage of power generation in Gisborne and Awakino is good values of 71.3% and 73.2%, the speed of wind is still far from cut-out speed to generate enough electricity.

Table 3-1:The power generation in typical wind pattern sites

Location	Latitude (deg)	Longitude (deg)	Annual Power (MW)	Annual Percentage of Power Generation
Christchurch	-43.510962 °S	172.581139 °E	137,550	74.3
Bluff	-46.60228 °S	168.339729 °E	225,076	83.7
Dunedin	-45.852222°S	170.50027778°E	237,060	83.7
Greymouth	-42.474123°S	171.208191°E	161,884	77.6
Blenheim	-41.521174°S	173.959236°E	155,116	76.7
Auckland	-36.54164°S	174.550781°E	172,315	79.9
Awakino	-38.659778°S	174.624939°E	131,836	73.2
Gisborne	-38.643691°S	178.015594°E	117,517	71.3
Wellington	-41.252774°S	174.718323°E	168,325	78.2
Akitio	-40.618122°S	176.412964°E	168,889	78.2

While wind patterns in New Zealand can be analyzed with wind roses, the main issue is recognizing the superior wind patterns based on their generated power. The results of reviewing information about wind speeds and directions on the New Zealand coastline reveals that Dunedin and Bluff can generate 237,060 and 225,076 MW power respectively in 83.7 % of year based on their wind pattern analyzed in Figure 3-3 (b) and (c).

Investment on wind power considering wind rose is crucial to increase the capacity of wind generation to an optimized level.

3.3 Tidal Potential of New Zealand

Open-water tidal circulation around the New Zealand coast is anti-clockwise. It is the reason why, when tides on the west coast are high tides on the east coast are low. It also creates strong reverse-direction tidal currents in open water where the two coasts meet i.e. North Cape to Cape Maria van Diemen, Cook Strait, Foveaux Strait, and South Cape of Stewart Island [146]. Close to shore, where open-water tidal circulation moves across shallow sea bed and enters bays, harbours or estuaries, normal reversals of tidal current are observed twice a day i.e. incoming and outgoing tides [85].

Tidal circulation is superimposed on surface water movements [147] which are part of ocean circulation between the Pacific and Antarctic (Figure 3-4):

1. East Auckland Current: From North Cape down the Auckland east coast to the Bay of Plenty.
2. West Auckland Current: From north and west of Cape Reinga down the Auckland west coast towards Kaipara.
3. Southland Current: From the West Coast Sounds region and to the west, east through Foveaux Strait and up the east coast of the South Island.
4. Canterbury Current: From Banks Peninsula north past Cook Strait and the east coast of the North Island as far as Gisborne.
5. Westland Current: From west coast South Island up to Cape Farewell and less markedly north along the Cape Egmont coastline and beyond towards Manukau Harbour.
6. D' Urville Current: From off the western entrance to Cook Strait, east into the Strait and thence south towards the narrows of Cook Strait.

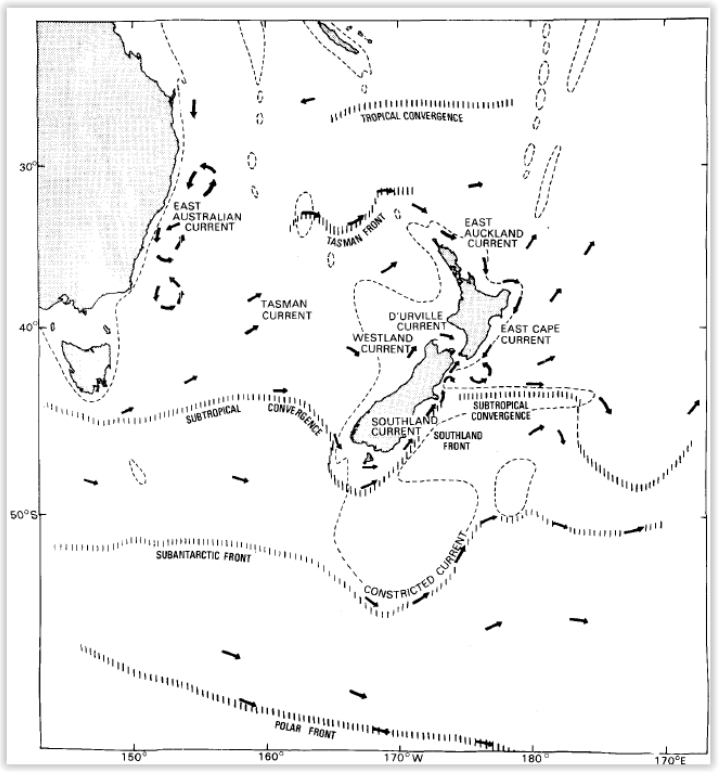

Figure 3-4: Ocean Currents around New Zealand [148].

Huckerby and Johnson (2008) modelled tidal flow around the New Zealand coasts[149, 150]. The national distribution of utilizable open ocean tidal currents is very limited. Most areas have very low mean current speeds (<1 m/second) and only four areas have mean current speeds that exceed this value (Figure 3-5). From north to south these are Cape Reinga, Cook Strait, Foveaux Strait and south of Stewart Island, identifying four areas where tidal velocities are particularly favourable for tidal generation. Two (north of Cape Reinga and south of Stewart Island) are exposed to severe storms and a third (Cook Strait) is deep water (most parts too deep to attach towers to seabed), also prone to undersea earthquakes. The fourth (Foveaux Strait and adjacent estuaries) is shallow water (seabed 10 to 40 metres below sea level), so easier and cheaper to install turbines. Only Foveaux for offgrid design and Cook Strait for ongrid design can be considered.

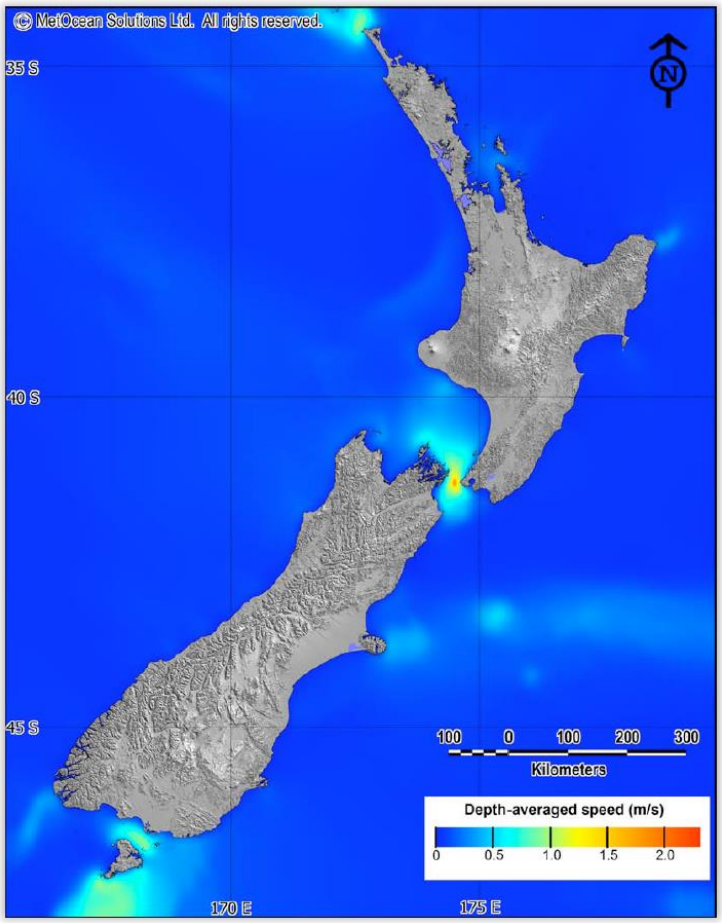

Figure 3-5: National Depth-averaged Tidal Current Speeds for Mean Spring Flows (in m/second) [149].

Tidal volumes and current velocities have been determined in harbours on the northern coast of the North Island (see Table 3-2) by Hicks and Hume [151]. Their investigation shows that the largest are Kaipara, Manukau, Hokianga, Rangaunu and Whangarei Harbours respectively. Of these five, the spring tidal flows of Kaipara Harbour are the greatest at tidal prism volume. The Kaipara Harbour's tidal currents flow four times daily, exchanging at each spring flood or ebb movement a tidal prism of ~1,990 million cubic meters at velocities of <2.4 meters per second and average current of 1.12 meters per second. Tidal currents only attain <2.4 meters per second and therefore marine turbines can produce power over a range of current flows without needing to 'feather' the blades.

Table 3-2:Characteristics of tidal inlets in North Island [151].

Inlet	Mean Spring Tide Range (m)	Mean Spring Tidal Prism 106 m^3)	Throat Width @MT (m)	Throat Area @ MT (m^2)	Throat Depth (mean) @ MT (m^2)
Hokianga	2.77	228	1090	13000	11.9
Kaipara	2.68	1990	5600	82000	14.6
Katikati	1.6	95.8	380	4680	12.3
Kawhia	2.9	121	600	11000	18.3
Mangawhai	1.8	6.55	216	500	2.31
Manukau	3.38	918	1900	46000	24.2
Ngunguru	1.71	3.83	109	310	2.84
Ohiwa	1.6	28.1	308	1880	6.10
Parengarenga	2.13	73.0	500	7000	14.00
Raglan	2.8	46.0	640	3600	5.63
Rangaunu	2.0	134	1012	6490	6.41
Tairua	1.6	5.02	130	430	3.31
Tauranga	1.6	131	480	6260	13.0
Whananaki	1.8	1.46	79	130	1.60
Whangarei	2.1	155	790	14600	18.5
Whangateau	2.2	10.5	174	660	3.79
Whitianga	1.6	12.6	240	1300	5.42

Farther south, some data are available from Heath [152] as shown in Table 3-3 showed large open bays have big tidal prisms but weak tidal flows. Small harbours or estuaries can have strong flows, but their prisms are small. Large harbours with deep narrow entrances combine large tidal prisms with strong tidal flows. Heath's measurements indicate Aotea, Waimea, Parengarenga, Tauranga, Kawhia, Rangaunu, Raglan, Whangarei, Bluff, Otago, Hokianga, Manukau, Lythelton, Kaipara, Akaroa and Wellington Harbour could be worth investigating.

Table 3-3:Physical characteristics of 32 New Zealand inlets[152].

Inlet Name	Cross-Sectional Area Entrance		Tidal Range (m)		Tidal Compartment	
	Low Tide Spring (10^3 m^2)	Mid Tide Spring (10^3 m^2)	Spring Tides (m)	Neap Tides (m)	Spring Tides (106 m^3)	Neap Tides (10^6 m^2)
Moutere	0.4	0.9	4.2	2.4	15	9
Avon-Heathcote	-	-	2.1	1.3	11	6
Aotea	2.2	3.6	2.9	1.7	59	35
Waimea	2.3	5.8	3.4	1.8	58	31
Whanganui Inlet	2.3	3.9	2.9	1.5	42	22
Parengarenga	6.2	7	2.13	1.4	73	48
Nelson	2	2.6	3.4	2.6	30	23
Tauranga	7.3	7.8	1.62	1.24	178	136
Kawhia	8	11	2.9	1.7	121	71
Porirua-Pauatahanui	1.4	1.8	1.6	1.3	22	17
Rangaunu	7.1	8.8	2.0	1.5	134	101
Raglan	2.9	3.6	2.8	1.8	46	29
Whangarei	13	14	2.46	1.74	164	116
Bluff	3.8	4.5	2.2	1.5	97	66
Otago	4.7	5.1	1.74	1.28	69	51
Hokianga	11	13	2.77	1.78	228	147
Manukau	42	46	3.38	1.95	918	530
Whangaruru	21	23	2	1.5	28	21
Lyttelton	28	30	1.92	1.64	72	61
Firth of Thames	400	440	3.72	2.68	2580	1860
Kaipara	73	82	2.68	1.52	1990	1130
Whangaroa	4.3	4.7	1.95	1.34	33	23
Akaroa	45	47	1.89	1.52	81	65
Doubtless Bay	642	652	1.9	1.4	346	255
Paterson Inlet	55	59	2.0	1.4	168	120
Tasman bay	2450	2560	3.44	1.8	16000	8300
Poverty Bay	140	146	1.4	1.2	81	70
Pelorus Sound	117	121	2.37	1.46	660	410
Bay of Islands	1034	1050	1.95	1.46	340	260
Wellington Harbor	38	39	1.01	0.94	88	82
Queen Charlotte Sound	880	890	1.4	0.5	98	35
Hawke Bay	5250	5300	1.34	1.22	3950	3600

Global Wind Atlas data have been used [153] to identify which of these harbour/estuary sites in Table 3-2 and Table 3-3, also have good wind runs (expressed as mean annual wind speed). The latitude, longitude, wind run and tide range of sites which appear to have potential for hybrid generation are summarized in Table 3-4.

Table 3-4: The geographical coordinates and tide range and wind run of New Zealand harbours and estuaries [152, 154].

Location	Latitude (deg)	Longitude (deg)	Spring Tides (m)	Neap Tides (m)	Annual Wind Speed(m/s)
Bluff	−46.6°S	168.3°E	2.2	1.5	10.7
Whanganui Inlet	−39.95°S	174.98°E	3.4	2.6	4.3
Hokianga	−35.52°S	173.37°E	2.77	1.78	4.5
Kawhia	−38.06°S	174.83°E	2.9	1.7	4.7
Manukau	−37.0°S	174.66°E	3.38	1.95	5
Kaipara	−36.41°S	174.21°E	2.68	1.52	6.4
Aotea	−37.98°S	174.84°E	2.9	1.7	4.7
Parengarenga	−34.51°S	172.94°E	2.13	1.4	8.5
Tauranga	−37.68°S	176.16°E	1.62	1.24	4.1
Rangaunu	−34.94°S	173.27°E	2.0	1.5	4.5
Whangarei	−35.75°S	174.35°E	2.46	1.74	6.5
Otago	−45.81°S	170.64°E	1.74	1.28	5.9
Lyttelton	−43.61°S	172.73°E	1.92	1.62	4.2
Akaroa	−43.79°S	172.49°E	1.89	1.52	4.2
Wellington	−41.28°S	174.83°E	1.01	0.94	7.3
Firth of Thames	−37.0°S	175.4°E	3.72	2.68	5.7

Many sites identified by Heath or Hicks and Hume as having strong tidal flows and large tidal prisms can be ruled out because wind run is not good (Hokianga, Kawhia, Aotea, Tauranga, Lyttelton, Akaroa). Some harbors in Table 3-4 can be ruled out, because they have commercial ports. Here turbine monopiles will be navigation hazards (except if the deep-water channel extends upstream beyond wharf). Commercial ports ruled out are Whangarei, Waitemata (Auckland), Manukau (Auckland), Tauranga (south entrance), Port Nicholson (Wellington), Lyttelton (Christchurch), Otago (Dunedin), and Bluff (from wharf to entrance).

Some estuaries must also be ruled out, because they contain marine reserves, or they are next to national parks etc. (Port Pegasus, Paterson Inlet, Akaroa, parts of Golden Bay, Whanganui Inlet). Here, the Department of Conservation will not allow resource consent.

Finally, a few estuaries with deep entrance channels have to be ruled out because their shores are inhabited by tangata whenua (Maori) who say that the estuaries are taonga (valuable possessions) for fishing, gathering shellfish etc; or that the shores

are wahi tapu (sacred places) which must not be disturbed. Examples are Parengarenga, Whangaroa, Bay of Islands, and Whangaruru. Maybe also Hokianga, Whaingaroa (Raglan), Aotea, and Kawhia.

3.4 Summary

The aim of this chapter was to identify the offshore sites having both high wind and tidal power generation. For wind, climate patterns revealed that Bluff near Foveaux and Wellington near Cook Strait can generate good wind power. While Dunedin, Auckland and Greymouth are also good sites for power generation, they have ruled out as they are onshore. For tidal energy, MetOcean model has identified that Foveaux and Cook Strait are ideal. So, based on this, accurate coordinates of these sites will be used for microgrid design and based on possibility of integration of turbines, appropriate methods will be proposed for structural design. As a result of the literature review, the research described in the following chapters will focus on resolving identified issues which are:

* Investigation the wind and tidal turbines can provide the demand of optimized sites (Chapter 4).

* Technical design of a hybrid system suitable for the site, including a microgrid for electrical linkage (Chapter 5).

* Whether such a system can generate be integrated using a same foundation for both wind and tidal turbines (Chapter 6).

* Predicating the power generation from different directions (Chapter 7).

Chapter 4

Selection of Turbines

4.1 Introduction

Several parameters contribute to selection of wind and tidal turbines as discussed. However, first parameter is site potential in terms of wind and tidal sources. After recognizing the sites capable for integration wind and tidal, the next question needs to be answered is where this power will be supplied and whether it is offgrid or ongrid. For both cases, the amount of load or power consumption is necessary. And finally, based on site location and the area electricity supplied, suitable turbines will be chosen.

4.2 Results of Evaluations

The literature review in Chapter Two identifies performance parameters which need to be considered when choosing a wind turbine for installation above sea level and a tidal turbine for below:

- Tip speed ratio
- Angle of attack
- Blade camber
- Hub height
- Rotor radius
- Rotor length
- Number of blades
- Rotational speed
- Air/water density
- Air/water temperature
- Air/water velocity

A preliminary evaluation of each performance parameter has been carried out for typical wind and tidal turbines, using QBlade simulation software and MATLAB. Results are presented in Appendix B. Evaluations of commercially available

turbines are summarized in Table 4-1 and Table 4-2. They will be referred to in Sections 4.3 (Selected turbines for offgrid design) and 4.4 (Selected turbines for ongrid design).

Table 4-1:Various wind turbine design characteristics

Type	Capacity (MW)	Cut-in (m/sec)	Cut-out (m/sec)	Axis (HAWT or VAWT)	Diameter (m)	Hub height (m)
Wind World W2500	0.22	2	25	HAWT	25	31
Bonus B35/450	0.45	4.5	28	HAWT	35	30/35
Bonus B76	2	3	25	HAWT	76	60/80
Vestas V80	2	4	25	HAWT	80	60/67/78/100
Siemens SWT 3.6-107	3.6	4	25	HAWT	107	80
Siemens SWT 6-154	6	4	25	HAWT	154	Site specific
General Electric GE 1.5xle	1.5	3.5	20	HAWT	82.5	58.7/80
Areva M5000-116	5	4	25	HAWT	116	-
V150-6	6	3	25	HAWT	150	105/125/155
Samsung S7-171	7	3	25	HAWT	171.2	110
Enercon E-126	7.580	3	34	HAWT	127	135
Evance R9000	0.005	3	No cut-out speed	HAWT	5.5	12/15/18.3
XANT M-21	0.1	3	20	HAWT	21	31
DeepWind	5	4	25	VAWT	121	143

Table 4-2: Various tidal turbine design characteristics

Device name	swept Ø (m)	Power rated (kW)	Rated (m/s)	cut in (m/s)	cp
MCT	16	600	2.5	1	0.37
Alstorm	18	1000	2.7	1	0.39
Minesto	43	500	1.2	0.4	0.38
sabella D-10	10	1000	4	1	0.39
sabella D-15	15	2300	4	1	0.40
seagen-S 2MW	20	1000	2.5	1	0.40
Atlantis AR2000	20	2000	3.05	1	0.40
Atlantis AR1000	18	1000	2.65		0.41
Verdant gen5	5	56	2.59		0.32
Voith	16	1000	2.9		0.40
Openhydro	10	200	2.5		0.32
minesto DG-8	85	110	1.3		0.28
minesto DG-14	155	850	1.73		0.31
schottel hydro d3	3	70	3.7	0.9	
schottel hydro d4	4	62	3.1	0.8	
schottel hydro d5	5	54	2.6	0.7	

4.3 Selected Turbines for Offgrid Design

For offgrid design, as will be discussed with more details in Chapter 4, Foveaux is chosen for providing electricity demand of Stewart Island investigated. SIESA [155] assessed three types of wind turbines suitable for providing the electricity demand of Stewart Island. They are the Northern Power Systems NPS100-24 (95 kW) turbine, the XANT M24 (95kW) turbine and the XANT M21 (100kW) turbine. Among them, only 21 m rotor XANT (the XANT M21) is designed to Class I wind conditions and can therefore be sited in locations with wind speeds of up to 10 m/s. The 24 m rotor XANT option and the NPS turbines are both only suited for wind conditions up to 7.5 m/s and both rated at 95 kW. That is why, XANT M21 (100 kW) is selected for the next step, combined with a suitable tidal turbine.

There are three options available: Schottel 54/62/70 kW. The microgrid results of Homer Pro software using XANT M21 (100 kW) and tidal turbines are presented in Table 4-3.

Table 4-3: Comparison of integration of different Schottel tidal turbine with selected XANT wind turbine.

Sl No	Wind Turbine	Tidal Turbines	NPC (M$)	Ren Fra (%)	WT production(kWh/year)	TT production(kWh/year)
1	XANT M-21 100kW (2)	Schottel 54kW (4)	2.08	85.8	792785.00	824298.0
2	XANT M-21 100kW (2)	Schottel 70kW (4)	2.77	74.8	792785.00	466992.0
3	XANT M-21 100kW (2)	Schottel 62kW (4)	2.34	82.7	792785.00	725254.0

Using Schottel 54 kW, produces more tidal power generation and increases the renewable fraction in comparison to other tidal turbines. Because cut-in speed of Schottel 54 is lower and can generate more electricity in lower speeds (This issue analysed with more details in Chapter 7). Also, this tidal turbine is more cost-effective as has a lower NPS.

The power curve and pertinent details of the wind turbine are set out in Figure 4-1 and Table 4-4.

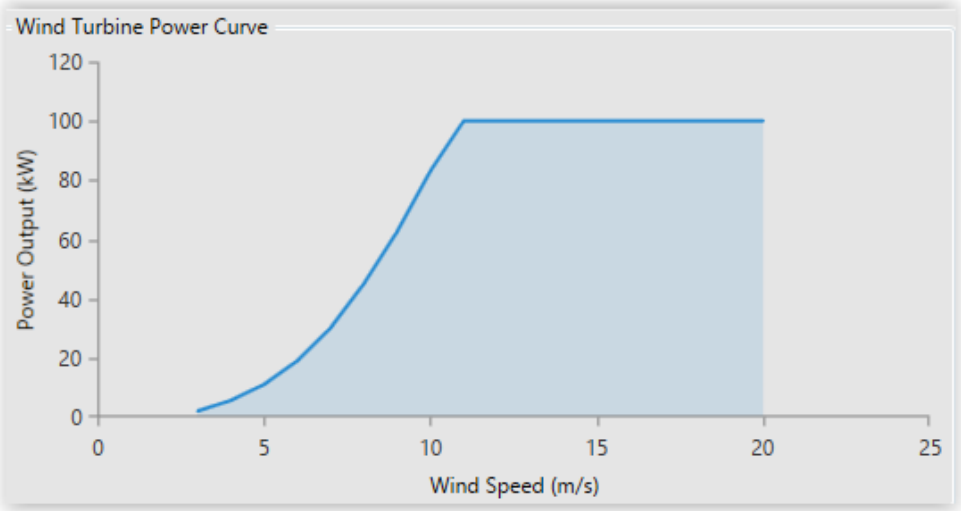

Figure 4-1:Power curve of the XANT M-21 [100 kW] wind turbine [29].

Table 4-4: Wind turbine details [156].

Wind Turbine	Value
Name	XANT M-21 [100 kW]
Rated Capacity (kW)	100
Manufacturer	XANT
Cut in wind speed	3 m/s
Cut out wind speed	20 m/s
Rated wind speed	11 m/s
Hub height	31.8 m
Swept area	346.36 m^2
Rotor diameter	21 m

The power curve and pertinent details of the tidal turbine are set out in Figure 4-2 and Table 4-5.

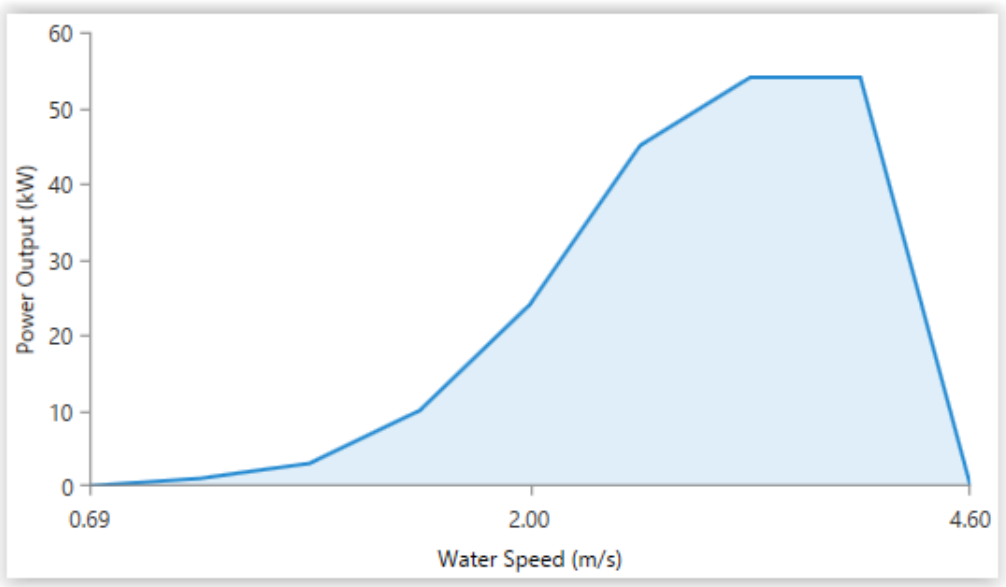

Figure 4-2: The power curve of the Schottel [54 kW] tidal turbine [29].

Table 4-5:Tidal turbine details [29].

Tidal Turbine	Value
Name	Schottel [54 kW]
Rated Capacity (kW)	54
Manufacturer	Schottel
Cut in tidal speed	0.7 m/s
Cut out tidal speed	4.6 m/s
Rated power at	2.6 m/s
Swept area	7.06 m^2
Rotor diameter	3 m

4.4 Selected Turbines for Ongrid Design

For ongrid design, as will be discussed with more details in Chapter 5, Terawhiti in cook strait is chosen for providing electricity demand of node CPK0331(Central Park) in south of northern island of New Zealand.

SIMEC Atlantic Energy limited (SAE) has invested more than £5m with partnership of GE to develop AR2000 (Figure 4-3 and Table 4-6) as the most powerful tidal turbine in the world. The project began in September 2018 and it is

expected to deploy turbine at Sound of Islay, the Mull of Galloway, Strangford Lough Portland Bill, and Lombok sites.

Some features which make this turbine unique are:

- New pitch controlling
- The yaw system enables 360-degree orientation.
- An upgraded condition monitoring used to diagnose faults and control overseeding.
- A good lifetime of 25 years with quarter-life intervals for routine O&M.
- Lower levelized cost, more reliability and larger rotor diameter for drew on lessons of Seagen-S 2MW in Northern Ireland. Another advantage of AR2000 in comparison of Seagen-S 2MW with same capacity is that AR2000 only needs 1 rotor, while Seagen-S 2MW consists of two 1MW rorors at each side of tower [157].

Figure 4-3: The AR2000 tidal turbine [158].

Table 4-6: General information of tidal turbine, Atlantic Resources AR 2000, for the hybrid system [159, 160].

Parameter	Symbol	Value	Unit
Turbine Power	P	2	MW
Turbine rotational Speed (Cut in/out)	Ω	1-3.05	rpm
Operational tidal speed range	V	1-4.5	m/s
Turbine rotor diameter	D	20	m
Height from the seabed	Z_S	25	m
Rotor Swept area	TSA	314	m^2
Mass of turbine	m	150	tonnes

The tidal power curve of the AR2000 tidal turbine is depicted in Figure 4-4. It is expected to produce power in cut-in speed of 1 m/s and from 3 m/s onwards, which is its rated speed, the capacity power is achievable.

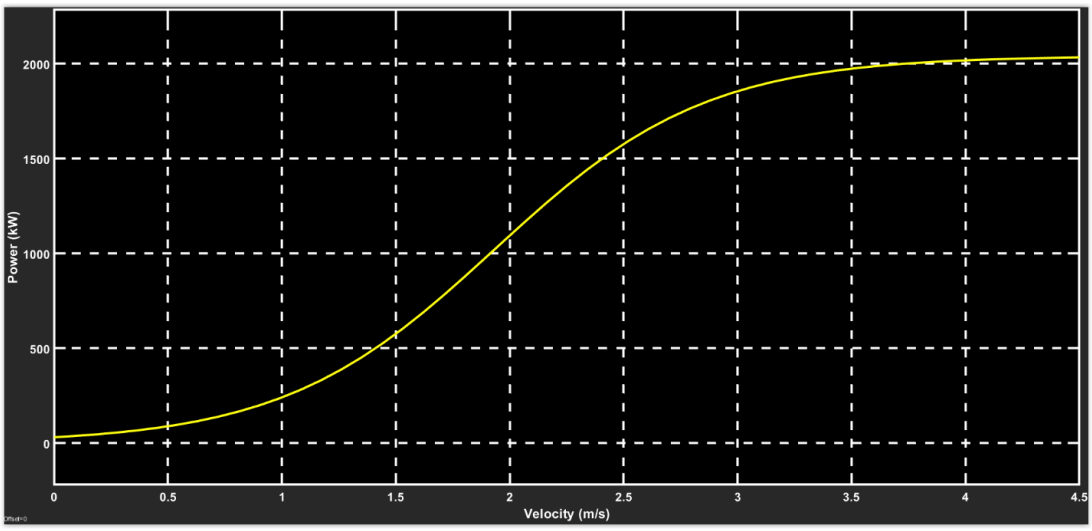

Figure 4-4: Output power of Tidal turbine – ($P_{Tidal\ max}$ for one rotor=2000 kW→ $P_{Tidal\ max}$ for two rotors=4000 kW)

The wind turbine SWT-3.6-107 Offshore is a production of Siemens Wind Power A/S. This company is taken by Siemens Gamesa Renewable Energy from 2017. [161].

The SWT-3.6-107 wind turbine is an ideal offshore turbine. A strong structural design, self-regulating lubrication systems with great supplies, temperature control of the internal conditions, and a simple generator system without slip rings provide special reliability at long service periods. Setting new standards enables feeding more power to the grid. Unique net Converter system of Siemens for grid codes has maximum adjustability to outputs and faults. Also, in design of all main components best engineering practice has been used in terms of safety and dimension sizing [96].

The Siemens SWT 154 6 6MW turbine marginally came out as the favourable choice using an option matrix by Plymouth University [162]. With respect of chosen tidal turbines, a comparable turbine of Siemens is chosen for the hybrid model. Design criteria specific to the selected wind turbine are presented in Table 4-7.

Table 4-7: General information of Wind turbine, Siemens SWT-3.6-107 Offshore 3.6 MW, for the hybrid system [159, 160].

Parameter	Symbol	Value	Unit
Turbine Power	P	3.6	MW
Turbine rotational Speed (Cut in/out)	Ω	5-13	rpm
Operational wind speed range	V	4-25	m/s
Rated wind speed	u_R	16.5	m/s
Mass of the nacelle (NA)	m_{NA}	125	tonnes
Hub height from mean sea level	H	87	m
Tower top diameter	D_t	3	m
Tower bottom diameter	D_b	5	m
Monopile/substructure diameter	D_P	6	m
Rotor and blade data			
Turbine rotor diameter	D	107	m
Rotor Swept area	TSA	8992	m^2
Mass of rotor+hub	m_R	100	tonnes
Rotor overhang	b	4	m
Blade root diameter	B_{root}	4	m
Blade tip chord length	B_{tip}	1	m
Blade length	L	52	m
Mass of tower	m_t	255	tonnes
Tower height	L_T	68	m
Tower wall thickness	t_T	0.027	m
Density of the tower material	ρ_T	7860	kg/m^3

The tidal power curve of the SWT-3.6-107 turbine is depicted in Figure 4-4. It is expected to produce power in cut-in speed of 1 m/s and from 3 m/s onwards, which is its rated speed, the capacity power is achievable.

The wind power curve of the SWT-3.6-107 Offshore wind turbine in Figure 4-5 shows that it is expected to produce power in cut-in speed of 4 m/s and s and from 16.5 m/s onwards, which is its rated speed, the capacity power is achievable.

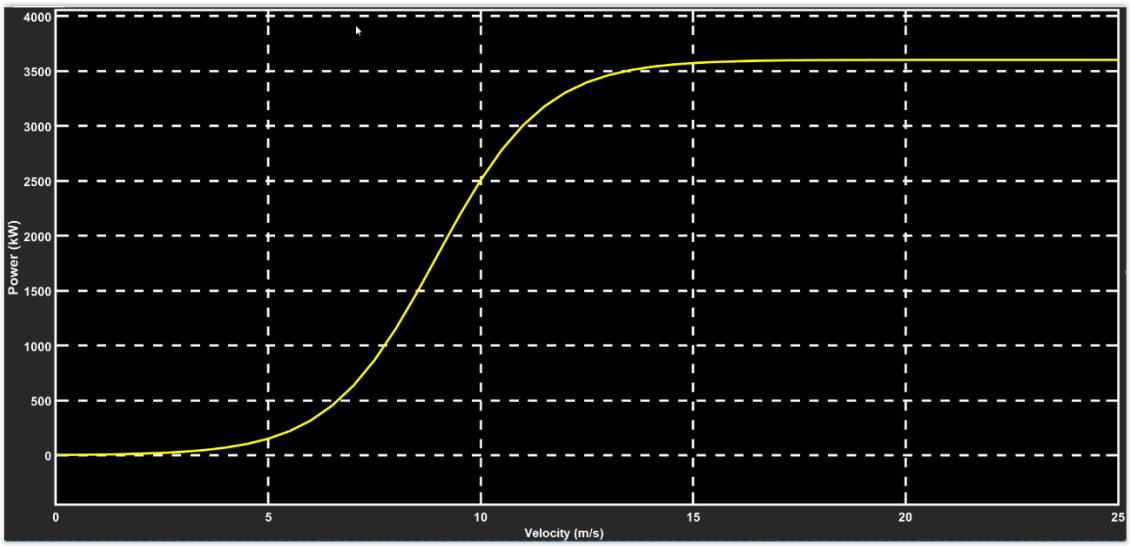

Figure 4-5: Output power of Wind turbine – ($P_{Wind\text{-}max}$=3600 kW)

SIMULINK will be used to design a microgrid system (explained with details in Chapter 5) for hybrid offshore wind and tidal energy generation (Figure 4-6 and Figure 4-7) and combined model (Figure 4-8) with Siemens SWT-3.6-107 wind turbines and Atlantis AR2000 tidal turbines.

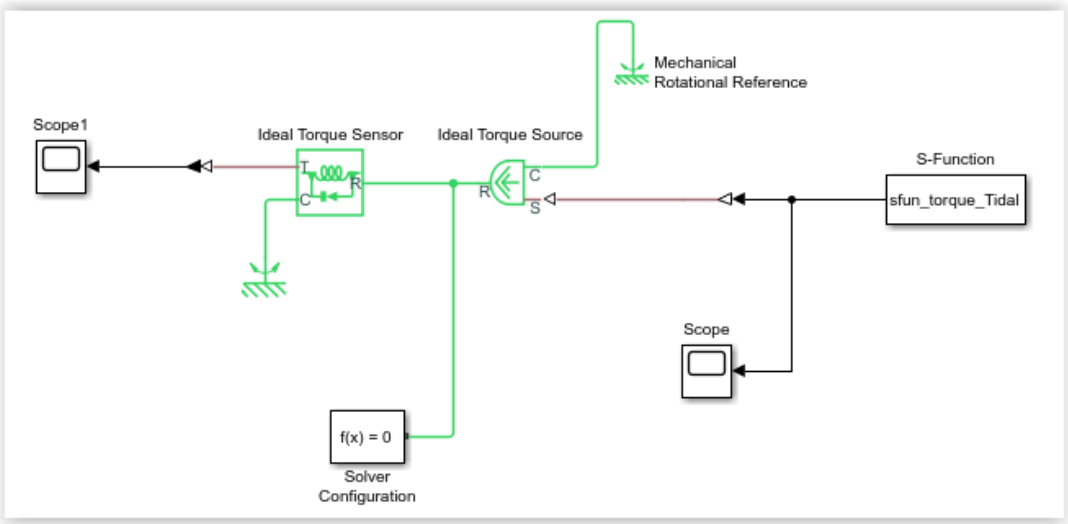

Figure 4-6: Simulink model of tidal turbine portion.

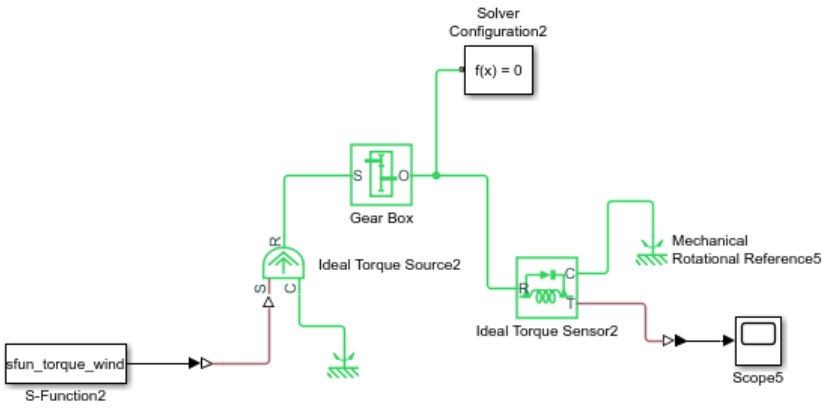

Figure 4-7: Simulink model of wind turbine portion.

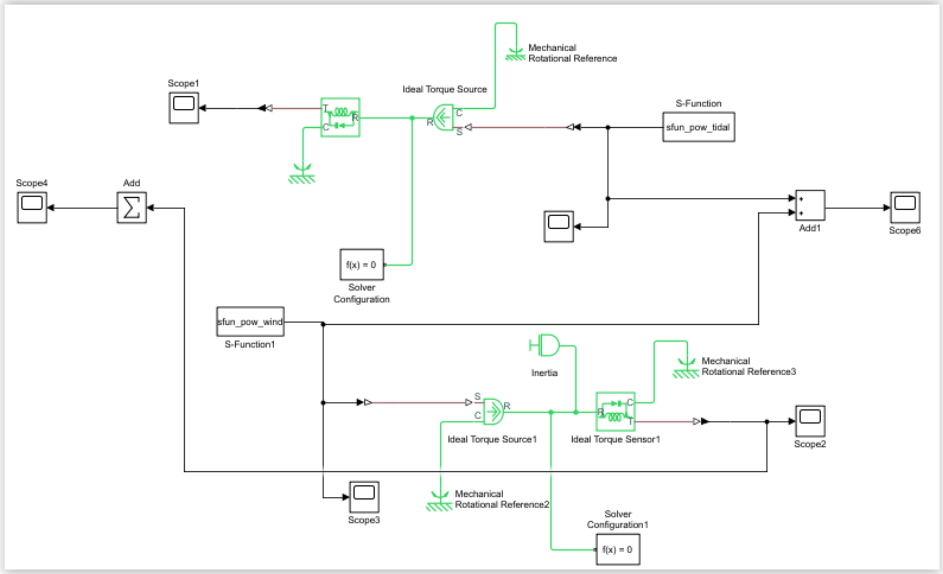

Figure 4-8: Simulink model of combined system.

4.5 Summary

As a result of evaluating design parameters for numerous turbines (section 4.2) the turbines proposed as most suitable for incorporation into a hybrid design linked by microgrid for off-grid supply are XANT M21 (100 kW) for wind above sea level and Schottel (54 kW) for tide at below sea level. Design criteria specific to selecting the turbines are discussed in section 4.3.

The turbines proposed as most suitable for incorporation into a hybrid design linked for on-grid supply are Siemens SWT3.6-107 (3600 kW) for wind above sea level and Atlantic Resources AR2000 (2000 kW) for tide at below sea level. Design criteria specific to selecting the turbines are presented in section 4.4.

Chapter 5

Microgrid Design of Hybrid Model in New Zealand

5.1 Introduction

This Chapter evaluates the feasibility of using a hybrid system consisting of wind and tidal turbines connected to a microgrid for power supply to coastal communities which are isolated from a main supply grid. The case study is Stewart Island, where the cost of electricity, provided by a central diesel power station, is higher than the grid network in New Zealand. Local residents believe that reducing the consumption of diesel and having a renewable source of electricity generation is one of the island 's highest priorities. Merging a tidal energy source (predictable) with wind (unpredictable) and diesel (back-up) through a microgrid, may be a way to increase reliability and decrease cost of generation. Several off-grid configurations are simulated using HOMER and WRPLOT software. Using two wind and four tidal turbines plus one diesel generator for back-up is the best design in terms of lower greenhouse gas emissions, higher renewable fraction, and reduced net present cost.

In the next stage, the grid-connected design is evaluated based on facility location in Cook Strait. The closest node is selected to Terawhiti in Cook Strait and several calculations are carried to reach an optimized design compatible with this node.

Several simulations are conducted to determine the required capacity of the hybrid system for more consistent supply of electricity which is an essential commodity for our daily living with the lowest cost of energy and maximizing natural resources. There have been several methods for microgrid design. The novelty of this chapter is to define a method for using tidal energy for off-grid and on-grid design and merge it with wind source for an optimized offshore site. The results enable to determine an optimized scenario for the hybrid model.

5.2 Off-grid Design in Foveaux for Stewart Island

Figure 5-1 shows different sources of energy generated in New Zealand. New Zealand consumed about 38,800 gigawatt-hours (GWh) of electricity. Renewable sources (hydro, geothermal, wind and solar) supplied 59%, 17%, 5% and 0.2% of the country's electricity needs, respectively, in 2017. Thermal sources (coal, diesel and gas) supplied the other 18.8% [15].

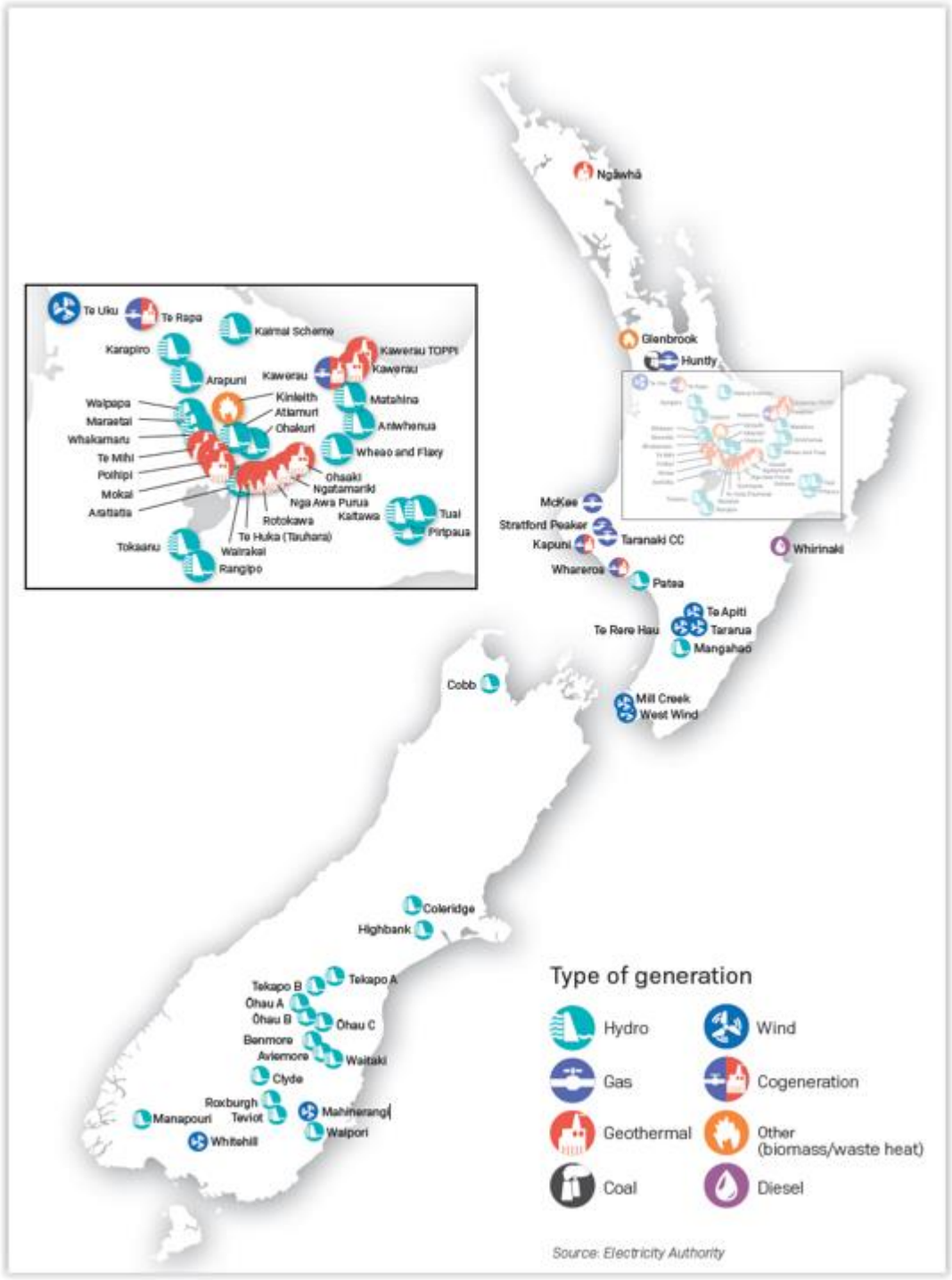

Figure 5-1: Types of power sources in New Zealand [15].

Transformation losses in electricity generation are derived from the net electricity generated, with the actual fuel input being used where available and the conversion factors shown in Table 5-1 [79].

Table 5-1: Default Electrical Transformation Factors in New Zealand [79].

Fuel	Default Efficiency
Biogas	30%
Coal	30%
Gas (Single cycle)	30%
Geothermal	15%
Hydro	100%
Oil	30%
Waste heat	15%
Wind	100%
Wood	25%

Figure 5-2 shows that most New Zealand cities and industries obtain their electricity through a nationwide mains supply grid operated by the government agency Transpower [15].

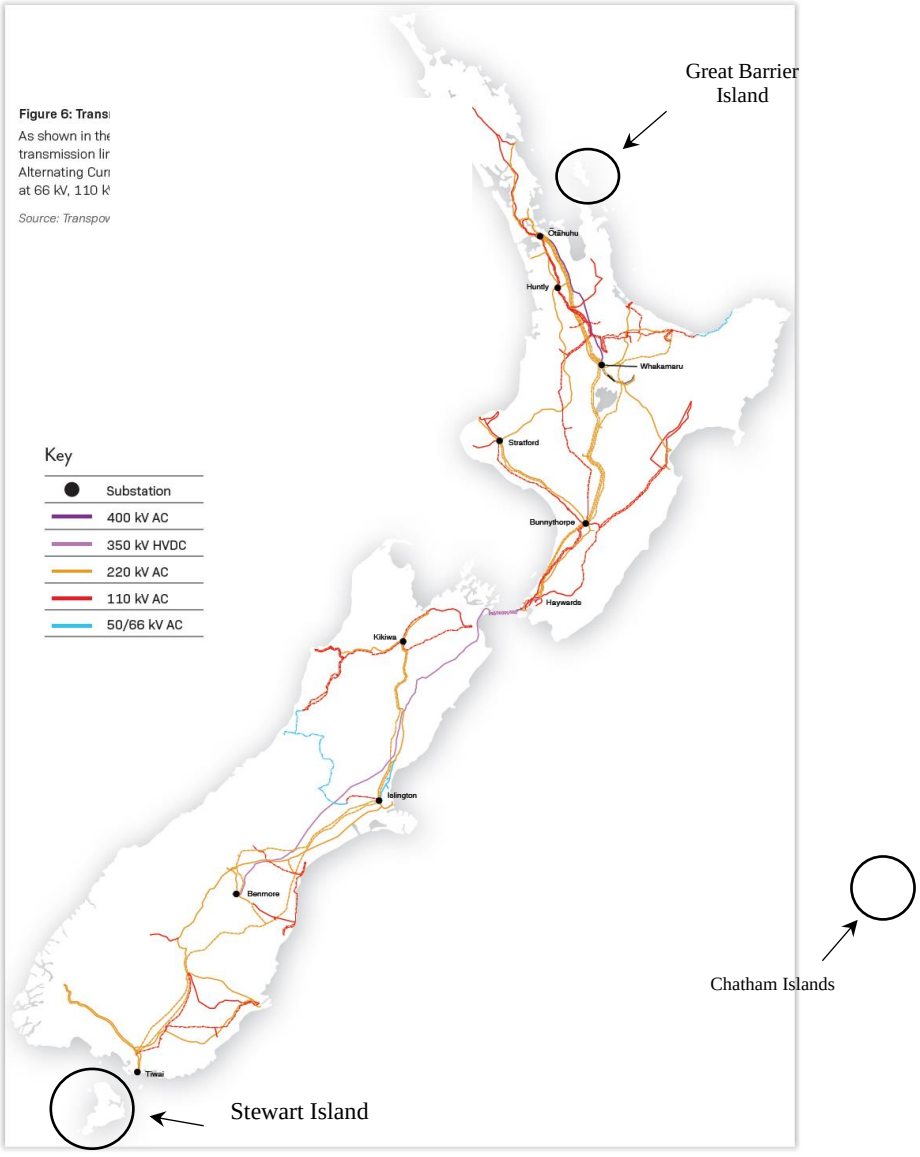

Figure 5-2:New Zealand transmission network map [15].

However, there are still small communities in remote parts of the main islands or offshore islands that are not connected to the main grid. Some examples of off-grid communities in remote areas are given in Table 5-2:

Table 5-2: Some Examples of Off-grid Power Generation in New Zealand

Island	Population (2018)	Source of off-grid supply
Great Barrier Island	930	Diesel and solar
Chatham Island	663	Diesel and wind
Stewart Island	408	Diesel

Stewart Island is selected as a case study to evaluate the feasibility of a hybrid system consisting of wind and tidal turbines connected to a microgrid for power supply to remote coastal communities isolated from a national supply grid. The island is one of several such communities in New Zealand (Figure 5-2). The cost of electricity is much higher than on the grid-connected mainland because power is supplied to just 408 customers from a small diesel power station located centrally in the island's main settlement Oban by the Stewart Island Electrical Supply Authority (SIESA). The retail charge is 62 c/kWh, of which 23 c/kWh is the direct cost of operating five diesel generators. Replacing diesel with a source of renewable energy is a top priority for residents [155]. Several recent investigations have been conducted to find a solution for providing electricity at a lower cost, such as an undersea cable from Bluff to Stewart Island, hydropower from Maori Creek [156], and integrating wind with solar energy [155].

In the case of Stewart Island, fuel cost makes up 40% of operations and maintenance expenditure (Figure 5-3), so drives the price being charged to customers. It is on a 5% annual increase. Additionally, fuel consumption is anticipated to increase 1% annually, which either will increase the cost of electricity for island consumers or decrease the supply authority's net income [163].

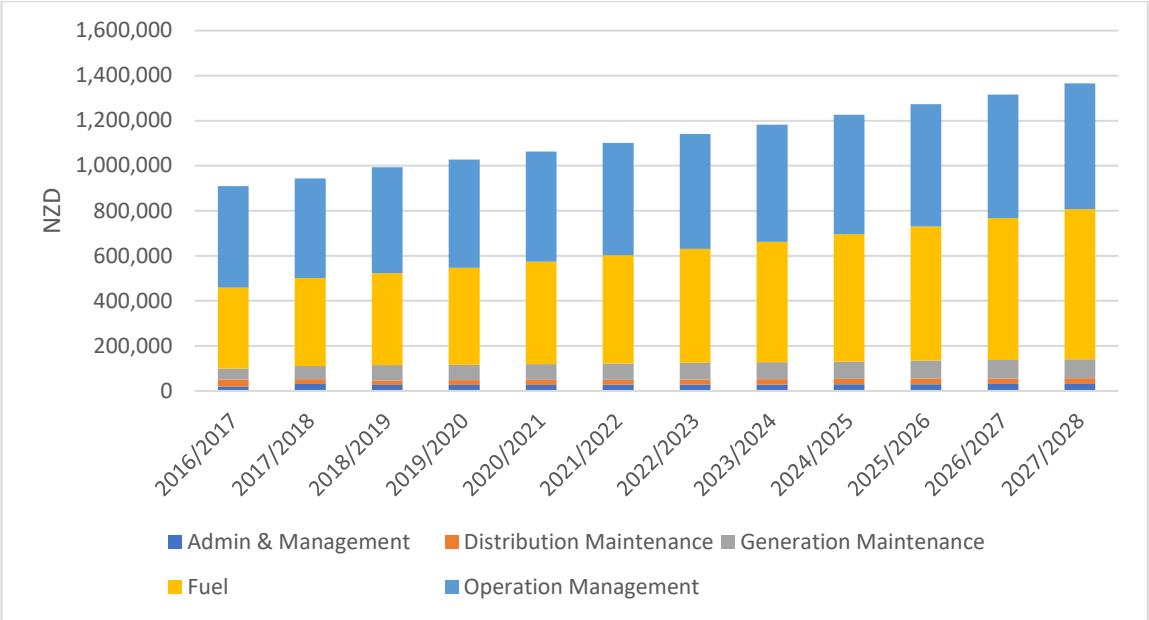

Figure 5-3. Electricity Supply Expenditure of Stewart Island [163].

5.2.1 Modelling of the DC Offgid Microgrid

In order to propose a solution for the electricity demand of a remote off-grid community, a number of steps needed to be carried out, which are:

- Selecting a suitable site for the case study.
- Identifying electricity demand i.e. load profile data.
- Defining all the components of microgrid design including multiple energy resources (turbines and generator), storage device (batteries), rectifier of AC to DC (converter) and predeterminer of electrical system (controller).
- Obtaining environmental data for the energy resources, including fuel type, wind, and water speeds.
- Optimizing the design identifying the location, size and number of devices required to harness energy resources.
- Feasibility analysis and financial viability of the optimized microgrid design.

5.2.2 Identifying the Site's Electricity Demand

Stewart Island, Electrical Supply Authority data, has been used to estimate monthly and hourly generation in the case study. Peak values are in January (209 kW) and at 6–7 pm (239 kW), and the lowest values are in August (162 kW) and at 3–4 pm (121 kW) [155].

5.2.3 Obtaining Environmental Data

Tidal current data have been obtained from a simulation model which MetOcean Solutions Limited (MSL) conducted on an NZ-wide grid with a 0.06° resolution (5.6 × 6.6 km). The simulation nested high-resolution domains over Foveaux Strait (0.004°; 340 × 450 m) shown in Figure 5-4. The Princeton Ocean Model (POM) was used to hindcast the tidal current in a vertically integrated two-dimensional mode with boundaries provided from the global TPX07.1 solution [164].

One of these points, referred to as the Foveaux site (Figure 3), has been selected for the case study, because despite being on the opposite side of Foveaux Strait, it appears to have stronger currents (better generation potential) than points close to Stewart Island ´s coast, and also because the Global Wind Atlas model [142] indicates that this point is in an area with frequent strong winds (high potential for wind energy), shown in Figure 5-5. For New Zealand, Global Wind Atlas extrapolates data from a network of meteorologic recorder stations operated by New Zealand Meteorological Service (NZMS) and National Institute of Water and Atmosphere (NIWA).

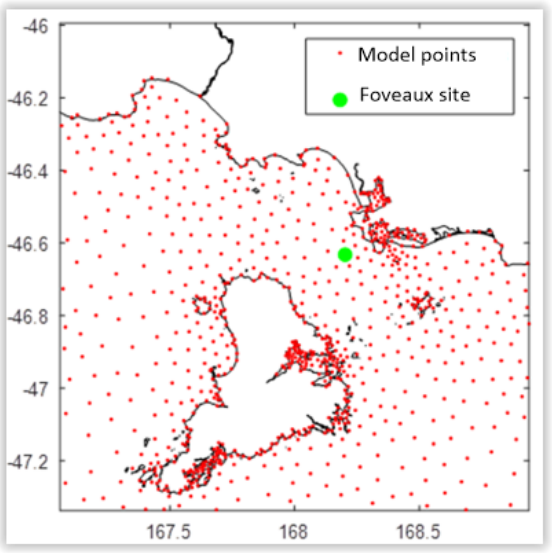

Figure 5-4: Tidal current model points near Stewart Island from NIWA.

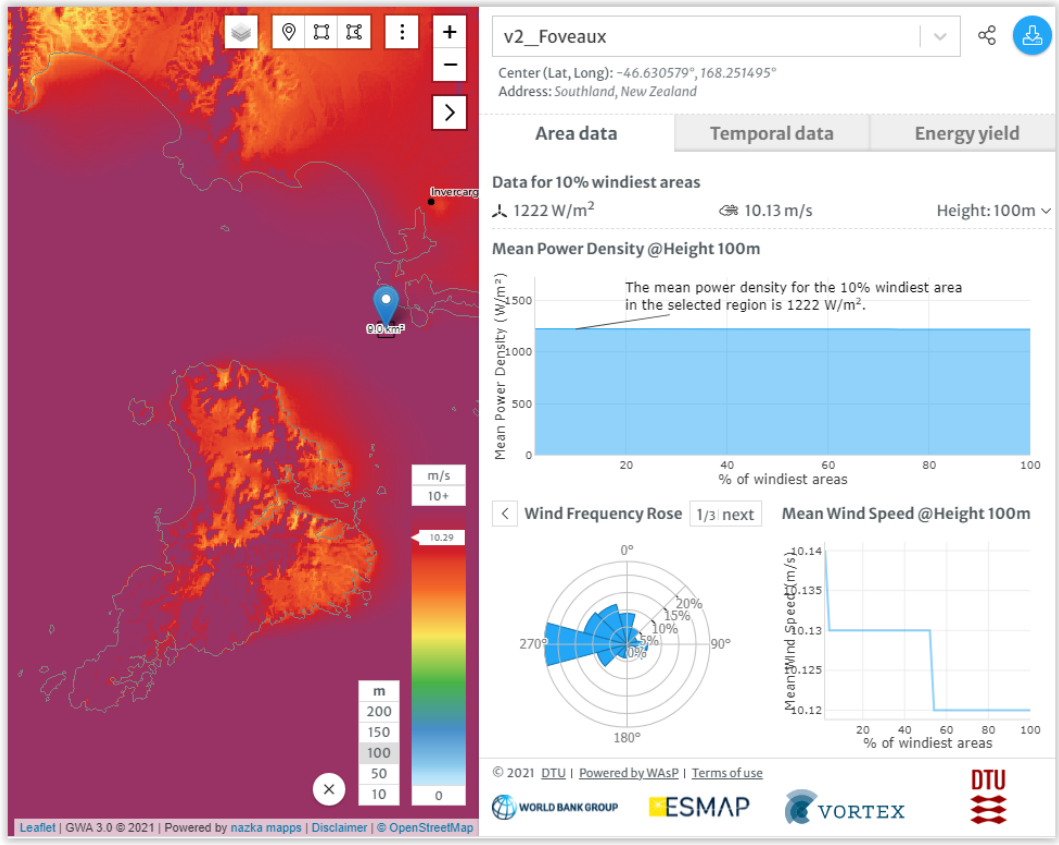

Figure 5-5: Wind conditions near Stewart Island (left) and at the Foveaux site (right) [142].

The environmental parameters of the site are summarised in Table 5-3, Figure 5-6 and Figure 5-7.

Table 5-3: The environmental parameters of the Foveaux site

Location	Latitude (deg)	Longitude (deg)	Annual Average Water Speed (m/s)	Water Depth (m)	Annual Average Wind Speed (m/s)
Foveaux	−46.6325° S	168.2025° E	0.52	30	8.31

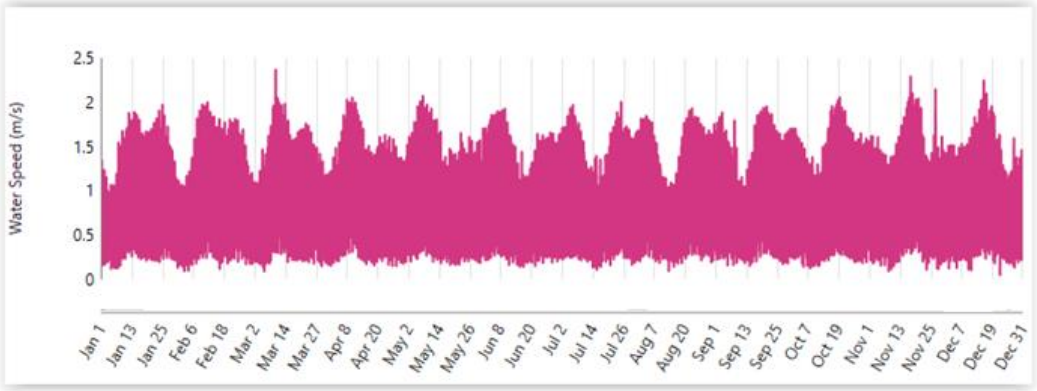

Figure 5-6: Annual water speed for Foveaux site

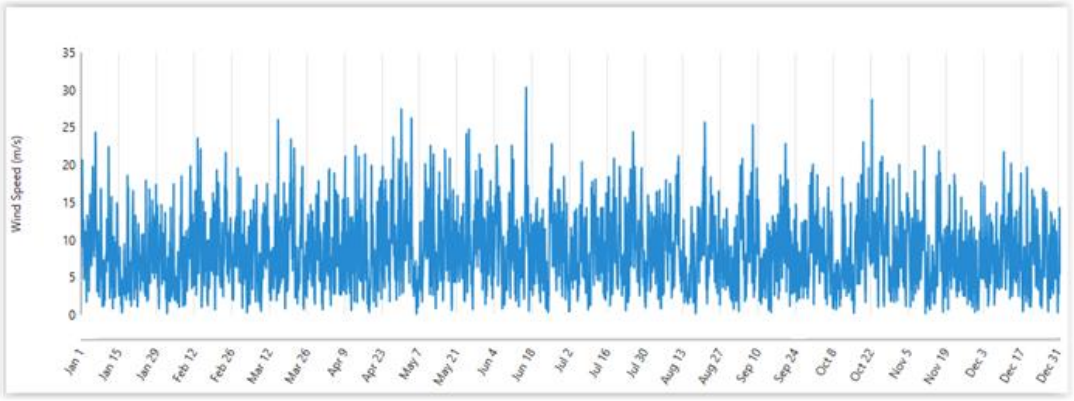

Figure 5-7: Annual wind speed for Foveaux site

The last resource input is fuel type for a back-up diesel generator. Biodiesel was selected rather than diesel, because:

- Diesel with 88% carbon content produces more carbon emissions than biodiesel with 77%.
- The lower heating value (LHV) of biodiesel is 43.20 MJ/kg, while this value for diesel is 38.5 MJ/kg [135].
- The price of biodiesel ($/litre 0.53) is cheaper than diesel ($/litre 1.00) [134].

5.2.4 Microgrid Components

The microgrid system under consideration consists of wind and tidal turbines combined with a diesel generator and battery energy storage systems (BESS) as shown in Figure 5-8. A DC bus connects all the components.

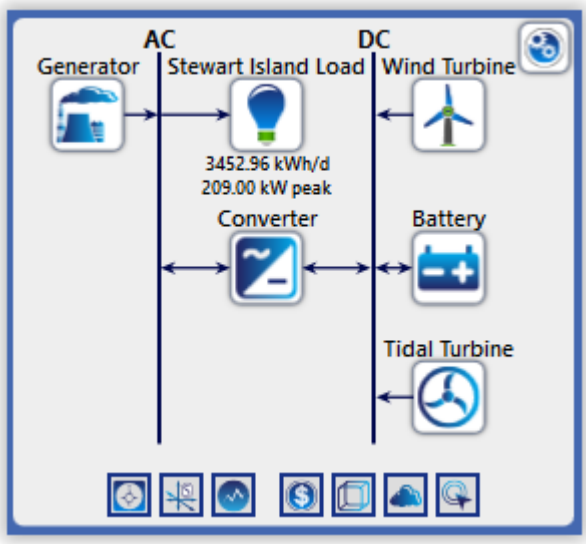

Figure 5-8: Schematic layout of DC microgrid

5.2.4.1 Wind Turbine

A suitable wind turbine in terms of low cut-in speed, a generating capacity capable of meeting peak load, supplying a substantial percentage of peak load and low purchase, installation & maintenance costs is the XANT M-21 [100 kW]. The capital, replacement, maintenance, and life of the turbine are taken as $50,000, $50,000, $25,00/year, and 20 years respectively. The power curve and percentage of generation in intervals of 4 m/s shown in Figure 5-9 is given by equation 5-1:

$$P_{wind} = \begin{cases} -0.0018V^6 - 0.07V^5 + 1.0826V^4 - 8.4544V^3 + 36.229V^2 - 78.056V + 66.38 \; for \; V \leq 10 \; m/s \\ 100 \; for \; 11 \leq V \leq 20 \end{cases} \quad (5\text{-}1)$$

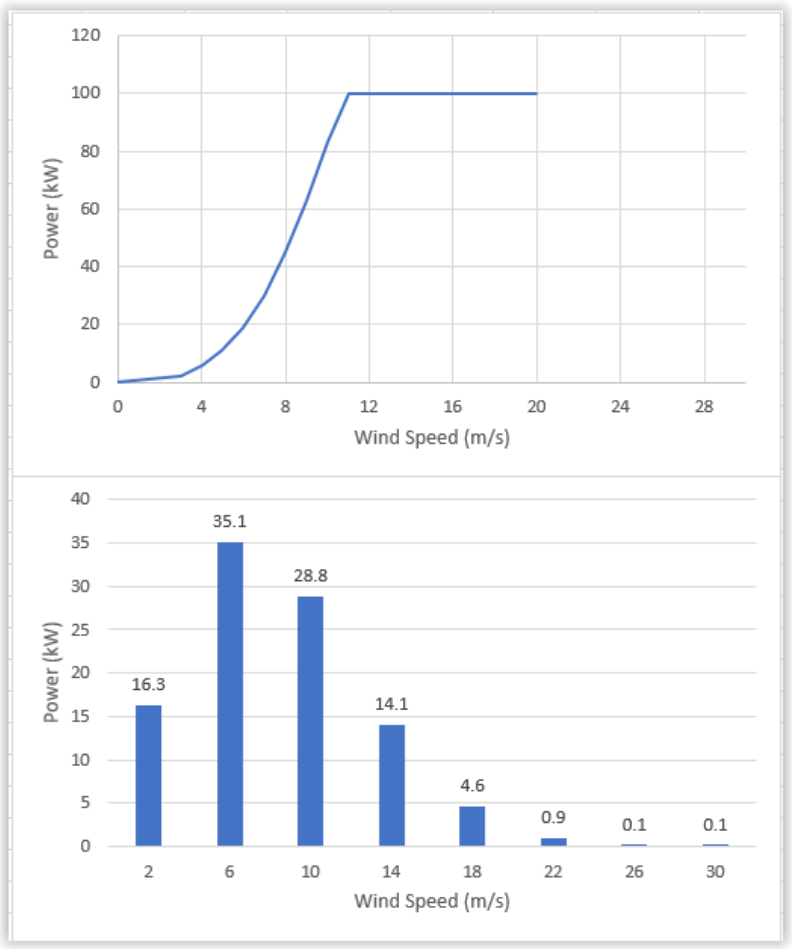

Figure 5-9: The power curve (top) and power generation distribution (bottom) of the XANT M-21 turbine.

Other pertinent details for the XANT wind turbine are given in Table 5-4.

Table 5-4:Wind turbine details [29].

Wind Turbine	Value
Name	XANT M-21 [100 kW]
Rated Capacity (kW)	100
Manufacturer	XANT
Cut-in wind speed	3 m/s
Cut-out wind speed	20 m/s
Rated wind speed	11 m/s
Hub height	31.8 m
Swept area	346.36 m^2
Rotor diameter	21 m

WRPLOT view software [30] was used to plot wind frequency distribution downloaded from NASA Surface Meteorology and Solar Energy database [143] at

the Foveaux site. As can be seen in Figure 9, for 90.5% of the year, the wind speed is more than cut-in speed, so the XANT M-21 wind turbine will be suitable for electricity generation at the Foveaux site.

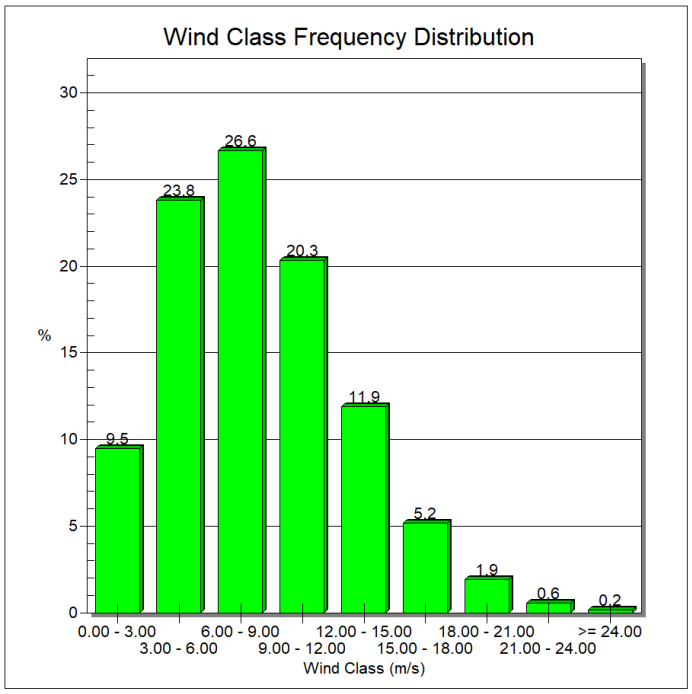

Figure 5-10: Wind speed frequency distribution at Foveaux site.

5.2.4.2 Tidal Turbine

A suitable tidal turbine in terms of low cut-in speed, a generating capacity capable of meeting peak load, supplying a substantial percentage of peak load and low purchase, installation & maintenance costs is the Schottel [54 kW] bidirectional turbine. The capital (or installation and wiring and mounting expenses), replacement, maintenance, and life of the turbine are taken as $54,000, $54,000, $2,700/year and 10 years, respectively. The power curve and percentage of generation in 0.5 m/s intervals shown in Figure 5-11 is given by equation (5-2):

$$P_{tidal} = \begin{cases} 2.0978V^3 + 2.7163V^2 - 1.7909V - 0.2358 \;\; for\, V \ll 2.5 \\ 54 \;\; \text{for} \;\; 2.75 \ll V \ll 4.59 \end{cases} \qquad (5\text{-}2)$$

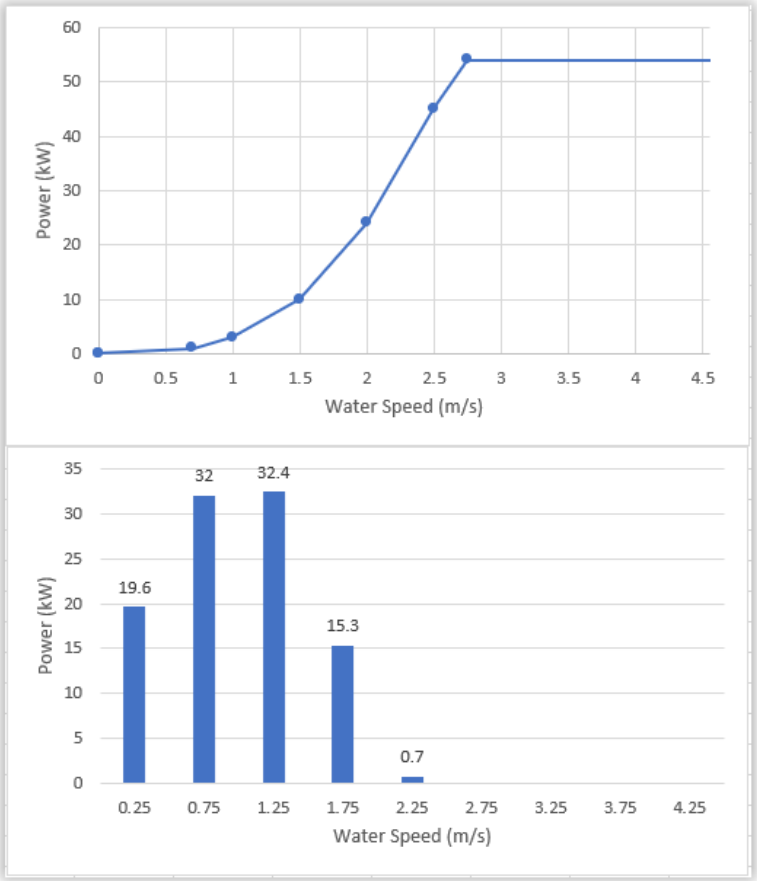

Figure 5-11: The power curve of the Schottel [54 kW] tidal turbine.

Other pertinent details for the Schottel tidal turbine are given in Table 5-5.

Table 5-5: Tidal turbine details.

Parameter	Value
Name	Schottel [54 kW]
Rated Capacity (kW)	54
Manufacturer	Schottel
Cut-in tidal speed	0.7 m/s
Cut-out tidal speed	4.6 m/s
Rated power at	2.6 m/s
Swept area	7.06 m^2
Rotor diameter	3 m

WRPLOT view software [30] was used to plot maximum tidal flow at 5 metres above seabottom. This was obtained by using Python code to create a tidal velocity profile from the MetOcean model ´s integrated average tidal velocity. As can be seen in Figure 5-12, water speed for 68.4% of the year is more than cut-in speed, so the Schottel 54 kW tidal turbine is suitable for generating electricity at the Foveaux site.

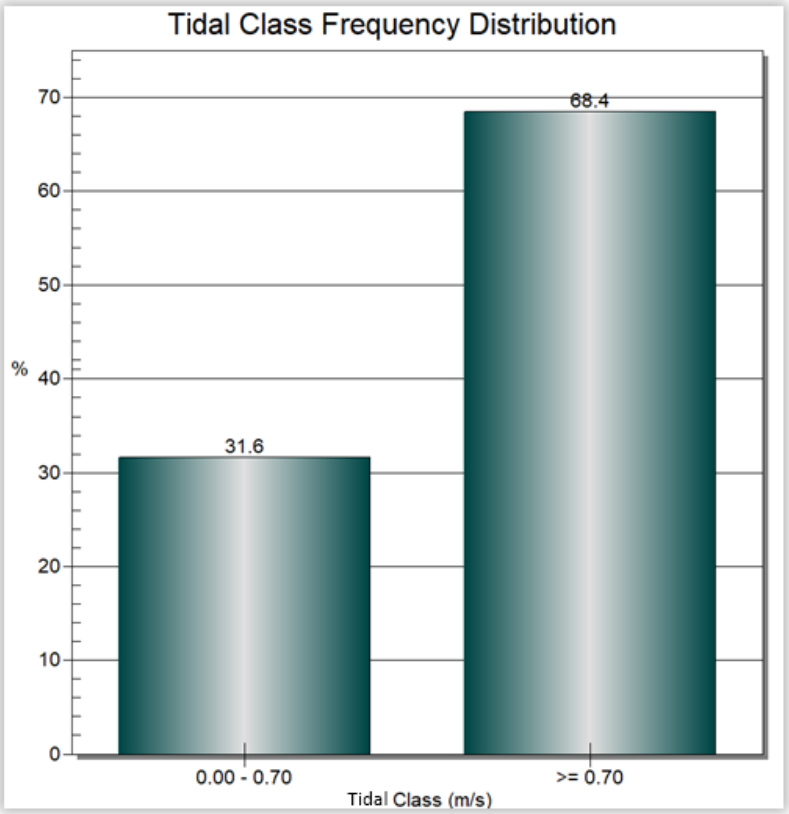

Figure 5-12: Tidal speed frequency distribution at Foveaux site.

5.2.4.3 Biodiesel Generator

A 320 kW CAT-400kVA-50Hz-PP generator is proposed, to cover the base load as a low-level load at less than 25% of nominal capacity. This solution enhances the performance of generation consuming just 6.37 l/h fuel. The lifetime is taken as 90,0000 hours. Capital, replacement, and O&M costs are $160,000, $128,000, and $4.80/hr, respectively [165]:

Capital cost=500 × 320 = $160,000

Replacement cost=400 × 320 = $128,000

O&M cost=0.015 × 320 = $ 4.80/hr

5.2.4.4 Battery Energy Storage

Energy storage is one of the most important component to achieve a tight integration of intermittent renewable generations. [129]. Adding significant

amounts of renewable sources to the system will alter the timing of peak demands so that as energy penetration grows, the time of the net peak (after subtracting wind and tidal output) will shift. This can be addressed in a number of ways: by improving demand response; by adding storage to the hybrid system; or by other generating options that can meet these new peaks. A generic 12-volt lead-acid battery with 1 kWh of energy storage is used for modelling the energy storage unit. This particular type of battery is chosen due to its relatively good performance and low cost. Also, it has a high lifetime and have been found in a wide variety applications including small scale storage along with large, grid-scale power systems [166]. Specifications are given in Table 5-6. The capital, replacement, maintenance, and life of the battery are taken as $154, $154, $15.40/year, and 10 years respectively [135].

Table 5-6: Properties of generic 1 kWh Lead-Acid battery [29].

Sl.No	Properties	Ratings
1	Nominal voltage	12 V
2	Round trip efficiency	80%
3	Lifetime throughput	800 kWh
4	Maximum charging current	16.67 A
5	Maximum discharge current	24.33 A

5.2.4.5 Converter

A generic system converter is proposed, to rectify the AC output of the generator to DC, which is much cheaper than a bidirectional converter. Selecting the Homer optimizer allows the Homer model to optimize the size of the converter. The capital, replacement, maintenance, life, and efficiency of the converter are taken as $154, $154, $15.40/year, 15 years, and 90%, respectively [129].

5.2.4.6 Controller

A load following (LF) controller is selected, because it will produce only enough power to meet the demand. The capital, replacement, maintenance, and life of the controller are taken as $200, $200, $5.00/year, and 25 years respectively.

5.2.5 Optimising the Design

For the feasibility study presented in this paper, an industry-recognized simulation software called HOMER Pro® is used [167].

5.2.6 Feasibility Analysis

In terms of financial viability, there are two main parameters. The net present cost (NPC) of a system is the total cost of the system (such as capital costs, replacement costs, operation and maintenance costs etc.) minus all the revenue during its lifetime. The levelized cost of energy (COE) is the average cost of production of 1 kWh of electricity. HOMER software includes an economic analysis module, so is used to estimated NPC and COE. The lowest possible NPC and COE is desirable [129].
In this section, different designs in terms of required turbines at the selected Foveaux site for providing electricity demand of Stewart Island are compared.
By way of background, the SIESA load profile will be discussed first. Peak hourly load is 209 kW. Homer software is used to plot the average hourly and monthly load as shown in Figure 5-13. The top graph shows average daily load fluctuates between 106 and 209 kW. The bottom graph the load for different months of the year. The minimum load fluctuates between 88 and 174 kW in August and the maximum load fluctuates between 106 and 209 kW in January. Daily demand for the year averages 3,452.9 kWh/d with a load factor of 0.69. Total demand is 1,260,332 kWh/yr.

(a)

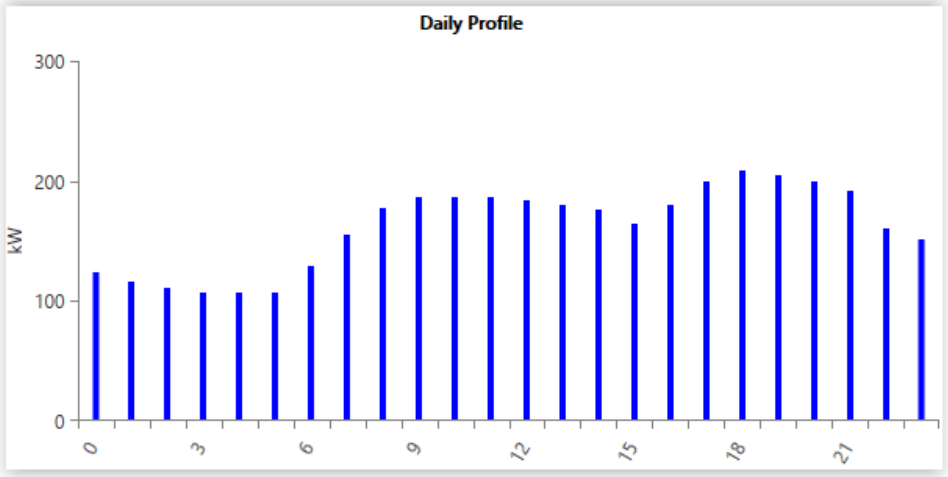

(b)

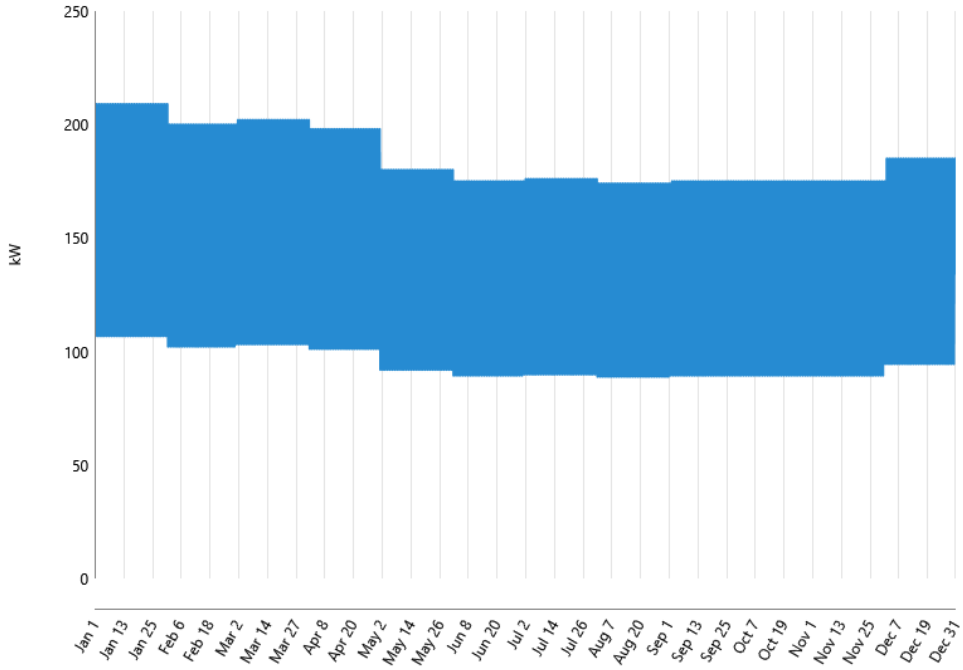

Figure 5-13: The daily (left) and monthly (right) load of Stewart Island.

The power which can be output by single wind and tidal turbines at the Foveaux site are shown in Figure 5-14. The maximum output of selected wind and tidal turbine are 100 kW and 39.3 kW respectively.

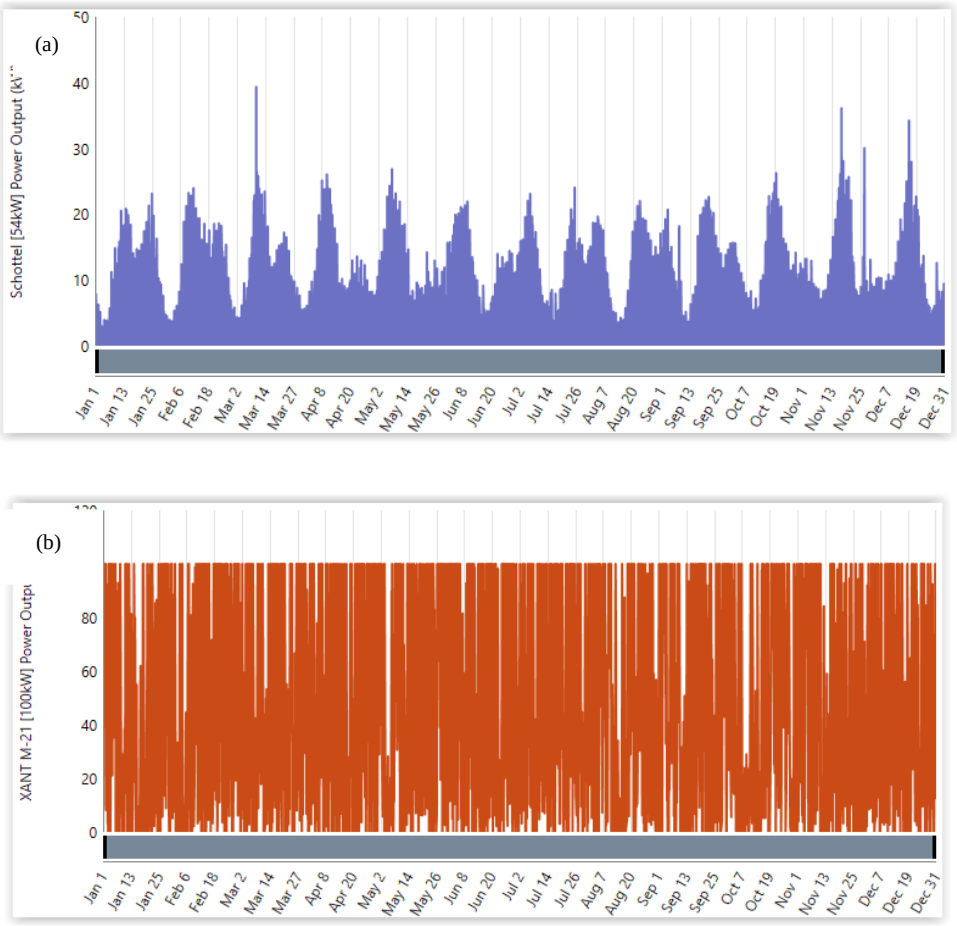

Figure 5-14: Power output fluctuation for (a) tidal turbine and (b) wind turbine at the Foveaux site.

Figure 5-15 compares fluctuations in power demand for three days with outputs obtained from a tidal turbine, a wind turbine, and a diesel generator. The black curve represents the overall power generated by the system, while the yellow one shows the demand. The curves show that more than one wind turbine and more than one tidal turbine would have to be configured in a hybrid system, to reduce Stewart Island ’s dependence on a diesel generator to meet its power demand.

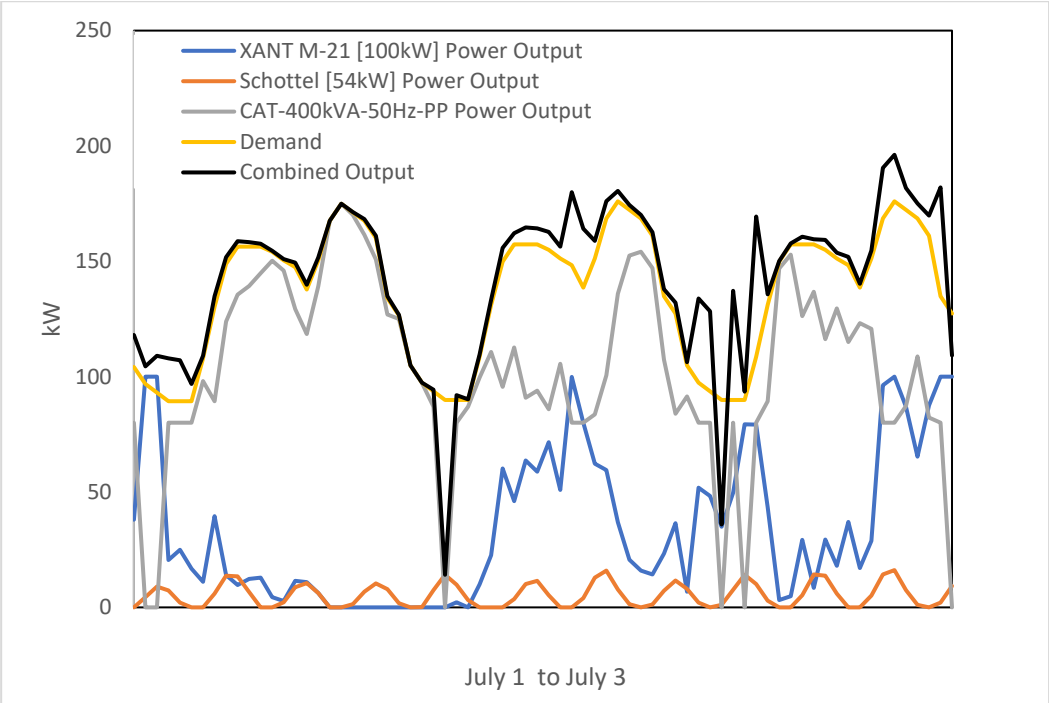

Figure 5-15: Variation of generated powers and required demand during a three-day period at Foveaux.

In view of what Figure 5-15 shows, Sections 5.2.7 and 5.2.8 evaluate different designs, using Homer software to optimise turbine and generator operation, so as to meet fluctuations in demand through the year. The scenarios, in terms of number of wind (W) and tidal (T) turbines and diesel generators (G), are 1W+1T, 1W+2T, 2W+2T, 2W+4T and 1W+10T. Sections 5.2.9 and 5.2.10 discuss the results, in terms of power generation and cost-effectiveness respectively.

5.2.7 Power Generation Results

Table 5-7 shows mean output, hours of operation, and total production for each scenario. Increasing the number of wind and tidal turbines, decreases the hours of operation and total production from diesel generators. The total power production for all scenarios exceeds Stewart Island demand (1,260,332 kWh/yr).

Table 5-7: Annual mean output, hours of operation, and power production for proposed scenarios at Foveaux site.

Parameter	1 W+1 T	1 W+2 T	2 W+2 T	2 W+4 T
Mean output of W (kW)	45.3	45.3	90.5	90.5
Mean output of T (kW)	4.5	8.9	8.9	17.9
Mean output of G (kW)	111.0	109.0	111.0	109.0
Operation hours of W (hr/yr)	7,747	7,747	7,747	7,747
Operation hours of T (hr/yr)	5,759	5,759	5,759	5,759
Operation hours of G (hr/yr)	7,966	7,835	4,887	4,519
Power production of W (kwh/yr)	396,392	396,392	792,785	792,785
Power production of T (kwh/yr)	39,124	78,248	78,248	156,495
Power production of G (kwh/yr)	880,263	850,602	540,402	490,358
Total Production (kwh/yr)	1,315,779	1,325,242	1,411,434	1,439,638

Figure 5-16 a-d shows monthly average power output (kW) for different scenarios. Wind energy can generate a large share of output in scenarios 2W+2T and 2W+4T. Tidal energy just starts to generate a significant share of output in scenario 2W+4T. Table 5-8 shows total electricity production, and the percentages contributed by each energy source. Scenario 2W+4T enables two thirds of production to be generated from renewable sources.

(a)

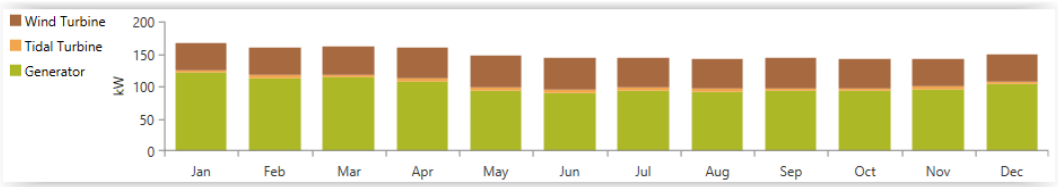

(b)

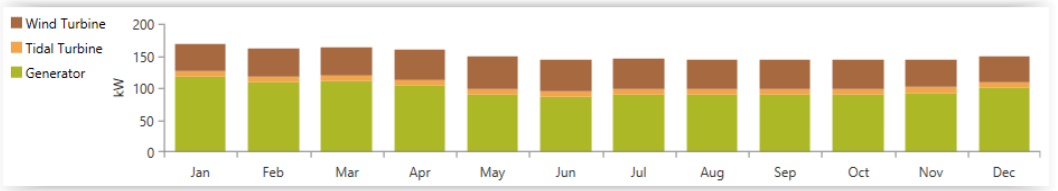

(c)

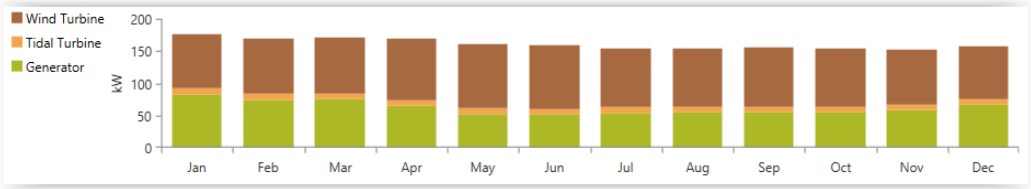

(d)

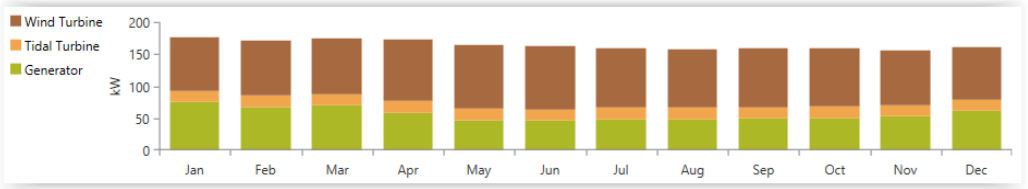

Figure 5-16: Monthly average output power for (a) 1W+1T, (b)1W+2T, (c) 2W+2T, (d) 2W+4T.

Table 5-8: Share of wind and tidal turbines in electricity production.

Scenario	Total Electricity Production (kWh/yr)	Share of Tidal Turbines	Share of Wind Turbines	Share of Generator
1W+1T	1,315,779	3.0%	30.1%	66.9%
1W+2T	1,325,242	5.9%	29.9%	64.2%
2W+2T	1,411,434	5.5%	56.2%	38.3%
2W+4T	1,439,638	10.9%	55.1%	34.1%

Figure 5-17 and Table 5-9 show a possible alternative scenario, 1W+10T, which might enable a tidal source to contribute as much renewable energy as a wind source. The mean output of wind and tidal turbines are 45.3 and 44.7 kW, and wind and tidal electricity production are 396,392 and 391,238 kWh/yr, respectively.

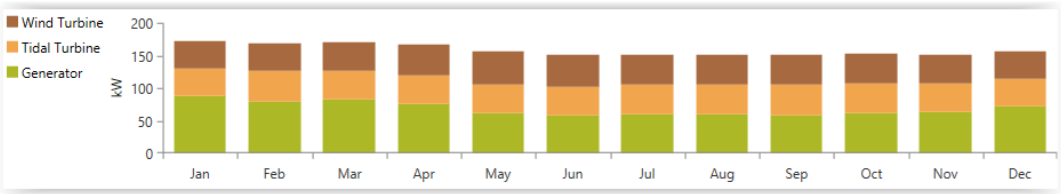

Figure 5-17: Monthly average output power for 1W+10T.

Table 5-9: Share of wind and tidal turbines in electricity production for 1W+10T.

Scenario	Total Electricity Production (kWh/yr)	Share of Tidal Turbines	Share of Wind Turbine	Share of Generator
1W+10T	1,383,325	28.3%	28.7%	43.0%

5.2.8 Financial Analysis Results

Table 5-10 is a summary of financial analysis for different scenarios at the Foveaux site.

Table 5-10: Financial analysis results for different scenarios.

Scenario	Capital (k$)	Fuel Cost (M$)	Operating Cost (k$)	Total NPC (M$)	Levelized Cost ($/kWh)
1 W+1T	350	3.3	323	4.53	0.278
1W+2T	402	3.2	321	4.55	0.279
2W+2T	484	2.0	225	3.39	0.208
2W+4T	593	1.8	222	3.47	0.213

The 2W+2T and 2W+4T scenarios seem more economic to install and operate. To show why, Table 9 depicts the optimization results for each scenario. Their renewable fractions are 30.2%, 32.5%, 57.1% and 61.1% respectively. A renewable fraction of 61.1% means that 61.1% of electricity is supplied from the wind and

tidal turbines and the rest of it from the diesel generator. Hybrid systems with a renewable fraction of more than 66% are high revenue. [168]. 2W+2T and 2W+4T almost meet this criterion. They have lower operating cost, fuel cost, and NPC than 1W+1T or 1W+2T. Most important, they have lower COE.

Table 5-11: Optimization results for (a) 1W+1T, (b)1W+2T, (c) 2W+2T, (d) 2W+ 4T.

(a)

Architecture							Cost				
Wind Turbine	Generator (kW)	Battery	Tidal Turbine	Converter (kW)	Dispatch	COE ($)	NPC ($)	Operating cost ($/yr)	Initial capital ($)	Ren Frac (%)
1	320	407	1	155	LF	$0.278	$4.53M	$323,222	$350,707	30.2

(b)

Architecture							Cost				
Wind Turbine	Generator (kW)	Battery	Tidal Turbine	Converter (kW)	Dispatch	COE ($)	NPC ($)	Operating cost ($/yr)	Initial capital ($)	Ren Frac (%)
1	320	395	2	155	LF	$0.279	$4.55M	$320,879	$402,914	32.5

(c)

Architecture							Cost				
Wind Turbine	Generator (kW)	Battery	Tidal Turbine	Converter (kW)	Dispatch	COE ($)	NPC ($)	Operating cost ($/yr)	Initial capital ($)	Ren Frac (%)
2	320	531	2	222	LF	$0.208	$3.39M	$225,051	$484,103	57.1

(d)

Architecture							Cost				
Wind Turbine	Generator (kW)	Battery	Tidal Turbine	Converter (kW)	Dispatch	COE ($)	NPC ($)	Operating cost ($/yr)	Initial capital ($)	Ren Frac (%)
2	320	539	4	222	LF	$0.213	$3.47M	$222,234	$593,458	61.1

Figure 5-18 show, the scenario with the lowest costs at the Foveaux site, the net present cost of each component in the system and the system as a whole. Capital, operating, replacement and salvage costs are small. The main costs are fuel for the generator and initial construction (no provision to enter it in Homer ’s financial analysis module).

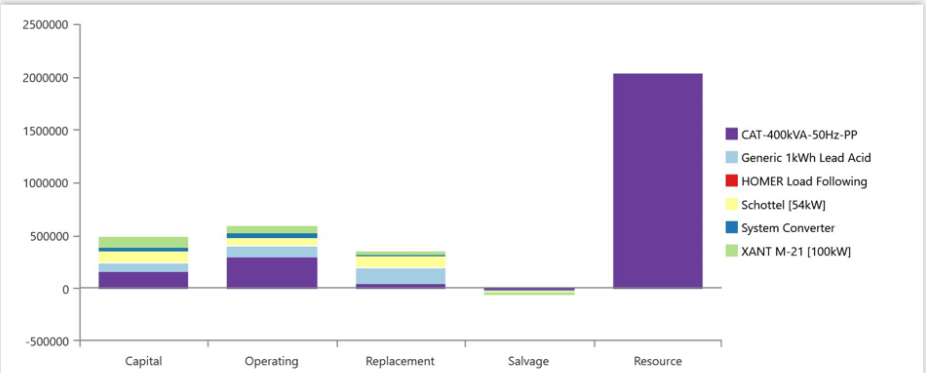

Net Present Costs

Name	Capital	Operating	Replacement	Salvage	Fuel	Total
CAT-400kVA-50Hz-PP	$160,000	$303,249	$44,674	-$19,701	$2.04M	$2.53M
Generic 1kWh Lead Acid	$81,774	$105,713	$159,340	-$8,123	$0.00	$338,704
HOMER Load Following	$200.00	$64.64	$0.00	$0.00	$0.00	$264.64
Schottel [54kW]	$108,000	$69,809	$95,411	-$12,936	$0.00	$260,284
System Converter	$34,129	$44,121	$14,480	-$2,725	$0.00	$90,005
XANT M-21 [100kW]	$100,000	$64,638	$31,881	-$17,967	$0.00	$178,551
System	$484,103	$587,594	$345,786	-$61,453	$2.04M	$3.39M

Figure 5-18:. Cost summary for components of scenario with lowest NPC (2W + 2T).

Table 5-12 depicts optimisation results for a possible alternative scenario which can balance wind and tidal generation, 1W+10T, which has a renewable fraction of 52.7%. However capital cost, operating cost, and NPC are higher than 2W+2T or 2W+4T. COE also becomes higher.

Table 5-12:Optimization results for balanced alternative scenario 1W+ 10 T.

Architecture						Cost				
Wind Turbine	Generator (kW)	Battery	Tidal Turbine	Converter (kW)	Dispatch	COE ($)	NPC ($)	Operating cost ($/yr)	Initial capital ($)	Ren Frac (%)
1	320	449	10	222	LF	$0.275	$4.48M	$284,477	$799,598	52.7

The reason why, is shown in Figure 5-19. Adding more tidal turbines increases whole-system capital, operating, replacement, and salvage costs. But it does not reduce whole-system fuel cost; and the scenario adds to whole-system construction cost (more floating platforms and cables for tidal turbines).

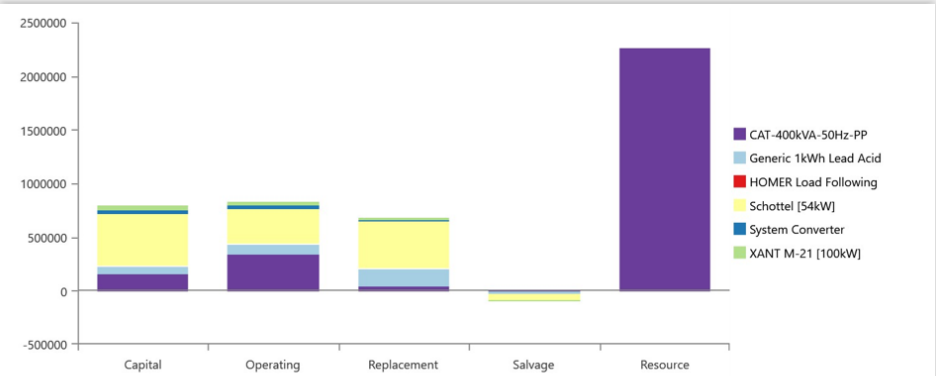

Net Present Costs

Name	Capital	Operating	Replacement	Salvage	Resource	Total
CAT-400kVA-50Hz-PP	$160,000	$350,470	$51,481	-$13,219	$2.27M	$2.82M
Generic 1kWh Lead Acid	$69,146	$89,389	$164,040	-$12,672	$0.00	$309,903
HOMER Load Following	$200.00	$64.64	$0.00	$0.00	$0.00	$264.64
Schottel [54kW]	$486,000	$314,139	$429,351	-$58,213	$0.00	$1.17M
System Converter	$34,252	$44,280	$14,532	-$2,735	$0.00	$90,329
XANT M-21 [100kW]	$50,000	$32,319	$15,940	-$8,983	$0.00	$89,276
System	$799,598	$830,660	$675,345	-$95,822	$2.27M	$4.48M

Figure 5-19: Cost and summary results for 1W+10T.

Homer provides an overview of the winning system - system with the lowest Net Present Cost in comparison to the base system. The base case system is the system with the lowest initial capital cost. There could be scenarios where the base case system is also the winning system. The NPC of the winning system for 2W+4T is 3.47 M$ which is lower than 4.53, 4.55 and, 4.48 M$ for 1W+1T, 1W+2T and,1W+10T respectively. This value is also lower than the NPC of the base system (5.57 M$) for 2W+4T. Figure 5-20 shows how the winning system of 36W can save money over the project lifetime.

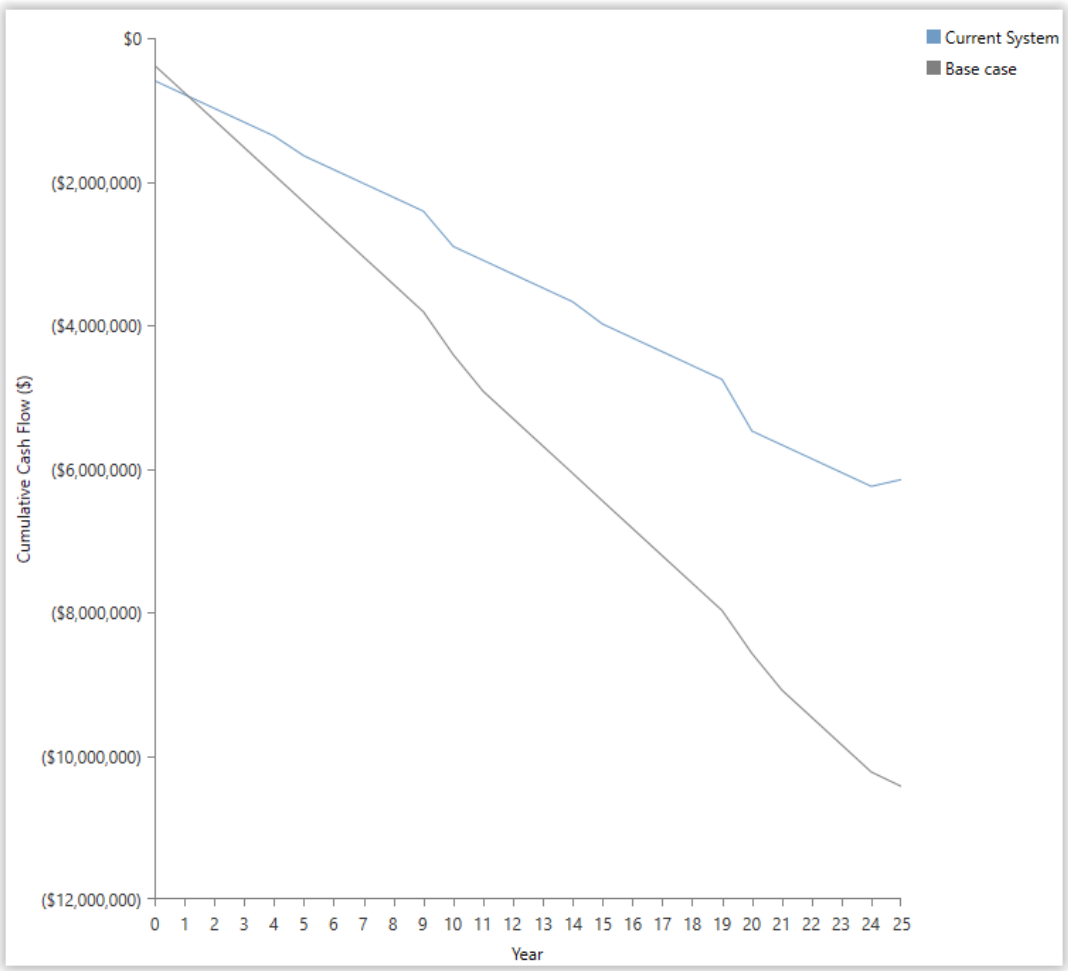

Figure 5-20: Cumulative cash flow of 2W+4T.

A sensitivity analysis was conducted to examine the impact of capital cost, operation and maintenance cost on the selection decision considering the comparison of the different scenarios discussed before. The project capital and the operation, and maintenance cost are allowed to vary by an increase up to 10% from -10% at increments of 5% using RETScreen [28]. Table 5-13 serves as a guide to interested investors on the best option for investment among current projects when considering such variations shows that the corresponding capital variation in the project internal rate of return is in the range of [9.8%, 13.6%] for 1W+1T, [7.3%, 10.7%] for 1W+2T, [9.8%, 13.6%] for 2W+2T, [9.7%, 13.5%] for 2W+4T and [9.7%, 13.4%] for 1W+10T and corresponding O&M variation in the project internal rate of return is in the range of [11.4%, 11.7%] for 1W+1T, [8.5%, 9.0%] for 1W+2T, [11.4%, 11.7%] for 2W+2T, [11.2%, 11.7%] for 2W+4T and [11.2%, 11.5%] for 1W+10T. According to the incremental internal rate of return analysis, the 2W+2T and 2W+4T scenarios are the most economically viable project when

considering the variation in the capital and O&M costs between -10% and 10% of the total cost of the project compared to others.

The economic assessment using the incremental rate of return method [169] and the application of sensitivity analysis on the capital cost and operation and maintenance cost to select the best economic project among wind, tidal, and combination of wind and tidal projects reveal that 2W+2T and 2W+4T scenarios are more attractive and feasible option compared to other distributed generation projects.

Table 5-13: Sensitivity analysis of capital and O&M costs on decision-making.

Type	Cost Variation	IRR(%) for Capital Cost	IRR(%) for O&M
1W+1T	-10%	13.6	11.7
1W+2T		10.7	9.0
2W+2T		13.6	11.7
2W+4T		13.5	11.7
1W+10T		13.4	11.5
1W+1T	-5%	12.5	11.7
1W+2T		9.7	8.9
2W+2T		12.5	11.7
2W+4T		12.4	11.6
1W+10T		12.3	11.4
1W+1T	0%	11.5	11.5
1W+2T		8.8	8.8
2W+2T		11.5	11.5
2W+4T		11.5	11.5
1W+10T		11.4	11.4
1W+1T	5%	10.7	11.4
1W+2T		8.0	8.7
2W+2T		10.7	11.4
2W+4T		10.5	11.4
1W+10T		10.5	11.2
1W+1T	10%	9.8	11.4
1W+2T		7.3	8.5
2W+2T		9.8	11.4
2W+4T		9.7	11.2
1W+10T		9.7	11.2

5.2.9 Discussion of Power Generation Results

Table 5-14 shows the mean output power for all scenarios. Stewart Island ‘s mean power demand is 143.9 kW. All scenarios can meet mean demand. Only 2W+2T ’s & 2W+4T ’s mean output exceeds peak demand (209 kW).

Table 5-14: Mean output for different scenarios.

Parameter	1W+1T	1W+2T	2W+2T	2W+4T	1W+10T
Mean Output of Wind Turbine (kW)	45.3	45.3	90.5	90.5	45.3
Mean Output of Tidal Turbines (kW)	4.47	8.9	8.9	17.9	44.7
Mean Output of Generator (kW)	111	109	111	109	105
Total (kW)	160.8	163.2	210.4	217.4	195.0

Table 5-15 shows the percentage of electricity produced by wind and tidal turbines. Stewart Island ’s total power demand is 1,260,332 kWh/yr. 2W+4T produces the highest renewable energy fraction and could contribute 75% of power demand.

Table 5-15: Share of wind and tidal turbines in producing electricity and meeting demand.

Parameter	1W+1T	1W+2T	2W+2T	2W+4T	1W+10T
Wind Turbine (% of production)	30.1	29.9	56.2	55.1	28.7
Tidal Turbine (% of production)	2.97	5.90	5.54	10.9	28.3
Generator (% of production)	66.9	64.2	38.3	34.1	43.1
Renewable Fraction (% of production)	33.1	35.8	61.7	66.0	57.0
W+T Generated power (kWh)	435,516	474,640	871,033	949,280	787,630
W+T Generated power (% of demand)	34.6	37.7	69.1	75.3	62.5

Table 5-16 shows the amount of pollutants and fuel consumed. 2W+4T is the most environmental-friendly scenario.

Table 5-16: Emissions of pollutants and fuel consumption.

Parameter	1W+1T	1W+2T	2W+2T	2W+4T	1W+10T
Carbon Dioxide (kg/yr)	677,709	657,185	415,995	378,894	462,949
Carbon Monoxide (kg/yr)	1,024	993	629	573	700
Unburned Hydrocarbons (kg/yr)	7.70	7.47	4.73	4.31	5.26
Particulate Matter (kg/yr)	0	0	0	0	0
Sulfur Dioxide (kg/yr)	1,684	1,633	1,034	942	1,151
Nitrogen Oxides (kg/yr)	3,713	3,600	2,279	2,076	2,536
Total Fuel Consumed (L)	256,757	248,981	157,604	143,548	175,393
Average Fuel per Hour (L/hr)	29.3	28.4	18.0	16.4	20.0

Comparing different designs shows that that 2W+4T is an optimized hybrid design which can provide the electricity demand of Stewart Island by using wind, tidal and diesel sources to cover each other during periods when one or another source can not generate. 2W+4T ´s mean output is highest at 90.5 kW. 2W+4T can meet peak load (209 kW). 2W+4T can supply 75.3% of Stewart Island ´s total demand.

In comparison with the optimum scenario, 2W+2T ‘s mean output is almost as high, and it can also meet peak load. Its renewable component can still supply 69.1% of total demand. However, 2W+2T ‘s diesel consumption is somewhat higher than the optimum scenario. So are its greenhouse gas emissions. 1W+1T and 1W+2T have lower mean output, their renewable output can’t meet peak load, and meets less than 40%. Fuel consumption and emission of pollutants are much higher than other scenarios.

1W+10T can balance wind and tidal power generation. The renewable components can supply 62.5% of demand. Although less than 69.1% from 2W+2T and 75.3% from 2W+4T, this is still a satisfactory renewable fraction.

5.2.10 Discussion of Financial Analysis Results

In this section, the scenarios are compared, based on financial analysis results from section 5.2.8 which are summarized in Table 5-17.

Table 5-17: Financial analysis summary.

Parameter	1W+1T	1W+2T	2W+2T	2W+4T	1W+10T
Capital equipment(k$)	350	402	484	593	799
Replacement (k$)	233	282	345	469	675
Construction(k$)	-	-	-	-	-
End-of-project removal/reinstatement (k$)	-	-	-	-	-
Operating cost (k$)	323	320	225	222	284
Fuel Cost (M$)	3.3	3.2	2.03	1.8	2.2
Total NPC (M$)	4.53	4.55	3.39	3.47	4.48
COE (c/kWh)	0.278	0.279	0.208	0.212	0.274

Capital equipment: Cost is least for scenarios 1W+1T and 1W+2T, but these scenarios don't generate much power from renewable sources. The scenarios which can (2W+2T, 2W+4T, 1W+10T), require higher initial expenditure on equipment purchase.

Replacement: Cost to replace equipment (at end of design life) is consequently least for the scenarios which don't generate much renewable power and is higher for the scenarios which can.

Construction: Cost of project installations is not shown, because Homer Pro 's financial analysis module does not include (It just compares equipment, operating and resource costs).

Removal/re-instatement: Cost to remove or re-instate project installations (at end of design life) is not shown, for same reason.

Operation: Cost is least for two scenarios (2W+2T,2W+4T) which generate much power from few turbines. Operating cost for 1W+10T is greater, because this scenario has numerous turbines. Operating cost is most expensive for the scenarios which don't generate much power from renewable sources. Reason is, the diesel generator (which has high operating cost) starts up often and runs longer.

Resource: Cost is least for scenarios which generate much power from wind and tidal turbines (2W+2T, 2W+4T, 1W+10T). Reasons are firstly, there is no resource cost for wind or tide. Secondly, fuel purchase for the diesel generator is reduced by up to 60%.

Total net present cost of project (NPC) is least for 2W+2T, because this scenario has low equipment and operating costs, and generates much power (62%) from renewable sources, so does not incur a high resource cost. NPC is almost the same for 2W+4T, which can generate a greater percentage of power (66%) from renewable sources. But 1W+10T which can still generate much renewable power (57%), is almost as costly as the scenarios which don't, because it requires more expenditure on equipment purchase and operation.

Total cost of energy: COE is least for 2W+2T and almost the same for 2W+4T, when their NPCs are levelized (per kWh over life of the project). But COE for 1W+10T, despite its high renewable percentage, is almost as great as the scenarios which don't, once the NPCs of all three are levelized for purpose of comparison.

The 2W+4T scenario is optimal for power generation because it produces the highest renewable fraction (66%), while the renewable fraction for 2W+2T is 62%. Its total NPC seems affordable at 3.47 million dollars. Its Levelized cost at 21 c/kWh appears better than the present scenario (5D = 0.23 c/kWh).

A possible alternative scenario, 1W+10T, would equalize generation from wind and tidal at 28% each, providing a balance of renewable sources. However, its total NPC is considerably higher at 4.48 million dollars, and the Levelized cost is also higher at 27 c/kWh.

A problem with Homer Pro's financial analysis is that it just evaluates equipment, operating and resource costs when calculating NPC and COE. A realistic comparison of NPC and COE should include construction and installation costs, particularly offshore platforms, marine cables, and a DC-AC shore converter station.

5.2.11 Reducing the Consumption

If the government with some policies could reduce the electricity consumption of Stewart Island by 20%, it does not affect the levelized cost of 2W+4T scenario and still it would be 21 c/kWh. But renewable fraction increases from 61.1% to 68.6% as a result of increasing the percentage share of renewables production and decreasing of generator one as shown in Figure 5-21.

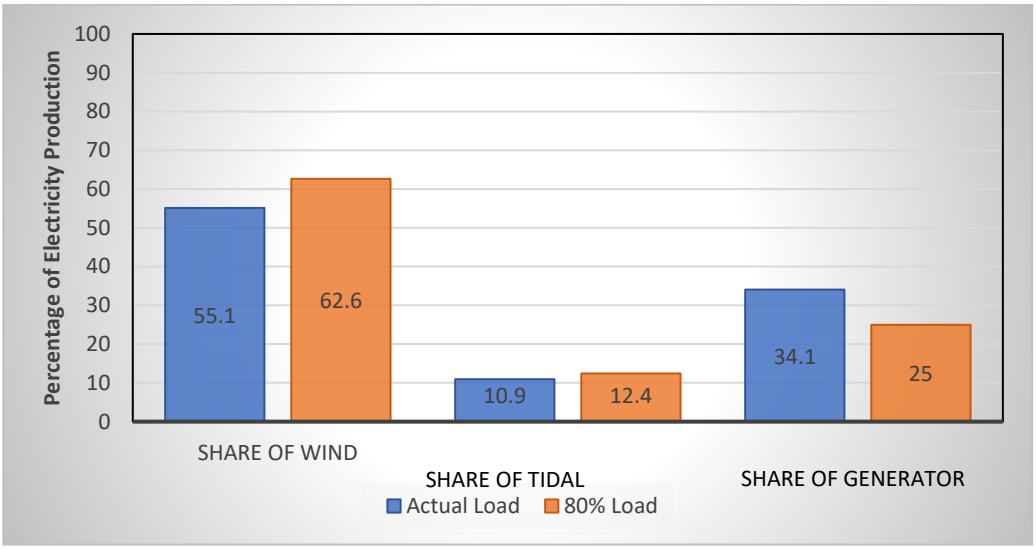

Figure 5-21: Share of wind and tidal turbines on electricity production in actual load and 80% of actual load.

Figure 5-22 shows that reducing of electricity consumption by 20%, reduces the amount of pollutants 33%. This can be used as an approximation to estimate how power consumption can affect pollution. The fuel consumption decreases from 143,548 litres to 95,451 litres.

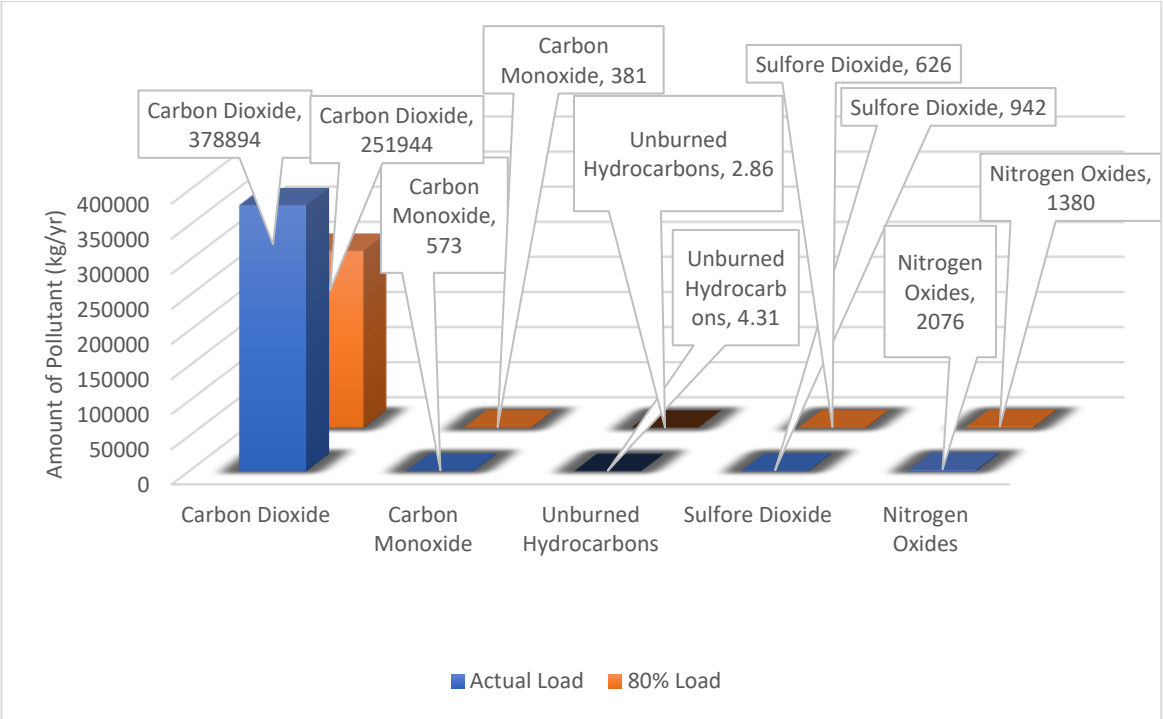

Figure 5-22: Share of wind and tidal turbines on electricity production in actual load and 80% of actual load.

The cost of microgrid design in this case is much better. Total NPC and operating cost reduce from $3,466,388 and $222,233.70 to $2,754,464 and $168,263.50.

So, reducing the consumption can not reduce the cost of electricity, but can be very effective to reduce emissions and microgrid system.

5.2.12 Summary of Offgrid Design

This section has proposed integration of two available offshore renewable energy sources -wind and tidal- using a microgrid, with the aim to decrease the cost of electricity in a remote off-grid coastal community and avoid the detrimental effects of off-grid diesel generation on the environment.

Stewart Island was selected as a case study, because it is typical of isolated coastal communities in New Zealand which depend on small locally-operated diesel power stations or single-household petrol generators.

Components of a suitable microgrid design were identified as multiple energy sources (wind and tidal turbines, with diesel generators for back-up), storage

devices (batteries), supply cables (marine connecting to land), and operating equipment (AC to DC converter, system controller).

An industry-recognized simulation software package, Homer Pro, was used to optimise the microgrid design, by evaluating scenarios composed of components assembled in different combinations, and to analyse their cost.

Power generation results and financial analysis results for various scenarios enable several conclusions:

- There is enough tide to generate electricity during 65% of year at an offshore site close to Stewart Island (referred to as the Foveaux site).
- There is also enough wind to generate electricity during 90% of year at the Foveaux site. However, this site is on the other site of Foveaux Strait, 40 km away from Stewart Island ´s community at Oban.
- DC electricity from the offshore Foveaux site can be integrated as a hybrid system with AC electricity from the existing onshore diesel generators at Oban by using a microgrid design as described in Section 5.2.4. The design solution is to mount tidal and wind turbines on the same offshore platform, feed power through a DC marine cable to a DC-AC converter at the Stewart Island shore, then through an AC land cable to a system controller at Oban ´s diesel generator station.
- The design can be optimised, in a way which enables Stewart Island ´s power to be supplied in part from renewable sources. Simulation of various component combinations (in Homer Pro) shows several scenarios which look promising. The combination which is optimal for maximising renewable generation is two wind and four tidal turbines plus a single diesel generator.
- The optimal scenario is worth implementing because it could supply 75% of Stewart Island ´s power demand from renewable sources, reducing diesel fuel consumption by 60%.
- It is unknown whether the design can be constructed at an affordable cost, because the Homer Pro financial analysis module does not include construction or installation.
- Once built and installed on site, the design can be operated at an affordable cost, because levelized cost of equipment and resources over project life (21 c/kWh) is lower than present operation cost of five diesel generators (23 c/kWh).
- A complete cost-benefit analysis is needed, to find out whether the supply authority can recover all construction, installation, operating and

maintenance/replacement costs from a lower charge to the community than its present retail charge (67 c/kWh).

Based on what presented by now, they are some research gaps for future work as below:

* The Foveaux site is too distant from Stewart Island. Current simulations exclude cost of buying and installing a 40 km marine cable. At that cost, SIESA may as well just connect to the NZ main grid. But a small community supply authority can't afford that.
* The optimal scenario at the Foveaux site doesn't generate much tidal energy - just 11% of Stewart Island 's demand. SIESA could get as much - maybe more - renewable power by installing a wind turbine at the Foveaux site, and forgetting about tidal.
* Current simulation also excludes cost of constructing and installing two large monopiles with platforms and masts on top. Those are going to be expensive. Once they're added to the net present cost, the levelized cost of supply will greatly exceed the present generating cost from diesel (23c/kWh). To recover construction, installation and operating costs over life of the project, SIESA would have to charge its customers more than the present retail charge (67c/kWh).
* The proposed site (Foveaux) proposed based on MetOcean model. However, there are sites with faster tidal currents in shallow water such as Barclay and Fish Rock, close to the shore of Stewart Island which MetOcean model could not recognize them.
* Foundation design of this design can be another further work; The selected wind turbine can operate closer to sea level, so it does not need big mast. Also, the small selected tidal turbine can operate in shallow water, so it does not need big monopiles.

The balance between power consumption and power generation depends on the number of necessary turbines. The main parameters for an optimized design are:

- More power generation which is analysed in this Chapter.
- Depending on the water depth of the site selected by microgrid design, a type of foundation needs to be designed as explained in Chapter 5.
- Less cost which is found in Chapter 7.

- Decision on which direction is in favour for wind and tidal turbines which will be analysed in Chapter 7.

5.3 Grid-Connected Design in Terawhiti for Node CPK0331 (Central Park)

The World Energy Outlook 2019 clarifies the effect of current decisions on energy systems in the future. If no policy actions are taken, then the current trend of energy demand is anticipated to increase by 1.30% per year until 2040, leading to an increase in emissions [9]. Nowadays with the increasing global energy demand and global climate change, two important solutions have been considered to tackle this issue: (i) reducing the cost of energy and (ii) finding new sources of energy that are environment-friendly [10]. With the negative climate impact of fossil fuel power generation and the requirement of global policy to shift towards a green mix of energy production, the investment in renewable energy is an opportunity in developing countries. However, a poor economy associated with limited income, funds availability, and regulations governing project funding and development are key factors that challenge investors in the energy sector [11].

In New Zealand, the Government set a target to reach 90% electricity production from renewable sources by 2025 [170, 171] and 100% by 2035 [15]. Currently, there are 11,349 kilometres of transmission lines that distribute electricity from remote areas, where generators are located, all over New Zealand. The Cook Strait cables connect the power line of the North Island to the South Island as shown in Figure 5-23. These bio-directional cables carry 350 kW electricity [15].

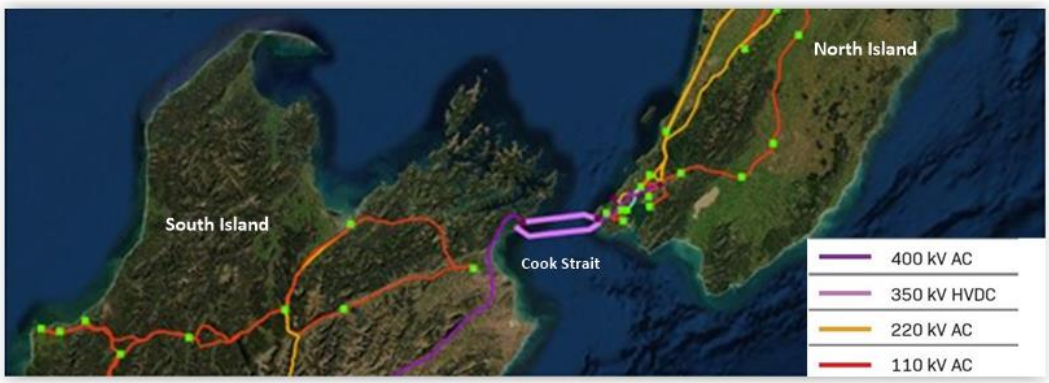

Figure 5-23: Map of Cook Strait cables [172].

New Zealand consumed about 38,800 gigawatt-hours (GWh) of electricity per year. In 2017, renewable sources (hydro, geothermal, wind, and solar) supplied 59%, 17%, 5%, and 0.2% of the country's electricity needs respectively, and thermal sources (coal, diesel, and gas) supplied the other 18.8% [15].

Wind power systems are a cost-effective technology for harnessing renewable energy and have expanded annually at a dramatic rate of 25–35% globally over the last decade [16, 17].

In more recent studies, the advantages of offshore wind generation against onshore wind generation have been highlighted through life cycle analysis (LCA), showing a 48% improvement in the sustainability of the project [18]. Offshore wind farms have increasingly attracted massive investment since 2015 [19]. However, the cost of electricity using offshore wind is still high [21]. Installing tidal turbines in New Zealand, as another good source of renewable energy, is usually considered to be not cost-effective because the turbines can be exposed to harsh currents that can reduce their life. and the foundation design can be complicated when the water depth is more than 30 m [22].

Wind power systems, as a form of renewable energy source, are often integrated with other forms of power-generating systems to form a small power grid, known as a microgrid. The integration of both wind and tidal turbines using the same foundation reduces the cost of electricity [23] and enables a more predictable power generation from two different sources of energy.

The North and South Islands of New Zealand are separated by Cook Strait that connects the Tasman Sea and the Pacific Ocean and is 22 kilometers wide at its narrowest point as shown in Figure 5-24 [173].

Figure 5-24: Location of Cook Strait [174].

Much of the seabed is at water depths of less than 150 m except through the Narrows where depths reach greater than 300 m, and to the southeast in the Cook Strait canyon system [173].

The Cook Strait has been particularly explored due to the following unique features:

- Strong convergent tidal flows in the context of a subtropical ocean convergence zone;
- Convergence of two crustal plates, underwater land sliding, and highly erosive currents;
- Wind funneling and the associated high waves [175].

This paper investigates the best scenario in Cook Strait for a microgrid using wind and tidal energy as Cook Strait has the greatest potential for tidal energy in New Zealand. Three different scenarios of electricity generation are analyzed (i) using tidal turbines only, (ii) using wind turbines only, and (iii) using both wind and tidal turbines.

From a technical point of view, the contributions of the study are as follows:

1. Explore the use of tidal energy for on-grid design;
2. Explore microgrid design to link tidal energy with other sources;
3. Explore the use of optimization software as a method how to apply wind and tidal data into microgrid design;

4. Define a method that could be used to optimize a microgrid of wind and tidal turbines anywhere to facilitate future feasibility studies.

Homer Pro and WRPLOT view software are used for the integration of energy sources and analyzing the resources' potential. The HOMER Pro® microgrid software is used to optimize the off-grid and on-grid designs in both engineering and economic aspects for residential, commercial, and community purposes [29]. The WRPLOT view software is used to provide the available classes of turbine speeds for a given location [30].

5.3.1 Modelling of the DC Ongid Microgrid

Homer [29] is used for the microgrid design of energy resources. Several simulations are carried out to design a DC-linked wind and tidal-based microgrid for electricity generation in the Terawhiti site in New Zealand. The resource conditions (wind speeds and tidal currents) can play an important role in selecting the microgrid components so that the microgrid can produce more electricity at a lower cost considering the technical constraints e.g. the 25 year project lifetime [129].

It is envisaged that the microgrid may also have the following:

- Biodiesel Generator: As a backup to cover the base load from renewable sources in off-grid scenarios.
- Battery Energy Storage: for energy storage applications. There is also a need to investigate where the microgrid will link the offshore tidal and wind electricity outputs into the main grid. Several supply links may already exist, but if there is no supply link, a new link will have to be chosen.

The link should consist of

- On-shore distribution lines: which can be overhead and underground lines with a percentage of distribution line losses.
- Transformer: to transfer electrical energy from one electrical circuit to another circuit.
- Controller: to manage or direct the load.

For the new hybrid wind and tidal system, other components will need to be purchased and installed. They are:

- Support structures for tidal and wind turbines
- Tidal and wind turbines (including electrical generators).

- Converters: to rectify the AC output of the generators to DC.
- Marine cable: to feed power to a DC–AC converter at a site, then through an AC land cable to a system controller at a station.
- Shore station: to feed the marine cable's output into an AC network, where the cable emerges onto land.

To achieve islanded power generation, no grid is required, while in a grid-connected system, there is a need to connect the output power of the generators to the grid [176]. Microgrids, either in grid-connected or islanded mode, could contribute to the future of clean energy by better controllability and adaptability [177].

The selection of the most economically viable project through the application of the incremental internal rate of return analysis can be affected by variations of any of the cash flow components, such as, for example, the capital cost, the operation, and maintenance cost, the fuel cost as in case of the diesel generator, the debt to equity ratio, the interest rate, etc. If a project is selected for investment, then it is to be funded by two resources. These are bank loans and promoters' contributions. Bank loans reflect the debt component of the project cost and represent 75% of the capital cost of the project. On the other hand, promoters are to cover 25% of this cost [11].

There are two main electrical parameters for the optimization process; the total Net Present Cost (NPC) and the Levelized Cost of Energy (COE). The total value which is calculated by Homer for the installation, replacement, operation and maintenance, fuel, and salvage of all components minus all the revenue during its lifetime is NPC or the Life Cycle Cost. The average generation cost of 1kWh electricity is COE [29].

Both of these parameters depend on the annualized cost of the system. The total NPC is calculated and can be expressed by (5-3) [178],

$$C_{NPC} = \frac{C_{T\ ANN}}{CRF_{i,N}} \tag{5-3}$$

where $C_{T\ ANN}$ is the total annualized cost, i is the actual interest rate, N is the number of years and $CRF_{(i,N)}$ is the capital recovery factor, which is calculated as,

$$CRF_{i,N} = \frac{i(1+i)^N}{(1+i)^{N-1}} \quad (5\text{-}4)$$

The Levelized Cost of energy is given by,

$$COE = \frac{C_{T\ ANN}}{E_{ls} + E_{grid}} \quad (5\text{-}5)$$

where E_{ls} and E_{grid} are the amount of energy served by the microgrid and sold to the grid [129].

5.3.2 Site Selection

Electricity Market Information website (EMI) [179] is part of the New Zealand Electricity Authority‘s information website. Based on the facility location of the project, the microgrid considered in this study will be designed to provide the electricity demand to node CPK0331 (Central Park) in the south of the northern island of New Zealand as shown in Figure 5-25.

Figure 5-25. Node load trends of New Zealand [180].

5.3.3 Identifying Demand

The EMI data has been used in the case study to estimate the monthly and hourly generation pattern. Figure 5-26 shows that the peak and trough months are July and January, respectively [179].

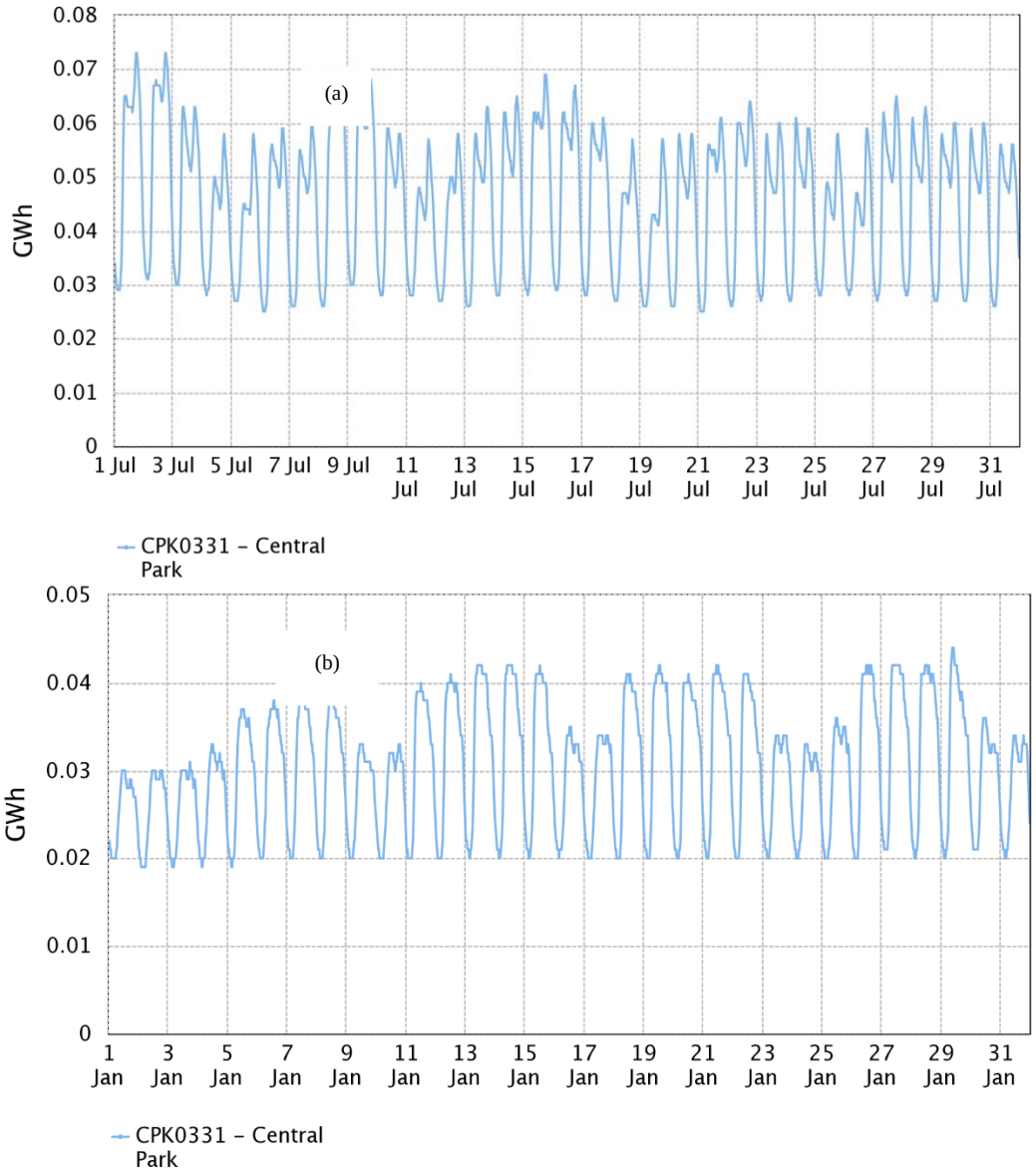

Figure 5-26: (a) Maximum and (b) Minimum load of CPK0331.

5.3.4 Obtaining Environmental Data

According to the MetOcean atmospheric model shown in Figure 5-27(a), the tidal currents in four areas, (i) Cape Regina (in the north), (ii) Cook Strait (between two Islands), (iii) Foveaux Strait (in the north of Stewart Island), and (iv) south of Stewart Island are more than 1 m/second. The south of Stewart Island is ruled out as it is far from clients and markets and any installation there will increase the cost of the project significantly [164].

So, for microgrid design, two areas are suitable (i) Cook Strait in the south of the northern island for the grid-connected design, and (ii) the Foveaux Strait in the south of the southern island for the off-grid design in Stewart Island.

Tidal current modeling was conducted on an NZ-wide grid with a 0.06° resolution (5.6 × 6.6 km). The simulation nested high-resolution domains over Cook Strait (0.002°; 170 × 230 m). The tidal current around New Zealand is hindcasted by the Princeton Ocean Model (POM) in a vertically integrated two-dimensional mode with boundaries provided from the global TPX07.1 solution [164]. This model is the result of solving a set of partial differential equations of spatial variability tides using the Goring simplified continuity equation, the Navier–Stokes equations by eliminating the vertical dimension (integrating velocities over depth), and a finite-element method [181].

The results show that among these points, the Terawhiti point in Cook Strait has the strongest tidal currents for tidal power generation.

(a)

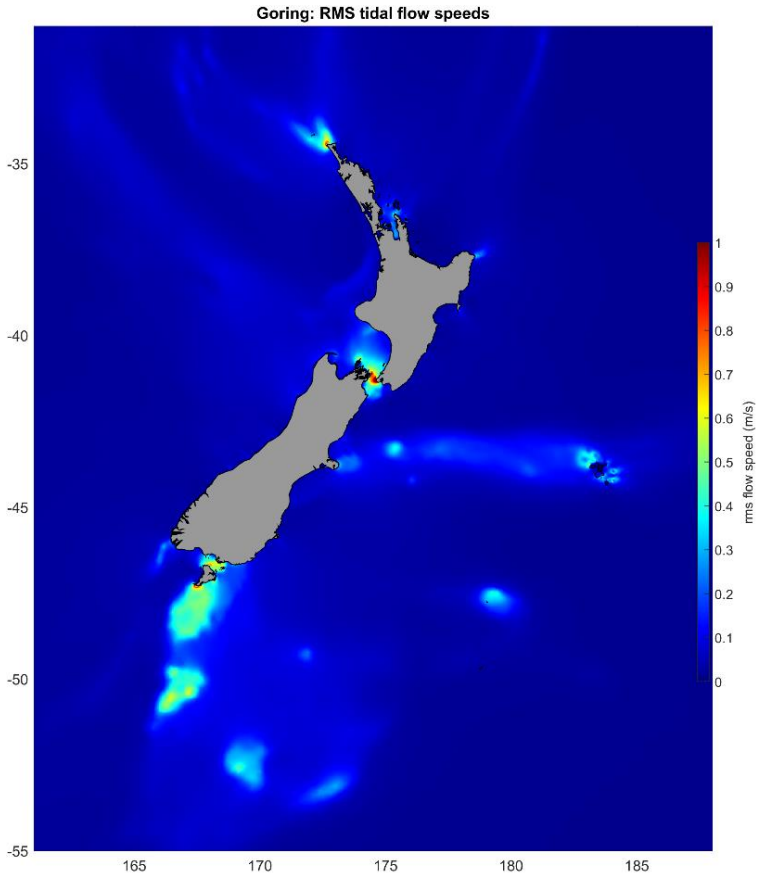

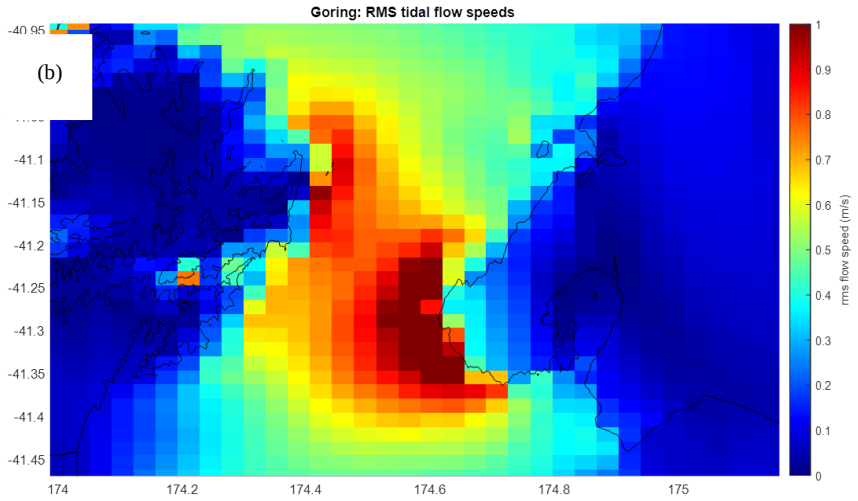

Figure 5-27: Tidal current speeds (a) around New Zealand and (b) Terawhiti in cook strait.

Global Wind Atlas [142] indicates that this point is also in the area with a high potential for wind energy (Figure 5-28).

(a)

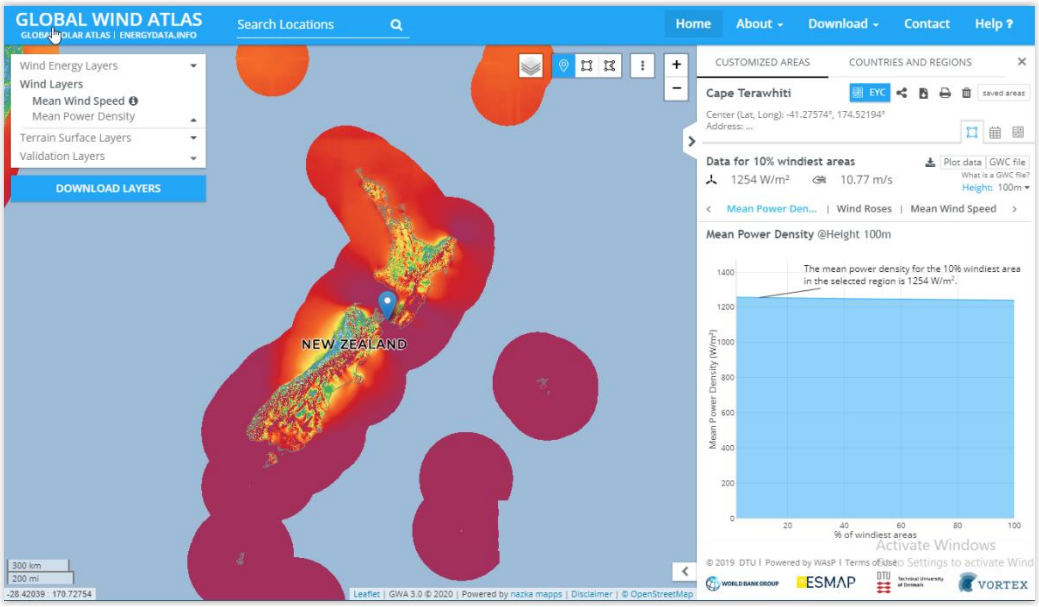

(b)

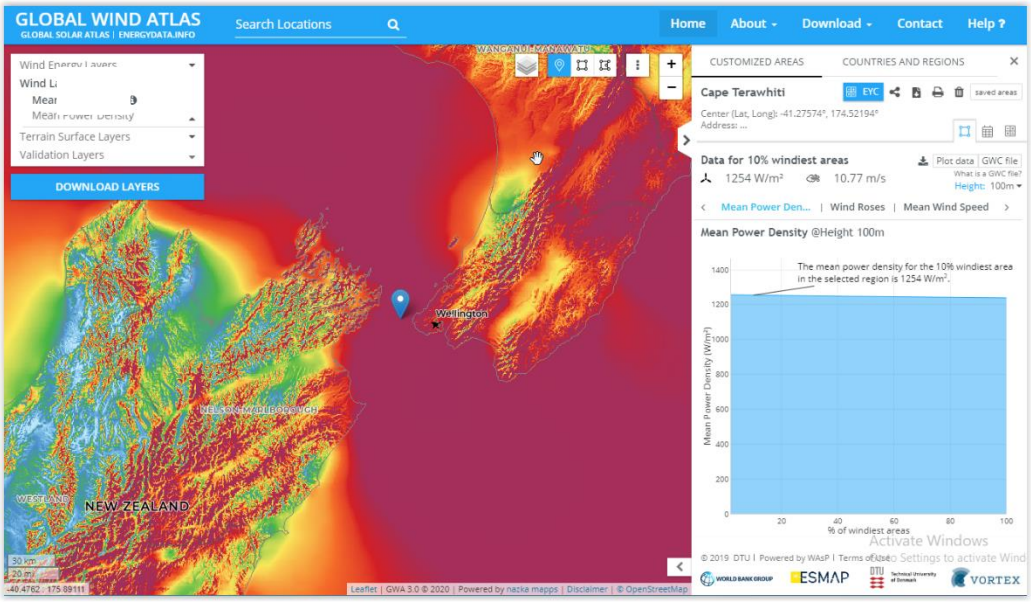

Figure 5-28. Wind blow conditions in (a) New Zealand and (b) Terawhiti [142].

The geographical coordinates of selected site are shown in Table 5-18 and Figure 5-29.

Table 5-18: The environmental parameters of Terawhiti for microgrid design

Location	Latitude (deg)	Longitude (deg)	Annual Water Speed(m/s)	Water depth(m)	Annual Wind Speed(m/s)
Terawhiti	−41.279497°S	174.524249°E	1.09	30	7.10

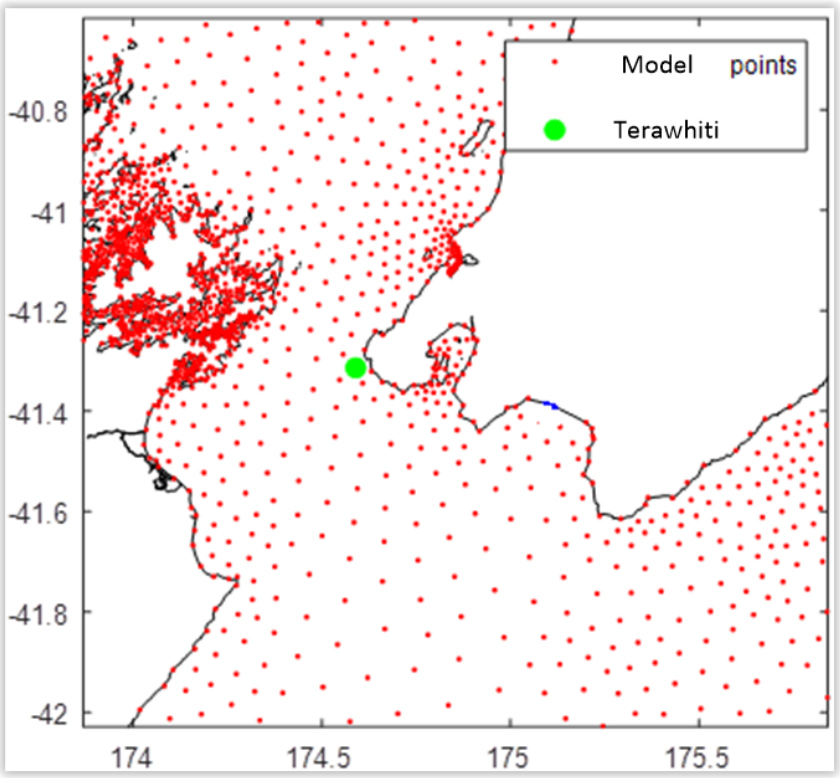

Figure 5-29: Location of Terawhiti in Cook Strait.

5.3.5 Microgrid Components and Resources

To carry out a microgrid design, the first step is to identify a site that is acceptable in terms of energy resources and power output generation. This was done by contacting the National Institute of Water and Atmospheric Research (NIWA) and analyzing the wind and tidal conditions in those locations.

The next step is to import the resource data, such as the wind and tidal speed. The wind speed values for the selected site can be automatically downloaded, from which the annual average wind speed can be calculated. However, the water speeds are not as easy to import as Homer needs 8760 hourly data for 12 months, which means a total of 8761 (total number of hours in a year) values of water speed need to be gathered and imported to Homer to calculate the annual average water speed. After that, various components need to be selected for the design including the data for the loads, wind and tidal turbines, convertor, controller, battery, and generator. The models and cost of all elements should be fed to Homer. After completing the

data entry, the simulation can proceed to analyze the cost-benefit comparison of the three technologies in these sites [129].

The main component for generating electricity from renewable energy resources (wind and tidal) is the turbine [182, 183]. Wind and tidal turbines with similar capacities are selected from 19 Siemens SWT-3.6MW-107 wind turbines and 38 AR2000 [2MW] tidal turbines. The SWT-3.6-107 wind turbine is found to be an ideal offshore turbine. A strong structural design, self-regulating lubrication systems with great supplies, temperature control of the internal conditions, and a simple generator system without slip rings provide high reliability with long service periods. The unique net converter system from Siemens for grid codes has maximum flexibility in the output adjustments and faults. Also, in the design of the main components, best engineering practice needs to be used in terms of safety and dimension sizing [184]. The Siemens SWT 154, 6 6 MW turbine marginally came out as the favorable choice using an options matrix by Plymouth University [162]. For the chosen tidal turbine, a comparable turbine of Siemens is chosen for the hybrid model.

A DC bus connects all the components, where, in this study, the wind and tidal turbines, are the sources of energy. There is another setup in Homer to choose the type of load profile that needs to be identified such as residential, commercial, industrial, or community, where, in this study, the residential load is considered. If energy storage is available, Homer also requires the energy storage type.

Storage of electricity seems the unavoidable solution for the effective energy management with the micro-grid. The energy storage in batteries is not a feasible option for the current battery prices, especially when selling energy to the main grid is an option. In the case that selling is not allowed or technically not possible, storage starts becoming an option. Especially when taking into account the battery cost reduction that is expected to take place in the coming years (50% by 2030), energy storage seems the only feasible way for achieving cost reduction and managing the peak demand on a daily base. Thereafter, the proper size of a battery system in terms of energy storage plays an important role for the total minimization of system's cost during its lifetime of microgrid system [185]. To ensure that the proposed microgrid can work autonomously, the BASF NAS 1250 kWh battery is considered for storage set up after a lot of simulations [135].

The grid-connected system under consideration consists of wind and tidal turbines combined with a battery energy storage system (BESS) [186] to account for periods of prolonged lack of wind and tidal as shown in Figure 5-30.

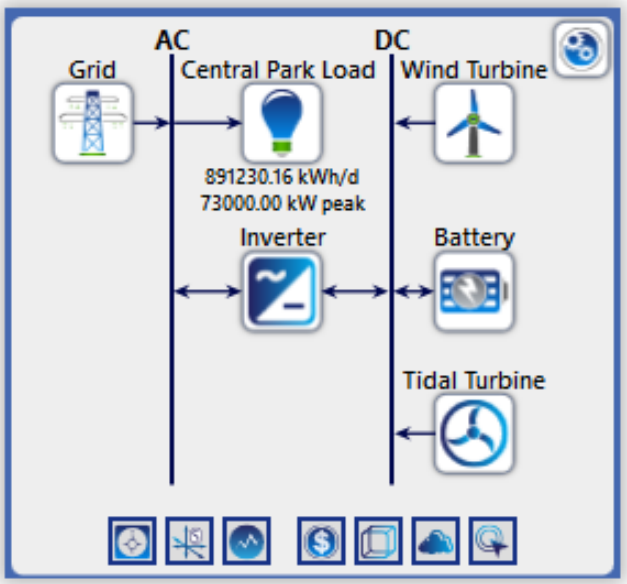

Figure 5-30: Schematic layout of DC microgrid

5.3.5.1 Wind Turbine

Figure 5-31 shows the power curve of the Siemens SWT-3.6-107 wind turbine. This turbine is the latest model from Siemens in the Multi-MW class having pitch technology with variable speed [187]. The capital, replacement, maintenance, and life of a turbine are taken as $6,000,000, $6,000,000, $120,000/year, and 20 years respectively. The power equation of wind turbine is presented by equation (5-6):

$$P_{wind} = 3.009/(0.0008354 + e^{-0.7916V}) \quad (5\text{-}6)$$

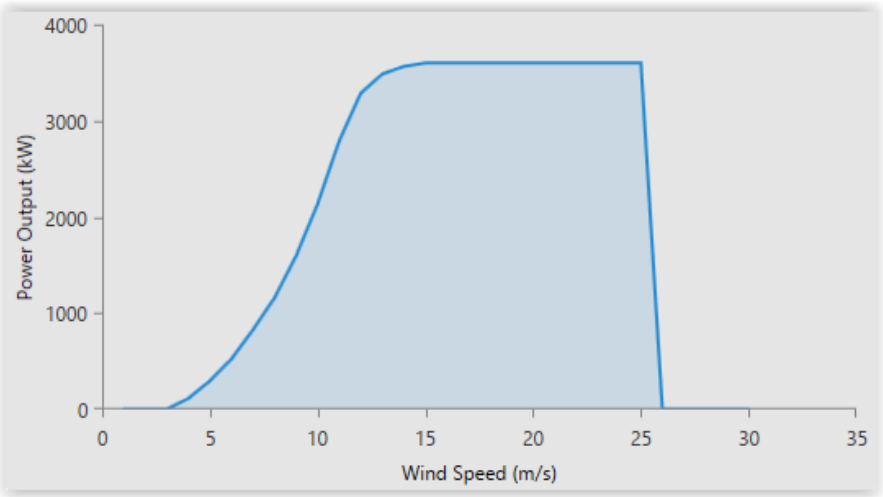

Figure 5-31: The power curve of the Siemens SWT-3.6MW-107m Offshore wind turbine [29].

The pertinent details for the Siemens SWT-3.6-107 wind turbine are set out in Table 5-19.

Table 5-19: Wind turbine details [159, 160].

Wind Turbine	Value
Name	Siemens SWT-3.6MW-107m [3.5MW]
Abbreviation	SWT-3.6-107
Rated Capacity (kW)	3,600
Manufacturer	Siemens
Cut-in speed	4 m/s
Cut-out speed	25 m/s
Rotational speed	5-13 rpm
Hub height	87 m
Swept area	8,992 m^2
Rotor diameter	107 m

The cut-in speed (the required wind speed for generating electricity) for Siemens SWT-3.6 wind turbine is 4 m/s [188]. The WRPLOT view software [30] was used to find the wind frequency distribution in Terawhiti. Figure 5-32 shows that for 78.2% of the year the wind speed is more than 4 m/s, hence it is suitable for electricity generation in Terawhiti.

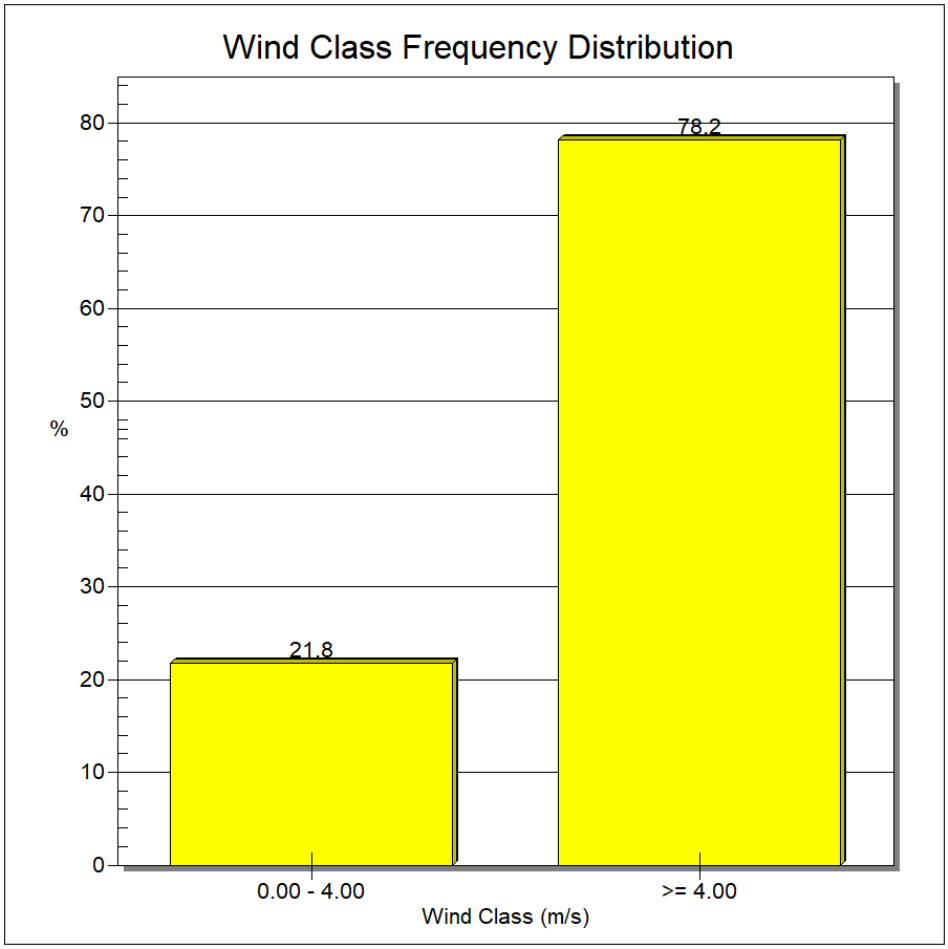

Figure 5-32: Wind frequency distribution in Terawhiti.

5.3.5.2 Tidal Turbine

To understand the potential for tidal energy in New Zealand it is important to appreciate some unique features of its tidal patterns. The tidal pulls caused by moon magnetism produce two high tides and two low tides over 24 hours and travel around the New Zealand coast in about 12 hr 25 min which takes about 6 hr 10 min for each incoming (flood) and outgoing (ebb) tide. Each tide time is about one hour later than the previous day. The tide times vary from New Zealand west to New Zealand east (Waitemata harbor, Auckland and Manukau harbor, Auckland) in an anti-clockwise direction. Each harbor is adjacent to only a small piece of land with 4 hours apart tidal patterns between the harbors (history records that Maori would take a canoe overland between Waitemata and Manukau harbors near Onehunga as a war party or for better fishing) [174]. Figure 5-33 is an example of a high tidal

range site (Port Taranaki) and a low tidal range site (Napier) using TPX09 software [31].

(a)

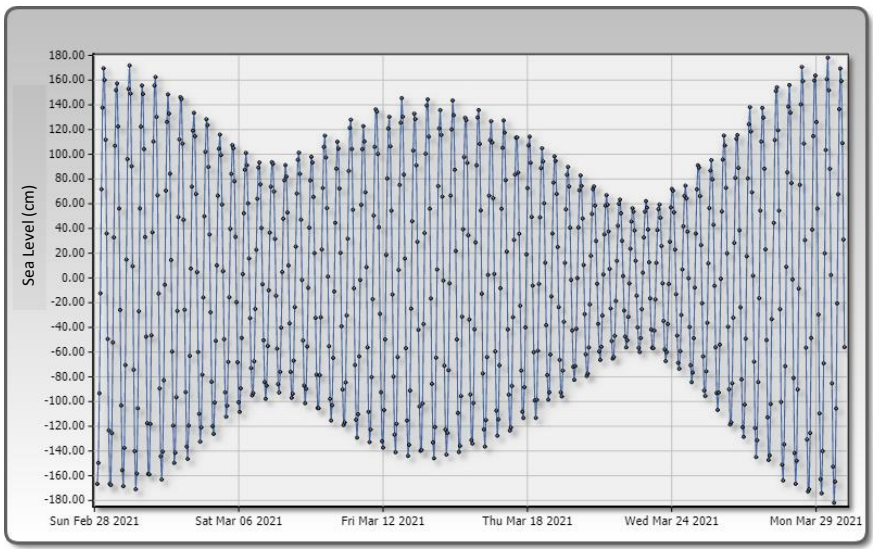

(b)

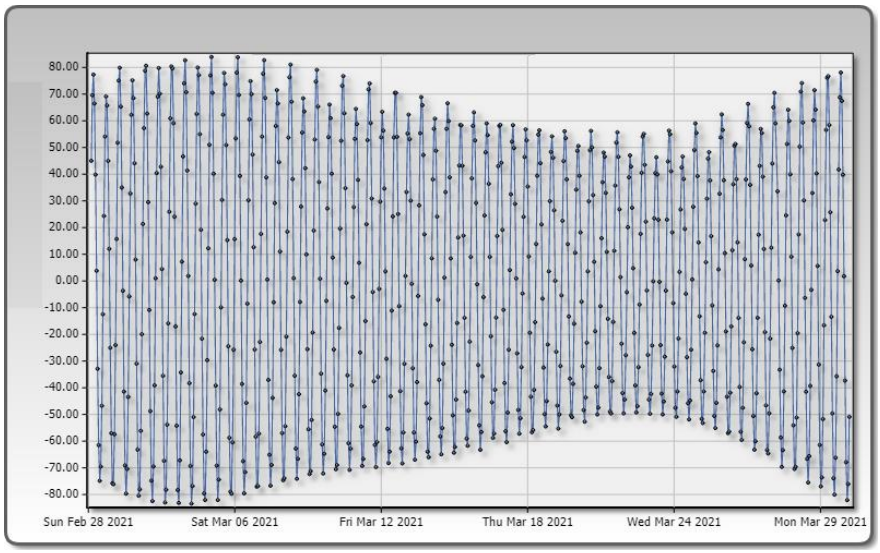

Figure 5-33: (a) An example of a high tidal range site at Port Taranaki, and (b) a low tidal range site at Napier.

The diurnal inequality is more evident in Port Taranaki with a high tidal range. A strong complicated tidal current can be found through Cook Strait, between the North and South Islands [174]. The Terawhiti site which is investigated in this paper for microgrid design is in the Cook Strait area.

Homer software provides different types of tidal turbines that are available in Hydrokinetic as a part of library components. Choosing two AR2000 tidal turbines,

four cost parameter needs to be fed to the software (i) the capital (or installation and wiring and mounting expenses), (ii) the replacement cost, (iii) the maintenance cost, and (iv) the lifetime of the tidal turbines. For the purpose of this research, the following parameters are used: $3,000,000, $3,000,000, and $60,0000/year and 20 years respectively. The power curves of the tidal turbine are given in Figure 5-34. The power equation of tidal turbine is presented by equation (5-7):

$$P_{tidal} = 31.61/(0.01549 + e^{-2.156V}) \quad (5\text{-}7)$$

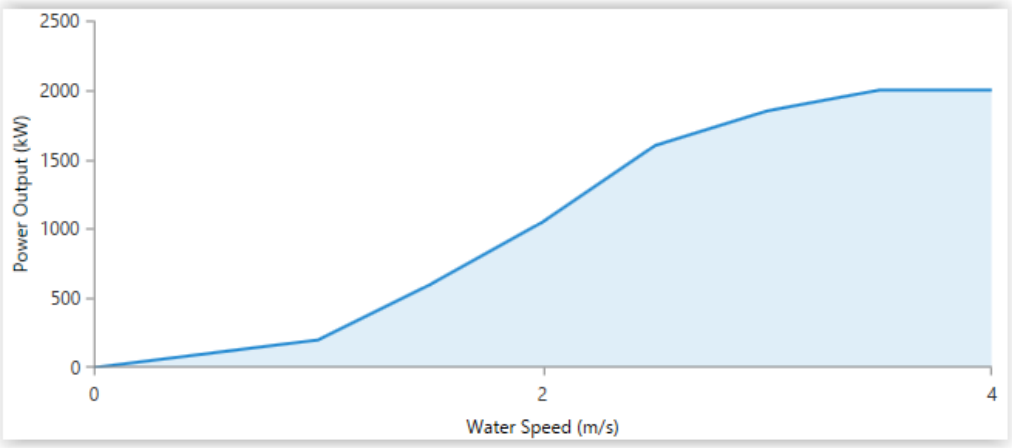

Figure 5-34. The power curve of the AR2000 tidal turbine [29].

The pertinent details for the AR2000 tidal turbines are set out in Table Table 5-20.

Table 5-20: Tidal turbine details.

Tidal Turbine	Value
Name	AR2000
Rated Capacity (kW)	2,000
Manufacturer	SAE/GE
Cut in tidal speed	1 m/s
Cut out tidal speed	3.05 m/s
Operational tidal speed range	1-4.5 m/s
Swept area	314 m^2
Rotor diameter	20 m

Figure 5-35 shows that water speed, for 69.3% of the year, is more than the cut-in speed required by the AR2000 tidal turbine.

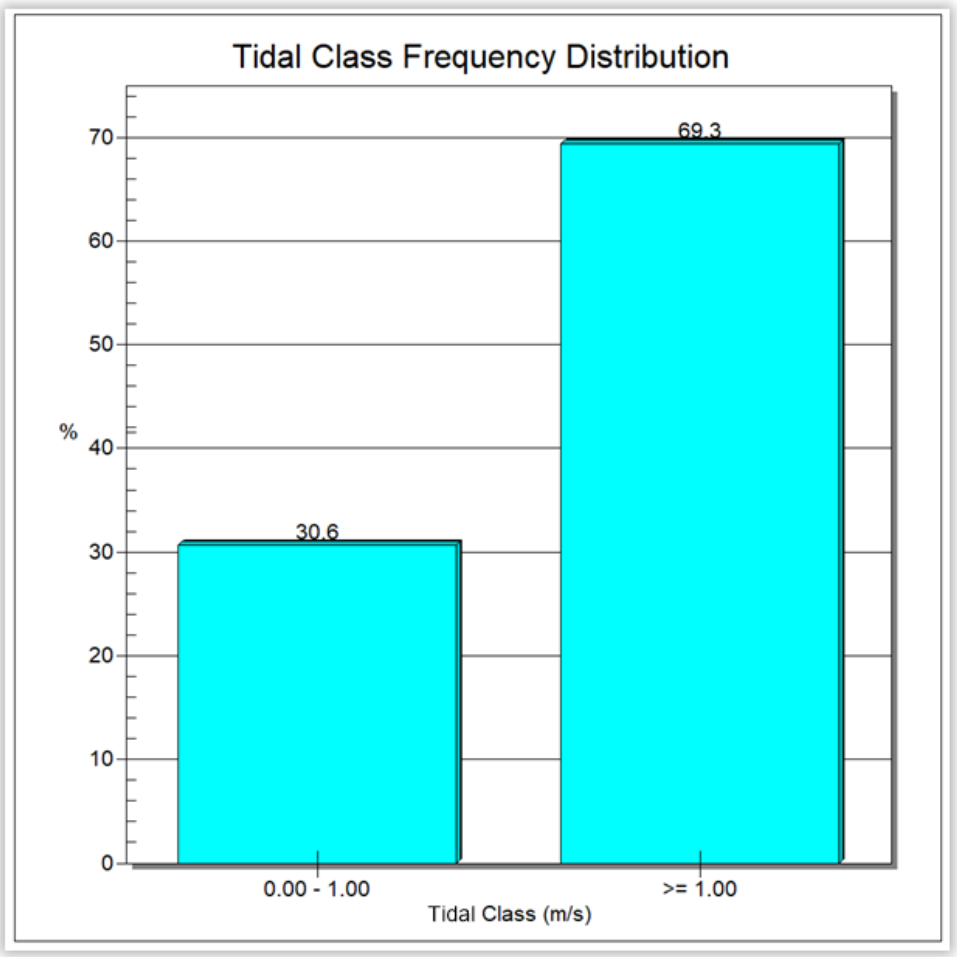

Figure 5-35: Tidal frequency distribution in Terawhiti.

5.3.5.3 Battery Energy Storage

The integration of renewable sources requires proper storage backup [129]. Several simulations conducted for storage selection and the storage unit considered is a BASF NAS ® 192-volt battery with 1,250 kWh of energy storage due to its reliable performance and cost-effective operation. (See Table 5-21). The capital, replacement, maintenance costs, and the life of the battery are given as $330,000, $330,000, $6,600/year, and 20 years respectively [135].

Table 5-21: Properties of BASF NAS ® battery [29].

Sl.No	Properties	Ratings
1	Nominal voltage	192 V
2	Round trip efficiency	80%
3	Lifetime throughput	6250000 kWh
4	Maximum charging current	985 A
5	Maximum discharge current	1490 A

In HOMER, two independent factors may limit the lifetime of the storage bank: the lifetime throughput in kWh/yr and the storage float life in yr. In other words, batteries can die either from use or from old age. When a new storage component created, whether the storage lifetime can be limited by time, throughput, or both. The storage throughput is the amount of energy that cycles through the storage bank in one year. Throughput is defined as the change in energy level of the storage bank, measured after charging losses and before discharging losses. This value is used to calculate the life of the storage bank. The float life of the storage system is the length of time it will last before it needs replacement [29]. In this case, the results show that BASF NAS ® 192-volt battery gives highest throughput and life in comparison of other batteries used for simulations which are Generic 1kWh lead Acid, Generic 4hr 1MW Li-ion, Gildemeister 250 kWh-4hr.

5.3.5.4 Inverter

Inverters are required to connect the DC microgrid to the grid connection. The inverter used is a generic system inverter which is much cheaper than the bidirectional inverter. Selecting the Homer optimizer allows the Homer grid to optimize the size of the inverter. The capital, replacement, and maintenance costs, the life, and the efficiency of the converter are given as $154, $154, 15.4$/year, 15 years, and 90% respectively [129].

5.3.5.5 Controller

The controller component specifies how the proposed system operates during the simulation. Among the dispatch strategies of the Homer software, the load following (LF) was selected to produce only enough power to meet the demand. The capital, replacement, and maintenance costs, and the life of the controller is given as $200, $200, $5/year, and 25 years respectively [29].

5.3.5.6 Grid

For the simulation of the grid-connected system, simple rates mode plus net metering is chosen. This type of design is beneficial from two aspects; It considers emission factors and the timing when excess power is sold to the grid, Homer calculates the power cost at the retail rate. So, net metering provides a lower cost of production and greater income [29].

5.3.6 Optimizing the Design

Microgrid design optimization is possible using the HOMER Pro® became a recognized global standard for off-grid and grid-connected systems [167]. The optimized scenario generates maximum electricity from renewable sources or has a higher renewable fraction.

5.3.7 Feasibility Analysis

As explained in Section 5.3.2, the economic analysis module of HOMER is used to estimate NPC and COE. A cost-effective analysis is an important part of the investigation to estimate the lowest possible NPC and COE [129].

5.3.8 Results and Discussions

Electricity Market Information data has been used to estimate monthly and hourly generation. The peak hourly load is 73,000 kW. The EMI load is shown in Figure 5-36. The top graph shows that the average daily load fluctuates between 19,809 and 61,954 kW. The bottom graph shows that the average monthly load for different months of the year fluctuates between 2,0419 and 39,354 kW in January and between 27,483 and 62,193 kW in July. The daily demand for the year averages 891,230.16 kWh/d with a load factor of 0.51, and the total demand is 325,299,008 kWh/yr [179].

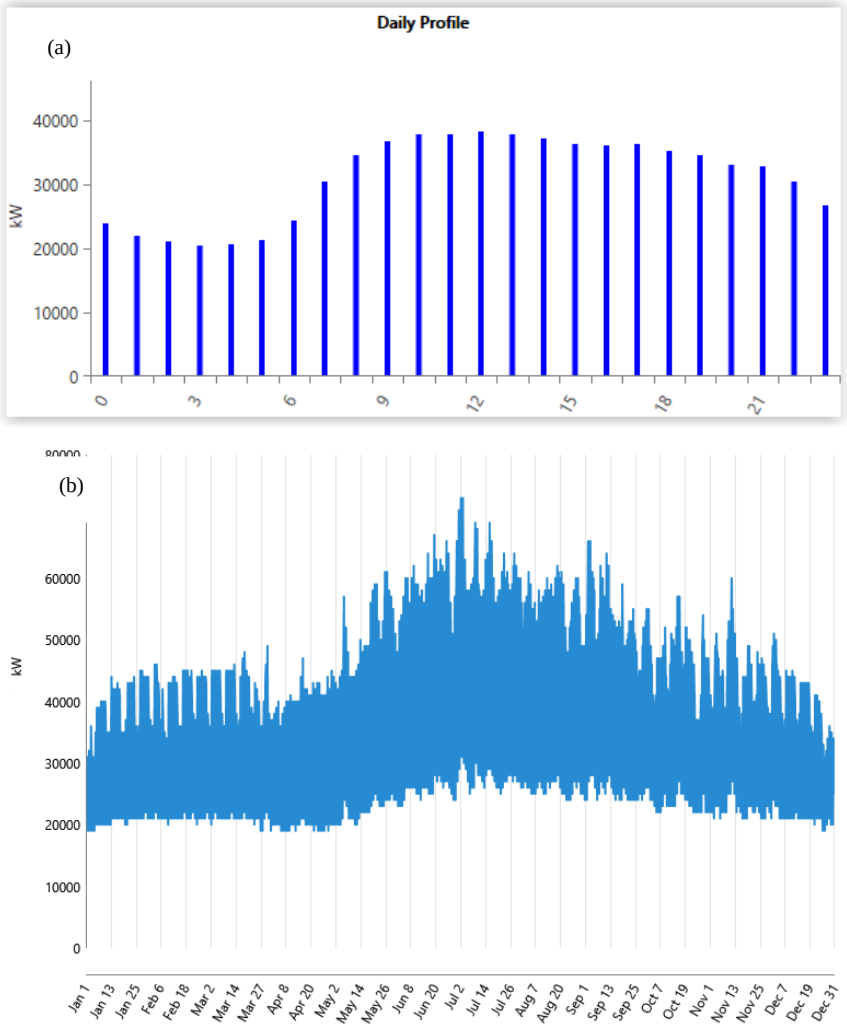

Figure 5-36: (a) The daily and (b) monthly load of central park.

Resources are external parameters of the microgrid system which are required by Homer. The selection of resources depends on the location and affects the power

generation and financial viability of microgrid design and hence a careful choice is necessary for a successful analysis [178].

The resource types essential for this microgrid design are wind speed (downloaded by Homer from the National Aeronautics and Space Administration (NASA)), and the water speed (provided by NIWA) for the year 2020.

Based on the resource frequency distribution as shown in Figure 5-32 and Figure 5-35, the power which can be produced by the wind and tidal turbines at the Terawhiti site is shown in Figure 5-37. The maximum output of the selected wind and tidal turbines are 3,600 kW and 2,000 kW respectively and Figure 5-37 indicates they can reach their rated output in Terawhiti at the peak power.

(a)

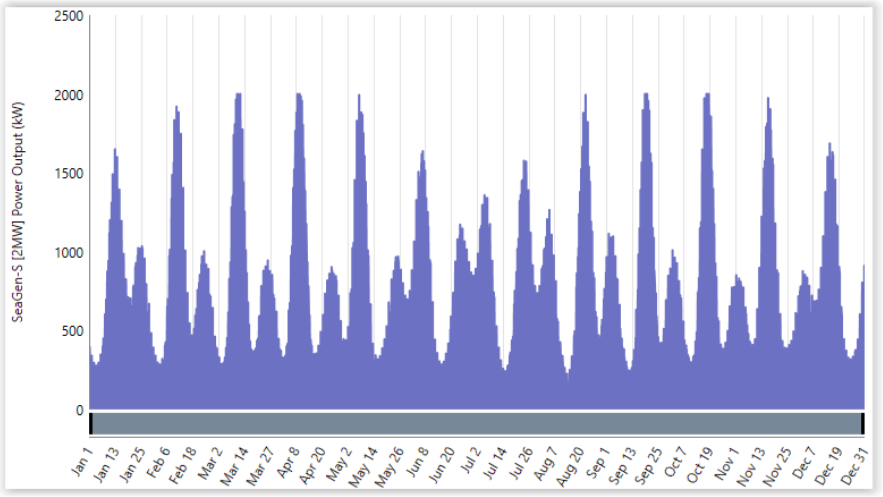

(b)

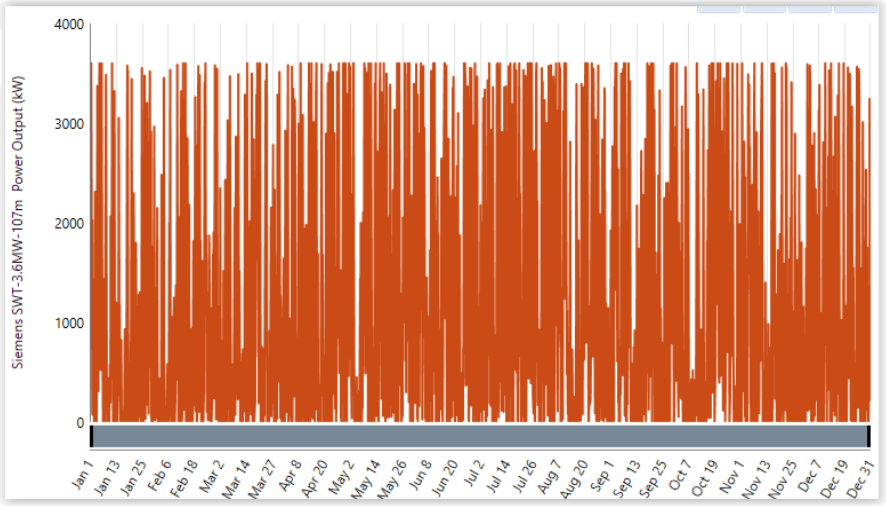

Figure 5-37: Power output fluctuation for (a) tidal turbine and (b) wind turbine at the Terawhiti site.

Figure 5-38 compares the fluctuations in the power demand for three days with the outputs obtained from the wind, tidal, and wind-tidal systems. Figure 5-38 show that the use of wind energy alone is better when compared with the other designs.

(a)

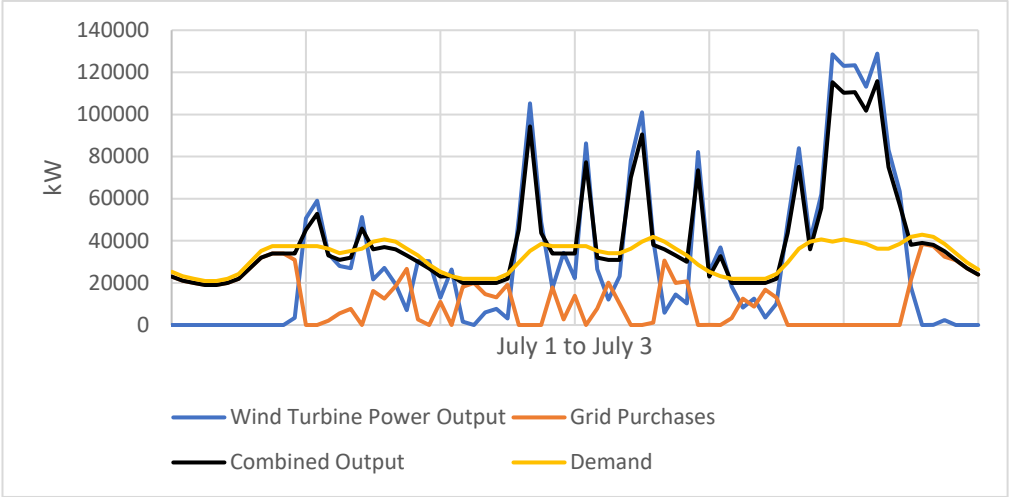

(b)

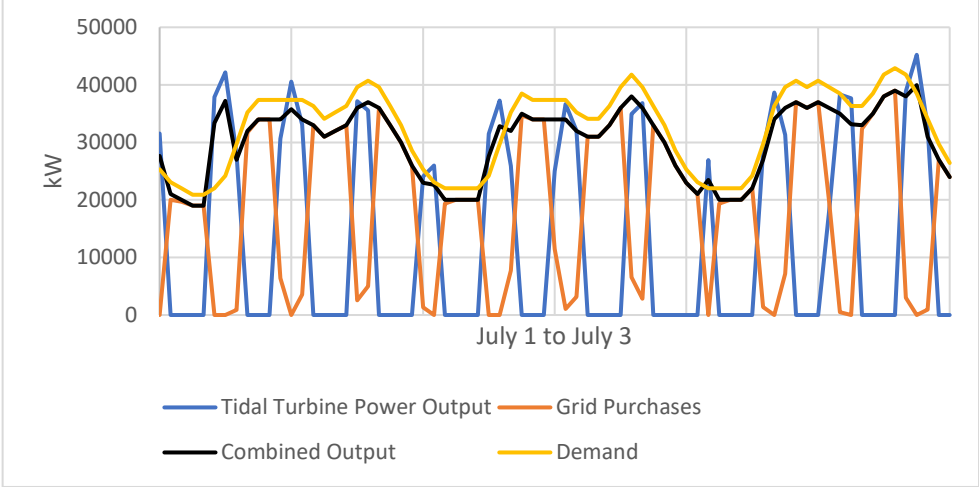

(c)

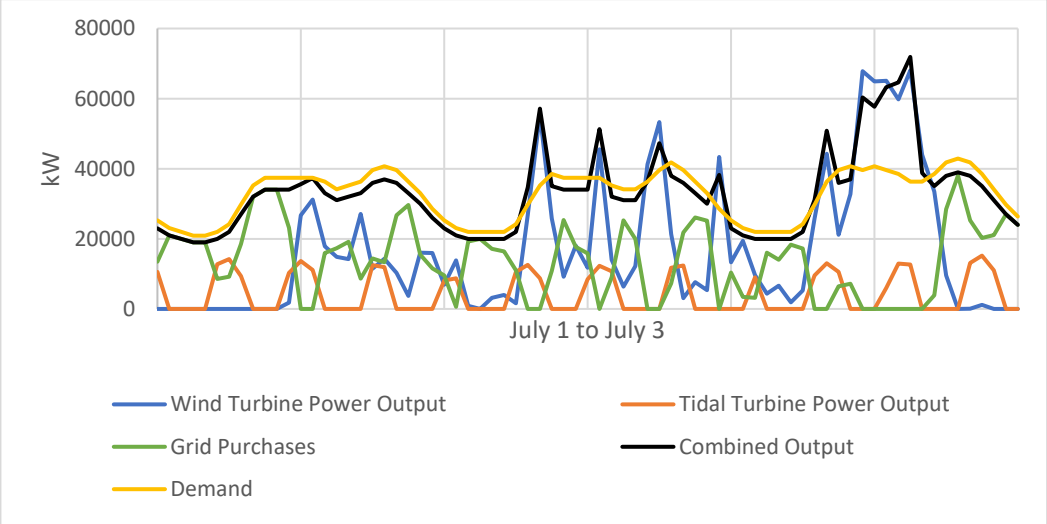

Figure 5-38: Variation of required demand and power generation during three days at Terawhiti with (a) only wind turbine, (b) only tidal turbine, and (c) wind and tidal turbine.

The graphs in Figure 5-38 show that the higher the capacity of the wind or tidal power, the lower the grid energy purchased. Figure 5-39 shows the electrical load served from different cases vs consumption in the same period and shows that wind power can generate higher power and the purchase from the grid is lower.

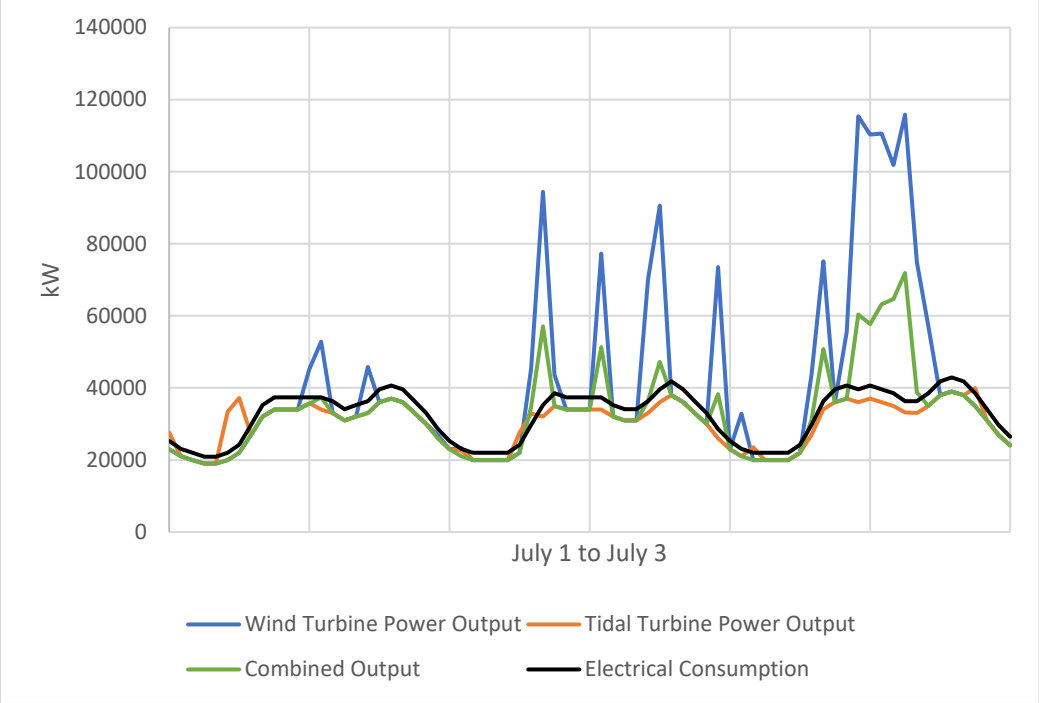

Figure 5-39: Electrical consumption during three days at Terawhiti versus electrical load served with the wind turbine, tidal turbine, and wind and tidal turbine combination.

Sections 5.3.7.1 and 5.3.7.2 evaluate different designs, using the Homer software to optimize the turbine and generator operations, to meet the demand fluctuations throughout the year, and Sections 5.3.7.3 and 5.3.7.4 discuss the results, in terms of power generation and cost-effectiveness respectively. The number of turbines used is 36 wind turbines (36W), 113 Tidal turbines (113T), and a combination of 19 wind and 38 tidal turbines (19W+38T).

5.3.8.1 Power Generation Results

Table 5-22 shows the mean output, the hours of operation, and the total production for each scenario. The number of turbines for each scenario is proportional to the

amount of power consumption. The total power demand from Central Park is 325,299,008 kWh/yr.

Table 5-22: The annual mean output, hours of operation, and power production for the proposed scenarios at the Terawhiti site.

Parameter	36W	113T	19W+38T
Mean output of W (kW)	36,408	-	19,215
Mean output of T (kW)	-	37,026	12,451
Operation hours of W (hr/yr)	7,467	-	7,467
Operation hours of T (hr/yr)	-	4,975	4,975
Power production of W (kWh/yr)	318,931,085	-	168,324,739
Power production of T (kWh/yr)	-	324,346,369	109,072,230
Grid Purchases (kWh/yr)	145,891,360	159,607,904	129,794,595
Total Production (kWh/yr)	464,882,446	483,954,273	407,191,564

Figure 5-40 (a)-(c) show the monthly average power output (kW) and the share of resources for different scenarios. The renewable fraction of wind scenario only (36W) is 66.3% which is higher than tidal scenario only (63.9%) and the combined wind and tidal sources (65.4%).

Figure 5-40: Monthly average output power for (a) 36W, (b)113T, (c) 19W+38T.

Homer results indicates that for 36W scenario, 122,551 kWh/year energy is lost due to battery loss and battery storage depletion which is lower than 113T and 19W+38T which are 396,486 and 273,186 respectively. Also, the mean output of the inverter in 36W is 32,738 kW which is higher than 113T and 19W+38T which are 32,187 and 27,983 respectively. The annual output of the inverter is shown in Figure 5-41.

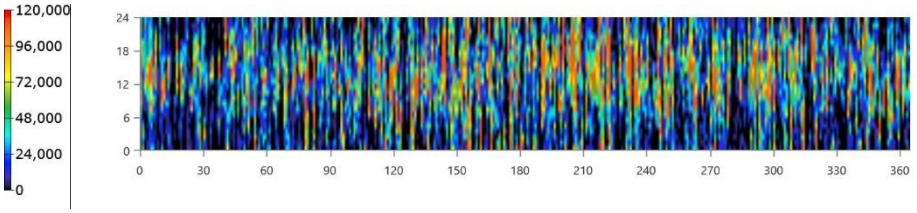

Figure 5-41: Annual inverter output for 36W.

The efficiency of the inverter in all calculations is 90%. The sensitivity analysis to the inverter efficiency was performed at increments of 5% as shown in Table 5-23. According to the sensitivity analysis of the inverter efficiency, the wind project was still the most technically viable.

Table 5-23: Sensitivity analysis of inverter efficiency on decision-making.

Type	Efficiency Variation	Mean Output (kW)
W	-10%	29,068
T		28,773
W+T		24,859
W	-5%	30,915
T		30,386
W+T		26,379
W	0%	32,738
T		32,173
W+T		27,983
W	5%	34,523
T		33,888
W+T		29,503
W	10%	36,284
T		35,371
W+T		31,066

5.3.8.2 Financial Analysis Results

Table 5-24 is a summary of financial analysis for different scenarios at the Terawhiti site. Based on what explained in section 5.3.1, the Homer identifies the optimized scenario with lowest NPC and COE after calculating the installation, replacement and operation and maintenance of all components of each microgrid design.

Table 5-24: Financial analysis results for different scenarios.

Scenario	Capital (M$)	Operating Cost (M$)	Total NPC (M$)	Levelized Cost ($/kWh)
36W	234	12.8	400	0.07
113T	360	17.5	586	0.1
19W+38T	241	16.6	456	0.09

The 36W scenario seems more economical to install and operate. Table 5-25 depicts the optimization results for each scenario. The renewable fractions are 66.3%, 63.9%, and 65.4% respectively. A renewable fraction (RF) of 66.3% means that 66.3% of electricity is supplied from wind turbines and the rest from the grid. Hybrid systems with a renewable fraction of more than 66% can produce high revenue. [168]. The 36W wind turbine meets this criterion. It has lower capital and operating cost, and NPC than the 113T or 19W+38T turbines, and most importantly, it has lower COE.

Table 5-25: Optimization results for (a) 36W, (b)113T, (c) 19W+38T.

(a)

Architecture					Cost				
W	B[1]	Grid(kW)	In[2](kW)	Dispatch	COE($)	NPC(M$)	Op[3] (M$)	C[4] (M$)	RF(%)
36	0	999,999	114,577	LF	0.0713	399	12.8	234	66.2
36	2	999,999	115,832	LF	0.0716	400	12.8	234	66.3
0	0	999,999	0	LF	0.1	421	32.5	200	0
0	1	999,999	143	LF	0.1	421	32.5	352.15	0.000319

1 battery
2 Inverter
3 Operating cost
4 Capital

(b)

Architecture					Cost				
T	B	Grid(kW)	In(kW)	Dispatch	COE ($)	NPC(M$)	Op(M$)	Cap (M$)	RF(%)
113	0	999,999	130,888	LF	0.102	583	17.3	359	63.6
113	4	999,999	129,006	LF	0.103	586	17.5	360	63.9

(c)

Architecture						Cost				
W	B	Grid(kW)	T	In (kW)	Dispatch	COE($)	NPC(M$)	Op (M$)	C (M$)	RF(%)
19	0	999,999	38	76,993	LF	0.0932	453	16.5	240	65.2
19	4	999,999	38	76,993	LF	0.0940	456	16.6	241	65.4
0	0	999,999	38	44,485	LF	0.111	475	27.4	121	28.8
0	4	999,999	38	45,055	LF	0.111	476	27.4	122	28.9

Table 5-26 and Figure 5-42 show, the scenario with the lowest costs at the Terawhiti site, the net present cost of each component in the system, and the system cost as a whole. The replacement and salvage costs are small. The main costs are capital and operating costs.

Table 5-26: Components of NPC for the scenario with the lowest NPC (36W).

Name	Capital (M$)	Operating (M$)	Replacement (M$)	Salvage ($)	Total (M$)
BASF NAS® Battery	0.66	0.17	0.25	-0.081	1
Grid	0	50.4	0	0	50.4
Homer Load Following	0.0002	0.0000064	0	0	0.000264
Siemens SWT-3.6MW-107m	216	55.8	68.9	-38.8	302
System Converter	17.8	23.1	7.57	-1.42	47
System	234	129	76.7	-40.3	400

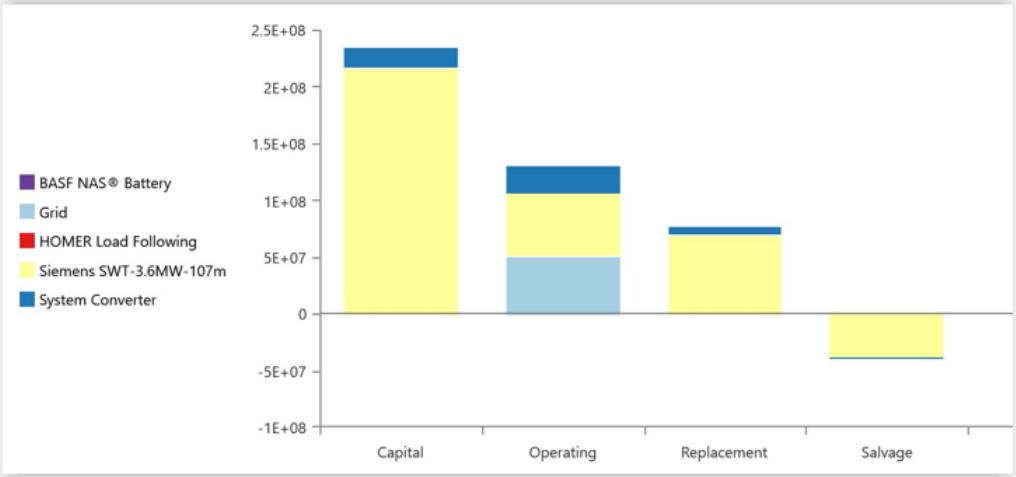

Figure 5-42: Cost summary for 36W.

Homer provides an overview of the winning system - system with the lowest Net Present Cost in comparison to the base system. The base case system is the system with the lowest initial capital cost. There could be scenarios where the base case system is also the winning system. According to Table 5-24, the NPC of the winning system for 36W is 400 M$ which is lower than 586 and, 456 M$ for 113T and,19W+38T respectively. This value is also lower than the NPC of the base system (421 M$) for 36W. Figure 5-43 shows how the winning system of 36W can save money over the project lifetime.

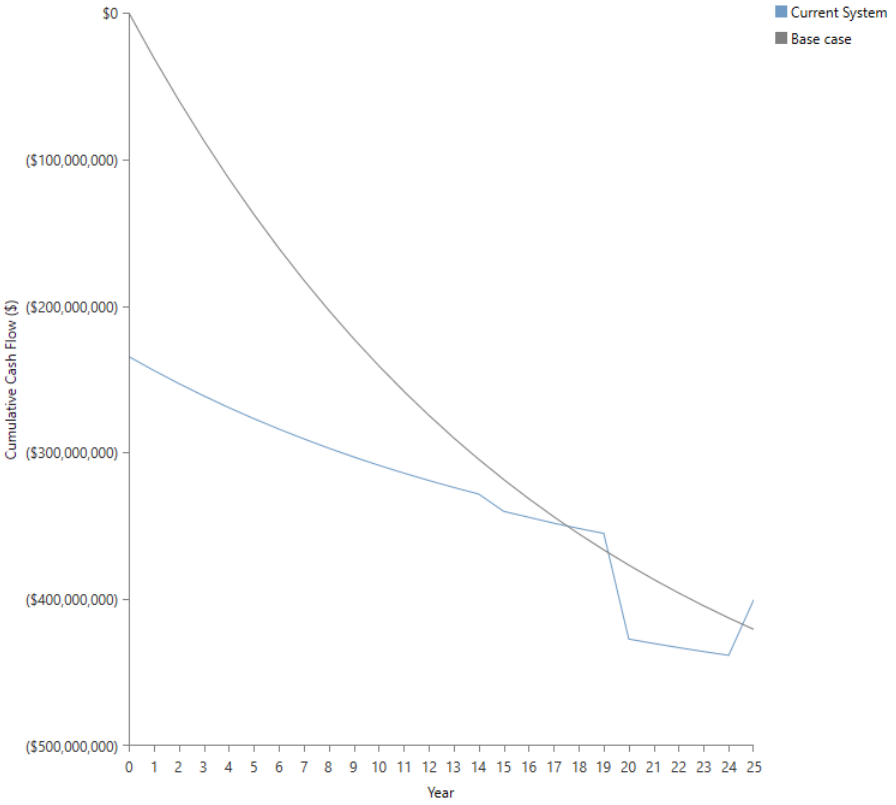

Figure 5-43: Cumulative cash flow of 36W.

A sensitivity analysis was conducted to examine the impact of capital cost, operation and maintenance cost on the selection decision considering the comparison of the different scenarios discussed before. The project capital and the operation, and maintenance cost are allowed to vary by an increase up to 10% from -10% at increments of 5% using RETScreen [28]. Table 5-27 serves as a guide to interested investors on the best option for investment among W, T, and W+T projects when considering such variations. It shows that the corresponding capital variation in the project internal rate of return is in the range of [15.7%, 20.3%] for W, [9.5%, 13.3%] for T, and [9.4%, 13.2%] for W+T and corresponding O&M variation in the project internal rate of return is in the range of [17.5%, 18.1%] for W, [11.1%, 11.5%] for T, and [10.9%, 11.3%] for W+T. According to the incremental internal rate of return analysis, the wind project was the most economically viable project when considering the variation in the capital and O&M costs between -10% and 10% of the total cost of the project compared to others. The minimum acceptable rate of return (MARR) is determined to be 14%. Also from below Table, it can be understood that the T and W+T projects are rejected, as the calculated IRR values are less than MARR.

The economic assessment using the incremental rate of return method [169] and the application of sensitivity analysis on the capital cost and operation and maintenance cost to select the best economic project among wind, tidal, and combination of wind and tidal projects reveal that 36W is a more attractive and feasible option compared to other distributed generation projects.

Table 5-27: Sensitivity analysis of capital and O&M costs on decision-making.

Type	Cost Variation	IRR(%) for Capital Cost	IRR(%) for O&M
W	-10%	20.3	18.1
T		13.3	11.5
W+T		13.2	11.3
W	-5%	19	17.9
T		12.2	11.4
W+T		12.1	11.2
W	0%	17.8	17.8
		11.3	11.3
		11.2	11.1
W	5%	16.7	17.6
T		10.4	11.2
W+T		10.2	11
W	10%	15.7	17.5
T		9.5	11.1
W+T		9.4	10.9

5.3.8.3 Discussion of Power Generation Results

Table 5-28 shows the mean output power for all scenarios. Central Park's mean power demand is 37,134.6 kW. All scenarios can meet mean demand, but none of the total outputs can meet peak demand (73000 kW).

Table 5-28:Mean output for different scenarios.

Parameter	36W	113T	19W+38T
Mean Output of Wind Turbine (kW)	36,408	0	19,215
Mean Output of Tidal Turbines (kW)	0	37,026	12,451
Mean Output of Inverter (kW)	32,738	32,272	27,983
Total (kW)	69,146	69,298	59,649

Table 5-29 shows the percentage of the electricity produced by the wind and tidal turbines. Central Park's total power demand is 325,299,008 kWh/yr. The 36W wind turbine produces the highest renewable energy fraction and could contribute 68.6% of power demand.

Table 5-29: Share of wind and tidal turbines in producing electricity and meeting demand.

Parameter	36W	113T	19W+38T
Wind Turbine (% of production)	68.6	0	41.3
Tidal Turbine (% of production)	0	67.0	26.8
Grid (% of purchases)	31.4	33.0	31.9
Renewable output (% of production)	68.6	67.0	68.1

Comparing different designs shows that the 36W wind turbine is the best design that can provide the electricity demand of Central Park by using wind.

Although the MetOcean model indicates that Terawhiti is in an area with the highest tidal energy, the renewable fraction of the 36W wind turbine is higher than in other scenarios. Based on the calculations, the ratio of renewable production to total consumption is considered to be 73% for all scenarios. The wind energy only option can maximize its contribution and minimize the grid purchases in comparison with other cases.

5.3.8.4 Discussion of Financial Analysis Results

In this section, the scenarios are compared, based on financial analysis results from Section 3.2 which are summarized in Table 5-29.

Table 5-30: Financial analysis summary.

Parameter	36W	113T	19W+38T
Capital equipment(M$)	234	360	241
Replacement (M$)	76.6	117.6	78.2
Construction(k$)	-	-	-
End-of-project removal/reinstatement (k$)	-	-	-
Operating cost (M$)	12.8	17.4	16.5
Total NPC (M$)	400	585	455
COE ($)	0.07	0.10	0.09

where:

Capital equipment/ Replacement: The cost is the least for the 36W wind turbine scenario.

Construction: The cost of project installations is not shown, because Homer Pro's financial analysis module does not include it. (It just compares equipment, operating, and resource costs).

Removal/reinstatement: The cost to remove or re-instate project installations (at end of design life) is not shown, for the same reason.

Operation: The cost is the least for the 36W wind turbine scenario which generates more power from fewer turbines. The operating cost for the 113T tidal turbine scenario is greater because this scenario has numerous turbines. The operating cost is most expensive for the scenarios which generate less power from renewable sources.

The total net present cost (NPC): The NPC is the least for the 36W wind turbine scenario, because this scenario has low equipment and operating costs, and generates more power (68.6%) from renewable sources.

The total cost of energy: the COE is the least for the 36W wind turbine scenario and almost the same for the 113T and 19W+38T scenarios when their NPCs are levelized (per kWh over the life of the project).

The 36W wind turbine scenario is optimal for power generation, because it produces the highest renewable fraction (66.3%), while the RF for 19W+38T and 113T scenarios are 65.4% and 63.9% respectively. Its total NPC seems affordable

at 400 million dollars. Its Levelized cost at 7c/kWh appears better than the investment in tidal energy based on the tidal models.

A problem with Homer Pro's financial analysis is that it only evaluates equipment, operating, and resource costs, when calculating NPC and COE. A realistic comparison of NPC and COE should include the construction and installation costs, particularly for the offshore platforms, marine cables, and a DC-AC shore converter station.

5.3.9 Summary of Ongrid Design

This section has investigated a DC-linked wind-tidal battery-based microgrid for electricity generation in node CPK0331 (Central Park) in the south of the northern island of New Zealand. The system considers the good potential of wind and tidal sources in this area to design an environmental-friendly microgrid connecting to the national grid with cheaper electricity generation.

Many simulations were conducted to design the DC-linked microgrid for integration with the electricity grid to supply the residential load in Terawhiti. Based on the selection of components, and by including the resource data of the wind speed and tidal currents, the microgrid design provides the capacity and cost for different options.

Homer Pro is used to compare different scenarios and propose an optimized microgrid system and required components to generate maximum power from renewable sources with the lowest cost of generation.

The power generation and financial analysis results for the various scenarios, as presented and discussed in Section 5.3.8, enable several conclusions:

- There are enough tidal currents to generate electricity during 69.3% of the year at an offshore site close to CPK0331 (referred to as the Central Park).
- There is also enough wind speed to generate electricity during 78.2% of the year at the Foveaux site.
- The DC power from the offshore Terawhiti site can be integrated into the national grid at CPK0331 by using the microgrid design as described in Section 5.3.5.

- The proposed solution is to mount the wind and tidal turbines on the same offshore platform, design a DC linked wind-tidal-battery based microgrid to feed the power through a DC marine cable to a DC-AC converter at the CPK0331 onshore, then transmit the power through an AC land cable to a system controller at the Central Park station.
- The offshore renewable sources enable several scenarios to provide the demand of Central Park with Homer Pro which looks promising. The optimal scenario generating maximizing electricity is thirty-six wind turbines (36W).
- The renewable output of 68.6% from the 36W scenario (look at Table 10) is worth implementing comparing other scenarios.
- Once built and installed on-site, the design can be operated at an affordable Levelized cost of 7 c/kWh (look at Table 6) over the project life which is lower than adding the tidal source.

5.4 Energy Yield

In this chapter, RETScreen software is used to scope energy yield achievable by a microgrid system for hybrid offshore wind and tidal energy generation by comparing large turbines (Siemens SWT-3.6-107 wind turbines and Atlantis AR2000 tidal turbines) with small turbines (XANT 100 kW M-21 wind turbines and Schottel 54 kW tidal turbines). RETScreen is a feasibility study tool and is freely downloadable software developed by the Ministry of Natural Resources, Canada, to evaluate financial and environmental costs and benefits of different renewable energy technologies for any location in the world [189].

5.4.1 Matters to Consider

Various types of turbine design-related losses like array density, airfoil soiling, icing, and miscellaneous must be considered in estimating wind energy yield. Array losses for a single turbine installation are 0%, while a well-designed cluster of less

than 8 to 10 turbines should keep array losses below 5%. Airfoil soiling and/or icing losses typically range from 1 to 10% [190]. RETScreen initially calculates the gross energy production for one (proxy) wind turbine, which is the total annual energy produced by the wind energy equipment before any losses, at the wind speed, atmospheric pressure and temperature conditions at the site. Next, the model calculates and applies the pressure adjustment coefficient, proportional to the average atmospheric pressure at the site. The coefficient should fall between 0.59 at an altitude of 4,000 m and 1.02 at an altitude of 0 m. Then the model calculates the temperature adjustment coefficient, which is inversely proportional to the average temperature at the site. Typically the coefficient falls between 0.98 and 1.15 for temperatures ranging from 20°C to -20°C. A value of 0.14 for wind shear exponent is recommended as a good approximation when wind shear at the site is yet to be determined [190]. Examples of RETScreen loss estimates for the Foveaux site are given in Table 5-31 for a single large turbine and a single small turbine.

Table 5-31: Wind energy-related coefficients used in energy yield estimation at Foveaux

Wind energy-related coefficients	
Array losses (%)	0
Airfoil soiling and/or icing losses (%)	2
Miscellaneous losses (%)	6
Pressure adjustment coefficient	0.997
Temperature adjustment coefficient	1.018
Wind shear exponent	0.14

Tidal energy yield is more difficult to estimate because RETScreen does not have links to a tidal flow atlas nor an energy yield estimation module for tidal flow. Presently the energy yield obtainable from tidal flow (Table 5-32) must be estimated in RETScreen by using the average tidal flow from NIWA and making several assumptions that are:

- Turbines in the "shadow" of others do not "see" as much current as the front ones, and energy production is decreased.
- For off-grid systems, miscellaneous (losses of energy production due to starts and stops, off-yaw operation, high current and cut-outs from a tidal gust) could also include losses due to low tidal energy absorption rate.

- The pressure coefficient is proportional to the atmospheric pressure of the site.
- The standard rating temperature of 15°C for wind turbine performance corresponds to a temperature adjustment coefficient of 1[28].

Table 5-32: Tidal energy-related coefficients used in energy yield estimation.

Energy-Related Coefficients	
Array losses (%)	0
Miscellaneous losses (%)	6
Pressure adjustment coefficient	0.999
Temperature adjustment coefficient	0.997
Energy adjustment coefficient	1.3

5.4.2 Energy Yield Results

Table 5-33 and Table 5-34 shows the average yield estimated from RETScreen for a large, specified turbine and a small, specified turbine, respectively.
Specific energy yield is calculated by dividing the energy produced by a proxy wind turbine by the rotor's swept area. Unadjusted energy delivered is the produced energy at standard conditions of temperature and atmospheric pressure. Annual gross energy yield is calculated by applying pressure, temperature and wind shear coefficients to unadjusted energy delivered.

Table 5-33: Wind energy yield at Foveaux site.

Parameter	SWT-3.6-107	XANT M-21
Annual mean wind speed (m/s)	8.31	8.31
Specific yield (kWh/m2)	2,034	531
Gross energy yield (MWh/y)	19,969	204
Unadjusted energy delivered (MWh/y)	20,259	205

Table 5-33 demonstrates that a single large wind turbine could yield more than enough energy for supply to Stewart Island, which has an annual demand of 1,260 MWh/y (Chapter 4). A single small turbine does not produce enough energy to meet Stewart Island's demand. So, several will be needed.

Table 5-34 shows the extra energy yield obtained from adding a single sizeable tidal turbine. It also yields more than enough to meet Stewart Island's annual demand. A single small turbine does not produce enough energy. So, more than will be needed.

Table 5-34: Tidal energy yield at Foveaux site.

Parameter	AR2000	Schottel 54 kW
Annual mean tidal flow (m/s)	0.51	0.51
Specific energy yield (kWh/m^2)	415	409
Gross energy yield (MWh/year)	4130	110
Tidal energy delivered (MWh/year)	3882	111

5.5 Summary

Chapter 5 introduced two microgrid systems to find integrating wind and tidal energy for an offgrid site of Stewart Island and ongrid design of Central Park can be feasible or not. For site selection, Foveaux and Terawhiti were selected respectively for offgrid and ongrid models. The way how they identified was explained in Chapter 3. For turbine selection, a base knowledge about wind and tidal turbines was essential as presented in Chapter 3. Lastly, RETScreen software was used to estimate energy yield achievable by a microgrid system for hybrid offshore wind and tidal energy generation by comparing large turbines (Siemens SWT-3.6-107 wind turbines and Atlantis AR2000 tidal turbines) with small turbines (XANT 100 kW M-21 wind turbines and Schottel 54 kW tidal turbines).

Chapter 6

Support Structure Design

6.1 Introduction

This chapter proposes and evaluates a feasibility analysis of the foundation design of a hybrid offshore system in New Zealand. A microgrid design for providing to an onshore supply is considered combining a wind plus two tidal turbines [24]. This design is performed based on standard IEC 61400, IEA Wind TCP Task 37-May 2019, DNV 2014 and IEC 2019 [25, 191-193]. Several simulations have been done using RETScreen, which was connected to GLOBAL ATLAS, to find Terawhiti in Cook Strait suitable for a hybrid model [3].

The most expensive component of an offshore wind turbine after turbine is the foundations typically representing 19% of the capital cost. Also, foundation installation with 6% of capital cost have the highest cost compared with other parts [145]. However, the cost of electricity using offshore wind is still high [21]. As another offshore energy source, installing tidal turbines has attracted less investment because tidal turbines are exposed to harsh currents. Their lifetime is low, and foundation design is complex in most cases, where the water depth is more than 30 metres [22]. Integration of both wind and tidal turbines with the same foundation may be a way to reduce the cost of electricity [7] and enable predictable power generation from two different energy sources. The monopile has been found to be a suitable foundation type for less than 30 metre water depth; It is one of the most inexpensive solutions for supporting the structures and widely used in wind farm projects. Also, the other reasons of choosing monopile for integrating wind and tidal turbines are the possibility of driving it in seabed, connecting it directly to the tower, it is a simple structure and widely is using in wind farm projects [159]. Also, the possibility of using foundation for water depths more than 60 metre is examined with proposing a floating system in Cook Strait after finding a 110 m site from the national institute of Water and Atmospheric Research (NIWA).

In this analysis, all available forces contribute for foundation design to a hybrid system is calculated using OPTUM G3. Moreover, the macro-element model is proposed, and natural frequency is yielded. The results enable to find optimum dimensions of monopile with allowable tilt and deflection.

6.2 Monopile Design in Cook Strait

This section describes a preliminary design for an offshore structure capable of supporting a hybrid assembly of one wind plus two tidal turbines as shown in Figure 6-1.

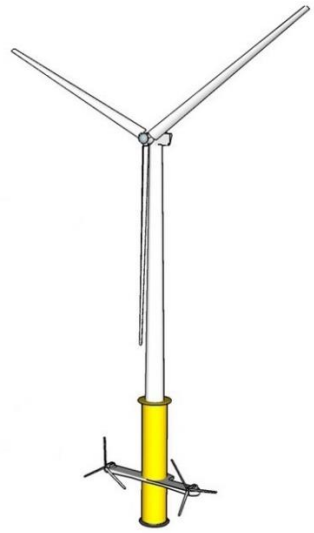

Figure 6-1: Schematic of a hybrid system consisting of wind and tidal turbines.

The design will be carried out using foundation concepts of an offshore design [160], The procedure of design has three steps:

(a) Site investigation
(b) Criteria for design
(c) Evaluation of the stability of design under combined loads according to criteria for design.

Reducing the cost of electricity generation and integrating renewable energy sources are two essential factors in encouraging developing novel ideas to tackle the lack of enough energy and proposing alternatives for fossil fuels [132].

Deployed on floating bodies or along with cables, offshore energy harvesters can convert wave, solar, tidal, ocean current, and other renewable energy sources to stable electrical energy [112]. Hybrid them with wind electricity generation would reduce the currently significant operations & maintenance (O&M) of a wind turbine (WT) which is around 10-25% of the total cost of the electricity, and a lower transmission cost [113, 114]. By bringing together two marine renewable technologies with considerable synergies, the combined harnessing of offshore energies presents an excellent potential for development. This is corroborated by some recent European Union (EU) funded projects: MARINA, ORECCA, TROPOS, MERMAID and H2OCEAN [121]. MARINA classifies combined wave–wind systems according to the technology, water depth (shallow, transition, or deep water), or location relative to the shoreline (shoreline, nearshore, offshore). ORECCA analyses the offshore renewable energies (ORE) combined resources in Europe. Looking particularly at the combined wave–wind resource in Europe, this can be divided into three main sea basins: the Mediterranean Sea, North and Baltic Seas, and the Atlantic Ocean. TROPOS is aimed at developing a floating multi-purpose platform system for deep water [121]. The MERMAID project seeks to develop concepts for the next generation of offshore activities for multi-use of ocean space. It proposes new design concepts for combining offshore activities, like energy extraction, aquaculture, and platform-related transport at various ocean areas [122]. H2OCEAN is developing a wind-wave power open-sea platform equipped for hydrogen generation with support for multiple energy users [123].

The main projects installed in the previous decade 2010-2019 were 2.3 MW Hywind in Norway year 2009, 2 MW Principle Power in Portugal year 2011, MOE project in Japan with capacities of 100-kW half-scale model in 2012, and 2 MW full scale in 2013 [124].

Da et al. propose a control scheme for a hybrid system. Adjusting the generator's rotation speed can maximize the system's output power under fluctuating wind or tidal current [125]. Li et al. show integration of floating wind turbines with a wave energy converter and tidal turbines increase the power production by 22% - 45% [126]. Lande et al. model co-location of a wind turbine with an array of tidal stream turbines in MeyGen site located in the Pentland Firth, UK. It will increase energy

yield by around 11% and decrease Levelized cost by 10% [127]. Nichita et al. present the “accelerated simulation time” method and its experimental validation; Wind/tidal turbine characteristics are obtained using the simulation approach developed at GREAH lab and are validated with an actual ocean turbine installed in the Circulating Water Channel at Inha University Ocean Engineering Laboratory, South Korea [128]. Phurailatpam et al. [129] present a DC microgrid for rural applications in India using wind turbine (WT) and photovoltaic panels (PV). Azaza et al. give some insight and techno-economic analysis of microgrid deployment in different Swedish regions using PV/WT/DG, a battery bank, and an energy management system to identify the optimal system size and configuration [130]. Thakur et al. design, construct and test a new physical simulator in a real microgrid environment under different operating conditions. The simulator replicates the behaviours of a designed wind turbine. The experiments have also shown that the designed wind turbine can work in harmony with PV power modules and battery storage in response to weather and load variations in an island microgrid environment [131].Wang et al. analyse the stability of a microgrid system containing an offshore wind farm (OWF), an offshore tidal farm (OTF), and a seashore wave farm (SWF) fed to an onshore power grid through a high-voltage direct current (HVDC) link based on a voltage-source converter (VSC) [24]. Adetunji et al. propose an optimized grid-connected microgrid for South Africa using photovoltaic panels (PV) and a supporting lead-acid battery for downtime [132]. Kitson et al. present a DC microgrid system, interfacing wind and solar using a power electronic interface with droop functions. A case study site in Nepal is simulated to demonstrate the system's performance to variable generation and loads [133]. Oulis Rousis et al. designed an off-grid system in Greece relying on PV, diesel generators, and batteries for energy storage [134]. Phurailatpam et al. compare different scenarios of DC microgrids for Indian context using wind and photovoltaic panels for rural and urban power supply in India [135]. Faridnia et al. designed a grid-connected microgrid for a tidal farm near Darwin, in the north of Australia, including tidal power as the main supply, a pumped hydro system (PHS) with 1000kWh capacity as the long-term storage system, and a micro-turbine (MT) with the objective of minimizing the operating cost [136]. Colombo et al. added Photovoltaic (PV) to power-to-gas (P2G) to reduce emissions [137].

6.2.1 Environmental Parameters for Design

MetOcean model identifies Cook Strait as the best area for offshore supply as shown in Figure 6-2 [164].

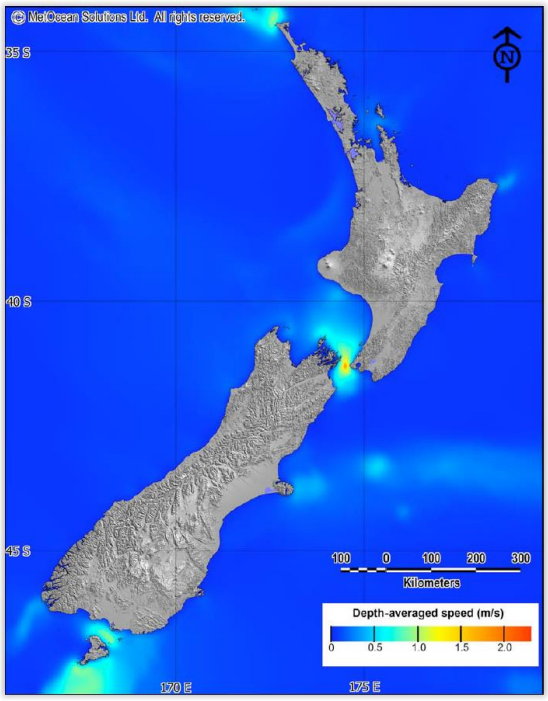

Figure 6-2: National Depth-averaged Tidal Current Speeds for Mean Spring Flows (in m/second) [164].

The main geographical parameters of the optimized site in Cook Strait are shown in Table 6-1.

Table 6-1:The main geographical parameters of the site for foundation design.

Location	Latitude (deg)	Longitude (deg)	Annual Water Velocity (m/s)	Depth of Water (m)	Annual Wind Velocity (m/s)
Terawhiti	−41.279497°S	174.524249°E	1.09	30	7.10

The most important data from NIWA [194] ’s analysis is summarized in Table 6-2.

Table 6-2: Wave data for Terawhiti

Parameter	Symbol	Value	Unit
Significant wave height with 50-year return period [195]	Hs	15	m
Peak wave period	Ts	13.73	s
Maximum wave height (50-year)	Hm	27.62	m
Maximum wave peak period	Tm	18.63	s
Maximum water depth (50-year high water level)	S	30	m
Water density	ρw	1,030	kg/m3

The tide 's direction and information in the Cook Strait are shown in Figure 6-3.

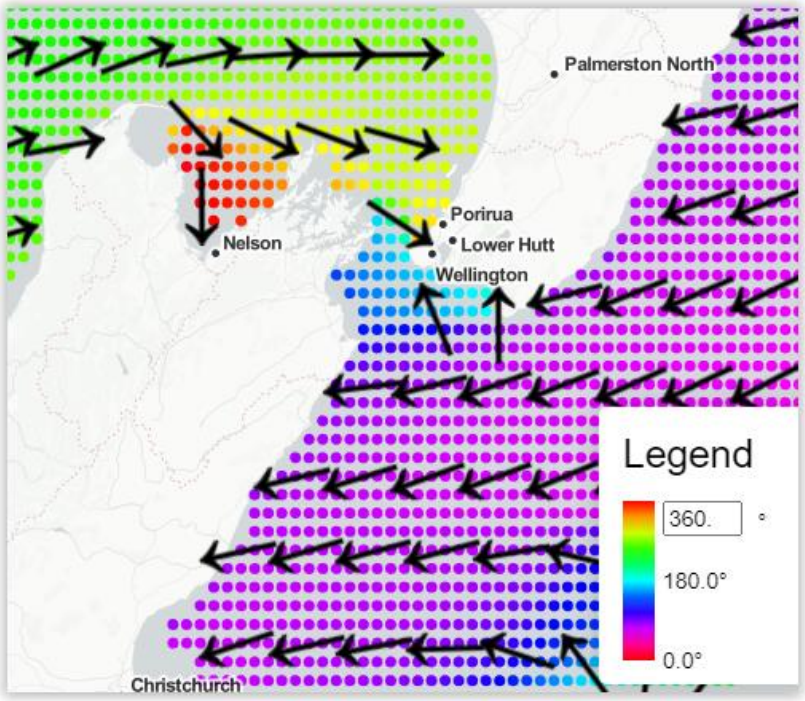

Figure 6-3: The tidal directions for Terawhiti [196].

The depth of the harbour mouth channel, where the turbines will be located, is an asset: neither too deep for access by divers if needed (31 meters to a maximum 52 meters), nor too shallow and therefore impacted by lack of water at low tide. The sandbar surrounding the mouth protects the project from oceanic waves [197].

Table 6-3: Tide data for Terawhiti [29, 174].

Site	Highest astronomical tide (HAT)	Lowest astronomical tide (LAT)	Average current (m/s)	Peak current (m/s)	Water depth (m)
Terawhiti	1.93	0.39	1.09	2.60	30

Equivalent wind data will be sourced from the meteorological recording site closest to the Terawhiti by NASA. These data will be presented in Table 6-4 and Figure 6-4. These data are essential to estimate the wind stresses transmitted through the turbine's support structure to its foundation.

Table 6-4: The geological and geotechnical wind data of Terawhiti [28, 160, 198, 199]

Parameter	Symbol	Value	Unit
Shape parameter-Weibull distribution [198]	s	1.98	[-]
Scale parameter-Weibull distribution [198]	K	7.99	m/s
Reference turbulence intensity [199]	I	16	%
Turbulence integral length scale [160]	L_K	340.2	m
Annual wind speed [29]	u_{ave}	7.10	m/s
Air density [160]	ρa	1.225	kg/m 3

Wind speed variability is often described by the Weibull two-parameter distribution function. It is considered a standard approach for evaluating local wind load probabilities because it has been found to fit a wide collection of wind data [200]. The Weibull shape and scale parameter are denoted by s and K, respectively. s is dimensionless and it indicates how peak the site under consideration is, while K has a unit of wind speed (m/s) and it shows how windy the site is [201].

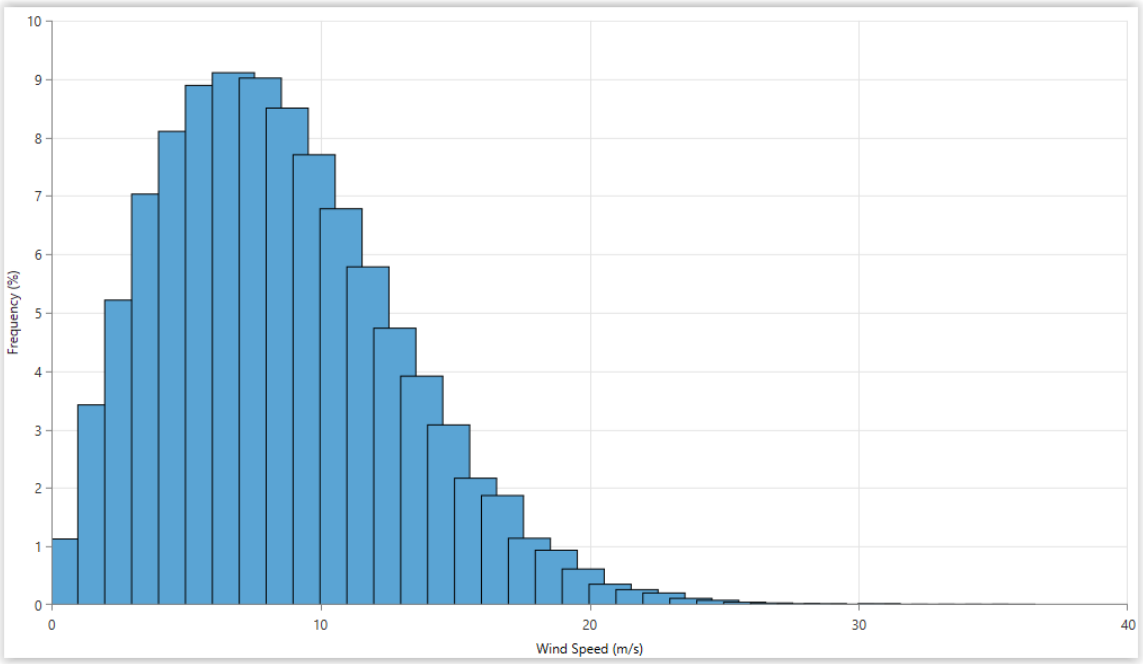

Figure 6-4: Wind Speed Histogram for Terawhiti [29].

To calculate Weibull parameters, the frequency percentage of Terawhiti results by Homer is used in the Weibull calculator [198] which results in s=1.98 and K=7.99 m/s.

The turbulence intensity varies with mean wind speed, which is for Terawhiti 7.10 m/s, and quantifies how much the wind varies typically within 10 minutes [160]. This value may be obtained , I= 16% ,from standard IEC 61400 [199].

Based on the DNV code, for height above sea level (z) less than 60 metres, L_k is 5.67z and, for z above 60 meters L_k is 340.2 meter [160]. As height above sea level is 87m, the turbulence integral length scale is 340.2 m in this case.

6.2.2 Monopile Design for Hybrid System in Cook Strait

The design criteria which will be checked for the possibility of a monopile design are presented in Table 6-5[160].

Table 6-5: Main criteria for foundation design [160].

Parameter	Limit	The section where checked
The maximum stress (σ_m) - yield strength (f_{yk})	$\sigma_m < f_{yk}$	3.3
Deflection of monopile (ρ_0)	$\rho_0 < 0.2\ m$	3.4
Tilt (θ_0)	$\theta_0 < 0.5\ °$	3.4
The structural natural frequency(f_0) -frequency of rotation of the rotor ($f_{1P,\ max}$)	$f_0 > 1.1 f_{1P,\ max}$ = 0.24 Hz	3.2
Pile wall thickness (t_P)	$t_P \geq 6.35 + \frac{D_P}{100}$	3.3

Design criteria specific to the selected turbines are presented in Table 6-6 and Table 6-7.

Table 6-6: General information of Wind turbine, Siemens SWT-3.6-107 Offshore 3.6 MW, for the hybrid system [159, 160, 202].

Parameter	Symbol	Value	Unit
Turbine Power	P	3.6	MW
Turbine rotational Speed (Cut in/out)	u_{in}/u_{out}	5-13	rpm
Operational wind speed range	V	4-25	m/s
Rated wind speed	u_R	16.5	m/s
Mass of the nacelle (NA)	m_{NA}	125	tonnes
Hub height from mean sea level	H	87	m
Density of tower, monopile and TP-S355 Steel	ρ	7,860	kg/m^3
Tower data			
top diameter	D_t	3	m
bottom diameter	D_b	5	m
weight	m_t	255	tonnes
Tower height	L_T	68	m
Wall thickness	t_T	0.027	m
Monopile data			
Monopile Young ‘s module-S355 Steel	E_P	200	GPa
Soil ‘s unit weight	γ	16	kN/m^3
Soil ‘s of internal friction	ϕ	30	°
Monopile length	L_P	60	m
Monopile diameter	D_P	6	m
Monopile thickness	t_P	0.083	m
Monopile yield stress	f_{yk}	355	MPa
Monopile weight	W_P	700	t
Transition piece (TP) data			
TP Young ‘s module-S355 Steel	E_{TP}	200	GPa
TP weight	W_{TP}	300	t
Transition piece internal diameter	D_{TP}	6.16	m
Transition piece thickness	t_{TP}	0.083	m
Transition piece length	L_{TP}	29	m
Grout and TP combined thickness	t_G+t_{TP}	0.15	m
Rotor and blade data			
Turbine rotor diameter	D	107	m
Swept area	TSA	8,992	m^2
Mass of rotor+hub	m_R	100	tonnes
Rotor overhang	b	4	m
Blade root diameter	B_{root}	4	m
Blade tip chord length	B_{tip}	1	m
Blade length	L	52	m

Table 6-7: General information of tidal turbine, Atlantic Resources AR 2000, for the hybrid system [159, 160].

Parameter	Symbol	Value	Unit
Turbine Power	P	2	MW
Turbine rotational Speed (Cut in/out)	Ω	1-3.05	rpm
Operational tidal speed range	V	1-4.5	m/s
Turbine rotor diameter	D	20	m
Height from the seabed	ZS	25	m
Rotor Swept area	TSA	314	m^2
Mass of two turbines	m	300	tonnes

There are five scenarios for an offshore foundation design exposed to both wind and wave loads [160] which are summarized in Table 6-8.

Table 6-8: Load Case Scenarios [160].

Scenario	Name and description	Wind model	Wave model	Alignment
E-1	Normal operational conditions. Wind and wave act in the same direction (no misalignment).	NTM at u_R (U-1)	1-yr ESS (W-1)	Collinear
E-2	Extreme wave load scenario. Wind and wave act in the same direction (no misalignment).	ETM at u_R (U-2)	50-yr EWH (W-4)	Collinear
E-3	Extreme wind load scenario. Wind and wave act in the same direction (no misalignment).	EOG at u_R (U-3)	1-yr EWH (W-2)	Collinear
E-4	Cut-out wind speed and extreme operating gust scenario. Wind and wave act in the same direction (no misalignment).	EOG at u_{out} (U-4)	50-yr EWH (W-4)	Collinear
E-5	Wind and wave misalignment scenario. Same as E-2, except the wind and wave are misaligned at an angle of ϕ=90°. The dynamic amplification is higher in the cross-wind direction due to low aerodynamic damping.	ETM at u_R (U-2)	50-yr EWH (W-4)	Misaligned at ϕ=90°

In, the Normal Turbulence Model (NTM) relates to the normal working conditions of the turbine. Extreme Turbulence model (ETM) is for extreme turbulence conditions. The Extreme operating Gust (EOG) is the highest single occurrence

wind load by a sudden change in the wind speed. ESS and EWH denote to extreme sea state and extreme wave height respectively. The significant wave height HS, uses in ESS scenarios, is the average of the maximum one-third of all waves in the three hours, while the maximum wave height Hm, uses in EWH scenarios, is the maximum wave height for three hours [160].

Initially, a finite element analysis is presented for different soils. Then, the results were used to find wind and wave loads and then evaluate if the calculated dimensions of monopile can result in an acceptable foundation design or not.

6.2.2.1 Finite Element Analysis

For the current application, an advanced method of analysis represents a finite element, discrete element, or finite difference method. OPTUM G3 is used considering the different soils for foundation and how the type of the soil affects the stability of the hybrid system. Optum CE develops fast, user-friendly software for the design of Geotech and Concrete structures. The software is developed with a focus on providing advanced FE analysis packages, but at the same time making the tools are accessible for engineering practitioners including structural engineers, contractors, and building companies [202]. Table 6-9 shows the parameters used by OPTUM for simulations.

Table 6-9: Geotechnical Parameters used by OPTUM software for simulations

Item	Loose Sand-MC	Medium Sand-MC	Dense Sand-MC	Soft Clay-MC	Firm Clay-MC	Stiff Clay-MC
Cohesion c (kPa)	0	0	0	5	10	20
Friction angle ϕ (°)	30	35	40	18	20	22
Soil Unit Weight γ (kN/m^3)	16	18	20	19	20	21

Unit weight of a soil mass is the ratio of the total weight of soil to the total volume of soil. The total mass of structure after summarizing the weights of each element

in Table 6-6 and Table 6-7 is 1,780 tonnes. Applying this load to the foundation, using OPTUM G3 [202], as shown in Figure 6-5, confirms that the soil type of Soft/medium sand is more stable with less displacement and dissipation.

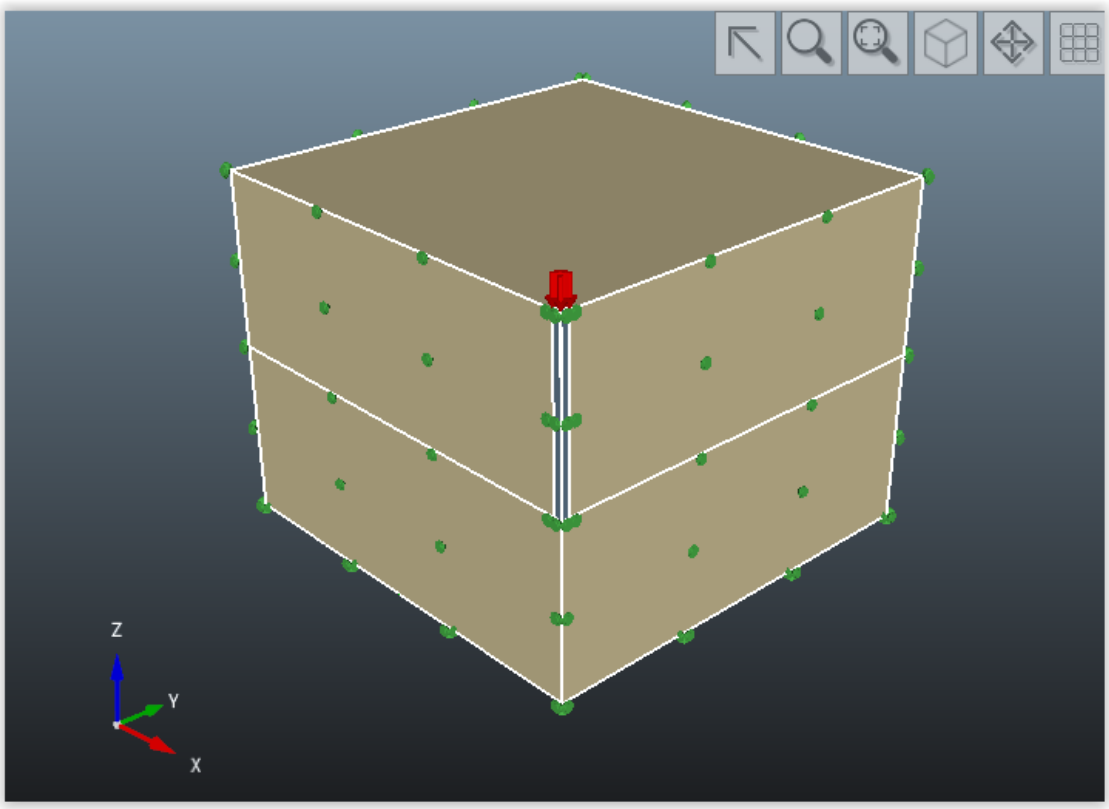

Figure 6-5: Applying load to the structure using OPTUM.

After simulation by OPTUM, the results for different kinds of soils are represented by Figure 6-6 to Figure 6-11.

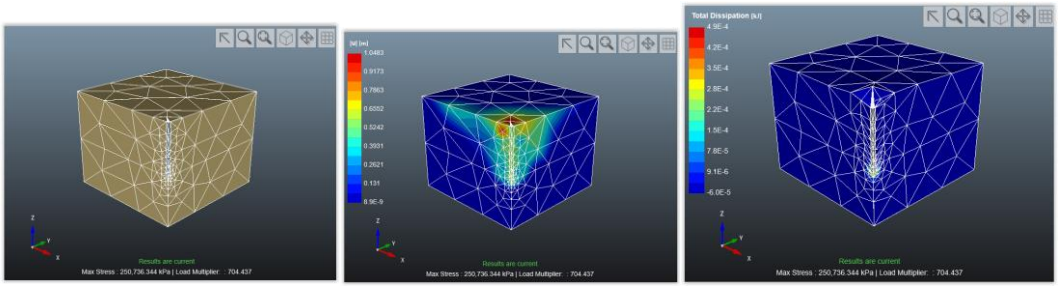

Figure 6-6: The geometry after meshing (left), displacement (middle), and total dissipation energy (right) for Loose Sand.

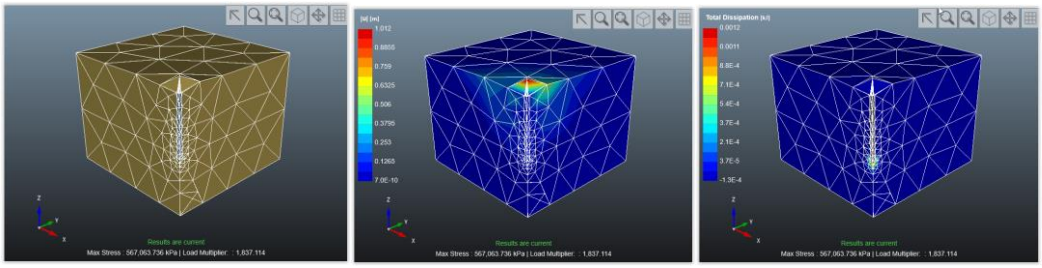

Figure 6-7: The geometry after meshing (left), displacement (middle), and total dissipation energy (right) for Medium Sand.

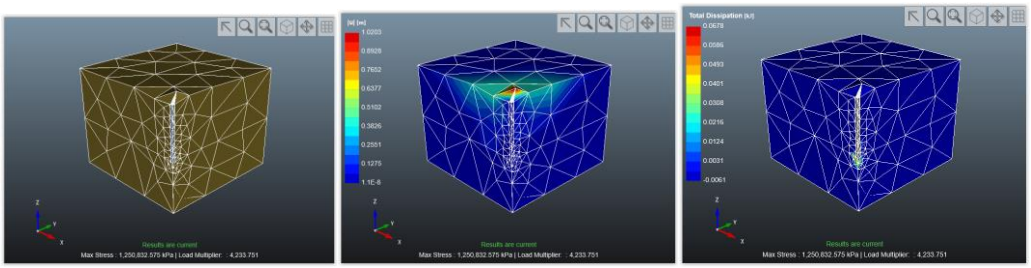

Figure 6-8: The geometry after meshing (left), displacement (middle), and total dissipation energy (right) for Dense Sand.

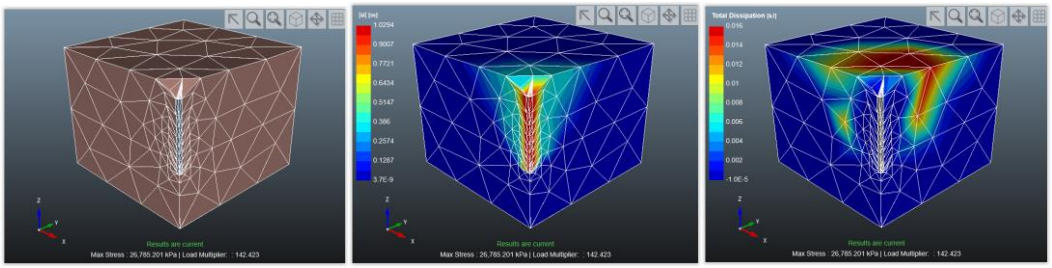

Figure 6-9: The geometry after meshing (left), displacement (middle), and total dissipation energy (right) for Soft Clay.

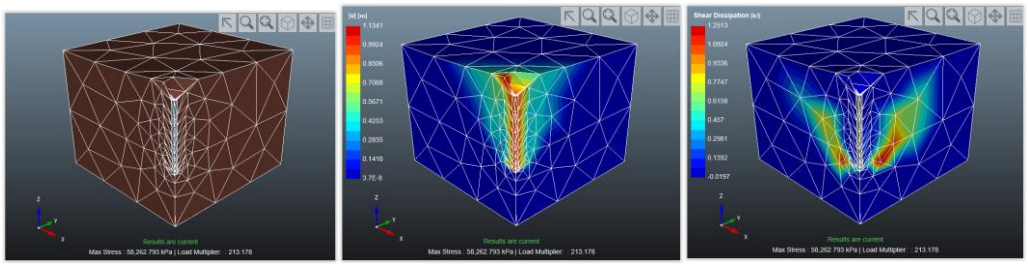

Figure 6-10: The geometry after meshing (left), displacement (middle), and total dissipation energy (right) for Firm Clay.

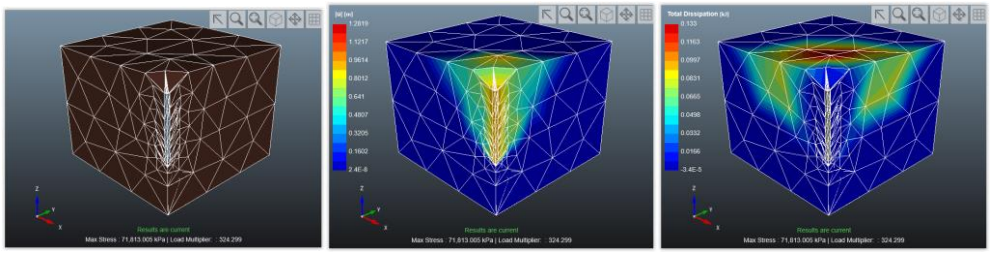

Figure 6-11: The geometry after meshing (left), displacement (middle), and total dissipation energy (right) for Stiff Clay.

The results can be shown in Table 6-10.

Table 6-10: OPTUM results for different types of seabed.

Item	Loose Sand-MC	Medium Sand-MC	Dense Sand-MC	Soft Clay-MC	Firm Clay-MC	Stiff Clay-MC
Max Displacement (m)	1.0483	1.012	1.0203	1.0294	1.1341	1.2819
Total Dissipation Energy (kJ)	0.00049	0.0012	0.0678	0.016	0.0456	0.133

The results indicate that the maximum displacement and dissipation will occur for Stiff-clay-MC soil and minimum displacement and dissipation for Medium Sand-MC and Loose-Sand-MC respectively.

6.2.2.2 Macro-Element Model

For estimating the natural frequency of an offshore foundation pile under load, a spring model based on the Euler-Bernoulli beam model (Figure 6-12) of a monopile foundation at the Terawhiti site is assumed with input parameters as follows:

- Steel monopile, diameter 6 meters, to ensure rigid behavior, as recommended by Jose and Mathai [203].
- Poisson ration 0.2 as recommended by Bowles [204] and OPTUM [202] to validate Hooke ‘s stress-strain law.
- stiffness 20 MPa, a typical value for the beam-on-elastic foundation sourced from Bowles [204] and OPTUM [202].

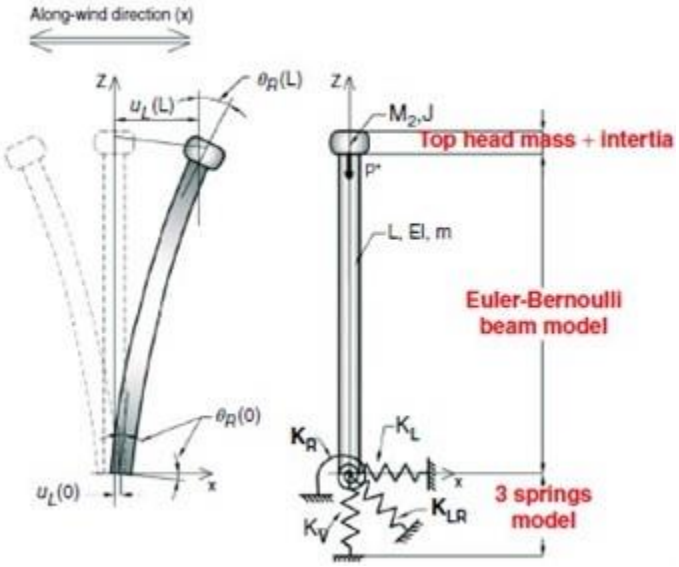

Figure 6-12: Mechanical Model of Foundation; KV (vertical stiffness), KL (lateral stiffness), KR (rocking stiffness), and KLR (cross-coupling). [205].

The initial stiffness of the foundation (i.e. K_L, K_R, and K_{LR}), can be determined based on the pile dimensions and soil type. Once K_L, K_R, and K_{LR} are known, one can predict the natural frequency of the system [205]. The results for this design are:

K_L=3,848.25 MN/m, K_{LR}= -133,488 MN and K_R=7,252,848 MNm/rad.

The simple cantilever beam formulas as recommended by Arany [206] was used to estimate the natural frequency of the tower f_0 which is 0.34 Hz which is acceptable, as the condition is that the target frequency of the selected wind and tidal turbines ,according to Table 5, is 0.24 Hz [160].

6.2.2.3 Wind Loads

Table 6-11 summarizes the main parameters of wind scenarios. The loads and moments will be used later in section 6.2.2.5 to identify driving combined scenarios either E1 or E5.

Table 6-11: Load and overturning moment of wind scenarios (U-1) – (U-4) for Terawhiti.

Parameters	Wind scenario (U-1)	Wind scenario (U-2)	Wind scenario (U-3)	Wind scenario (U-4)
Standard deviation of wind speed $\sigma_U[m/s]$	2.69	3.1	2.7	2.7
Standard deviation in $f>f_{1P}$	0.89	1.01	-	-
Turbulent wind speed component $u[m/s]$	1.13	2.02	7.1	7.1
Total wind load F_{wind} [MN]	1.68	1.86	3	0.69
Total wind moment M_{wind} [MNm]	196.5	217.62	351	80.7

The maximum wind load and moment found for U3. As recommended by DNV 2014 [193] and IEC 2019 [192], the environmental load factor of γ_L = 1.35 multiplies on U3 moment load to result a total wind moment of 473.85 [MNm].

6.2.2.4 Wave Loads

The wave conditions recommended by Bhattacharya [160], as explained before in Table 6-5, are used for calculating critical wave loads acting on the substructure.
The dynamic amplification of the wave loading is calculated using the peak wave frequency and an assumed damping ratio. The total damping ratios for the along-wind (x) and cross-wind (y) directions are chosen conservatively as 3% and 1%, respectively from Camp et al. 2004 [207]. The DAFs are
calculated as

$$\mathrm{DAF} = \frac{1}{\sqrt{(1-(\frac{f}{f_0})^2)^2 + (2\xi\frac{f}{f_0})^2}} \quad (6\text{-}1)$$

where f ($= \frac{1}{T}$) is the excitation frequency, f0 is the Eigen frequency and ξ is the damping ratio and wave periods are from Table 6-12 and f_0 is 0.34 Hz. In calculating DAFs, as the difference in DAF_x and DAF_y for wave scenarios are negligible, a higher value is applied on loads.

Table 6-12: Dynamic amplification factors and wave loads.

Parameters	**Wave scenario (W-1)**	**Wave scenario (W-2)**	**Wave scenario (W-3)**	**Wave scenario (W-4)**
Wave period T[s]	12.2	16.66	13.73	18.63
Wave frequency f [Hz]	0.081	0.060	0.072	0.053
Dynamic amplification-along-wind DAF_x [-]	1.060049	1.032081	1.046857	1.024857
Dynamic amplification-cross-wind DAF_y [-]	1.1060158	1.032136	1.046939	1.024899
Total wave load F_w[MN]	3.1	7.4	4.6	8.04
Total wave moment M_w [MNm]	55.6	164.3	119	210.93
Total wave load with DAF $F_{w,DAF}$[MNm]	3.42	7.63	4.81	8.24
Total wave moment with DAF $M_{w,DAF}$[MNm]	61.5	169.5	124.5	216.1

6.2.2.5 Load Combinations for Ultimate Limit State (ULS)

Table 6-13 uses the calculated loads of Table 6-11 and Table 6-12 . It can be seen

Parameter	Normal operation E-1	Extreme wave scenario E-2	Extreme wind scenario E-3	Cut-out wind+ Extreme wave scenario E-4	Wind- wave misalignment E-5
Maximum wind load [MN]	1.68	1.86	3	0.69	1.86
Maximum wave load [MN]	3.1	8.04	7.4	8.04	8.04
Combined maximum load [MN]	4.78	9.9	10.4	8.73	9.9
Maximum wind moment [MNm]	196.5	217.62	351	80.7	217.62
Maximum wave moment [MNm]	55.6	210.93	164.3	210.93	210.93
Combined maximum moment [MN]	252.1	428.55	515.3	291.63	428.55
Cycle time period [s]	12.2	18.63	16.66	18.63	18.63
frequency [Hz]	0.081	0.053	0.060	0.053	0.053

that superior loads belong to E-3.

Table 6-13: Calculated wind and wave loads.

Parameter	Normal operation E-1	Extreme wave scenario E-2	Extreme wind scenario E-3	Cut-out wind+ Extreme wave scenario E-4	Wind- wave misalignment E-5
Maximum wind load [MN]	1.68	1.86	3	0.69	1.86
Maximum wave load [MN]	3.1	8.04	7.4	8.04	8.04
Combined maximum load [MN]	4.78	9.9	10.4	8.73	9.9
Maximum wind moment [MNm]	196.5	217.62	351	80.7	217.62
Maximum wave moment [MNm]	55.6	210.93	164.3	210.93	210.93
Combined maximum moment [MN]	252.1	428.55	515.3	291.63	428.55
Cycle time period [s]	12.2	18.63	16.66	18.63	18.63
frequency [Hz]	0.081	0.053	0.060	0.053	0.053

The wall thickness of monopile is estimated according to API 2A-WSD [208] as

$$t_P \geq 6.35 + \frac{D_P}{100}[\text{mm}] \tag{6-2}$$

This value is used for finding the area moment of inertia:

$$I_P = \frac{1}{8}(D_P - t_P)^3 t_P \pi = \frac{1}{8}(D_P - 6.35 - \frac{D_P}{100})^3 (6.35 + \frac{D_P}{100})\pi \tag{6-3}$$

where I_P, D_P, and t_P are the moment of inertia, diameter, and thickness of monopile respectively. The following criteria for maximum stress σ_m (see Table 6-5) needs to be allowable [160]:

$$\sigma_m = \frac{M_{wind,EOG}}{I_P}\frac{D_P}{2} < \frac{f_{yk}}{\gamma_M} \tag{6-4}$$

where γ_M = 1.1 is pile material safety factor and f_{yk}=355 MPa is pile yield stress (from Table 7). From equation (4) the required diameter is determined as:

$$\frac{D_P}{I_P} < \frac{2f_{yk}}{\gamma_M M_{wind,EOG}} \tag{6-5}$$

The last dimension for a monopile design is length estimated by the formula given by Poulos and Davis [209] :

$$L_P \geq 4\left(\frac{E_P I_P}{n_h}\right)^{\frac{1}{5}} \tag{6-6}$$

Substituting total overturning moment of 515.3 MNm from Table 5-13 and other values mentioned above in equation (6-5):

$$\frac{D_P}{I_P} < \frac{2f_{yk}}{\gamma_M M_{wind,EOG}} \rightarrow \frac{D_P}{I_P} < \frac{2 \times 355}{1.1 \times 515.3} \rightarrow D_P < 1.25 I_P$$

Substituting the above value ($D_P = 1.25 I_P$) in equation (6-3), results in finding area moment of inertia (I_P) and monopile diameter (D_P) as below:

$I_P = 5.12\ kg.m^2 \rightarrow D_P < 1.25 \times 5.12 = 6.414\ m = 6414\ mm$

Substituting D_P in equation (6-2) results in the required thickness:

$$t_P \geq 6.35 + \frac{6414}{100}[\text{mm}] = 70.49\ \text{mm}$$

Lastly, the maximum length of monopile for investigating this foundation design should be

$L_P \geq 4\left(\frac{E_P I_P}{n_h}\right)^{\frac{1}{5}} = 4\left(\frac{200 \times 10^9 \times 5.12}{4000 \times 10^3}\right)^{\frac{1}{5}} = 48.27\ m$

So, based on total load, the foundation dimensions should be:

$D_P < 6.41\ m$, $t_P \geq 70.49\ mm$, $L_P \geq 48.27\ m$

The chosen values of DP and LP satisfy above conditions. So, the pile dimensions for the Terawhiti site to withstand total load are:

D_P = 6 [m] t_P = 0.083 [m] L_P = 60 [m]

6.2.2.6 Long-Term Deflection & Rotation of the Pile Mudline Moment

Stiffness values of section 6.2.2.2 is used to find deformations in the foundation using:

$$\begin{bmatrix} F_x \\ M_y \end{bmatrix} = \begin{bmatrix} K_L & K_{LR} \\ K_{LR} & K_R \end{bmatrix} \begin{bmatrix} \rho \\ \theta \end{bmatrix} \quad (6\text{-}7)$$

where Fx and My are highlighted in Table 12. Solving the matrix results in:

$$\rho = \frac{K_R}{K_L K_R - K_{LR}^2} F_x - \frac{K_{LR}}{K_L K_R - K_{LR}^2} M_y \quad (6\text{-}8)$$

$$\theta = -\frac{K_{LR}}{K_L K_R - K_{LR}^2} F_x + \frac{K_L}{K_L K_R - K_{LR}^2} M_y \quad (6\text{-}9)$$

From Table 6-12, the maximum load is 10.4 MN and the maximum moment is 515.3 MNm. Also, from section 2.2, K_L=3848.25 MN/m, K_{LR}= -133488 MN and K_R=7252848 MNm/rad. Using these values in Equations (8) and (9) results in
$\rho = 0.005$ m, $\theta = 0.00012°$
Based on the criteria design (Table 6-5), as $\rho < 0.2\ m$ and $\theta < 0.5\ °$, the pile tip deflection and the rotation are acceptable.

6.2.3 Summary of Monopile Design

This section proposes a standard design for the foundation of a hybrid (wind+tidal) system for Terawhiti:
The proposed tower is a hollow steel tube wall thickness 0.027 meters, 68 meters high above the platform, tapering from 5 meters at the base to 3 meters at the top, weighing 255 tonnes.
The proposed transition piece is a steel tube, internal diameter ($6 + \frac{2\times83}{1000} =$) 6.16 meters to fit the top of the monopile, wall thickness 0.083 meters extending 29 meters below platform level, and sheathing top of the monopile. Weight 300 tonnes.

The proposed foundation is a monopile inserted into the seabed. It will be solid steel, 6 meters diameter and 60 meters long, weighing 700 tonnes. It will project above the seabed for 30 meters (upper 20 meters will insert into the transition piece), and lower 20 meters will be placed in the seabed. The pile will be driven with a hydraulic hammer into the seabed.

The acting loads are transferred to the foundation; They can be static depending on the total weight of the structure which is calculated analyzed with OPTUM G3 software or dynamic (cyclic) which is investigated by combining wind and wave loads.

The wind and water produce aerodynamic and hydrodynamic loads (thrust and drag) on the structure which depends on the operational speed of turbines. But, to know the acceptability of foundation design, it is necessary to combine wind and wave loads in ULS design and calculate maximum loads and find driven scenario. Then find required dimensions of the pile and based on maximum load of driven scenario, calculated deflection, and check in ULS if deflection is allowable or not:

- The combination of wind and wave loads indicates that the maximum load is in is E-3 scenario. Applying loads of this scenario results in acceptable deflection, tilt, and natural frequency for Terawhiti.
- Several iterations were done to reach the required dimensions of the pile after finding the maximum combined load for the driving scenario.

6.3 Floating Design in Cook Strait

With increasing of electricity demand and global warning attributed to the combustion of fossil fuels, exploitation of offshore energy sources in the form of wind, sea currents, and waves has attracted [126].

While a life cycle analysis (LCA) of offshore wind generation against onshore shows a 48% improvement in the sustainability of the project, the cost of electricity using offshore wind is still high [18, 21]. This obstacle makes investment on tidal turbines difficult too because in harsh water currents their life decreases and in deep sea levels their foundation design is complicated [1]. Using the same foundation for wind and tidal turbines can reduce the cost of electricity with increasing power generation enables from two different sources of energy [23]. However, if a support

structure is not correctly designed for offshore conditions, failure will be disastrous, and the structure will be costly to replace. For this reason, foundations are an important design consideration. Aspects to be considered while choosing and designing the foundation for a particular site include weather conditions, seabed conditions, seabed geology, vessels and equipment required to install, and protecting the environment in accordance with local regulations.

Floating foundation is the best solution for deep water sites as enhanced stability is added in the ballast water. Compared with the grounded systems, the advantages of the floating systems are more suitable for mass production and easy to install in offshore and more economic [210, 211]. The mooring system has six degrees of freedom inhabits motion while connecting to seabed makes it possible to operate under different water depths [212, 213]. This makes its market broader and more ecocomical for investment in any range of water height [213]. So, in the recent decades, there has been a great tendency from standing-driven foundations in seabed working less than 60 m of water (e.g., Vindey Denmark 2017) to floating moored foundations in 120 m of water (e.g., Hywind Scotland 2018) and even in about 1000 m of water (e.g., 2021 call for proposals from Bureau of Ocean Energy Management (BOEM) in California, USA) [214]. Currently,the key companies of spar buoy are Hywind/Statoil (Norway), Toda (Japan), Sway (Norway), NauticrAft (Australia) and SeaTwirl (Sweden) [215].

In contrast to grounded foudations, aerodynamic and hydrodynamic loads creat a considerable motion for floating ones [213]. So, it is essential to define a simple methodology to estimate the loads on the anchor to establish a feasibility analysis [211]. The paper aims to provide a simplified approach for finding maximum allowable loads necessary for a foundation which can support the selected wind and tidal turbines and mast and flange. An example of an offshore wind and tidal turbine supported on a floating spar is then considered based on the environmental data from NIWA. Finally, a simplified anchor sizing procedure is presented, which is demonstrated to produce conservative upper bound estimates for the required suction caisson for Cook Strait.

Design will be carried out by developing spreadsheets relevant to different aspects of foundation design based on standard IEC 61400, IEA Wind TCP Task 37-May 2019, DNV 2014 and IEC 2019 [192, 193, 199, 216].

6.3.1 Concept Description

A broad platform provides stability by largely lying below the sea surface and using water as ballast as shown in Figure 6-13. It is loosely anchored to the sea floor. A long single column extends far below the water to dampen movement and uses sand and water as ballast. It is also loosely moored to the sea floor [215]. The total ballast is approximately 8,000 tons which would be split between a solid part and water. The percentage split and type of ballast material is subject to further design optimisation. The ballast water will typically be dosed with lye, NaOH, giving a pH value above 10.5 [217].

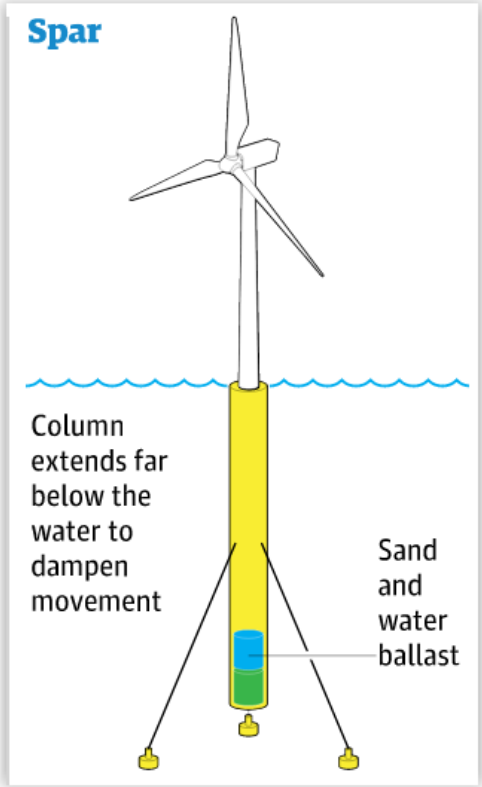

Figure 6-13: The mechanism of enhancing stability of spar by adding ballast [215].

The base case is secured to the seabed using suction anchors. The suction anchors are likely to have a maximum diameter of 7 m which corresponds to an estimated footprint of maximum 40 m^2 per anchor. Suction anchors are designed such that 1 m of sand erosion/scouring is acceptable. Base case is that there is no need for rock dump around anchors to prevent scour. However, due to the likely presence of mobile sediments in the area scour protection around the anchors may be required to some extent (e.g. rock dumping, mattresses). The footprint of such scour protection is expected to extend no more than 15 m out from the anchor perimeter [217].

The schematic structure of turbines installed with a floating foundation is shown in Figure 6-14.

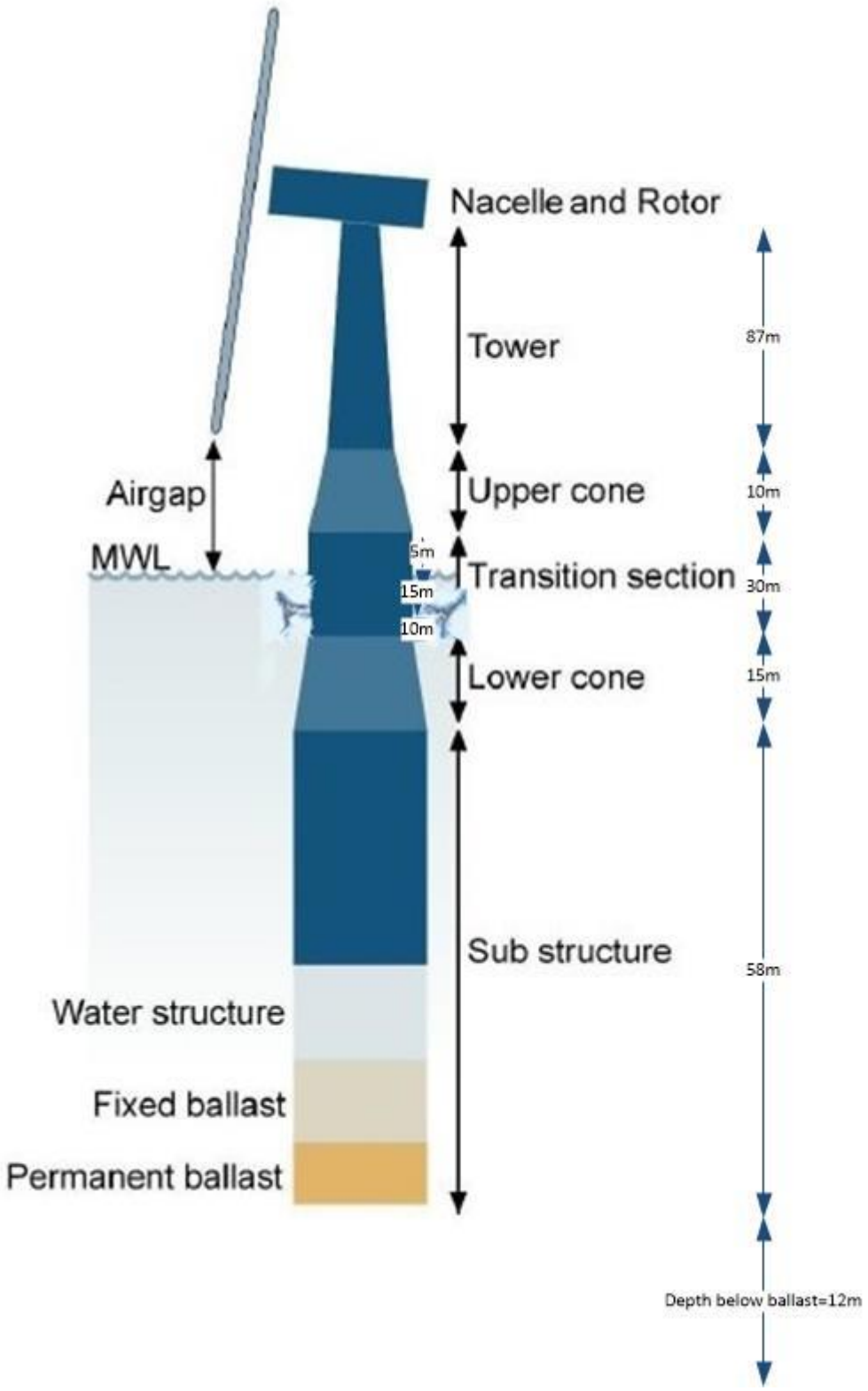

Figure 6-14: General view of support structure

Table 6-14 summarises features of the proposed foundation considering the total weight of wind and tidal turbines used for hybrid system is approximately equal to

Statoil turbine. Key design parameters will receive further discussion in section 6.3.4 [159].

Table 6-14:General information of the spar mooring parameters.

Parameter	Symbol	Value	Unit
Spar diameter	D_S	14	m
Spar draft (depth below sea level)	B	93	m
Length of upper/lower cone	L_C	10	m
Diameter of lower cone (upper section)	-	6	m
Diameter of upper cone (lower section)	-	6	m
Diameter of upper cone (upper section)	-	5	m
Mass of ballast	m_B	8000	tons
Mass of spar buoy	m_S	1000	tons
Mooring radius	r_m	700	m
Diameter of mooring chains		130	mm
Unit weight of mooring chains	μ_C	300	kg/m
Mass of the mooring cables	m_S	350	tons

6.3.2 Environmental Parameters for Design

Severe environmental conditions where the wind speed and the significant wave height have a large value are more common in deep water seas [212]. Therefore, tidal current modelling conducted by MetOcean Solutions Limited (MSL) , is used for site optimization [2].The resolution of this model in NZ-wide grid is 0.06°(5.6 × 6.6 km). MetOcean used The Princeton Ocean Model (POM) model with a high-resolution domain over Cook Strait (0.002°; 170 × 230 m) as the best area for offshore supply as shown in Figure 6-15 [164]. POM was used in a vertically integrated two-dimensional mode with boundaries provided from the global TPX0 solution [31].

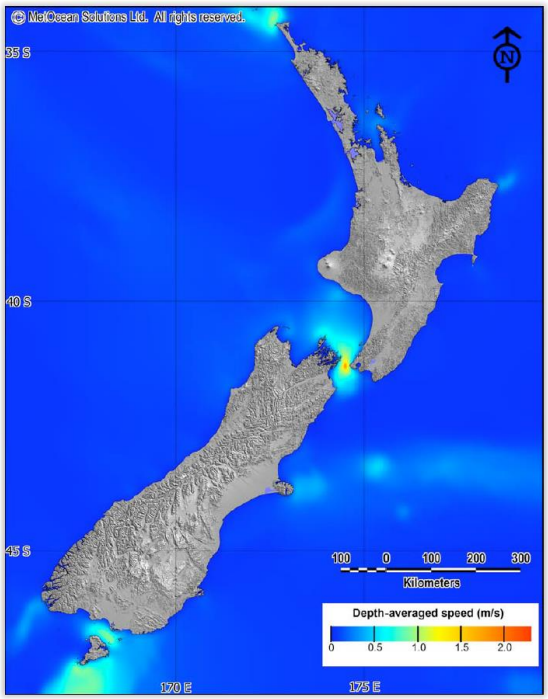

Figure 6-15: National depth-averaged tidal current speeds for mean spring flows (in m/second) [164].

The main geographical parameters of the optimized site in Cook Strait are shown in Table 6-15.

Table 6-15: Tide data for Terawhiti [29, 174].

Location	Latitude (deg)	Longitude (deg)	Annual Water Velocity (m/s)	Depth of Water (m)	Annual Wind Velocity (m/s)
Terawhiti	−41.3138°S	174.5898°E	1.32	110	7.10

The most important data from NIWA [194] ’s analysis is summarized in Table 6-16.

Table 6-16: Wave data for Terawhiti

Parameter	Symbol	Value	Unit
Significant wave height with 50-year return period [195]	Hs	15	m
Peak wave period	Ts	13.73	s
Maximum wave height (50-year)	Hm	27.62	m
Maximum wave peak period	Tm	18.63	s
Maximum water depth (50-year high water level)	S	30	m
Water density	ρw	1,030	kg/m3

Equivalent wind data will be sourced from the meteorological recording site closest to the Terawhiti by NASA. These data will be presented in Table 6-17 and Figure 6-16. These data are essential to estimate the wind stresses transmitted through the turbine's support structure to its foundation.

Table 6-17: The geological and geotechnical wind data of Terawhiti [28, 160, 198, 199]

Parameter	Symbol	Value	Unit
Shape parameter-Weibull distribution [198]	s	1.98	[-]
Scale parameter-Weibull distribution [198]	K	7.99	m/s
Reference turbulence intensity [199]	I	16	%
Turbulence integral length scale [160]	L_K	340.2	m
Annual wind speed [29]	u_{ave}	7.10	m/s
Air density [160]	ρa	1.225	kg/m 3

Wind speed variability is often described by the Weibull two-parameter distribution function. It is considered a standard approach for evaluating local wind load probabilities because it has been found to fit a wide collection of wind data [200]. The Weibull shape and scale parameter are denoted by s and K, respectively. s is dimensionless and it indicates how peak the site under consideration is, while K has a unit of wind speed (m/s) and it shows how windy the site is [201].

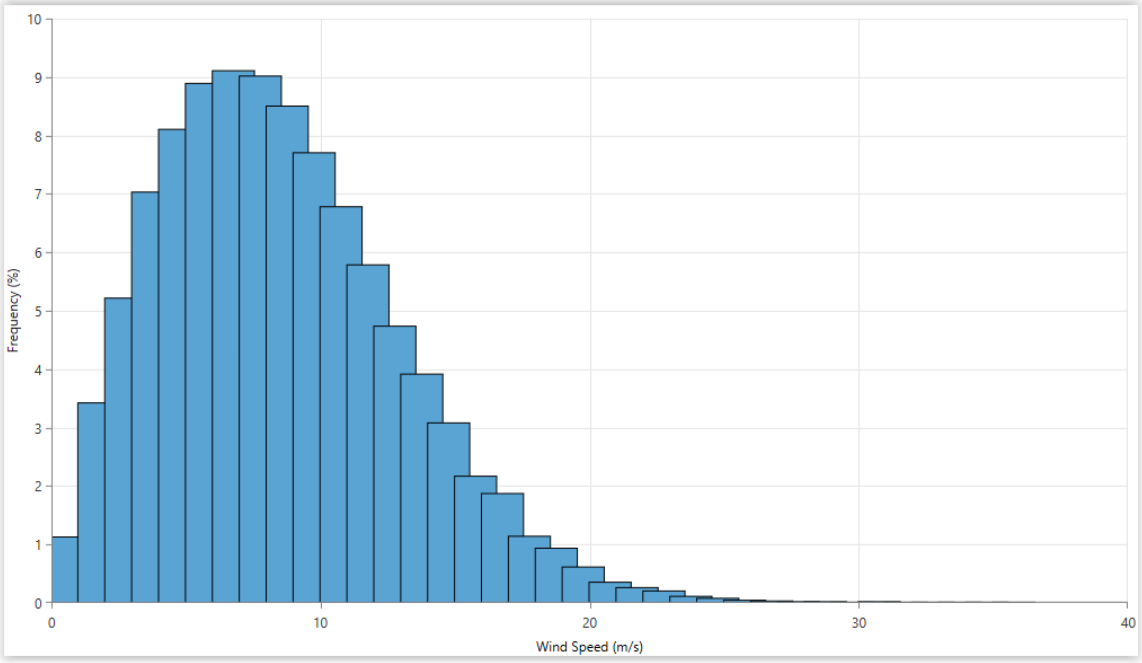

Figure 6-16: Wind speed histogram for Terawhiti [29].

To calculate Weibull parameters, the frequency percentage of Terawhiti results by Homer is used in the Weibull calculator [198] which results in s=1.98 and K=7.99 m/s.

The turbulence intensity varies with mean wind speed, which is for Terawhiti 7.10 m/s, and quantifies how much the wind varies typically within 10 minutes [160]. This value may be obtained , I= 16% ,from standard IEC 61400 [199].

Based on the DNV code, for height above sea level (z) less than 60 metres, L_k is 5.67z and, for z above 60 meters L_k is 340.2 meter [160]. As height above sea level is 87m, the turbulence integral length scale is 340.2 m in this case.

6.3.3 Design Process

The steps given in Figure 6-17 are used to evaluate the feasibility of an offshore hybrid structure in Cook Strait.

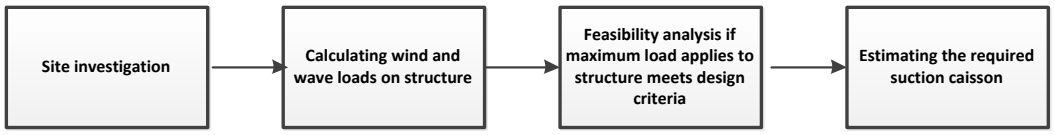

Figure 6-17: Design process of floating wind and tidal structure.

The design criteria which will be checked for the possibility of a floating design are presented in Table 6-18.

Table 6-18: Main criteria for foundation design [160].

Parameter	Limit
The maximum stress (σ_m) - yield strength (f_{yk})	$\sigma_m < f_{yk}$
Deflection (ρ_0)	$\rho_0 < 0.2\ m$
Tilt (θ_0)	$\theta_0 < 0.5\ °$
The structural natural frequency(f_0) -frequency of rotation of the rotor ($f_{1P,\ max}$)	$f_0 > 1.1 f_{1P,\ max}$ = 0.24 Hz
Pile wall thickness (t_P)	$t_P \geq 6.35 + \frac{D_P}{100}$

Design criteria specific to the selected turbines are presented in Table 6-19 and Table 6-20.

Table 6-19: General information of Wind turbine, Siemens SWT-3.6-107 Offshore 3.6 MW, for the hybrid system [159, 160, 202].

Parameter	Symbol	Value	Unit
Turbine Power	P	3.6	MW
Turbine rotational Speed (Cut in/out)	u_{in}/u_{out}	5-13	rpm
Operational wind speed range	V	4-25	m/s
Rated wind speed	u_R	16.5	m/s
Mass of the nacelle (NA)	m_{NA}	125	tonnes
Hub height from mean sea level	H	87	m
Density of tower and TP-S355 Steel	ρ	7,860	kg/m^3
Tower data			
top diameter	D_t	3	m
bottom diameter	D_b	5	m
weight	m_t	255	tonnes
Tower height	L_T	68	m
Wall thickness	t_T	0.027	m
Rotor and blade data			
Turbine rotor diameter	D	107	m
Swept area	TSA	8992	m^2
Mass of rotor+hub	m_R	100	tonnes
Rotor overhang	b	4	m
Blade root diameter	B_{root}	4	m
Blade tip chord length	B_{tip}	1	m
Blade length	L	52	m

Table 6-20: General information of tidal turbine, Atlantic Resources AR 2000, for the hybrid system [159, 160].

Parameter	Symbol	Value	Unit
Turbine Power	P	2	MW
Turbine rotational Speed (Cut in/out)	Ω	1-3.05	rpm
Operational tidal speed range	V	1-4.5	m/s
Turbine rotor diameter	D	20	m
Height from the seabed	ZS	25	m
Rotor Swept area	TSA	314	m^2
Mass of two turbines	m	300	tonnes

There are five scenarios for an offshore foundation design exposed to both wind and wave loads [160] which are summarized in Table 6-21.

Table 6-21: Load Case Scenarios [160].

Scenario	Name and description	Wind model	Wave model	Alignment
E-1	Normal operational conditions. Wind and wave act in the same direction (no misalignment).	NTM at u_R (U-1)	1-yr ESS (W-1)	Collinear
E-2	Extreme wave load scenario. Wind and wave act in the same direction (no misalignment).	ETM at u_R (U-2)	50-yr EWH (W-4)	Collinear
E-3	Extreme wind load scenario. Wind and wave act in the same direction (no misalignment).	EOG at u_R (U-3)	1-yr EWH (W-2)	Collinear
E-4	Cut-out wind speed and extreme operating gust scenario. Wind and wave act in the same direction (no misalignment).	EOG at u_{out} (U-4)	50-yr EWH (W-4)	Collinear
E-5	Wind and wave misalignment scenario. Same as E-2, except the wind and wave are misaligned at an angle of ϕ=90°. The dynamic amplification is higher in the cross-wind direction due to low aerodynamic damping.	ETM at u_R (U-2)	50-yr EWH (W-4)	Misaligned at ϕ=90°

In Table 8, the Normal Turbulence Model (NTM) relates to the normal working conditions of the turbine. Extreme Turbulence model (ETM) is for extreme turbulence conditions. The Extreme operating Gust (EOG) is the highest single

occurrence wind load by a sudden change in the wind speed. ESS and EWH denote to extreme sea state and extreme wave height respectively. The significant wave height HS, uses in ESS scenarios, is the average of the maximum one-third of all waves in the three hours, while the maximum wave height Hm, uses in EWH scenarios, is the maximum wave height for three hours [160].

6.3.4 Results of Floating Design

6.3.4.1 Wind Loads

In this section the main parameters of wind scenarios are calculated. The loads and moments will be used later in section 6.3.4.3 to identify driving combined scenarios either E1 or E5.

Wind scenario U-1: Normal Turbulence (NTM) at Rated Wind Speed (U_R):

The mean wind speed is the rated wind speed (U_R) where the highest thrust force (Th) is expected, and the wind turbulence is modelled by the Normal Turbulence Model (NTM). This scenario is typical for normal operation of the turbine. The standard deviation of wind speed in normal turbulence following IEC (2005) can be written as

$$\sigma_{u,NTM} = I_{ref}(0.75u + b) \quad with \quad b = 5.6\, m/s \tag{6-10}$$

where I_{ref} is the reference turbulence intensity (expected value at u = 15[m / s]), $\sigma_{u,NTM}$ is the standard deviation of wind speed in normal turbulence model (NTM) and b is model parameter which is defined 5.6 according to IEC 2005. For the calculation of the maximum turbulent wind speed component (u_{NTM}), the time constant of the pitch control is assumed to be the same as the time period of the rotation of the rotor. In other words, it is assumed that the pitch control can follow changes in the wind speed that occur at a lower frequency than the rotational speed of the turbine. Then maximum turbulent wind speed component (u_{NTM}) may be determined by calculating the contribution of variations in the wind speed with a higher frequency than f_{1P}, max to the total standard deviation of wind speed. From

the Kaimal spectrum used for the wind turbulence process, its standard derivation can be calculated using equation (6-11).

$$\sigma_{u,NTM,f>f_{1P}} = \sigma_{u,NTM}\sqrt{\frac{1}{(\frac{6L_k}{u_R}f_{1P,max}+1)^{\frac{2}{3}}}} \tag{6-11}$$

where $\sigma_{u,NTM,f>f_{1P}}$ is the variations in the wind speed with a higher frequency than $f_{1P,}$ $\sigma_{u,NTM}$ is the standard deviation of wind speed in normal turbulence, L_k being the integral length scale, u_R is rated wind speed, f_{1P} is the frequency of rotation of the rotor (1P).

The turbulent wind speed encountered in normal operation in normal turbulence conditions is found by assuming normal distribution of the turbulent wind speed component and taking the 90% confidence level value. This is substituted into the quasi-static equation used in equation (6-13). Equation (6-14) shows expressions for the corresponding wind moment at the mudline [160].

$$u_{NTM} = 1.28\sigma_{u,NTM,f>f_{1P}} \tag{6-12}$$

$$F_{wind,NTM} = \frac{1}{2}\rho_a A_R C_T (u_R + u_{NTM})^2 \tag{6-13}$$

$$M_{wind,NTM} = F_{wind,NTM}(S + z_{hub}) \tag{6-14}$$

where u_{NTM} is the maximum turbulent wind speed component, $\sigma_{u,NTM,f>f_{1P}}$ is the variations in the wind speed with a higher frequency than $f_{1P,}$ ρ_a is air density, A_R is rotor swept area, C_T is the thrust coefficient, u_R is rated wind speed, $F_{wind,NTM}$ and $M_{wind,NTM}$ are mudline load and moment in normal turbulence, S is water depth and z_{hub} is hub height.

I_{ref} is assumed to be 16% from Table 6-17. Thus, $\sigma_{u,NTM} = 0.16(0.75 \times 15 + 5.6) = 2.69\, m/s$. $1.1f_{1P,\,max}$ is assumed to be 0.24 Hz or $f_{1P,\,max}$= 0.218 Hz from Table 6-18. L_K is assumed to be 340.2 m from Table 6-17 and u_R= 16.5 m/s from Table 6-19. So, $\sigma_{u,NTM,f>f_{1P}}$ (Equation (6-11)) will be 0.89 m/s. This value in equation (6-12) results, $u_{NTM} = 1.28 \times 0.89 = 1.13\, m/s$. Using this, the total

wind load and moment for the Terawhiti are estimated as $F_{wind,\,NTM}$ =1.68 [MN], $M_{wind,NTM}$ =374.64 [MNm]

Wind scenario U-2: Extreme Turbulence (ETM) at Rated Wind Speed (U_R):
The ETM is used to calculate the standard deviation of wind speed at the rated wind speed, and from that the maximum wind load under normal operation in extreme turbulence conditions. The standard deviation of wind speed in ETM is given in IEC (2005) as

$$\sigma_{u,ETM} = cI_{ref}\left[0.072(\frac{u_{avg}}{c}+3)(\frac{u_R}{c}-4)+10\right] \quad with \quad c = 2\,[m/s] \qquad (6\text{-}15)$$

where equation (6-15) terms are already defined (same as equation (6-10)), but U_{avg} is the long-term average wind speed at the site. The maximum turbulent wind speed component u_{ETM} is determined similarly to the previous case.

$$\sigma_{u,ETM,f>f_{1P}} = \sigma_{u,ETM}\sqrt{\frac{1}{(\frac{6L_k}{u_R}f_{1P,max}+1)^{\frac{2}{3}}}} \qquad (6\text{-}16)$$

The turbulent wind speed encountered in normal operation in extreme turbulence conditions, which is used for cyclic/dynamic load analysis, is found by assuming normal distribution of the turbulent wind speed component. As opposed to the normal turbulence situations, the 95% confidence level value is taken. This is substituted into the quasi-static equation used in equation (6-13). Equation (6-19) shows the expression for wind moments at the mudline [160].

$$u_{ETM} = 2\sigma_{u,ETM,f>f_{1P}} \qquad (6\text{-}17)$$

$$F_{wind,ETM} = \frac{1}{2}\rho_a A_R C_T(u_R + u_{ETM})^2 \qquad (6\text{-}18)$$

$$M_{wind,ETM} = F_{wind,ETM}(S + z_{hub}) \qquad (6\text{-}19)$$

where equation (6-17) to (6-19) terms are already defined (same as equations (6-12) to (6-14)), but U_{avg} from Table 6-17 is 7.1 m/s for Terawhiti. So, results are estimated as:

$$\sigma_{u,ETM} = 3.1\ m/s, \qquad \sigma_{u,ETM,f>f_{1P}} = 1.01\ m/s, \qquad u_{ETM} = 2.02\ m/s,$$

$$F_{wind,ETM} = 1.86\ MN, \qquad M_{wind,ETM} = 414.78\ MNm$$

Wind scenario U-3: Extreme operating Gust (EOG) at Rated Wind Speed (UR):

The EOG is a sudden change in the wind speed and if it hits the rotor when it is operating at the rated wind speed of the turbine, the pitch control of the wind turbine has no time to alleviate the loading. IEC (2005) suggests that for simplified foundation design 50-year extreme operating gust (EOG) is assumed to estimate the highest single occurrence wind load. The 50-year extreme wind speed, which is typically used in wind turbine design for extreme wind conditions, can be determined by standard equations (6-20) to (6-23) sourced from Bhattacharya [160].

$$U_{10,50-year} = K[-ln\,(1 - 0.98^{\frac{1}{52596}})]^{\frac{1}{s}} \tag{6-20}$$

where the number 52596 = 365.25[days ⁄ year] · 24[hours ⁄ day] · 6[10 min intervals ⁄ hour] represents the number of 10-minutes intervals in a year. The 10-year extreme wind speed is represented by

$$\mathrm{u}_{10,1-\mathrm{year}} = 0.8\mathrm{U}_{10,50-\mathrm{year}} \tag{6-21}$$

The characteristic standard deviation of wind speed can be calculated by

$$\sigma_{U,c} = 0.11\mathrm{U}_{10,1-\mathrm{year}} \tag{6-22}$$

Which c is the return period of EOG.
The extreme gust speed is then calculated at the rated wind speed from

$$u_{EOG} = min\left\{1.35\left(u_{10,1-\mathrm{year}} - u_R\right); \frac{3.3\sigma_{u,c}}{1+\frac{0.1D}{\Lambda_1}}\right\} \tag{6-23}$$

where D is the rotor diameter= 107 m, $\Lambda_1 = L_k / 8$ with L_k being the integral length scale. Using this, the total wind load is estimated as

$$F_{wind,EOG} = Th_{EOG} = \frac{1}{2}\rho_a A_R C_T (u_R + u_{EOG})^2 \quad (6\text{-}24)$$

where equation (6-24) terms are already defined (same as equations (4)). For wind speeds between cut-in and cut-out, thrust coefficient is estimated as recommended by Arany et al.[218]:

$$C_T \approx \frac{7}{\bar{u}} \quad (6\text{-}25)$$

Using equation (D-28)(refer to Appendix D for explanation), $C_T = 7 / \bar{u} = 7 / 7.1 = 0.98$ and rated wind speed u_R= 16.5 m/s. Using the water depth S and the hub height above sea level z_{hub}, the mudline bending moment (without the load factor γ_L) can be estimated using equation (6-26) sourced from [160].

$$M_{wind,\ EOG} = F_{wind,\ EOG}\,(S + z_{hub}) \quad (6\text{-}26)$$

The EOG wind speed is calculated using data from Table 6-18 and Equations (6-20) to (6-23)

$$U_{10,50-year} = 31.1\ m/s, u_{10,1-year} = 24.8\ m/s, \sigma_{U,c} = 2.7\ m/s,\ u_{EOG} = 7.1\ m/s$$

Using this, the total wind load is estimated as $F_{wind,\ EOG}$

$$Th_{wind,\ EOG} = \frac{1}{2} \times 1.225 \times \frac{\pi}{4}(107)^2 \times \frac{7}{7.1} \times (16.5 + 7.1)^2 \approx 3[MN]$$

and using the water depth S =110 [m] and the hub height above mean sea level z_{hub} = 103 [m]

$M_{wind,\ EOG} = 3\,(110 + 103) = 639$ [MNm]

Wind scenario U-4: Extreme operating Gust (EOG) at the Cut-Out Wind Speed (U_{out}):

If the 50-year EOG hits the rotor slightly below the cut-out speed of the turbine, due to the sudden change in wind speed the turbine cannot shut down. Note that the EOG calculated at the cut-out wind speed is different from that evaluated at the rated wind speed according to IEC 2005.

Wind load caused by the EOG at the cut-out wind speed U_{out} is calculated taking into consideration that according thrust coefficient expression of Frohboese and Schmuck 2010(equation (6-25)) [219] is no longer valid, and instead should be determined by assuming that the pitch control keeps the power constant. This means that the thrust force is inversely proportional to the wind speed above rated wind speed U_R and the thrust coefficient is inversely proportional to the cube of the wind speed. So, between cut-in (U_{in}) and rated wind speed (U_R), equation (6-25) is used for calculating thrust coefficient and after rated wind speed, equation (6-27) is used for calculating thrust coefficient.

$$C_T = \frac{7u_R^2}{u^3} \tag{6-27}$$

The EOG speed at cut-out wind speed $u_{EOG,Uout}$ is determined from equations (6-20) to (6-23) by substituting a value for U_{out} (which is not the same at U_R). The thrust force and moment can be estimated using equations (6-28) and (6-29) sourced from [160].

$$T_{wind,\, u_{out}} = \frac{1}{2}\rho_a A_R C_{DT}(u_{out} + u_{EOG,u_{out}})^2 \tag{6-28}$$

$$M_{wind,\, u_{out}} = (S + z_{hub})\, T_{wind,\, u_{out}} \tag{6-29}$$

where equations (6-28) & (6-29) terms are already defined (same as equations (6-13) & (6-14)). So, using equation (6-23) $u_{EOG,u_{out}} = 7.1\ m/s$ and as a result:

$$T_{wind,\, u_{out}} = \frac{1}{2} \times 1.225 \times \frac{\pi}{4}(107)^2 \times \frac{7 \times 16.5^2}{25^3} \times (25 + 7.1)^2 = 0.69 \text{ [MN]}$$

$M_{wind,\, EOG} = 0.69\,(110 + 103) = 146.9$ [MNm]

Table 6-22 summarises the important parameters and presents the wind loads for the different wind scenarios to determine the turbulent wind speed component and through that the thrust force and overturning moment. The wind loads on the structure are independent of the substructure diameter, and therefore the wind loads can be evaluated before the pile and substructure design are available.

Table 6-22: Load and overturning moment of wind scenarios (U-1) – (U-4) for Terawhiti.

Parameters	(U-1)	(U-2)	(U-3)	(U-4)
Standard deviation of wind speed $\sigma_U[m/s]$	2.69	3.1	2.7	2.7
Standard deviation in $f>f_{1P}$	0.89	1.01	-	-
Turbulent wind speed component $u[m/s]$	1.13	2.02	7.1	7.1
Total wind load F_{wind} [MN]	1.68	1.86	3	0.69
Total wind moment M_{wind} [MNm]	374.64	414.78	639	146.9

Applying an environmental load factor of $\gamma_L = 1.35$ as recommended by DNV 2014 [193] and IEC 2019 [192], the total wind moment is 862.65 [MNm] for U3. It is found that the EOG at U_R (U-3) gives the highest load and overturning moment.

6.3.4.2 Wave Loads

The wave conditions recommended by Bhattacharya [160] for calculating critical wave loads acting on the substructure are:

(W-1) One-year extreme sea state (ESS). A wave with height equal to the 1-year significant wave height $H_{S,1}$.

(W-2) One-year extreme wave height (EWH). A wave with height equal to the 1-year maximum wave height $H_{m,1}$.

(W-3) 50-year ESS. A wave with height equal to the 50-year significant wave height $H_{S,50}$.

(W-4) 50-year EWH. A wave with height equal to the 50-year maximum wave height $H_{m,50}$.

Bhattacharya [160] states that the one-year ESS and EWH are used as a conservative overestimation of the normal wave height ($_{NWH}$) prescribed in IEC 2019[192]. It is important to note here in relation to the ESS that the significant wave height and the maximum wave height have different meanings. The significant wave height H_S is the average of the highest one-third of all waves in the three-hour sea state, while the maximum wave height Hm is the single highest wave in the same three-hour sea state.)

The highest wind load is expected to be caused by scenario U-3 and the highest wave load is due to scenario W-4. In practice, the 50-year extreme wind load and the 50-year extreme wave load have a negligible probability to occur at the same time, and the DNV 2014 code [193] also doesn't require these extreme load cases to be evaluated together. The designer has to find the most severe event with a 50-year return period based on the joint probability of wind and wave loading. Therefore, for the ULS analysis, two combinations are suggested by Arany et al. 2017[218]:

(1) The ETM wind load at rated wind speed combined with the 50-year EWH – the combination of wind scenario U-2 and wave scenario W-4. This will provide higher loads in deeper water with higher waves.

(2) The 50-year EOG wind load combined with the one-year maximum wave height. This will provide higher loads in shallow water in sheltered locations where wind load dominates. These scenarios are somewhat more conservative than those required by standards and can be adopted for simplified analysis. From the point of view of SLS and FLS, the single largest loading on the foundation is not representative, because the structure is expected to experience this level of loading only once throughout the lifetime.

In simplified load calculation methodologies, to determine the wave loading, simple linear waves are assumed. Higher-order theories like Stokes waves or Dean's stream function theory would provide better estimates, especially in shallow waters. However, the linear theory allows for simpler load calculation and its application is justified for foundation design loads.

The circular substructure area A_S is also calculated from this diameter. The methodology used here builds on linear (Airy) wave theory, which gives the surface elevation η, horizontal particle velocity w, and the horizontal particle acceleration $\dot{w}$ as

$$\eta(x,t) = \frac{H_m}{2}\, cos\,(\frac{2\pi t}{T_S} - kx) \tag{6-30}$$

$$w(x,z,t) = \frac{\pi H_m\, cosh\,(k(S+z))}{T_S\, sinh(KS)}\, cos(\frac{2\pi t}{T_S} - kx) \tag{6-31}$$

$$\dot{w}(x,z,t) = \frac{-2\pi^2 H_m cosh(k(S+z))}{T_S^2\, sinh(kS)}\, sin(\frac{2\pi t}{T_S} - kx) \tag{6-32}$$

where H_m is maximum wave height, T_s is peak wave period, S is mean water depth, t is time, x is the horizontal coordinate in the along-wind direction. The wave number k is obtained from the dispersion relation

$$\omega^2 = gk\,tanh(kS) \quad with \quad \omega = \frac{2\pi}{T_S} \tag{6-33}$$

The force on a unit length strip of the substructure is the sum of the drag force F_D and the inertia force F_I:

$$dF_{wave}(z,t) = dF_D(z,t) + dF_I(z,t) = \frac{1}{2}\rho_w D_S C_D w(z,t)|w(z,t)| + C_m \rho_w A_S \dot{w}(z,t) \tag{6-34}$$

where w horizontal particle velocity as a function of z coordinate and t time, C_D is the drag coefficient, C_m is the inertia coefficient, and ρ_w is the density of seawater, D_S and A_S are the diameter and circular substructure area. The total horizontal force and bending moment at the mudline is then given by integration as

$$F_{wave}(t) = \int_{-S}^{\eta} dF_D\,dz + \int_{-S}^{\eta} dF_I\,dz \tag{6-35}$$

$$M_{wave}(t) = \int_{-S}^{\eta} dF_D(S + z_{hub})\,dz + \int_{-S}^{\eta} dF_I(S + z_{hub})\,dz \tag{6-36}$$

The peak load of the drag and inertia loads occur at different time instants, and therefore the maxima are evaluated separately. The maximum of the inertia load occurs at the time instant t = 0 when η = 0 and the maximum of the drag load occurs when t = T_S/4 and η = H_m / 2.

The maximum drag load & moment $F_{D,max}$ & $M_{D,max}$ is then obtained by carrying out the integrations:

$$F_{D,max} = \frac{1}{2}\rho_w D_S C_D \frac{\pi^2 H_m^2}{T_S^2 sinh^2(kS)} P_D(k,S,\eta) \tag{6-37}$$

$$M_{D,max} = \frac{1}{2}\rho_w D_S C_D \frac{\pi^2 H_m^2}{T_S^2 sinh(kS)} Q_D(k,S,\eta \tag{6-38}$$

$$P_D(k,S,\eta) = \frac{e^{2k(S+\eta)} - e^{-2k(S+\eta)}}{8k} + \frac{S+\eta}{2} \tag{6-39}$$

$$Q_D(k,S,\eta) = (\frac{S+\eta}{8k} - \frac{1}{16k^2})e^{2k(S+\eta)} - (\frac{S+\eta}{8k} + \frac{1}{16k^2})e^{-2k(S+\eta)} + (\frac{S+\eta}{2})^2 + \frac{1}{8k^2} \tag{6-40}$$

The maximum inertia load & moment $F_{I,max}$ & $M_{I,max}$ are obtained by:

$$F_{I,max} = \frac{1}{2}\rho_w C_m D_S^2 \frac{\pi^3 H_m}{T_S^2 sinh(kS)} P_I(k,S,\eta) \tag{6-41}$$

$$M_{I,max} = \frac{1}{2}\rho_w C_m D_S^2 \frac{\pi^3 H_m}{T_S^2 sinh(kS)} Q_I(k,S,\eta) \tag{6-42}$$

$$P_I(k,S,\eta) = \frac{sinh(k(S+\eta))}{k} \tag{6-43}$$

$$Q_I(k,S,\eta) = (\frac{S+\eta}{2k} - \frac{1}{2k^2})e^{k(S+\eta)} - (\frac{S+\eta}{2k} + \frac{1}{2k^2})e^{-k(S+\eta)} + \frac{1}{k^2} \tag{6-44}$$

In the simplified method for obtaining foundation loads, it can be conservatively assumed that the sum of the maxima of drag and inertia loads is the design wave load. This assumption is conservative, because the maxima of the drag load and inertia load occur at different time instants. All wave scenarios (W-1)–(W-4) are evaluated with the same procedure, using different values of wave height H and wave period T [160].

In this step, a simplified estimation of the extreme wave height and the corresponding wave period for a given site is explained which involves the following sub-steps:

1. Obtain the relevant significant wave height H_S from a reliable source. The 1-year equivalents are calculated following DNV 2014[193] from the 50-year significant wave height according to

$$H_{S,1} = 0.8H_{S,50} \quad (6\text{-}45)$$

2. Calculate the peak wave period corresponding to the significance wave height, T_S using:

$$T_S = 11.1\sqrt{\frac{H_S}{g}} \quad (6\text{-}46)$$

3. Calculate the number of waves in a 3-hour period, N: Typically, significant wave heights are given for a 3-hour period. In other words, this means that the significant wave height is calculated as the mean of the highest 1/3 of all waves. Therefore, many different wave heights occur within this 3-hour period, and the highest occurring wave height is called the maximum wave height Hm. To find this, one needs to know the number of waves in the 3-hour period, because the more waves there are, the higher the chance of higher waves occurring.

$$N = \frac{3hours}{T_S} = \frac{10800s}{T_S} \quad (6\text{-}47)$$

4. Calculate the maximum wave height, H_m by

$$H_m = H_S\sqrt{\frac{1}{2}ln(N)} \quad (6\text{-}48)$$

5. Calculate the peak wave period corresponding to the maximum wave height, Tm. The same formulae can be used as in step 2.

$$T_m = 11.1\sqrt{\frac{H_m}{g}} \quad (6\text{-}49)$$

The 50-year significant wave height, $H_{S,50}$ at Terawhiti can be found from NIWA [220]. Alternatively, ERA-40 Wave Atlas [195] provides an approximate value of 15m which was shown in Table 6-16. So, according to equation (6-45), $H_{S,1}$ is 12m. Going to step 2, $T_{S,1}$ can be 12.2s. Equation (6-47) gives N=885.24 and as a result

$H_{m,1}$=22.10m and $T_{m,1}$=16.66 s. Also, $H_{m,50}$ is 27.62m according to equation (6-48).

The wave periods for 4 scenarios are:

(W-1): $T_{S,1} = 11.1\sqrt{\frac{H_{S,1}}{g}}$ =$11.1\sqrt{\frac{12}{9.8}}$ =12.2 s

(W-2): $T_{m,1} = 11.1\sqrt{\frac{H_{m,1}}{g}}$ =$11.1\sqrt{\frac{22.10}{9.8}}$ =16.66 s

(W-3): $T_{S,50} = 11.1\sqrt{\frac{H_{S,50}}{g}}$ =$11.1\sqrt{\frac{15}{9.8}}$ =13.73 s

(W-4): $T_{m,50} = 11.1\sqrt{\frac{H_{m,50}}{g}}$ =$11.1\sqrt{\frac{27.62}{9.8}}$ =18.63 s

The wave heights and wave periods are summarised for all wave scenarios (W-1) to (W-4) in Table 5-23 according to the explanations presented.

Table 6-23: Wave heights and wave periods for different wave scenarios for Foveaux.

Parameters	(W-1)	(W-2)	(W-3)	(W-4)
Wave height H[m]	$H_{S,1}$=12	$H_{m,1}$=22.10	$H_{S,50}$=15	$H_{m,50}$=27.62
Wave period T[s]	$T_{S,1}$=12.2	$T_{m,1}$=16.66	$T_{S,50}$=13.73	$T_{m,50}$=18.63

The wave loads (equations (6-37) and (6-38)) are calculated only for the most severe wave scenarios used for Load Cases E-2 and E-3, i.e. wave scenario (W-2) and (W-4), the 1-year and 50-year extreme wave heights (EWHs), using the definitions presented in Table 8 where $\rho_w = 1030$ kg/m^3 and S=110m (from Table 6-15)

This section can be modelled using an equivalent diameter of D_D = 11.33m for drag load calculations, and D_I = 12.89m for inertia load calculations.

C_D=0.5 and C_m=2 (based on DNV [193])

Hm, Ts, η, k for W-1 scenario: H_m =12m, T_s =12.2s, η = 0 for inertia loads and η = 6m for drag loads, k=0.034m^{-1} (based on equation (6-33))

Using equations (6-37) to (6-44) for W-1 scenario:

$F_{D,max} = 0.57MN$, $M_{D,max} = 581.1$ MNm,

$F_{I,max} = 0.37MN$, $M_{I,max} = 43.3\ MNm$

The results are:

$F_{wave,\ W\text{-}1}$= 0.57+0.37= 0.94 MN, $M_{wave,\ W\text{-}1}$= 581.1+43.3=624.4 MNm

Hm, Ts, η, k for W-2 scenario: H_m =22.10m, T_s =12.2s, η = 0 for inertia loads and η = 11.05m for drag loads, k=0.034m^{-1}(based on equation (6-33))

Using equations (6-37) to (6-44) for W-2 scenario:

$F_{D,max} = 2.8MN$, $M_{D,max} = 643.2\ MNm$, $F_{I,max} = 1.05MN$, $M_{I,max} =$ 86.7 MNm

The results are:

$F_{wave,\ W\text{-}2}$= 2.8+1.05= 3.85 MN, $M_{wave,\ W\text{-}2}$= 643.2+86.7= 729.9 MNm

Hm, Ts, η, k for W-3 scenario: H_m =15m, T_s =13.73s, η = 0 for inertia loads and η = 7.5m for drag loads, k=0.029m^{-1}(based on equation (6-33))

Using equations (6-37) to (6-44) for W-3 scenario:

$F_{D,max} = 0.93$ MN , $M_{D,max} = 13880.07$ MNM , $F_{I,max} = 0.24$ MN , $M_{I,max} =$ 1399.4 MNm

The results are:

$F_{wave,\ W\text{-}3}$= 1.2 MN, $M_{wave,\ W\text{-}3}$= 15279.4 MNm

Hm, Ts, η, k for W-4 scenario: H_m =27.62m, T_s =13.73s, η = 0 for inertia loads and η = 13.81m for drag loads, k=0.029m^{-1}(based on equation (6-33))

Using equations (6-37) to (6-44) for W-4 scenario:

$F_{D,max} = 0.04$MN , $M_{D,max} = 5672.8\ MNM$, $F_{I,max} = 2.1\ MN$, $M_{I,max} = 1678.1MNm$

The results are:

$F_{wave,\ W\text{-}4}$= 2.14 MN, $M_{wave,\ W\text{-}4}$= 7350.9 MNm

6.3.4.3 Anchor Load Combinations for Ultimate Limit State (ULS)

The current load is calculated as [160]

$$F_C = \frac{1}{2}\rho_w D_D C_D V^2 B = \frac{1}{2} \times 1030 \times 11.33 \times 0.5 \times 1.32^2 \times 93 = 0.47 \quad (6\text{-}50)$$

The loads under the combined actions of wind and waves calculated using different scenarios of Table 6-22 and adding the current load as below:

F_{E-1}=1.68+0.94+0.47=3.09 MN

F_{E-2}=1.86+2.14+0.47=4.47 MN

F_{E-3}=3+3.85+0.47=7.32 MN

F_{E-4}=0.69+2.14+0.47=3.3 MN

F_{E-5}=1.86+2.14+0.47=4.47 MN

As expected, the wave load dominates, and the scenario with the combination of the 1-year EWH and the 50-year extreme operating gust (EOG) or E3 produces the ULS load. It should be noted here that this load is conservative for anchor design, as the load that acts on the anchor is reduced by the weight of the suspended section of the mooring line, the friction on the horizontal section (Touch Down Zone) of the mooring line, the soil reaction on the inverse catenary-shaped forerunner in the soil, and the weight of the forerunner. The vertical load acts on the spar at the instant when the surface elevation at the spar is at its highest point (wave crest), while the horizontal load is dominated by the inertia load, which is highest when the surface elevation is at the mean water level. Therefore, the ultimate load is taken as the horizontal load as calculated above [160].

6.3.5 Minimum Caisson Dimensions for Terawhiti with Sandy Soils

The diameter of the caisson D and the embedment depth L are the two main independent parameters that govern the holding capacity of the caisson for a given soil profile. Soil type is Soft/medium sand with angle of internal friction of $\phi' = 30°$, effective unit weight

of γ' = 9 and mooring chain friction on sand $\mu = 0.25$.

The holding capacity of suction caissons is typically determined in terms of an envelope based on the horizontal and vertical load components at the anchor as:

$$FP = \left(\frac{H_u}{H_m}\right)^a + \left(\frac{V_u}{V_m}\right)^b \quad (6\text{-}51)$$

where

a=$\frac{L}{D} + 0.5$, b=$\frac{L}{3D} + 4.5$

H_m is the horizontal capacity and V_m is the vertical capacity. On the other hand, H_u and V_u are the applied load. FP is the failure criterion and the maximum value can be 1 (limiting condition). The horizontal capacity in sand can be calculated as follows:

$$H_m = -LQ_{av} = 0.5A_bN_q\gamma'L^2 \tag{6-52}$$

where

A_b is effective unit bearing area of the forerunner (equals the diameter of the rope or wire, and 2.5–2.6 times the bar diameter for a chain), Nq is bearing capacity factor as defined by:

$$N_q = e^{\pi tan\phi}tan^2(45° + \frac{\phi}{2}) \tag{6-53}$$

with ϕ being the internal angle of friction of the soil.

The vertical capacity in sand will be

$$V_m = W' + \gamma' Z_e^2 y(\frac{h}{Z_e})(K\ tan\delta)_e(\pi D_e) + \gamma' Z_i^2 y(\frac{h}{Z_i})(K\ tan\delta)_i(\pi D_i) \tag{6-54}$$

where

$Y(x)=e^{-x}-1+x$

$K\ tan\delta$: factor that only appears together.

K: the effective stress factor used to calculate the horizontal effective stress as constant times the effective vertical stress ($\sigma_H = K\sigma_V'$), δ is the mobilised angle of friction between the caisson wall and the soil, e represents the external and i is the internal circumference of the caisson.

Z: D / [4K tan δ] with e and i referring to external and internal values, respectively.

The anchor padeye tensions and angles can be determined by (look at Figure 6-17):

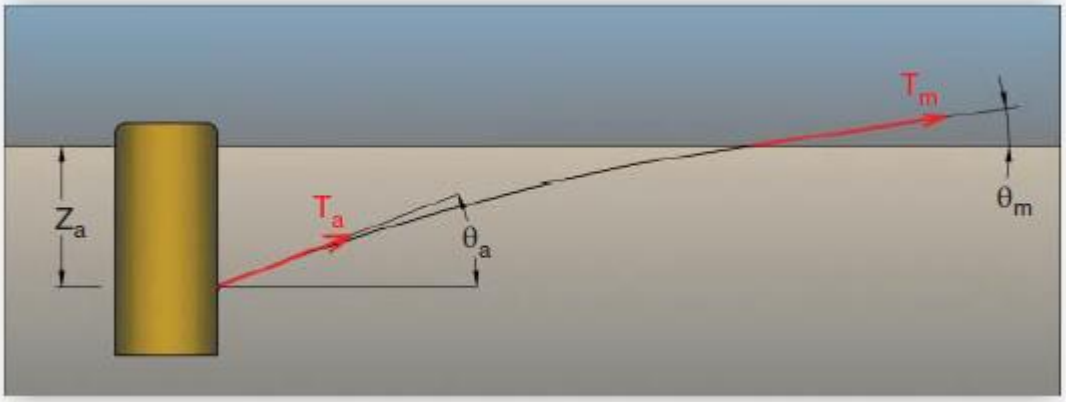

Figure 6-18: Loads on the anchor lines [160] .

$$\frac{T_a}{2}(\theta_a^2 - \theta_m^2) = z_a Q_{av} \tag{6-55}$$

$$\frac{T_m}{T_a} = e^{\mu(\theta_a - \theta_m)} \tag{6-56}$$

where

T_a tension at the anchor padeye.

T_m tension at the mudline.

θ_a angle of the tension at the anchor padeye to horizontal.

θ_m angle of the tension at the mudline to horizontal.

z_a depth of the anchor padeye below mudline.

μ friction coefficient between the forerunner (chain, rope, or wire) and the soil.

Q_{av} average soil resistance between the mudline and the padeye is calculated as:

$$z_a Q_{av} = A_b N_c \int_0^{z_a} \gamma' \, z dz \tag{6-57}$$

Where N_c is bearing capacity factor and between 9 and 14

$s_u(z)$ is distribution of the undrained shear strength with depth.

For sand, $z_a/L=2/3$ [160]. Statoil 2015 [217] advised the maximum diameter of 7 m for each anchor. As these design is a hybrid design of Hywind statoil by adding tidal turbines and considering wind and tidal conditions of New Zealand, the caisson dimensions will be according to [211]:

Table 6-24:Caisson dimensions for hybrid system

Parameter	Symbol	Value
Length-to-diameter ratio	L/D	3.2
Caisson diameter [m]	D	6.9
Corresponding length [m]	L	22.07
Wall thickness [m]	t_w	0.099
Effective weight of caisson [kN]	W_c	3,361
External skin friction factor [-]	$(K\tan\delta)_e$	7
Internal skin friction factor [-]	$(K\tan\delta)_i$	5
External shaft friction [kN]	F_e	7,343
Internal shaft friction [kN]	F_i	6,901
Maximum vertical load capacity [kN]	V_m	14,247
Maximum horizontal load capacity [kN]	H_m	278,358
Anchor padeye depth [m]	z_a	14.72
Padeye location [%]	r_z	0.67
Angle at the padeye [deg]	θ_a	50.14
Tension at the padeye (variable) [kN]	T_a	18,561
Horizontal load on the anchor [kN]	H_u	11,897
Vertical load on the anchor [kN]	V_u	14,247
Horizontal load check exponent [-]	a	3.7
Vertical load check exponent [-]	b	5.5667
Vertical utilization [-]	V_u/V_m	1
Horizontal utilization [-]	H_u/H_m	0.04

6.3.6 Summary of Floating Design

The floating design aims to develop a unique method for structural design of hybrid offshore systems in deep waters using spar buoy floating. The method enables to find required dimensions tolerating against wind and wave loads. Terawhiti in Cook Strait was selected as a case study because according to MetOcean model, this location can generate maximum electricity and suitable for this type of foundation.

Based on the selection of turbines and Terawhiti as facility site and by including the wind and wave loads, the design provides the stability of structure.

The wind and water produce aerodynamic and hydrodynamic loads (thrust and drag) on the structure which depends on the operational speed of turbines. But, to know the acceptability of foundation design, it is necessary to combine wind and wave loads in ULS design and calculate maximum loads and find driven scenario. Based on different scenarios of foundation design, next step will be calculating maximum loads, and find driven scenario. Then, the minimum required sizes of caisson based on the maximum load of the driven scenario for the Hybrid floating offshore structure can be estimated. These dimensions satisfy the failure criterion.

The results, as presented and discussed in Section 6.34 and 6.3.5, enable several conclusions:

- The proposed tower is a hollow steel tube wall thickness 0.027 meters, 68 meters high above the platform, tapering from 5 meters at the base to 3 meters at the top, weighing 255 tonnes.
- The proposed transition piece is a steel tube, internal diameter $(6 + \frac{2\times83}{1000} = 6.16)$ meters to fit the top of the cone, wall thickness 0.083 meters extending 29 meters below platform level, and sheathing top of the cone. Weight 300 tonnes.
- The proposed foundation is a spar buoy floating inserted into the seabed. The total ballast is approximately 8,000 tons which would be split between a solid part and water and spar buoy mass is 1000 tons. The diameter of the caisson and the embedment depth is 6.9 and 22.07 meter respectively. It will project above the seabed for 110 meters (upper 25 meters will insert into the transition piece), and lower 12 meters will be placed in the seabed. It will be driven with a hydraulic hammer into the seabed. It is loosely anchored to sea floor
- The maximum load occurs in extreme wind load scenario when wind and wave act in same direction or E-3.
- Several iterations were done to reach the required caisson dimensions after finding the maximum combined load for the driving scenario.

The future work in this aspect can be estimating the cost analysis in terms of comparing the proposed hybrid system with a wind floating and with a floating tidal system and analyzing how much using the same structure for both wind, and tidal turbines can reduce the cost of electricity generation rather than having a foundation design just for wind and also just for tidal turbines.

Chapter 7

Wind and Tidal Directions

7.1 Introduction

Historically, wind directions are determined from eolian sandstones [14]. In modern wind turbines, control mechanisms and operation of yaw systems maximise wind power extraction from different wind directions [15]. Accurate predictions on the wind power to be produced by the turbines are required for the grid operators from very short time scales to a few days ahead, in order to strike the balance between power supply and demand. Uncertainties and frequent fluctuations in wind speed and direction may create problems for customers who are in need of electricity supply. Further, the temporal, geographical and climatic factors, such as the particular time of the day, terrain, humidity and temperature, also affect the wind power generation that depends on generator hours of wind turbines, speed and direction of the wind, air density and position of the turbines. If the wind speed in different directions could be precisely forecast, it could bring about multiple benefits in adjusting control systems, maintenance scheduling, reducing economic and technical risks and profit maximization of the power trade.

Due to the importance attached to the wind speed among all numerical weather prediction data, the objective of this chapter was focused on studying the variation in wind power generated by different directions. This is essential to predicate in order to maximise power generation from wind. Therefore, this chapterr presents a novel research study based on the climate model to forecast its wind power generation in different wind patterns. In this sense, this study provides an insight into an optimized off-shore sites of Foveaux and Terawhiti to propose wind power as an alternative source for their demand.

To do this, Global Wind Atlas [16] is used to plot the wind rose in current wind patterns. In the next step, wind speed data from the Foveaux site are imported from the NASA database [17] to WRPLOT view software [18] and Homer Pro [19] to find wind frequency distribution and output power in each site.

For tidal power, same approach will be followed. Just in terms of tidal rose, water speeds and directions provided by NIWA will be used to identify the strength of tidal power in different directions.

7.2 Wind Rose in Foveaux and Terawhiti

Global Wind Atlas used to find wind rose of Foveaux and Terawhiti as shown in Figure 7-1. It can be seen that the dominant direction for Foveaux and Terawhiti is west and North respectively.

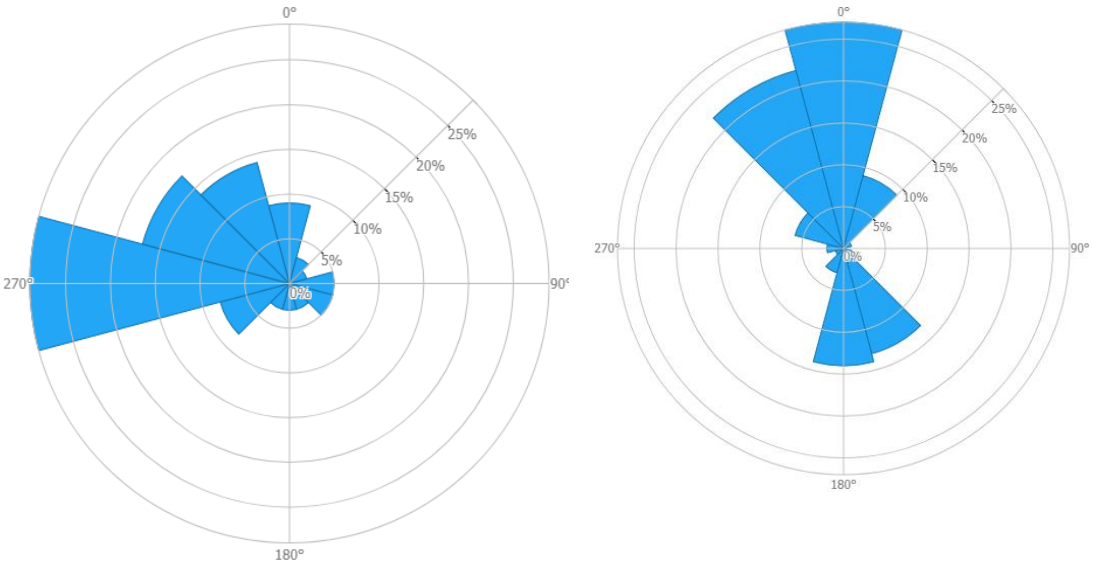

Figure 7-1: Wind roses of Foveaux (left) and Terawhiti (right)

7.3 Tidal Rose in Foveaux and Terawhiti

For plotting tidal roses, the flow speeds in x directions (u) and y directions (V) of National Institute of Water and Atmospheric Research (NIWA) used. Figure 7-2 shows that this site has a single distinct ebb and flood direction separated almost exactly by 180°.The minimum and maximum values in axes verifies that Terawhiti has higher tidal energy than Foveaux.

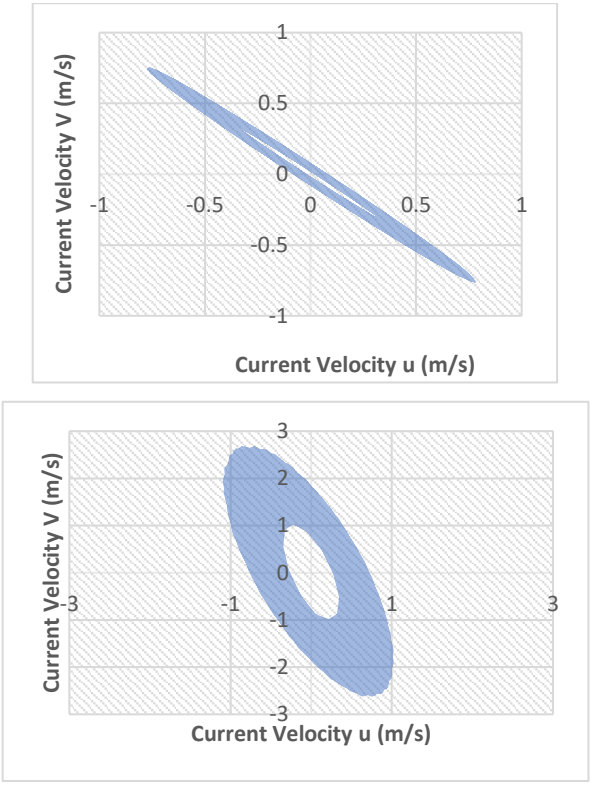

Figure 7-2: Tidal flow components in Foveaux (left) and Terawhiti (right)

The values used for plotting Figure 7-3 are average flow speeds of eastward and northward components. The data presented by NIWA shows these components of water speed are always in vice versa directions or tidal turbine can be working bidirectional. Plotting tidal rose with WRPLOT View software [30], indicates a NW-SE direction(NW (43.11% of time) and SE (43.06% of time)) for tidal turbine as shown in Figure 7-3.

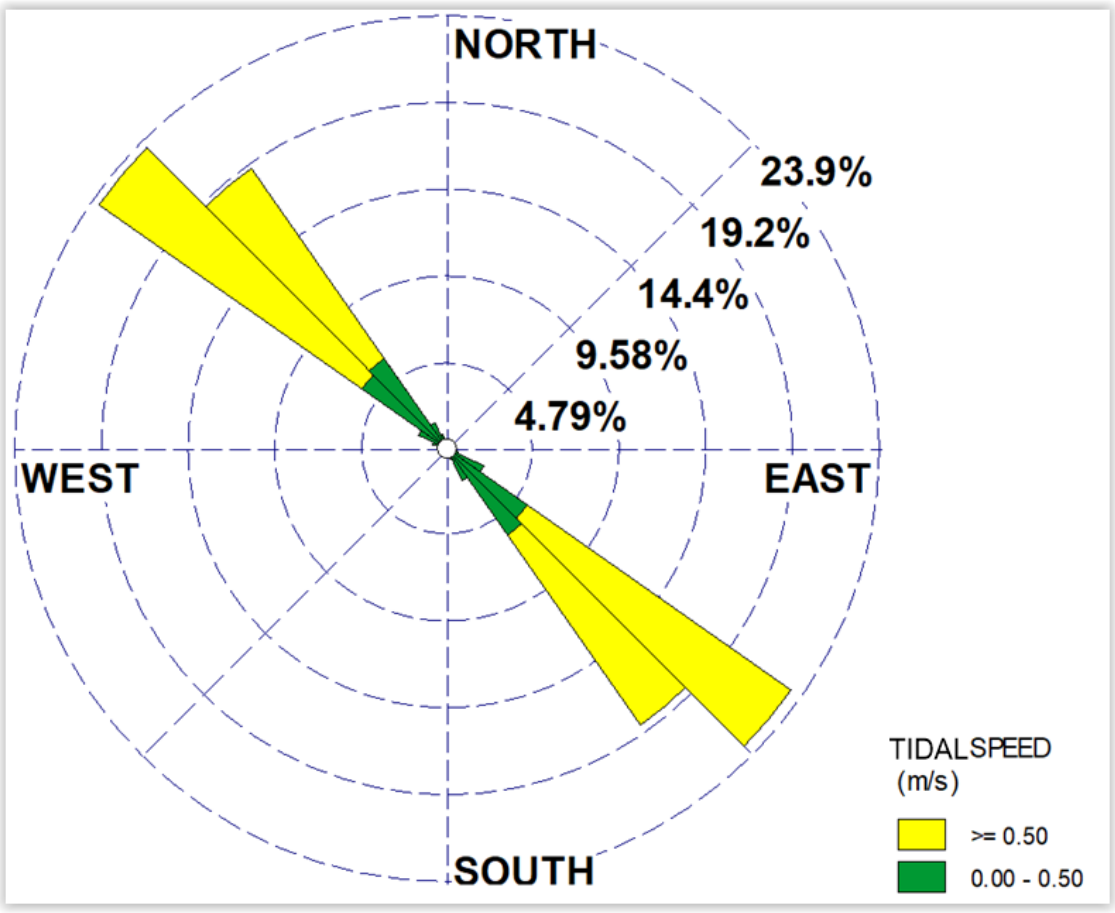

Figure 7-3: Tidal Rose of Foveaux

Figure 7-4 shows the tidal distribution for different speeds in Foveaux.

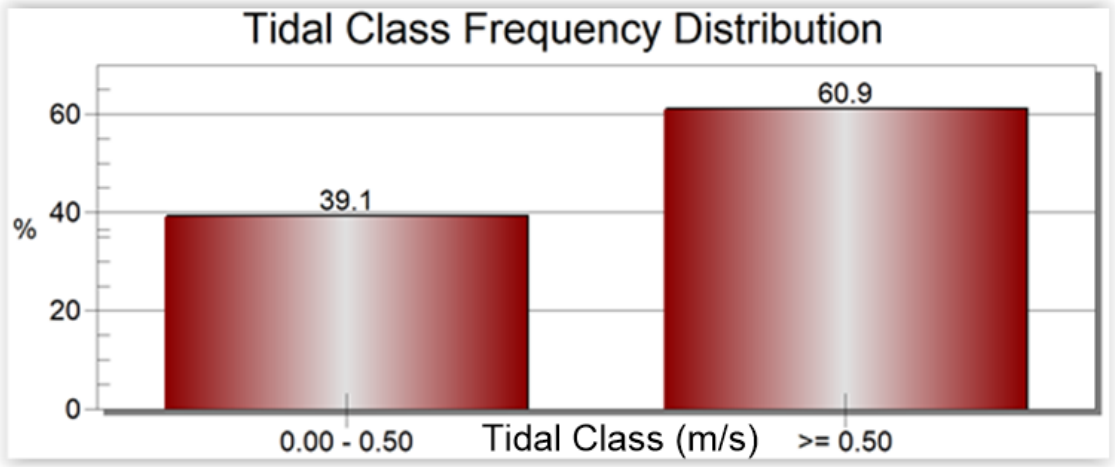

Figure 7-4: Tidal distribution for different speeds in Foveaux

Tidal rose of Terawhiti indicates a NNW-SSE direction (NNW 23.06% and SSE 22.77% of time) as shown in Figure 7-5.

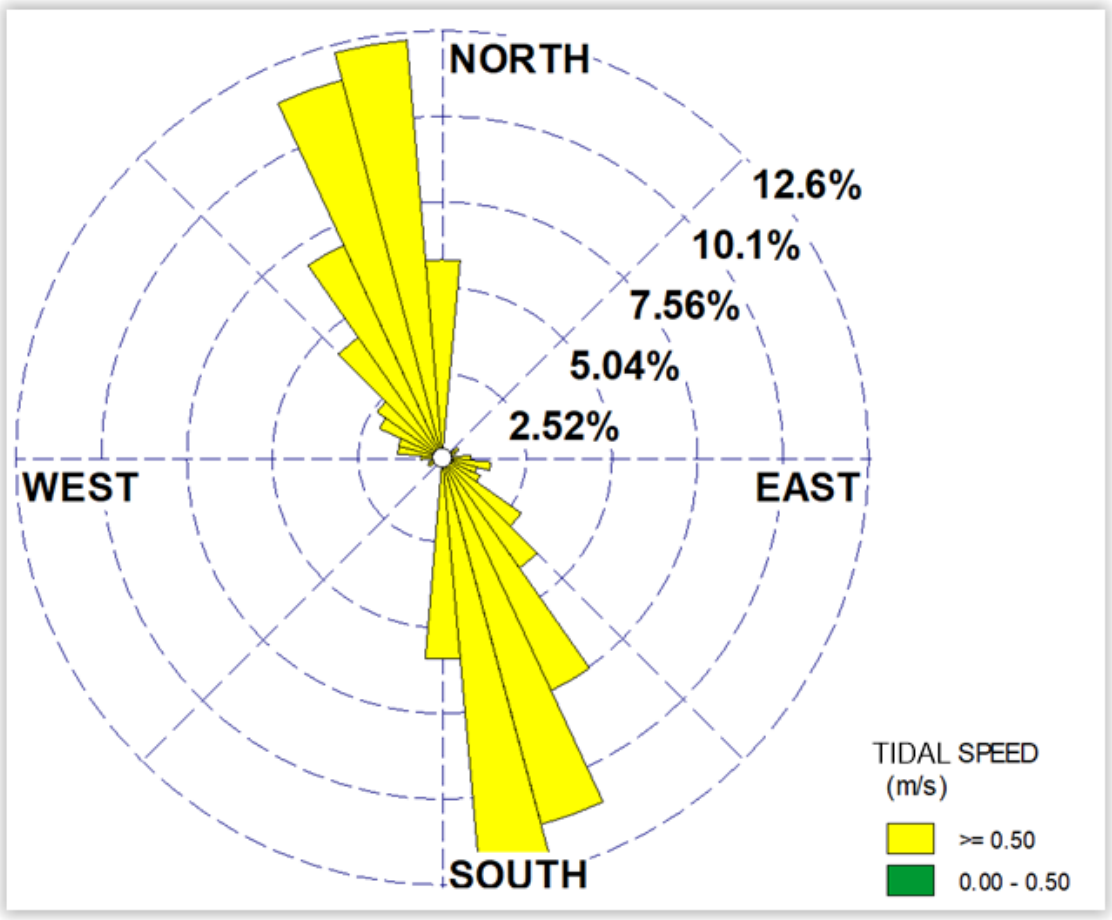

Figure 7-5: Tidal Rose of Terawhiti

Tidal distribution speed of Terawhiti (Figure 7-6), shows a big difference in amount of calm range (less than 0.5 m/s speed). While it is for Foveaux is %39.1, for Terawhiti is only %3.1.

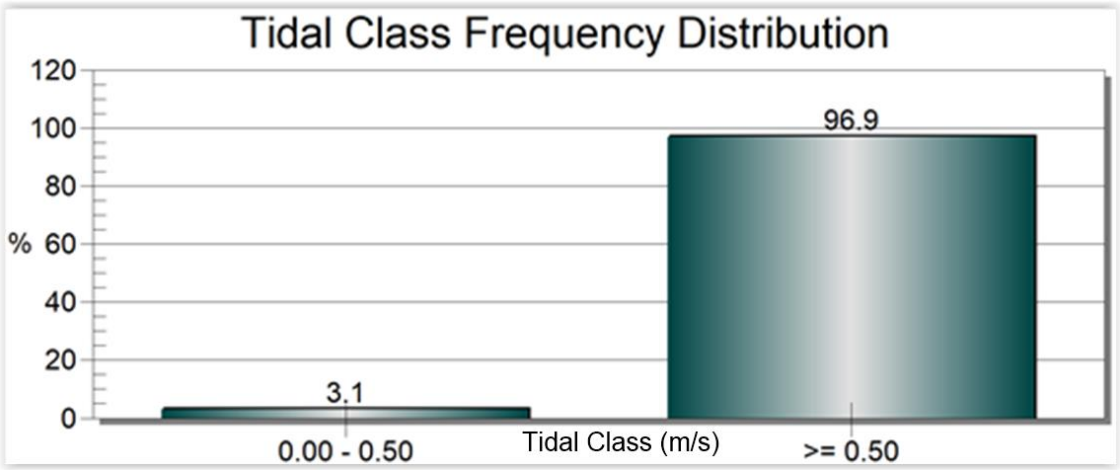

Figure 7-6: Tidal distribution for different speeds in Terawhiti

These values for 3 April 2020(as an example) for Foveaux are presented in Table 7-1 and Figure 7-7.

Table 7-1: Eastward and Northward components of Water Velocity for Foveaux at 3 April 2020.

hour	Eastward Velocity (u)	Northward Velocity (v)
0	-0.3	0.3
1	-0.5	0.4
2	-0.5	0.5
3	-0.4	0.4
4	-0.2	0.3
5	0.007	0.04
6	0.3	-0.2
7	0.4	-0.4
8	0.5	-0.5
9	0.5	-0.5
10	0.3	-0.3
11	0.05	-0.090
12	-0.2	0.2
13	-0.4	0.4
14	-0.5	0.5
15	-0.5	0.5
16	-0.3	0.4
17	-0.1	0.1
18	0.2	-0.1
19	0.4	-0.3
20	0.5	-0.5
21	0.5	-0.5
22	0.4	-0.4
23	0.2	-0.2
24	-0.09	0.03

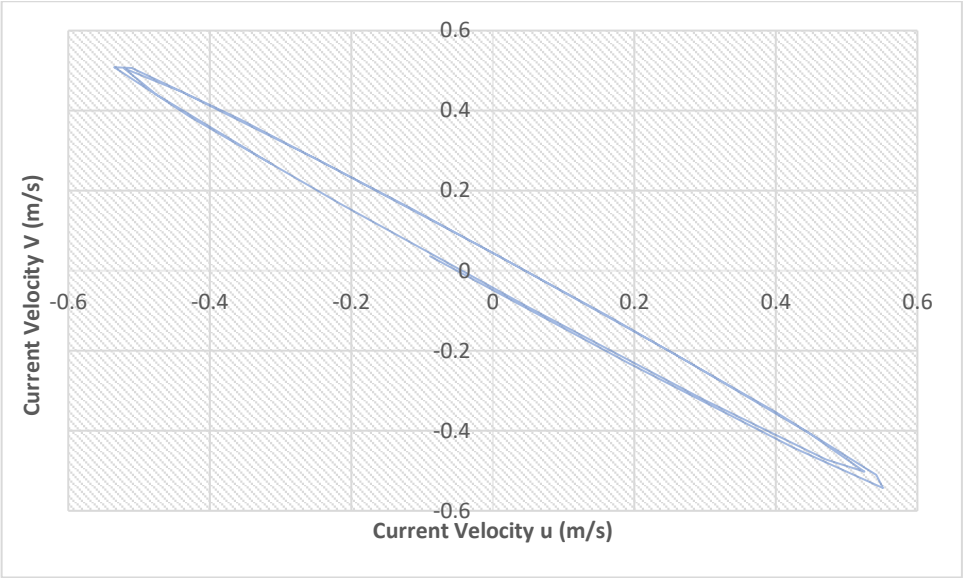

Figure 7-7:Tidal Direction of Foveaux at 3 April 2020.

7.3 Determining the Proper Direction of Turbine Face Based on Wind Blows Results

The yearly hours wind blows from different directions in Stewart Island [155] are shown in Figure 7-8. It is generated from a wind model commissioned by Stewart Island Electricity Supply (SIESA) for Mamaku point at Stewart Island. The wind model adopts local Stewart Island meteorological records according to terrain elevation and exposure.

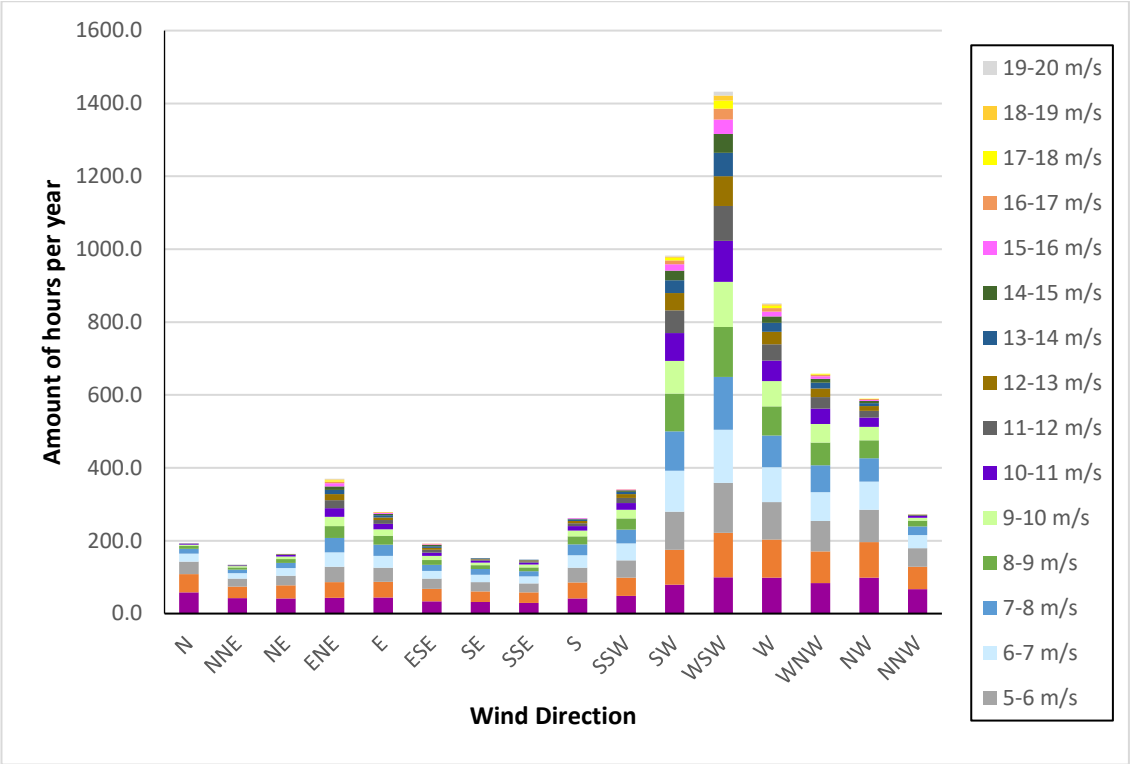

Figure 7-8: The yearly hours wind blows from different directions for different speeds.

Figure 7-9 shows the percentage of year when wind blows within direction ranges. The maximum percentage can be seen in WSW (%16.3), SW (%11.2) and W (%9.7) direction respectively.

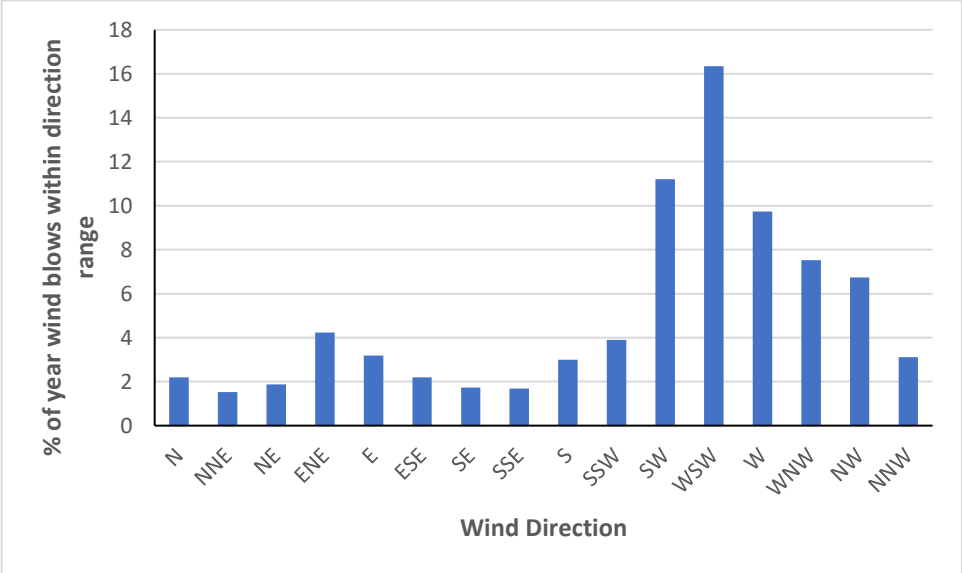

Figure 7-9: The percentage of year when wind blows within direction ranges

Figure 7-10 shows the annual wind run obtained while turbine generates, within specified direction range. The maximum wind run can be seen in WSW (46,477 km/year), SW (29,546 km/year) and W (24,216 km/year) direction respectively.

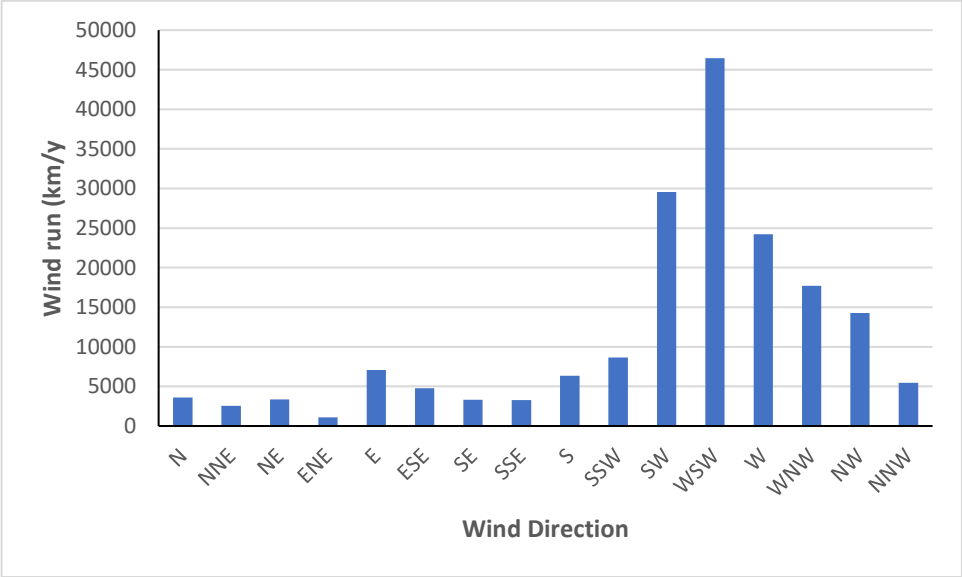

Figure 7-10: the annual wind run obtained while turbine generates, within specified direction range.

Figure 7-11 shows the annual power output obtained within operating range at which turbine generates for specified direction ranges. The maximum wind run can be seen in WSW (32,299 kWhours/year), SW (20,111 kWhours/year) and W (15,622 kWhours/year) direction respectively.

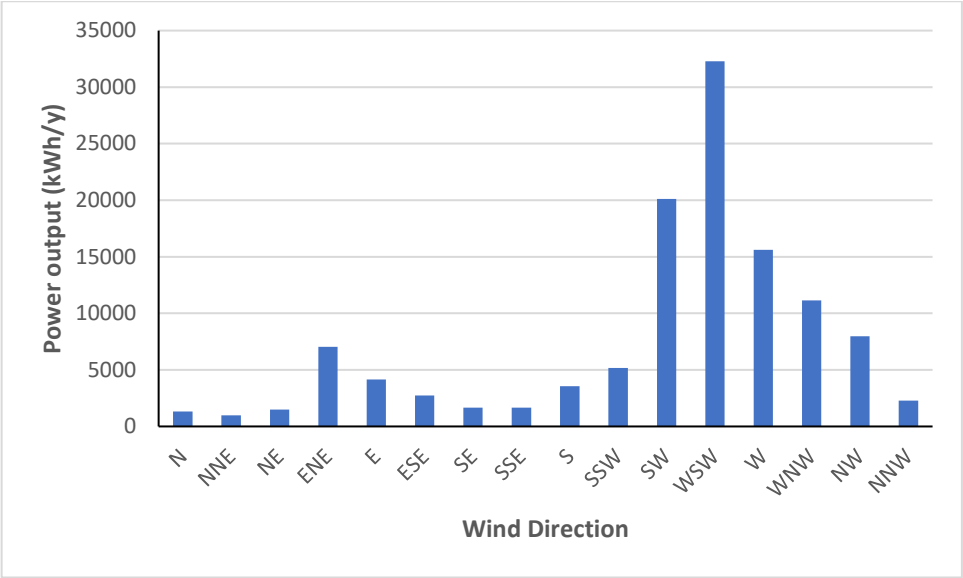

Figure 7-11: the annual power output obtained while wind turbine generates, within specified direction range.

So, maximum wind power can be generated in WSW and SW directions.

7.4 Determining the Proper Direction of Turbine Face Based on Tidal Flows Results

The examples of the ocean tide data from the TPXO9 model [31] over the period between 1st and 7th of January 2020 and year 2020 (with 1-hour data sampling interval) are shown in Figure 7-12 and Figure 7-13.

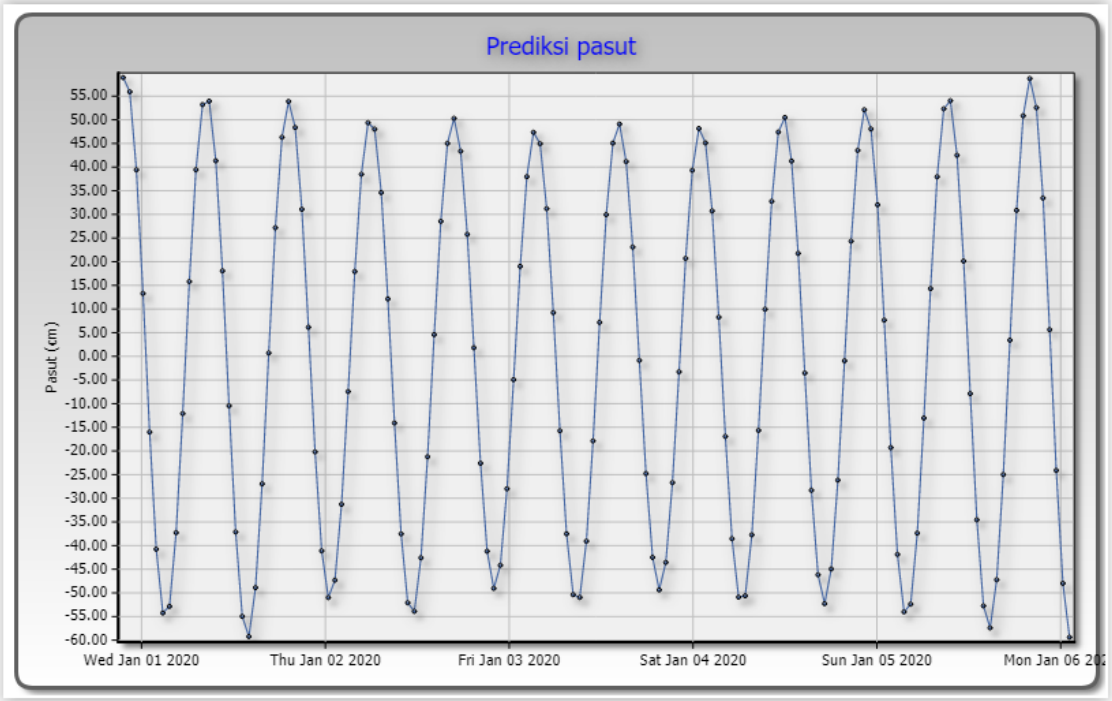

Figure 7-12: The TPXO9 Results for Foveaux between 1st and 7th of January,2020 (1-hour data sampling interval).

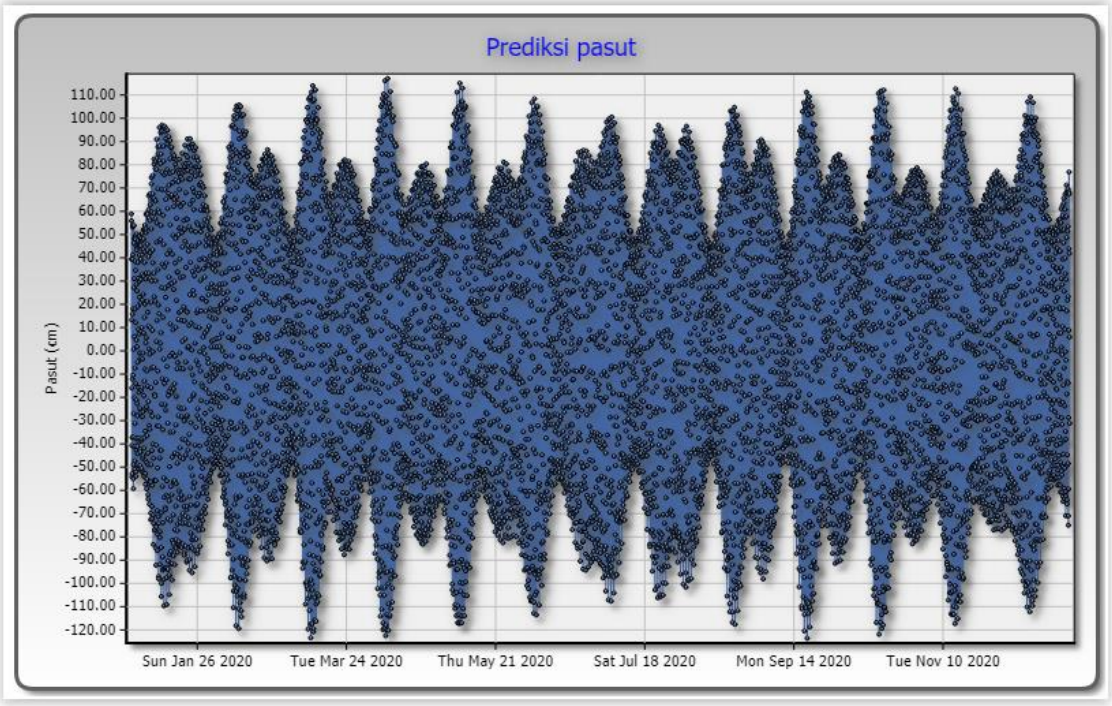

Figure 7-13: The TPXO9 Results for Foveaux in year,2020 (1-hour data sampling interval).

Based on NIWA ‘s Goring model results, the yearly hours tidal flows from different directions in Foveaux are shown in Figure 7-14. NW and SE with 3776 and 3772 hours per year are prominent directions.

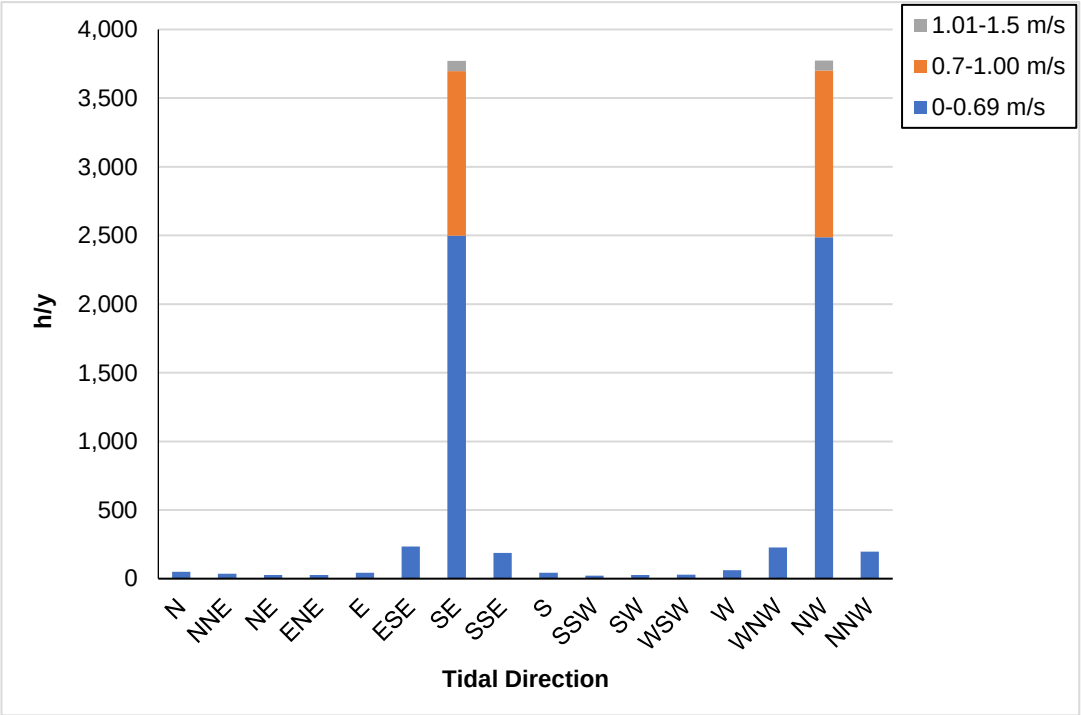

Figure 7-14: The yearly hours tidal flows from different directions in Foveaux.

Figure 7-15 shows the percentage of year when tide flows within direction ranges. About %90 of tidal flow is from NW, with %43.11, and SE with %43.06.

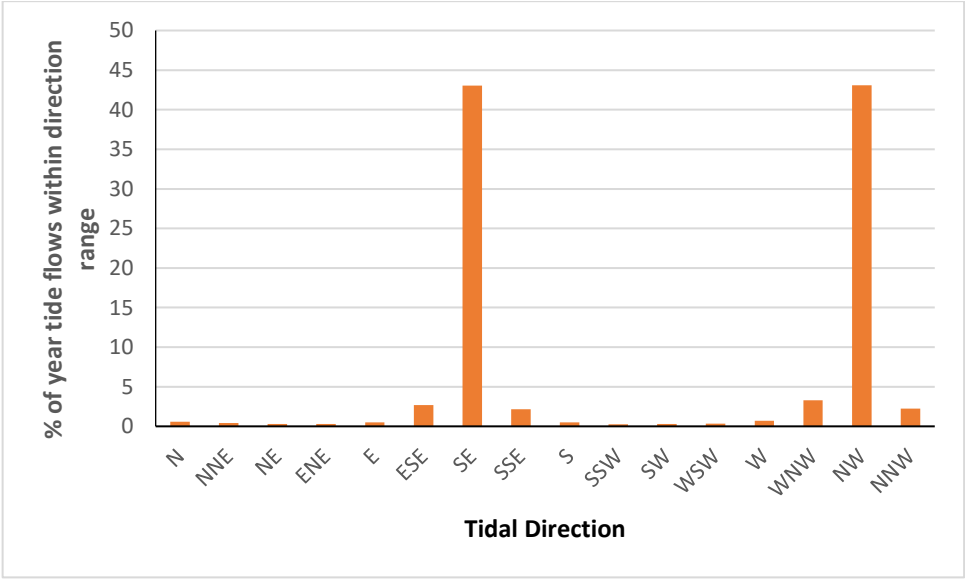

Figure 7-15: The percentage of year when tide flows within direction ranges in Foveaux.

Figure 7-16 shows the annual tide run at instantaneous speed, within specified direction range. From this Figure, it can be seen that SE and NW directions with 10924 and 10936 km/year tidal run are superior.

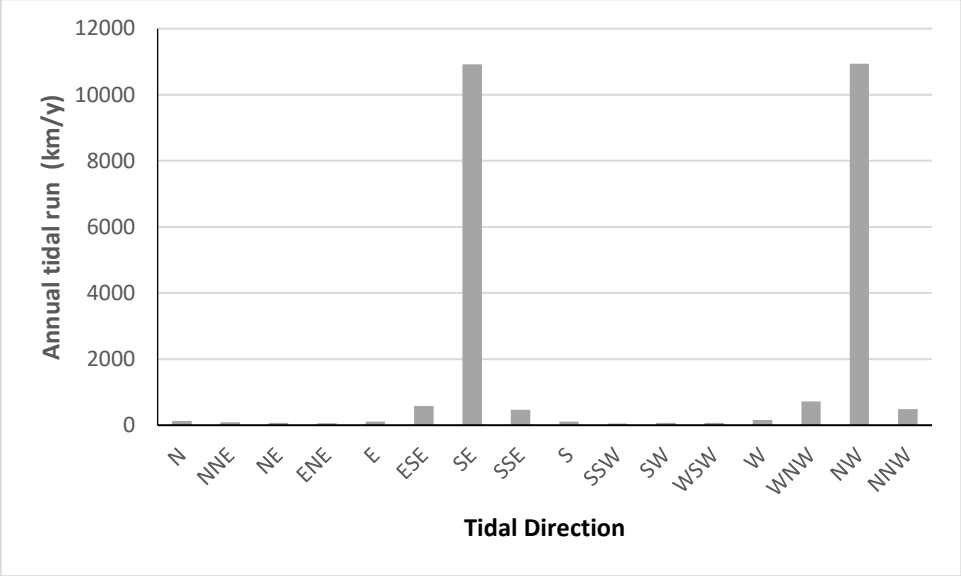

Figure 7-16: Annual tide run obtained when tide flows, within specified direction range in Foveaux.

Figure 7-17 shows the annual power output obtained while turbine generates, within specified direction range. It indicates that power generation in SE and NW directions is only 4341 and 4362 kWhours/year respectively.

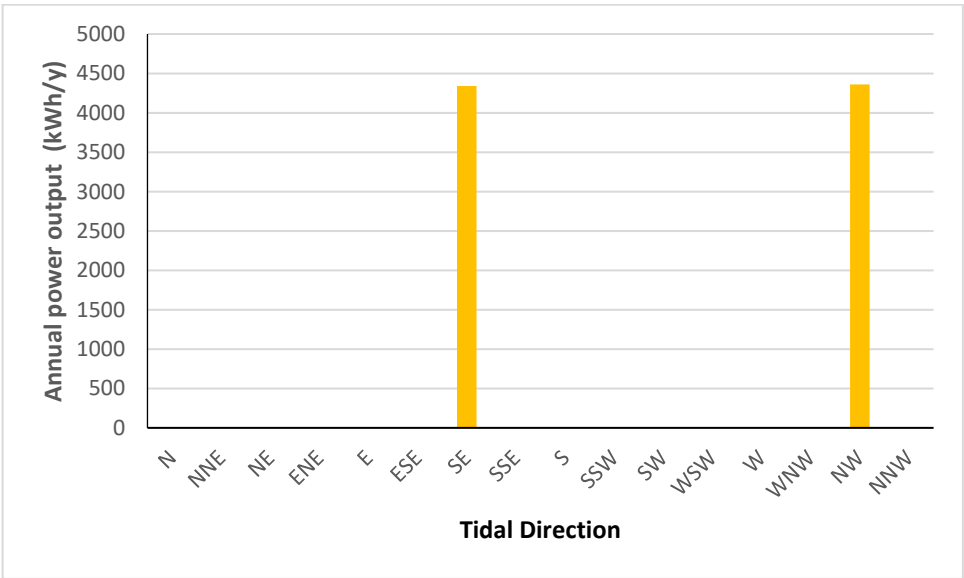

Figure 7-17: The annual power output obtained while tidal turbine generates, within specified direction range in Foveaux.

So, tidal power can only be generated in SE and NW directions.

7.5 Tidal Pattern in Terawhiti

The examples of the ocean tide data from the TPXO9 model [31] over the period between 1st and 7th of January 2020 and year 2020 (with 1-hour data sampling interval) are shown in Figure 7-18 and Figure 7-19.

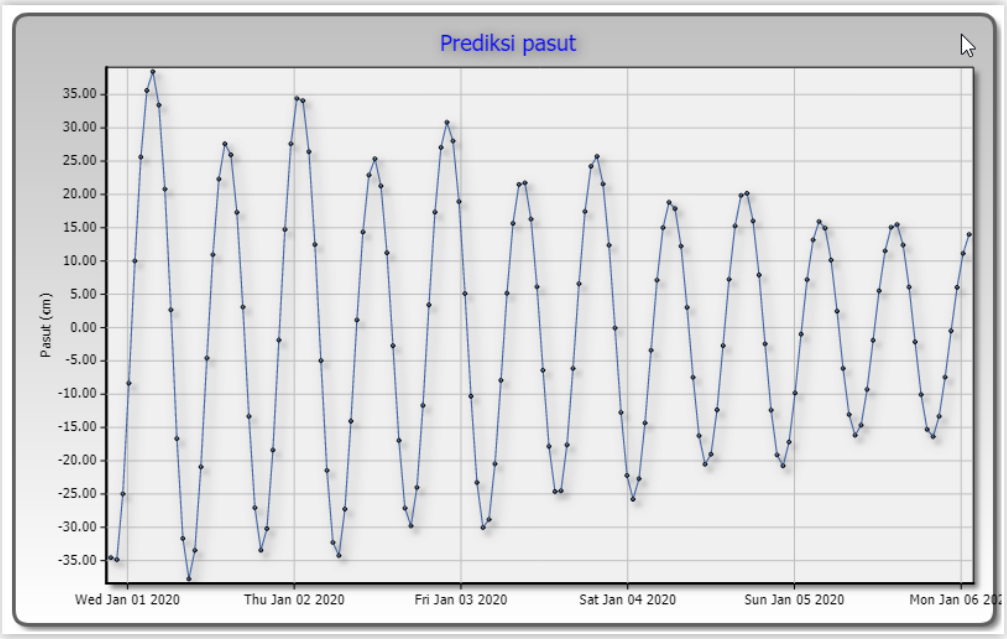

Figure 7-18: The TPXO9 Results for Terawhiti between 1st and 7th of January,2020 (1-hour data sampling interval).

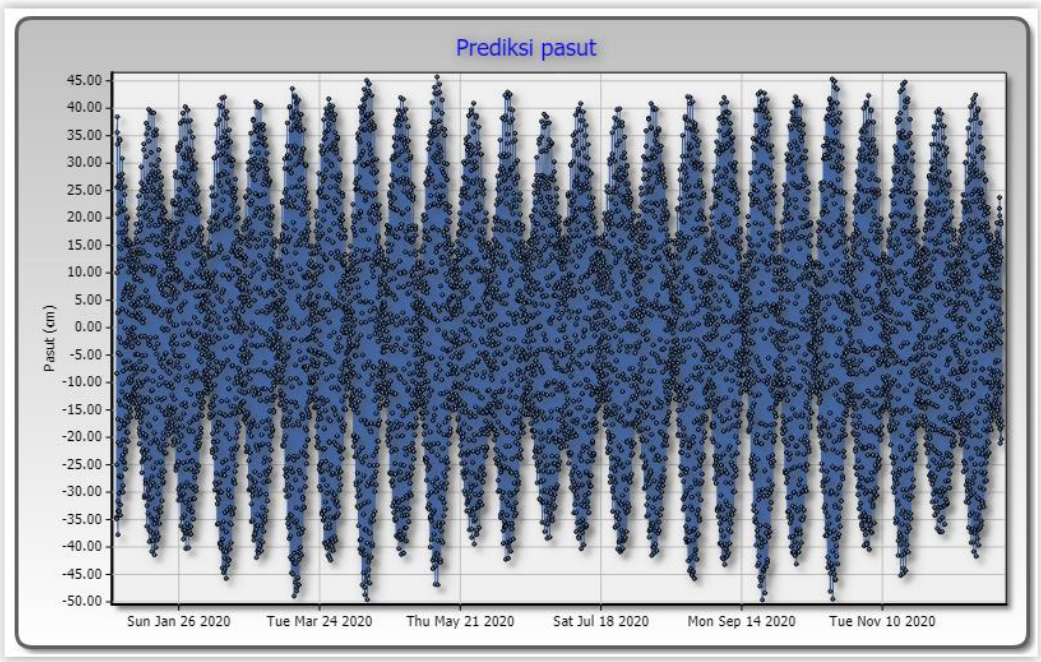

Figure 7-19:The TPXO9 Results for Terawhiti in year,2020 (1-hour data sampling interval).

While, results of section 7.4 shows the direction of tidal flow for Foveaux which found unsuitable for microgrid design based on Chapter 5, it also indicates the poor tidal generation in south of Southern Island. Tidal flow of Terawhiti in different directions in this section will be analyzed to cover this lack. Comparing the results of Figure 7-20 with what was shown before in Figure 7-14, shows the tidal speed in Terawhiti is much higher than Foveaux.

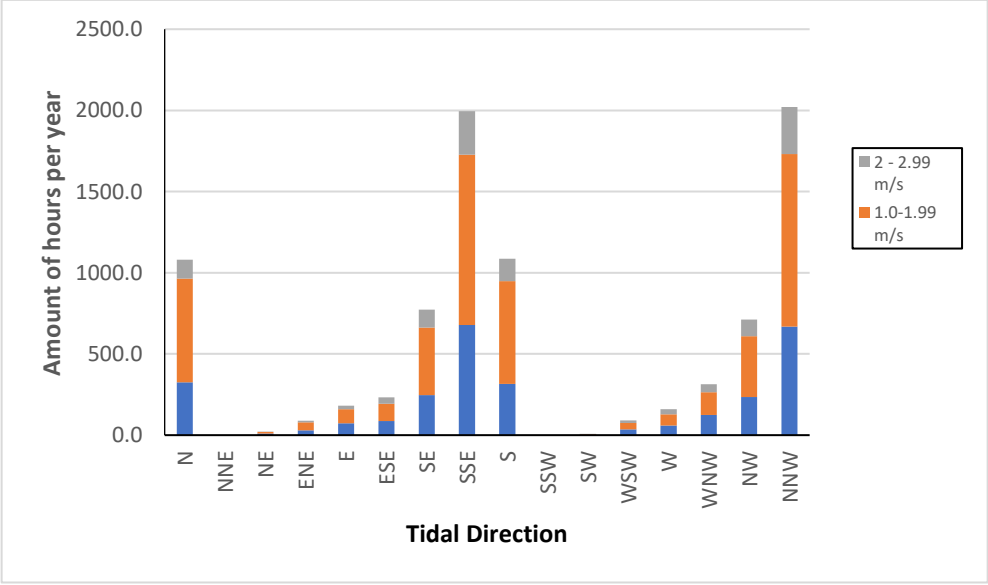

Figure 7-20: The yearly hours tidal flows from different directions in Terawhiti.

Figure 7-21 shows the percentage of year when tide flows within direction ranges. The highest percentage can be seen in NNW (%23.06) and SSE (%22.77) directions.

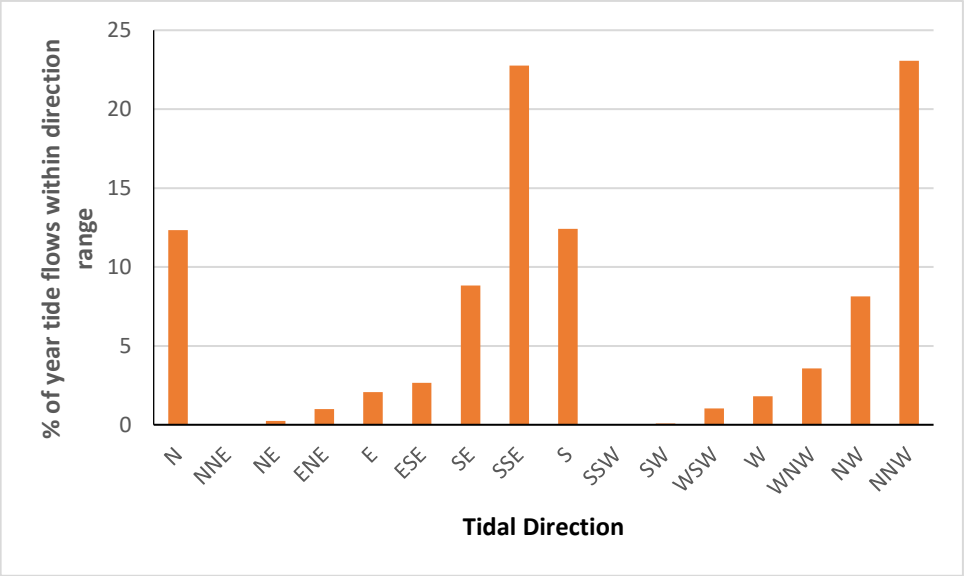

Figure 7-21: The percentage of year when tide flows within direction ranges in Terawhiti.

Figure 7-22 shows the annual tide run at instantaneous speed, within specified direction range which again NNW and SSE directions with 9540 and 9293.4 km/year tidal run are superior.

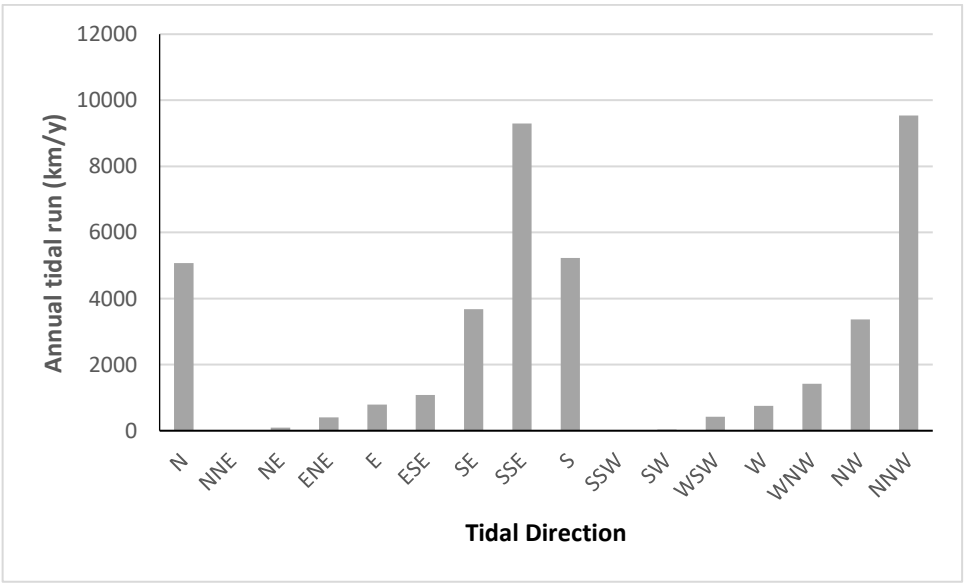

Figure 7-22: Annual tide run obtained when tide flows, within specified direction range in Terawhiti.

Figure 7-23 shows the annual power output obtained while turbine generates, within specified direction range. It indicates that highest power generation is in NNW and SSE directions with 16400 and 15840 kWhours/year respectively.

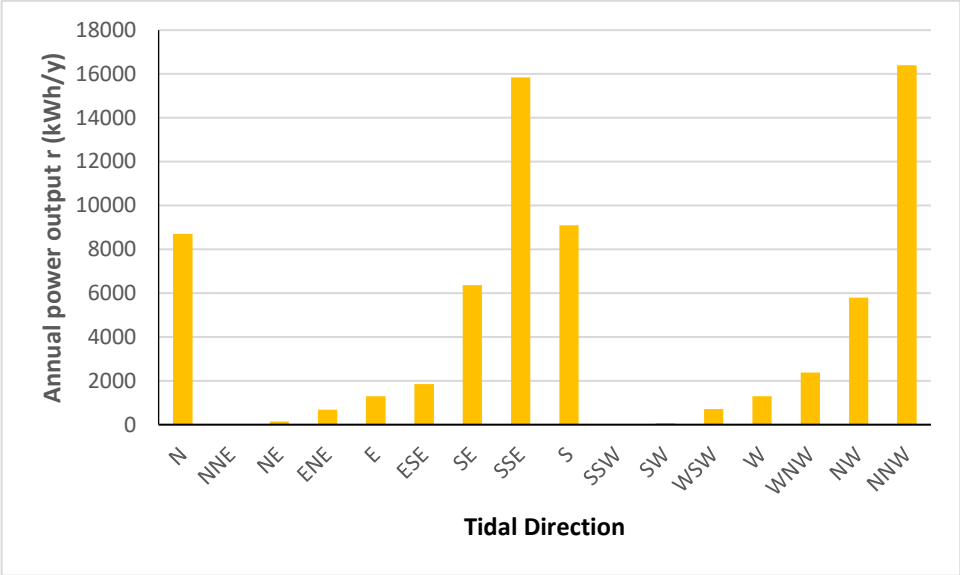

Figure 7-23: The annual power output obtained while tidal turbine generates, within specified direction range in Terawhiti.

Looking at Figure 7-20 to Figure 7-23 and tidal rose of Terawhiti (Figure 7-5) and comparing results with tidal pattern in Foveaux, indicates that while superior tidal direction in Foveaux is NW-SE and in Terawhiti NNW-SSE, however the power capacity in Terawhiti is about 20 times more than Foveaux.

7.6 Effect of Reducing Cut-in Speed in Tidal Turbines

The speed at which turbines start to turn while there is insufficient torque is called the cut-in speed. Cut-in speed is an important parameter in design of a system to provide the electricity demand of any site. Tidal flows less than 1 ms^{-1} in most of the turbines can not generate electricity. Also, the selection of turbine needs to be compatible to strength of tidal power. This means that to select a turbine, it is necessary to look at tidal currents of site at first and then according to power curves of tidal turbines, select a suitable turbine. In this study, Foveaux Strait in south of

New Zealand is analysed. Based on tidal flows of Foveaux, the results will show how the cut-in speed can affect power generation. According to characteristics of Foveaux, two tidal turbines (Schottel 70 kW and Schottel 54 kW) are compared in this section to show how a turbine with lower cut-in speed can make a big difference in power generation. The pertinent details for the tidal turbines for analysis in this section are set out in Table 7-2.

Table 7-2: Tidal turbines details [29].

Parameter	Schottel [70 kW]	Schottel [54 kW]
Rated Capacity (kW)	70	54
Cut-in Speed (ms^{-1})	0.9	0.7
Cut-out Speed (ms^{-1})	6.75	4.6
Rated Power at (ms^{-1})	3.8	2.6
Swept Area (m^2)	7.06	7.06
Rotor Diameter (m)	3	3

Figure 7-24, which is plotted with WRPLOT [30], indicates a NW-SE direction for tidal currents. It categorized in three tidal class: Current speeds of 0-0.7 m/s when electricity can not be generated in both tidal turbines, 0.7-0.9 m/s when electricity is produced in only Schottel 54 kW and, more than 0.9 m/s when electricity.

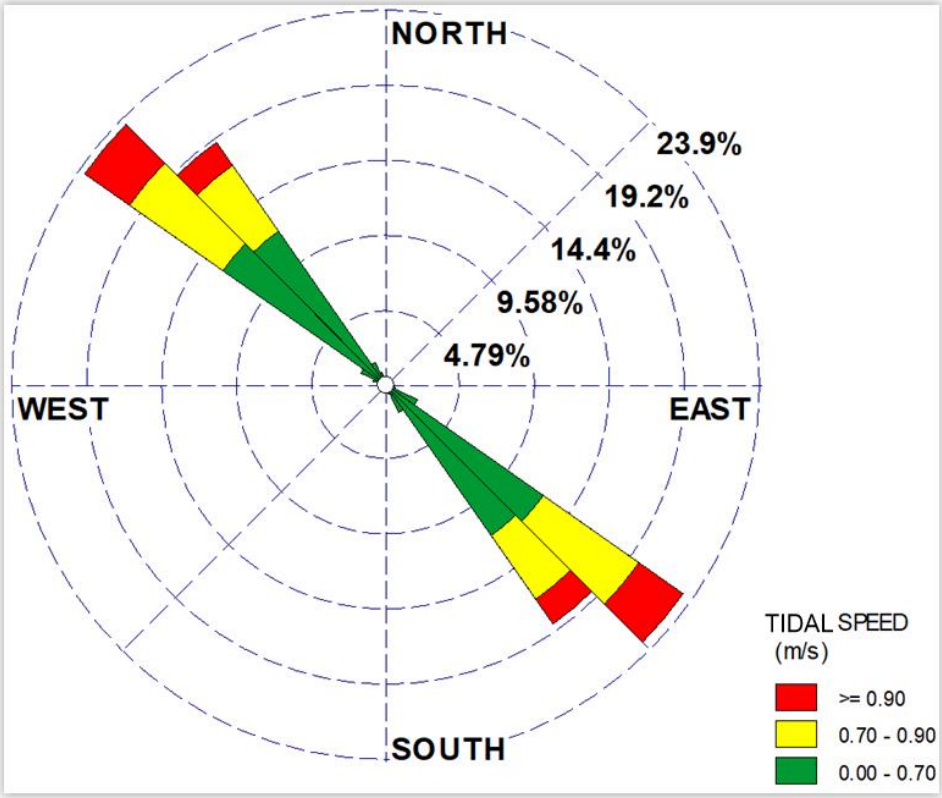

Figure 7-24: Tidal Rose of Foveaux

Figure 7-25 shows the tidal distribution for different speeds in Foveaux. It indicates that 35.4% of tidal currents are more than 0.7 m/s when a Schottel 54 kW can generate electricity, while using Schottel 70 kW makes electricity generation possible for only 10.6% of tidal currents.

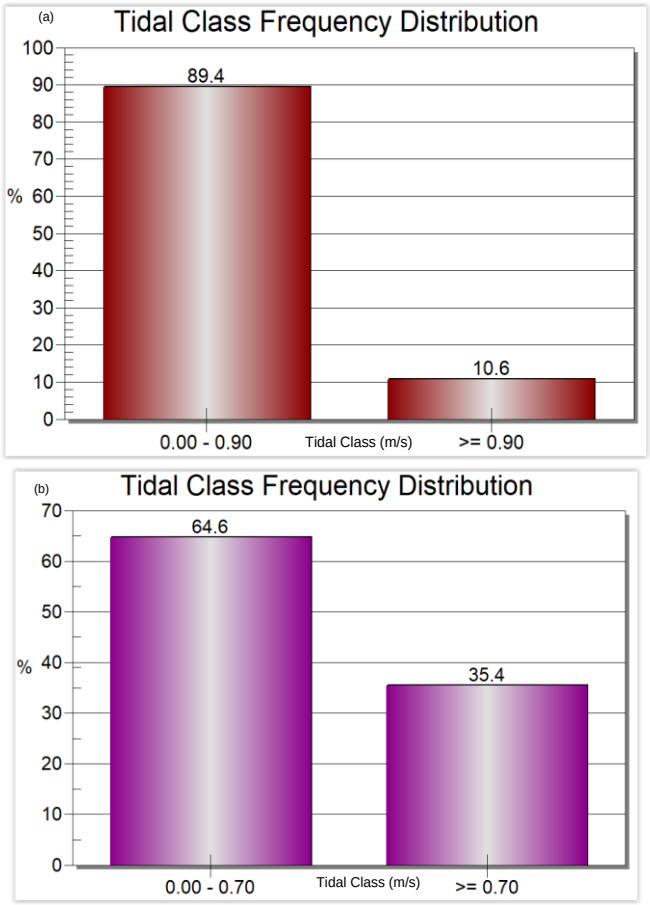

Figure 7-25: Tidal distribution for different speeds in Foveaux using Schottel (a) 70 kW, (b) 54 kW

Figure 7-26 shows the annual tide run at instantaneous speed, within specified direction range. From this Figure, it can be seen that SE and NW directions with 7,128 and 7,120.8 km/year tidal run are superior using 70 kW turbine. Changing turbine to 54 kW increases these values to 10,924 and 10,936 km/year respectively.

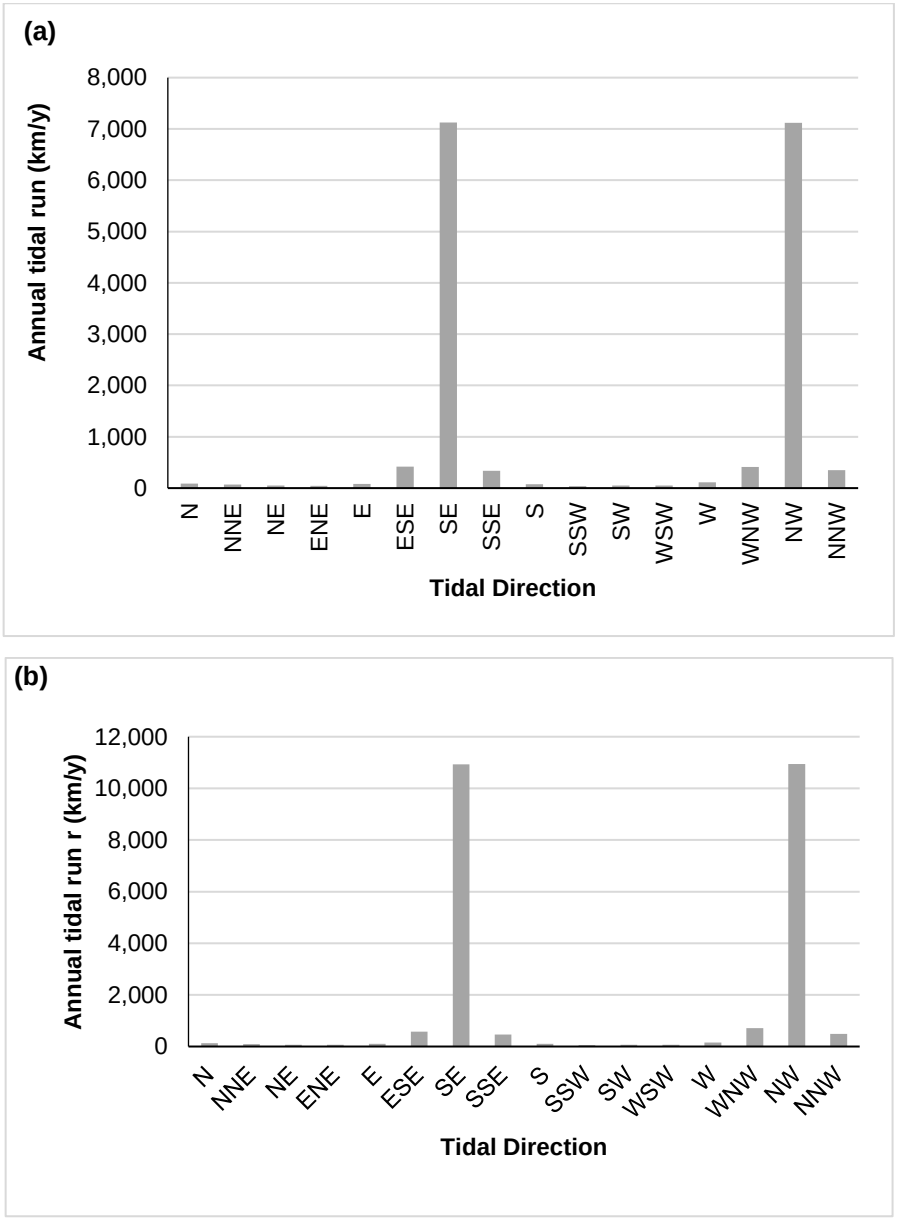

Figure 7-26: Annual tide run obtained when tide flows, within specified direction range in Foveaux using Schottel (a) 70 kW, (b) 54 kW.

Figure 7-27 shows the annual power output obtained while turbine generates, within specified direction range. It indicates that power generation in SE and NW directions for 70 kW turbine is only 940 and 900 kWhours/year respectively. Changing turbine to 54 kW increases these values to 4,341 and 4,362 kWhours/year respectively

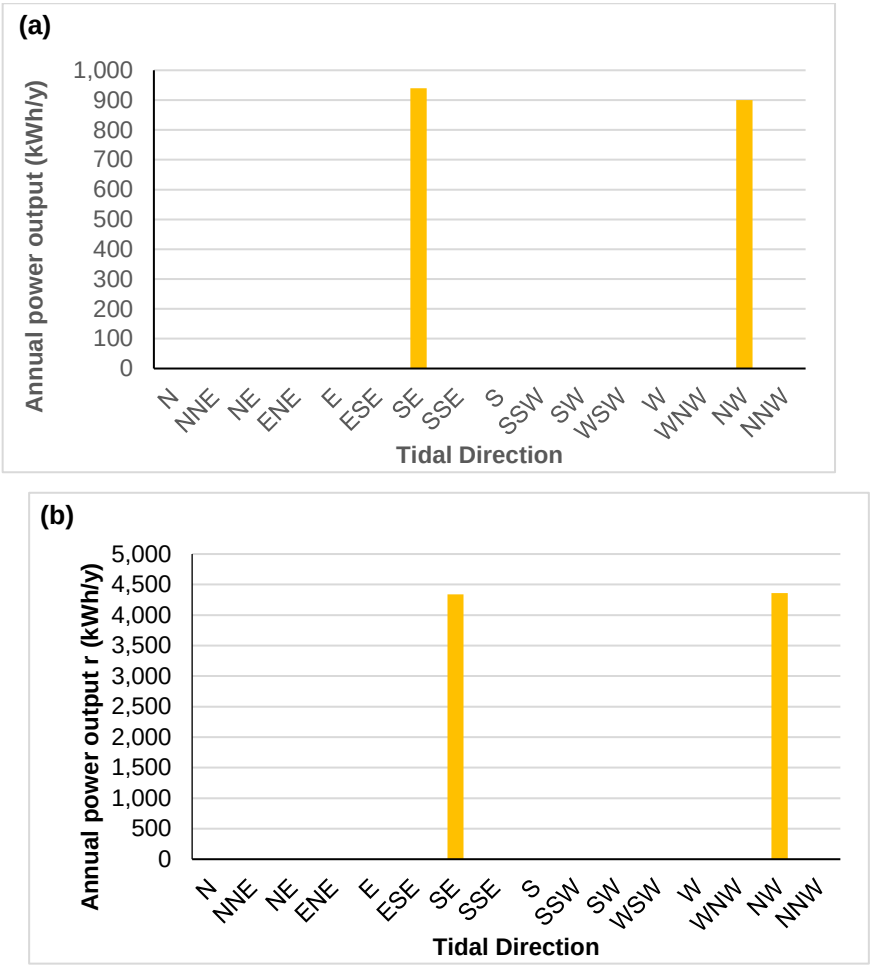

Figure 7-27: The annual power output obtained while tidal turbine generates, within specified direction range in Foveaux using Schottel (a) 70 kW, (b) 54 kW.

The cut-in speed of Schottel 54 kW tidal is 0.7 ms^{-1} which is 0.2 ms^{-1} less than 70 kW turbine. This means in the range of 0-0.69 ms^{-1}, power generation is zero. Using this turbine increases electricity generation 4.7 times more in comparison of Schottel 70 kW tidal turbine. Considering this point is important that rated capacity of 70 or 54 kW is achievable only after rated speed which according to Table 7-2 is 2.6 and 3.8 ms^{-1} for Schottel 54 and 70 kW respectively. Definitely, the rated water speed of 2.6 ms^{-1} is rarely occurs during a year. That is why it is important to consider a turbine at lower cut-in speed.

7.7 Yaw Control Strategy

The analysis of the preceding section was based on application of tidal yaw strategies, analogous to that used in wind turbines.

Various yaw control strategies could be employed for tidal turbines. These include Fixed Yaw (e.g. MCT SeaGen [221]), Slack-tide Yaw (e.g. Alstom/GE DEEP-Gen IV[222]) and Continuous Yaw (e.g. Delta Stream [223]).

For fixed yaw, each turbine generates power only when incident flow is close to normal to the turbine which limits operation to during tides with headings differing by 180°[224].

And the nacelle remains fixed but pitching of the blades enables the turbine to generate power on both the ebb and flood of a bi-directional tide [22].

In slack-tide yaw, the turbine nacelle only yaws during a slack tide, defined in the model as the local minimum in current velocity $d^2U=dt^2 > 0$). The turbine is orientated to the heading which will maximize energy yield during the subsequent half tidal period (i.e. the time between two slack tides) and this is based on the power curve of a single turbine. In reality, this strategy would require accurate prediction of the heading for the next half-tidal cycle [22].

For both fixed and slack-tide yaw strategies, misalignment, θ of onset flow to the turbine axis is accounted for by resolving the component of velocity onto the turbine axis. As shown in [225], C_P then remains constant for up to $\theta = \pm 7{:}5°$, such that power from the turbine is given by Equation (7-1) [224].

$$P = \frac{1}{2} C_P \rho A (U_0 \cos\theta)^3 \tag{7-1}$$

For continuous operation the turbine is always orientated normal to the incident flow. This is analogous to the typical operation of a wind turbine. Each method is depicted in Figure 7-28 [224].

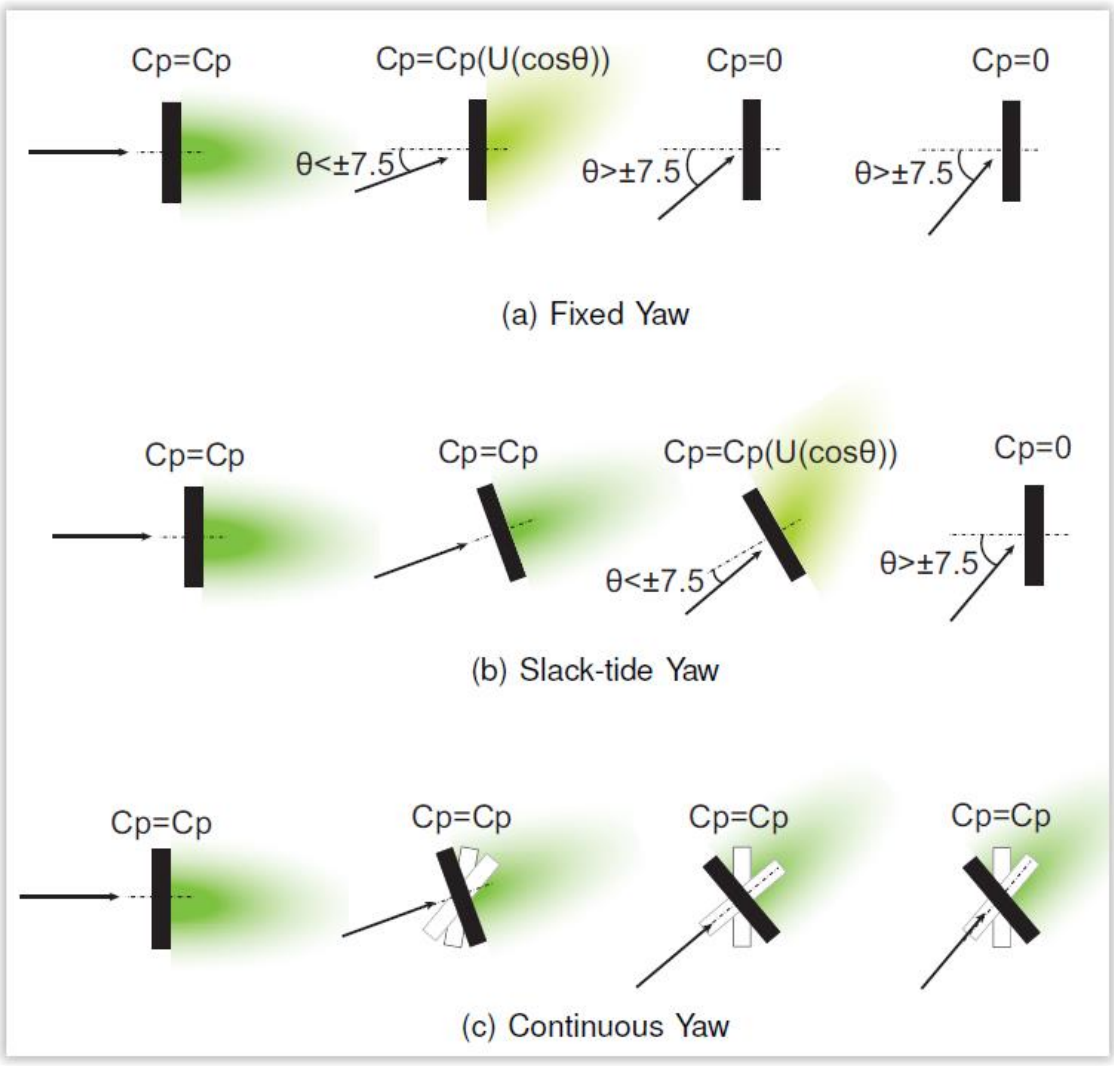

Figure 7-28: Implementation of different yaw control strategies.

The results by Sudall [22, 224] indicates that a fixed mechanism will give an equally good capacity factor & energy yield, at a site where tidal flow is bi-directional. However, a slack-tidal yaw mechanism will give an acceptably high capacity factor & energy yield, at a site where tidal flow direction varies.

So, fixed yaw applies for tidal flows over a narrow arc (≤15°) like Foveaux (see Figure 7-3) and slack-tide yaw applies for tidal flow over an intermediate arc like Terawhiti (see Figure 7-5) and continues yaw applies for tidal flows over a wide arc.

7.8 Conclusion

This chapter investigated climate models for predicting generated wind power in different wind patterns in Foveaux and Terawhiti.

Stewart Island was selected as a case study because it is typical of isolated coastal communities in New Zealand, which depend on small locally operated diesel power stations or single-household petrol generators. Based on the selection of turbine and Foveaux as facility sites and by including the resource data of the wind speed, the design provides the capacity of wind energy from different directions. Applying control mechanisms and the operation of yaw systems maximize wind power extraction from different wind directions. To do this, NIWA and MetOcean models were used to find Foveaux and Terawhiti as the optimized sites. Then, Global Wind Atlas was used to plot wind rose of current wind patterns. WRPLOT view software was used to plot wind frequency distribution downloaded from NASA Surface Meteorology and Solar Energy database. An industry-recognized simulation software package, Homer Pro, was used to import wind speeds from the NASA Surface Meteorology and Solar Energy database.

The results, as presented and discussed in this chapter, enable several conclusions:

- There is enough wind to generate electricity for 90% of the year at the Foveaux site. However, this site is on the other side of Foveaux Strait, 40 km away from Stewart Island´s community at Oban.
- The design can be optimised in a way that enables Stewart Island´s power to be supplied partly from renewable sources. Simulation of various climate models shows several directions, which look promising. The maximum wind power can be generated in WSW and SW directions.
- The investigation is worth implementing because it could supply Stewart Island´s power demand from a renewable source, reducing the detrimental effects of using diesel fuel on the environment.
- Decreasing the cut-in speed from 0.9 m/s to 0.7 m/s in Schottel tidal turbine proposed in Foveaux, increases electricity generation 4.7 times more. However, in both Schottel 54 kW and 70 kW tidal turbines, superior power directions are SE and NW.
- The dominant direction for blowing wind in Terawhiti is north and the highest tidal flow directions can be seen in NNW and SSE directions respectively.

Chapter 8

Conclusion

8.1 Research Objective

This research has investigated the integration of two available offshore renewable energy sources -wind and tidal- using a microgrid, to decrease the cost of electricity in the coastal communities and reduce the detrimental effects of fossil fuel on the environment.

8.2 Research Method

A literature review was carried out first (Chapter 2). After identifying offshore sites where renewable energy resources are sufficient to install a hybrid system, the technical design of a hybrid system suitable for the sites, including a microgrid for electrical linkage, and generate enough power to supply a node in grid and a remote community isolated from a main or mini-grid and whether such a system is economical to install, operate, and maintain has followed.

Stewart Island was selected as a case study for offgrid design because it is typical of isolated coastal communities in New Zealand which depend on small locally-operated diesel power stations or single-household petrol generators. Also, Terawhiti in Cook Strait was selected for grid-connected design. Renewable energy sources close to the sites were initially evaluated using RETScreen the Goring tide model was developed by NIWA to show spatial variability of tides around the New Zealand coast. Wind Atlas extrapolates data from a network of meteorologic recorder stations operated by the New Zealand Meteorological Service (NZMS) and the National Institute of Water and Atmosphere (NIWA).

Next, a preliminary hybrid system design was prepared using the simulation software tool Simulink as one of MATLAB products. The design was refined using HOMER Pro® microgrid software, which was developed at the National Renewable Energy Laboratory, was used to configure a detailed design to identify and select components and Python code to find RMS tidal currents and optimized height of tidal turbine.

An initial scoping of energy yield and initial cost for specimen large and specimen small turbines (wind plus tidal) was carried out using the energy yield and cost estimation modules of RETScreen, (Chapter 5, Section 5.4) to estimate power generation according to environmental conditions of selected sites.

Finally, the performance modelling and financial analysis modules of Homer Pro were used to optimize the microgrid design by comparing scenarios composed of small turbines and microgrid components assembled in different combinations and assessing their economic viability (Chapter 5, Sections 5.2 and 5.3).

8.3 Research Findings

The Stewart Island renewable resource investigation (Chapter 7) indicated offshore renewables are the dominant direction for Foveaux is coming from the west (9.7% of the time), west-south-west (16.3% of the time) and south-west (11.2% of the time). Wind speed from these directions is more than the cut-in speed for a specimen turbine (XANT M-21) during 90.5% of the year. Also, resultant flow velocities are always in vice versa directions, NW (43.11% of the time) and SE (43.06% of the time). So, a tidal turbine can work bi-directionally. Tidal speeds from these directions are more than the cut-in speed for a specimen turbine (Schottel 54 kW) during 35.4% of the year. Cook Strait renewable resource investigation (Chapter 7) indicated offshore renewables are the dominant direction for Terawhiti is coming from the north (25% of the time), north-north-west (17% of the time) and south-south-east (15% of the time). Wind speed from these directions is more than the cut-in speed for a specimen turbine (SWT-3.6MW-107m) during 78.2% of the

year. Also, resultant flow velocities are always in vice versa directions, NNW (23.06% of the time) and SSE (22.77% of the time). So, a tidal turbine can work bi-directionally. Tidal speeds from these directions are more than the cut-in speed for a specimen turbine (AR2000) during 69.3% of the year.

The hybrid system design (Chapter 5) identified components of a suitable microgrid design as multiple energy sources (new wind and tidal turbines, with existing diesel generators for back-up), storage devices (new batteries), supply cables (marine connecting to land), and operating equipment (offshore AC to DC converter at support structure, DC to AC converter at a shore station, system controller at diesel generation plant) connecting to the existing supply network.

The initial scoping of energy yield and installation cost (Chapter 5, Section 5.4) found that a single large wind turbine could yield more than enough energy for supply to Stewart Island, which has an annual demand of 1,260 MWh/y. This extra energy yield could be obtained from adding a single sizeable tidal turbine. It also yields more than enough to meet Stewart Island's annual demand. But the cost of installing a significant wind plus a large tidal turbine on monopile at Foveaux site, plus the cost of 40 km marine cable to Stewart Island, is enormous, more than SIESA can afford. The reasons why small turbines (XANT and Schottel) will be a better scenario at the selected Foveaux site are best explained by fluctuations in the SIESA load profile (Chapter 5). The average daily load fluctuates between 106 and 209 kW. Daily demand for the year averages just 3,452.9 kWh/d with a load factor of 0.69. Total demand is just 1,260,332 kWh/yr. In large scale, daily demand of CPK0331(Central Park) node near Cook Strait using EMI (Electricity Market Information) data for the year averaged 891,230.16 kWh/d, with a load factor of 0.51, and the total demand is 325,299,008 kWh/year proved using 36 wind turbines (36W) is the optimized design to produce higher electricity with lower cost in comparison of using only tidal turbines and both wind and tidal turbines.

Power generation results and financial analysis results for various scenarios (Chapter 5, Section 5.2.) revealed:

- There is enough tide for small turbines to generate electricity during 65% of the year at an offshore site close to Stewart Island (referred to as the Foveaux site).
- There is also enough wind for small turbines to generate electricity for 90% of the year at the Foveaux site. However, this site is on the other side of Foveaux Strait, 40 km away from Stewart Island´s community at Oban.
- DC electricity from the offshore Foveaux site can be integrated as a hybrid system with AC electricity from the existing on-shore diesel generators at Oban by using a microgrid design as described in Chapter 5. The design solution is to mount tidal and wind turbines on the same offshore platform with an AC-DC converter, feed power through a DC marine cable to a DC-AC converter at the Stewart Island shore, then through an AC land cable to a system controller at Oban´s diesel generator station.
- The design can be optimized to enable Stewart Island´s power to be supplied in part from renewable sources. Simulation of various component combinations shows several scenarios which look promising. The optimal combination for maximizing renewable generation is two wind and four tidal turbines plus a single diesel generator.

Power generation results and financial analysis results for various scenarios (Chapter 5, Section 5.3.) revealed:

- There are enough tidal currents to generate electricity during 69.3% of the year at an offshore site close to CPK0331 (referred to as the Central Park).
- There is also enough wind speed to generate electricity during 78.2% of the year at the Foveaux site.
- The DC power from the offshore Terawhiti site can be integrated into the national grid at CPK0331 by using the microgrid design as described in Chapter 5.
- The proposed solution is to mount the wind and tidal turbines on the same offshore platform, design a DC linked wind-tidal-battery based microgrid to feed the power through a DC marine cable to a DC-AC converter at the

CPK0331 onshore, then transmit the power through an AC land cable to a system controller at the Central Park station.

Depending on water height less and over 30m, two types of foundation (monopile and floating) evaluated after contacting NIWA and getting long/lat. Different load scenarios of wind and wave imposed to structures to find ULS (ultimate limit state) and calculating the required sizes for each foundation to tolerate against loads. The results for monopile system revealed:

- The proposed transition piece is a steel tube, internal diameter 6.16 meters to fit the top of the monopile, wall thickness 0.083 meters extending 29 meters below platform level, and sheathing top of the monopile. Weight 300 tonnes.
- The proposed foundation is a monopile inserted into the seabed. It will be solid steel, 6 meters diameter and 60 meters long, weighing 700 tonnes. It will project above the seabed for 30 meters (upper 20 meters will insert into the transition piece), and lower 20 meters will be placed in the seabed. The pile will be driven with a hydraulic hammer into the seabed.
- The acting loads are transferred to the foundation; They can be static depending on the total weight of the structure which is calculated analyzed with OPTUM G3 software or dynamic (cyclic) which is investigated by combining wind and wave loads. Applying static loads to structure indicated in occurring minimum displacement from medium sand-MC and loose-sand-MC respectively. ULS design for aerodynamic and hydrodynamic loads from wind and water used to find required dimensions of the pile and based on maximum load of driven scenario. indicates that the maximum load is in is E-3 scenario. Applying loads of this scenario results in acceptable deflection (0.005 m), tilt (0.00012°), and natural frequency (0.34 Hz) for Terawhiti.

The results for floating system revealed:

- The optimized area in Cook Strait is 110 meters depth. 12 meters of structure is under ballast and rest of it under water surface including 25 meters of transition section,15 meters lower cone and 58 meters sub structure. Applying wind and water loads indicated that the required diameter of the

caisson and the embedment depth for maximum scenario of E-3 are 6.9 and 22.07 meters respectively with padeye angle of 50.14°.

8.4 Conclusions

A new method defined for using tidal energy for off-grid and on-grid designs to apply wind and tidal data into a microgrid system in an optimized offshore site. This method is used in two sites that represent highest potential according to moana project of MetOcean company and Goring model of NIWA. It provided the opportunity to compare different design scenarios which are using only wind turbines, using only tidal turbines, and lastly using both wind and tidal turbines. It may reduce the electricity cost and/or increase the total power generation.

Key parts of this work were identifying the optimized scenario of wind, tidal and both wind and tidal systems, using tidal energy with wind for microgrid design and proposing minimum dimensions required to withstand against loads.

Results showed that for offgrid design in Foveaux:

- The optimal scenario consisting of two wind and four tidal turbines (2W+4T) can achieve technical objectives because it could supply 75% of Stewart Island´s power demand from renewable sources, reducing diesel fuel consumption by 60%.
- It is unknown whether the design can be constructed at an affordable cost because the Homer Pro financial analysis module does not include construction or installation.
- Once built and installed on-site, the design can be operated at an affordable cost because the Levelized cost of equipment and resources over project life (21 c/kWh) is lower than the present operation cost (23 c/kWh) of five diesel generators that presently supply power.
- A complete cost-benefit analysis is needed to determine whether the supply authority can recover all construction, installation, operating,

and maintenance/replacement costs from a lower charge to the community than its present retail charge (67 c/kWh).

- In comparison to other scenarios, the proposed system can generate higher power, higher renewable fraction, lower pollutants and more economic.
- To ensure about results, a sensitivity analysis about efficiency of inverter and economical viability performed validated 2W+4T is the optimized scenario.

For ongrid design in Cook Strait

- The offshore renewable sources enable several scenarios to provide the demand of of node CPK0331 (Central Park) with Homer Pro which looks promising. The optimal scenario generating maximizing electricity is thirty-six wind turbines (36W). In comparison to other scenarios, the proposed system results higher renewable fraction in lower COE.
- The renewable output of 68.6% from the 36W scenario is worth implementing comparing other scenarios.
- Once built and installed on-site, the design can be operated at an affordable Levelized cost of 7 c/kWh over the project life which is lower than adding the tidal source.
- To ensure about results, a sensitivity analysis about efficiency of inverter and economic viability was performed and validated that 36W is the optimized scenario.

Identical optimal scenarios can be designed based on the load of load of Stewart Island using SIESA and load of CPK0331 using EMI. Going model of NIWA for both case studies validated with moana project of MetOcean for proposing microgrid designs. Results showed that the optimized scenarios can be designed to reduce the emissions using renewable sources. RF in 2W+4T and 36W are 66% and 68.6% respectively which results in lower amount of emissions from pollutants accordingly.

Next contribution of the research has been achieved by defining a foundation design of integrated wind and tidal structures in shallow and deep-water depths using

monopile and buoy floating respectively. In contrast of foundation design of wind turbines, this design considered the loads of both wind and tidal turbines to determine minimum dimensions required after finding maximum combined loads. Based on monopile design, diameter, thickness, and length of monopile can be 6, 0.083, and 60 meter respectively. In spar buoy floating foundation, the minimum diameter of the caisson and the embedment depth can be 6.9 and 22.07 meter respectively. The maximum load for both type of foundations occurs in extreme wind load scenario when wind and wave act in same direction.

8.5 Recommended Future Works

In conclusion, this research has demonstrated that using a microgrid to integrate tidal energy with other sources of renewable energy such as wind is a technically feasible way to supply power to a small off-grid coastal community and a node connected to national grid while reducing its dependence on non-renewable sources and minimizing its environmental impact of burning fossil fuels.

The research has also identified directions for future work in microgrid design to improve hybrid systems for harnessing offshore renewable energy.

Recommendations for future investigation are:

- Estimating the cost of electricity in terms of wind rose and analysing the wind patterns which can generate electricity with lower cost for customers.
- Estimating the cost of electricity in terms of wind and tidal rose and analysing the tidal patterns which can generate electricity with lower cost for customers.
- The microgrid design by Homer doesn’t consider the foundation cost of wind and tidal turbines. It is estimated adding a large monopile, platform and mast to this system will cause the Levelized cost of supply to exceed significantly the present generating cost. While, in this project separate analyses conducted to find the possibility of foundation design both in shallow and deep water heights, it is still unknown how much these designs

can be cost-effective or affect the calculations done for microgrid design financial wise. Separate research can be conducted for proposed floating system.

References

1. Majdi Nasab, N., et al., *Optimization of a Grid-Connected Microgrid Using Tidal and Wind Energy in Cook Strait.* Fluids, 2021. **6**(12): p. 426.
2. Nasab, N.M., J. Kilby, and L. Bakhtiaryfard, *Case Study of a Hybrid Wind and Tidal Turbines System with a Microgrid for Power Supply to a Remote Off-Grid Community in New Zealand.* Energies, 2021. **14**(12): p. 3636.
3. Nasab, N.M., J. Kilby, and L. Bakhtiaryfard, *The Potential for Integration of Wind and Tidal Power in New Zealand.* Sustainability, 2020. **12**(5): p. 1-21.
4. Nasab, N.M., J. Kilby, and L. Bakhtiaryfard, *Comparative Critique on Power Generation in Wind Turbines.* Chemical Engineering Transactions, 2019. **76**: p. 883-888.
5. Nasab, N.M., J. Kilby, and L. Bakhtiaryfard, *Wind Power Potential Assessment for Three Locations in New Zealand.* Chemical Engineering Transactions, 2020. **81**: p. 73-78.
6. Nasab, N.M. and J. Kilby, *Feasibility Study: Effect of Tidal Turbines Cut-in Speed for Power Generation in New Zealand.* Chemical Engineering Transactions, 2021. **88**: p. 13-18.
7. Nasab, N.M., J. Kilby, and L. Bakhtiaryfard. *Effect of rotor length on generating power in horizontal axis wind turbines*. in *IOP Conference Series: Earth and Environmental Science*. 2020. IOP Publishing.
8. Nasab, N.M., J. Kilby, and L. Bakhtiaryfard. *Effect of Number of Blades on Generating Power In Wind Turbines*. in *2019 29th Australasian Universities Power Engineering Conference (AUPEC)*. 2019. IEEE.
9. *World Energy Outlook 2019-Flagship Report-November 2019*. [cited 2021 7 November]; Available from: https://www.iea.org/reports/world-energy-outlook-2019.
10. Algarvio, H., F. Lopes, and J. Santana, *Strategic Operation of Hydroelectric Power Plants in Energy Markets: A Model and a Study on the Hydro-Wind Balance.* Fluids, 2020. **5**(4): p. 209.
11. Saad Al-Sumaiti, A., et al., *Economic Assessment of Distributed Generation Technologies: A Feasibility Study and Comparison with the Literature.* Energies, 2020. **13**(11): p. 2764.
12. Fernandez, M.A. and A.J. Daigneault, *A double win: new pathways to reduce greenhouse gas emissions and improve water quality in New Zealand.* Environmental Research Letters, 2020. **15**(7): p. 074004.
13. *New Zealand's Greenhouse Gas Inventory*. 2021, Ministry for the Environment: New Zealand.
14. Ndebele, T., *Assessing the potential for consumer-driven renewable energy development in deregulated electricity markets dominated by renewables.* Energy Policy, 2020. **136**: p. 111057.
15. ea, *Electricity in New Zealand*. 2018, Electricity Authority.
16. Roy, L., et al., *Double-Multiple Streamtube Analysis of a Flexible Vertical Axis Wind Turbine.* Fluids, 2021. **6**(3): p. 118.

17. Lu, M.-S., et al., *Combining the wind power generation system with energy storage equipment.* IEEE Transactions on Industry Applications, 2009. **45**(6): p. 2109-2115.
18. Noori, M., M. Kucukvar, and O. Tatari, *Economic input–output based sustainability analysis of onshore and offshore wind energy systems.* International journal of green energy, 2015. **12**(9): p. 939-948.
19. Lande-Sudall, D., T. Stallard, and P. Stansby. *Energy yield for co-located offshore wind and tidal stream turbines*. in *Progress in Renewable Energies Offshore: Proceedings of the 2nd International Conference on Renewable Energies, 2016 (RENEW2016)*. 2016. Taylor & Francis Books Ltd.
20. Lande-Sudall, D., T. Stallard, and P. Stansby, *Energy yield for co-located offshore wind and tidal stream turbines*. Progress in Renewable Energies Offshore: Proceedings of the 2nd International Conference on Renewable Energies, 2016 (RENEW2016). 2016: Taylor & Francis Books Ltd. 675-681.
21. Heptonstall, P., et al., *The cost of offshore wind: Understanding the past and projecting the future.* Energy Policy, 2012. **41**: p. 815-821.
22. Lande-Sudall, D., T. Stallard, and P. Stansby, *Co-located offshore wind and tidal stream turbines: Assessment of energy yield and loading.* Renewable Energy, 2018. **118**: p. 627-643.
23. Gruszczynski A, et al. *Hybrid Offshore Wind and Tidal*. 2017 [cited 2021 8 September]; Available from: http://www.esru.strath.ac.uk/EandE/Web_sites/16-17/WindAndTidal/index.html.
24. Wang, L., et al., *Stability analysis of a microgrid system with a hybrid offshore wind and ocean energy farm fed to a power grid through an HVDC link.* IEEE Transactions on Industry Applications, 2017. **54**(3): p. 2012-2022.
25. Bortolotti, P.T., Helena C Dykes, Katherine L Merz, Karl Sethuraman, Latha Verelst, David Zahle, Frederik, *IEA Wind TCP Task 37: Systems Engineering in Wind Energy-WP2. 1 Reference Wind Turbines*. 2019, National Renewable Energy Lab.(NREL), Golden, CO (United States).
26. *Simulink*. [cited 2021 2 September]; Available from: https://au.mathworks.com/help/simulink/index.html?s_tid=srchtitle_simulink_1.
27. QBlade. *Basic Functionality of Q-Blade software*. 2014 [cited 2019 9 December]; Available from: http://www.q-blade.org/.
28. *RETScreen*. [cited 2020 4 June]; Available from: https://www.nrcan.gc.ca/maps-tools-publications/tools/data-analysis-software-modelling/retscreen/7465.
29. *Homer Pro*. [cited 2020 2 March]; Available from: https://www.homerenergy.com/.
30. *WRPLOT View™ - Freeware*. [cited 2020 8 July]; Available from: https://www.weblakes.com/products/wrplot/index.html.
31. *Tidal Prediction Using TPX09*. [cited 2020 8 December]; Available from: http://oceanomatics.com/.
32. *Python*. [cited 2021 17 January]; Available from: https://www.python.org/.
33. Kanoğlu, M., Y.A. Çengel, and J.M. Cimbala, *Fundamentals and applications of renewable energy*. 2020: McGraw-Hill Education.
34. Lund, H., *Renewable energy strategies for sustainable development.* Energy, 2007. **32**(6): p. 912-919.

35. Evans, A., V. Strezov, and T.J. Evans, *Assessment of sustainability indicators for renewable energy technologies.* Renewable and sustainable energy reviews, 2009. **13**(5): p. 1082-1088.
36. Martínez, M.L., et al., *A systemic view of potential environmental impacts of ocean energy production.* Renewable and Sustainable Energy Reviews, 2021. **149**: p. 111332.
37. Solman, H., et al., *Co-production in the wind energy sector: A systematic literature review of public engagement beyond invited stakeholder participation.* Energy Research & Social Science, 2021. **72**: p. 101876.
38. Sierra-García, J.E. and M. Santos, *Improving Wind Turbine Pitch Control by Effective Wind Neuro-Estimators.* IEEE Access, 2021. **9**: p. 10413-10425.
39. Agency, I.E. *Energy Policies of IEA Countries: New Zealand 2017 Review*. 2017. IEA.
40. *Wind energy to be 20% of NZ generation by 2035* [cited 2021 11 July].
41. Zhang, J., et al., *Comparative analysis of nonlinear dynamic response for offshore wind turbine structures under incoming wind speed.* Ships and Offshore Structures, 2021. **16**(3): p. 326-333.
42. Kang, J., L. Sun, and C. Guedes Soares, *Fault Tree Analysis of floating offshore wind turbines.* Renewable Energy, 2019. **133**: p. 1455-1467.
43. Jeon, S.H., et al., *Dynamic response of floating substructure of spar-type offshore wind turbine with catenary mooring cables.* Ocean Engineering, 2013. **72**: p. 356-364.
44. Hallowell, S.T., et al., *System reliability of floating offshore wind farms with multiline anchors.* Ocean Engineering, 2018. **160**: p. 94-104.
45. Chen, Z. and F. Blaabjerg, *Wind farm—A power source in future power systems.* Renewable and Sustainable Energy Reviews, 2009. **13**(6): p. 1288-1300.
46. Karlõševa, A., et al., *Marine trade-offs: Comparing the benefits of off-shore wind farms and marine protected areas.* Energy Economics, 2016. **55**: p. 127-134.
47. Kaldellis, J. and M. Kapsali, *Shifting towards offshore wind energy—Recent activity and future development.* Energy policy, 2013. **53**: p. 136-148.
48. Peyrard, C. *Offshore wind turbine foundations.EDF R&D . LNHE Laboratoire d Hydraulique St Venant*
Available from: https://docplayer.net/37756517-Offshore-wind-turbine-foundations-christophe-peyrard-edf-r-d-lnhe-laboratoire-d-hydraulique-st-venant.html.
49. Green, R. and N. Vasilakos, *The economics of offshore wind.* Energy Policy, 2011. **39**(2): p. 496-502.
50. Vieira, M., et al., *European offshore wind capital cost trends up to 2020.* Energy Policy, 2019. **129**: p. 1364-1371.
51. *An Innovator's Guide to the offshore wind market*. 2000, SME GROWTH PLATFORM REPORT.
52. Zuo, T., et al., *Collector System Topology Design for Offshore Wind Farm's Repowering and Expansion.* IEEE Transactions on Sustainable Energy, 2021. **12**(2): p. 847-859.
53. Wang, M., et al., *Recent progress on reliability analysis of offshore wind turbine support structures considering digital twin solutions.* Ocean Engineering, 2021. **232**: p. 109168.
54. *Wind energy in Europe: 2021 Statistics and the outlook for 2022-2026*. [cited 2022 4 November]; Available from:

https://windeurope.org/intelligence-platform/product/wind-energy-in-europe-2021-statistics-and-the-outlook-for-2022-2026/.
55. Mikulčić, H., et al., *Energy transition and the role of system integration of the energy, water and environmental systems.* Journal of Cleaner Production, 2021. **292**: p. 126027.
56. *Offshore Wind Power Market Installed Capacity to Reach 94 GW by 2026*. [cited 2022 4 November]; Available from: https://www.globenewswire.com/en/news-release/2022/05/04/2435537/0/en/Offshore-Wind-Power-Market-Installed-Capacity-to-Reach-94-GW-by-2026-Industry-Size-Share-Growth-and-Trends-Forecast.html.
57. Wang, P., et al., *Wind, wave and earthquake responses of offshore wind turbine on monopile foundation in clay.* Soil Dynamics and Earthquake Engineering, 2018. **113**: p. 47-57.
58. Morató, A., S. Sriramula, and N. Krishnan, *Kriging models for aero-elastic simulations and reliability analysis of offshore wind turbine support structures.* Ships and Offshore Structures, 2019. **14**(6): p. 545-558.
59. Kavari, G., M. Tahani, and M. Mirhosseini, *Wind shear effect on aerodynamic performance and energy production of horizontal axis wind turbines with developing blade element momentum theory.* Journal of Cleaner Production, 2019. **219**: p. 368-376.
60. Ke, S., et al., *Aerodynamic performance and wind-induced effect of large-scale wind turbine system under yaw and wind-rain combination action.* Renewable energy, 2019. **136**: p. 235-253.
61. Wen, B., et al., *Design approaches of performance-scaled rotor for wave basin model tests of floating wind turbines.* Renewable Energy, 2020. **148**: p. 573-584.
62. Li, Z., et al., *Aerodynamic and aeroelastic characteristics of flexible wind turbine blades under periodic unsteady inflows.* Journal of Wind Engineering and Industrial Aerodynamics, 2020. **197**: p. 104057.
63. Afsharian, S., P.A. Taylor, and L. Momayez, *Investigating the potential impact of wind farms on Lake Erie.* Journal of Wind Engineering and Industrial Aerodynamics, 2020. **198**: p. 104049.
64. Allan, G., et al., *The economic and environmental impacts of UK offshore wind development: The importance of local content.* Energy, 2020. **199**: p. 117436.
65. Balasubramanian, K., et al., *A novel review on optimization techniques used in wind farm modelling.* Renewable Energy Focus, 2020. **35**: p. 84-96.
66. Barter, G.E., A. Robertson, and W. Musial, *A systems engineering vision for floating offshore wind cost optimization.* Renewable Energy Focus, 2020. **34**: p. 1-16.
67. Dabachi, M.A., A. Rahmouni, and O. Bouksour, *Design and aerodynamic performance of new Floating H-Darrieus Vertical Axis Wind Turbines.* Materials Today: Proceedings, 2020. **30**: p. 899-904.
68. Peng, X., Z. Liu, and D. Jiang, *A review of multiphase energy conversion in wind power generation.* Renewable and Sustainable Energy Reviews, 2021. **147**: p. 111172.
69. Peng, H.Y., H.J. Liu, and J.H. Yang, *A review on the wake aerodynamics of H-rotor vertical axis wind turbines.* Energy, 2021. **232**: p. 121003.
70. Pandit, R., D. Infield, and T. Dodwell, *Operational Variables for Improving Industrial Wind Turbine Yaw Misalignment Early Fault Detection*

Capabilities Using Data-Driven Techniques. IEEE Transactions on Instrumentation and Measurement, 2021. **70**: p. 1-8.
71. Mishnaevsky, L., et al., *Leading edge erosion of wind turbine blades: Understanding, prevention and protection.* Renewable Energy, 2021. **169**: p. 953-969.
72. Liu, Q., Y. Sun, and M. Wu, *Decision-making methodologies in offshore wind power investments: A review.* Journal of Cleaner Production, 2021. **295**: p. 126459.
73. Khan, A., et al., *Analytical review on common and state-of-the-art FR strategies for VSC-MTDC integrated offshore wind power plants.* Renewable and Sustainable Energy Reviews, 2021. **148**: p. 111106.
74. Karanikas, N., et al., *Occupational health hazards and risks in the wind industry.* Energy Reports, 2021. **7**: p. 3750-3759.
75. Kaldellis, J.K., P. Triantafyllou, and P. Stinis, *Critical evaluation of Wind Turbines' analytical wake models.* Renewable and Sustainable Energy Reviews, 2021. **144**: p. 110991.
76. Jiang, Z., *Installation of offshore wind turbines: A technical review.* Renewable and Sustainable Energy Reviews, 2021. **139**: p. 110576.
77. Huynh, P., S. Tungare, and A. Banerjee, *Maximum Power Point Tracking for Wind Turbine Using Integrated Generator–Rectifier Systems.* IEEE Transactions on Power Electronics, 2021. **36**(1): p. 504-512.
78. *New Zealand Energy Strategy 2011–2021*. Ministry of Economic Development: New Zealand. p. 32.
79. mbie, *Energy in New Zealand 2020*. 2020, Markets Evidence and Insights Ministry of Business, Innovation & Employment: New Zealand.
80. *Wind Generation Stack Update*. 2020, Roaring40s Wind Power Ltd: New Zealand.
81. nzwea, *The growing role for Wind Energy in New Zealand's electricity system 2030*. 2012, New Zealand Wind Energy: New Zealand.
82. Evans, P.S., *Hydrodynamic characteristics of macrotidal straits and implications for tidal stream turbine deployment*. 2014, Cardiff University.
83. Mejia-Olivares, C.J., et al., *Tidal range energy resource assessment of the Gulf of California, Mexico.* Renewable Energy, 2020. **155**: p. 469-483.
84. Díaz, H., J.M. Rodrigues, and C. Guedes Soares, *Preliminary assessment of a tidal test site on the Minho estuary.* Renewable Energy, 2020. **158**: p. 642-655.
85. Danao, L.A., B. Abuan, and R. Howell. *Design analysis of a horizontal axis tidal turbine*. in *3rd Asian wave and tidal conference*. 2016.
86. Ewing, F., et al. *A Physics-based prognostics approach for Tidal Turbines*. in *2019 IEEE International Conference on Prognostics and Health Management (ICPHM)*. 2019.
87. Fraenkel, P., *Marine Current Turbines: Exploiting Currents for Large-Scale Power Generation*. 2007: UK.
88. Aly, H.H.H. and M.E. El-Hawary. *State of the art for tidal currents electric energy resources*. in *2011 24th Canadian Conference on Electrical and Computer Engineering(CCECE)*. 2011.
89. Aguayo, M.M., et al., *A mixed-integer programming methodology to design tidal current farms integrating both cost and benefits: A case study in the Chacao Channel, Chile.* Applied Energy, 2021. **294**: p. 116980.
90. Rourke, F.O., F. Boyle, and A. Reynolds, *Tidal energy update 2009.* Applied Energy, 2010. **87**(2): p. 398-409.

91. *Barrage de la Rance Tidal Power*. Available from: https://www.edf.fr/en/the-edf-group/industrial-provider/renewable-energies/marine-energy/tidal-power.
92. Chowdhury, M., et al., *Current trends and prospects of tidal energy technology.* Environment, development and sustainability, 2020: p. 1-16.
93. Liu, L.-q., et al., *The development and application practice of neglected tidal energy in China.* Renewable and Sustainable Energy Reviews, 2011. **15**(2): p. 1089-1097.
94. Zhou, Z., et al. *An up-to-date review of large marine tidal current turbine technologies*. in *2014 International Power Electronics and Application Conference and Exposition*. 2014. IEEE.
95. Zhou, Z., et al., *Developments in large marine current turbine technologies–A review.* Renewable and Sustainable Energy Reviews, 2017. **71**: p. 852-858.
96. *Study on Lessons for Ocean Energy Development*. Available from: http://publications.europa.eu/resource/cellar/03c9b48d-66af-11e7-b2f2-01aa75ed71a1.0001.01/DOC_1.
97. Borg, M.G., et al., *A numerical performance analysis of a ducted, high-solidity tidal turbine.* Renewable Energy, 2020. **159**: p. 663-682.
98. Borg, M.G., et al. *Numerical Analysis of a Ducted High-Solidity Tidal Turbine*. in *2018 OCEANS - MTS/IEEE Kobe Techno-Oceans (OTO)*. 2018.
99. Brockhaus, G.T. and F. Zilic de Arcos. *Blade-resolved cfd analysis and validation of blockage correction methods for tidal turbines*. in *Advances in Renewable Energies Offshore - Proceedings of the 3rd International Conference on Renewable Energies Offshore, RENEW 2018*. 2019.
100. Borg, M.G., et al. *Analysing Fibre Composite Designs for High-Solidity Ducted Tidal Turbine Blades*. in *OCEANS 2019 - Marseille*. 2019.
101. Borg, M.G., et al., *A numerical structural analysis of ducted, high-solidity, fibre-composite tidal turbine rotor configurations in real flow conditions.* Ocean Engineering, 2021. **233**: p. 109087.
102. Álvarez, M., et al., *The influence of dredging for locating a tidal stream energy farm.* Renewable Energy, 2020. **146**: p. 242-253.
103. Baker, A.L., et al., *Modelling the impact of tidal range energy on species communities.* Ocean & Coastal Management, 2020. **193**: p. 105221.
104. Brown, S.A., E.J. Ransley, and D.M. Greaves, *Developing a coupled turbine thrust methodology for floating tidal stream concepts: Verification under prescribed motion.* Renewable Energy, 2020. **147**: p. 529-540.
105. Chen, L., Y. Yao, and Z.-l. Wang, *Development and validation of a prediction model for the multi-wake of tidal stream turbines.* Renewable Energy, 2020. **155**: p. 800-809.
106. Nachtane, M., et al., *A review on the technologies, design considerations and numerical models of tidal current turbines.* Renewable Energy, 2020. **157**: p. 1274-1288.
107. Djebarri, S., et al., *Design methodology of permanent magnet generators for fixed-pitch tidal turbines with overspeed power limitation strategy.* Journal of Ocean Engineering and Science, 2020. **5**(1): p. 73-83.
108. Liu, H., et al., *Load reduction for two-bladed horizontal-axis tidal current turbines based on individual pitch control.* Ocean Engineering, 2020. **207**: p. 107183.
109. López, A., et al., *Study of a cost model of tidal energy farms in early design phases with parametrization and numerical values. Application to a second-*

generation device. Renewable and Sustainable Energy Reviews, 2020. **117**: p. 109497.
110. Dong, Y., et al., *Development of a 300 kW horizontal-axis tidal stream energy conversion system with adaptive variable-pitch turbine and direct-drive PMSG.* Energy, 2021. **226**: p. 120361.
111. Delafin, P.L., et al., *Performance improvement of a darrieus tidal turbine with active variable pitch.* Energies, 2021. **14**(3).
112. Zhao, T., et al., *Recent progress in blue energy harvesting for powering distributed sensors in ocean.* Nano Energy, 2021. **88**: p. 106199.
113. Sarma, N., et al., *Rotor Electrical Fault Detection in DFIGs Using Wide-Band Controller Signals.* IEEE Transactions on Sustainable Energy, 2021. **12**(1): p. 623-633.
114. Karumalai, D., et al. *Offshore Integrated Renewable Power System*. in *IOP Conference Series: Materials Science and Engineering*. 2020. IOP Publishing.
115. Papathanassiou, S., N. Hatziargyriou, and K. Strunz. *A benchmark low voltage microgrid network.* in *Proceedings of the CIGRE symposium: power systems with dispersed generation*. 2005.
116. Dhua, D. and S. Bandyopadhyay. *Optimization of Generation Capacity at the Incoming Microgrid in an interconnected Microgrid System using ANN*. in *2014 International Conference on Advances in Green Energy (ICAGE)*. 2014. IEEE.
117. Kaplan, S.M., *Smart Grid: Modernizing electric power transmission and distribution; Energy independence, Storage and security; Energy independence and security act of 2007 (EISA); Improving electrical grid efficiency, communication, reliability, and resiliency; integrating new and renewable energy sources*. 2009, United States: The Capitol Net Inc.
118. Pittet, A. *An overview of technical aspects of mini-grids*. 2013 [cited 2021 15 June]; Available from: https://www.eda.admin.ch/dam/countries/countries-content/india/en/resource_en_224456.pdf.
119. INEGI. *La discapacidad en México,datos al 2014*. 2017 [cited 2020; Available from: http://internet.contenidos.inegi.org.mx/contenidos/Productos/prod_serv/contenidos/espanol/bvinegi/productos/nueva_estruc/702825094409.pdf.
120. Ton, D.T. and M.A. Smith, *The US department of energy's microgrid initiative.* The Electricity Journal, 2012. **25**(8): p. 84-94.
121. Pérez-Collazo, C., D. Greaves, and G. Iglesias, *A review of combined wave and offshore wind energy.* Renewable and Sustainable Energy Reviews, 2015. **42**: p. 141-153.
122. Christensen, E.D., et al., *Go offshore-Combining food and energy production*. 2015: Technical University of Denmark. Department of Mechanical Engineering.
123. *H2OCEAN*. [cited 2021 7 September]; Available from: http://www.vliz.be/projects/mermaidproject/project/related-projects/h2ocean.html.
124. Chen, P., J. Chen, and Z. Hu, *Review of Experimental-Numerical Methodologies and Challenges for Floating Offshore Wind Turbines.* Journal of Marine Science and Application, 2020: p. 1-23.

125. Da, Y. and A. Khaligh. *Hybrid offshore wind and tidal turbine energy harvesting system with independently controlled rectifiers*. in *2009 35th Annual Conference of IEEE Industrial Electronics*. 2009. IEEE.
126. Li, L., et al., *Dynamic response and power production of a floating integrated wind, wave and tidal energy system.* Renewable energy, 2018. **116**: p. 412-422.
127. Lande-Sudall, D., T. Stallard, and P. Stansby, *Co-located deployment of offshore wind turbines with tidal stream turbine arrays for improved cost of electricity generation.* Renewable and Sustainable Energy Reviews, 2019. **104**: p. 492-503.
128. Nichita, C., et al., *Preliminary study of a concept of wind-tidal turbine coupling using functional similarities of real time emulation.* Renewable Energy and Power Quality Journal, 2019. **17**: p. 371-376.
129. Phurailatpam, C., B. Rajpurohit, and L. Wang. *Optimization of DC microgrid for rural applications in India*. in *2016 IEEE Region 10 Conference (TENCON)*. 2016. IEEE.
130. Azaza, M. and F. Wallin, *Multi objective particle swarm optimization of hybrid micro-grid system: A case study in Sweden.* Energy, 2017. **123**: p. 108-118.
131. Thakur, D. and J. Jiang, *Design and construction of a wind turbine simulator for integration to a microgrid with renewable energy sources.* Electric Power Components and Systems, 2017. **45**(9): p. 949-963.
132. Adetunji, K.A., OA Joseph, MK. *Developing a microgrid for tafelkop using homer*. in *2018 International Conference on Advances in Big Data, Computing and Data Communication Systems (icABCD)*. 2018. IEEE.
133. Kitson, J., et al., *Modelling of an expandable, reconfigurable, renewable DC microgrid for off-grid communities.* Energy, 2018. **160**: p. 142-153.
134. Oulis Rousis, A., et al., *Design of a hybrid AC/DC microgrid using HOMER Pro: case study on an islanded residential application.* Inventions, 2018. **3**(3): p. 55.
135. Phurailatpam, C., B.S. Rajpurohit, and L. Wang, *Planning and optimization of autonomous DC microgrids for rural and urban applications in India.* Renewable and Sustainable Energy Reviews, 2018. **82**: p. 194-204.
136. Faridnia, N., et al., *Optimal scheduling in a microgrid with a tidal generation.* Energy, 2019. **171**: p. 435-443.
137. Colombo, P., et al., *Dynamic dispatch of solid oxide electrolysis system for high renewable energy penetration in a microgrid.* Energy Conversion and Management, 2020. **204**: p. 112322.
138. *Electricity statistics in New Zealand*. 2022 [cited 2022 14 February]; Available from: https://www.mbie.govt.nz/building-and-energy/energy-and-natural-resources/energy-statistics-and-modelling/energy-statistics/electricity-statistics/.
139. Esteban, M.D., et al., *Why offshore wind energy?* Renewable energy, 2011. **36**(2): p. 444-450.
140. Parrish, J.T. and F. Peterson, *Wind directions predicted from global circulation models and wind directions determined from eolian sandstones of the western United States—A comparison.* Sedimentary Geology, 1988. **56**(1-4): p. 261-282.
141. Song, D., et al., *Maximum power extraction for wind turbines through a novel yaw control solution using predicted wind directions.* Energy conversion and management, 2018. **157**: p. 587-599.

142. *Global Wind Atlas*. [cited 2020 20 December]; Available from: https://globalwindatlas.info/.
143. HOMER, P., *NASA surface meteorology and solar energy database*. 2019.
144. McDowall, C., *We are Here: An Atlas of Aotearoa*. 2019: Massey University Press.
145. Blanco, M.I., *The economics of wind energy*. Renewable and sustainable energy reviews, 2009. **13**(6-7): p. 1372-1382.
146. Pinkerton, R.M., *The variation with Reynolds number of pressure distribution over an airfoil section.* 1938.
147. Brodie, J.W., *Coastal surface currents around New Zealand.* New Zealand journal of geology and geophysics, 1960. **3**(2): p. 235-252.
148. Barnes, E., *Eastern Cook Strait region circulation inferred from satellite‐derived, sea‐surface, temperature data.* New Zealand journal of marine and freshwater research, 1985. **19**(3): p. 405-411.
149. Huckerby, J., D. Johnson, and N.P. Nobs Line. *New Zealand's Wave and Tidal Energy Resources and their Timetable for Development*. in *International Conference on Ocean Energy (ICOE)*. 2008.
150. Johnson, D., et al., *Marine energy resources: Ocean wave and tidal current resources in New Zealand*. 2008, Tech. Rep. P0021-01, MetOcean Solutions Ltd., New Plymouth, New Zealand.
151. Hicks, D.M. and T.M. Hume, *Morphology and size of ebb tidal deltas at natural inlets on open-sea and pocket-bay coasts, North Island, New Zealand.* Journal of coastal research, 1996: p. 47-63.
152. Heath, R., *Broad classification of New Zealand inlets with emphasis on residence times.* New Zealand journal of marine and freshwater research, 1976. **10**(3): p. 429-444.
153. *Foveaux Strait M2 Tidal Component*. Available from: https://niwa.co.nz/our-science/coasts/research-projects/all/physical-hazards-affecting-coastal-margins-and-the-continental-shelf/news/fovmov.
154. *Retscreen International, Clean Energy Project Analysis Software*. [cited 2019 2 December]; Available from: https://www.nrcan.gc.ca/maps-tools-publications/tools/data-analysis-software-modelling/retscreen/7465.
155. P. Botha, G.M., *Stewart Island Wind Investigation* 2018, Roaring40s Wing Power.
156. McCutcheon, J., *Stewart Island Future Supply*. 2016, Power Business Limited.
157. *Tidal Turbines-AR2000*. 2019; Available from: https://simecatlantis.com/services/turbines/.
158. *Marine Energy*. Available from: https://marineenergy.biz/2018/09/13/simec-atlantis-tidal-turbine-grows-stronger/.
159. Karimirad, M., *Offshore energy structures: for wind power, wave energy and hybrid marine platforms*. 2014: Springer.
160. Bhattacharya, S., *Design of foundations for offshore wind turbines*. 2019: Wiley Online Library.
161. *The wind turbine SWT-3.6-107 Offshore*. Available from: https://en.wind-turbine-models.com/turbines/1272-siemens-swt-3.6-107-offshore.
162. *Offshore Renewable Energy for Guernsey*. Available from: http://www.guernseyrenewableenergy.com/documents/managed/Offshore%20Renewable%20Energy%20for%20Guernsey.pdf.
163. *Stewart Island Electricity Supply (SIESA) Part B*. 2018.

164. Huckerby, J.J., David Nobs Line, New Plymouth. *New Zealand's wave and tidal energy resources and their timetable for development*. in *International Conference on Ocean Energy (ICOE)*. 2008. Brest.
165. *Generator Cost in Homer*. Available from: https://www.homerenergy.com/products/pro/docs/latest/generator.html.
166. Taylor, M., et al., *Renewable power generation costs in 2014.* International Renewable Energy Agency: Masdar City, Abu Dhabi, UAE, 2015.
167. Deshmukh, M. and A.B. Singh, *Modeling of Energy Performance of Stand-Alone SPV System Using HOMER Pro.* Energy Procedia, 2019. **156**: p. 90-94.
168. Hiendro, A., et al., *Optimum Renewable Fraction for Grid-connected Photovoltaic in Office Building Energy Systems in Indonesia.* International Journal of Power Electronics and Drive Systems, 2018. **9**(4): p. 1866.
169. Newnan, D.G., T. Eschenbach, and J.P. Lavelle, *Engineering economic analysis*. Vol. 2. 2004: Oxford University Press.
170. Parker, H.D., *New Zealand Energy Strategy to 2050: Powering Our Future*. 2007, New Zealand Government: Wellington.
171. Efficiency, E. and C. Authority, *New Zealand energy efficiency and conservation strategy.* Making It Happen, 2007.
172. *Transpower Geospatial Map*. [cited 2021 21 September]; Available from: https://data-transpower.opendata.arcgis.com/.
173. Mountjoy, J.J., P.M. Barnes, and J.R. Pettinga, *Morphostructure and evolution of submarine canyons across an active margin: Cook Strait sector of the Hikurangi Margin, New Zealand.* Marine Geology, 2009. **260**(1-4): p. 45-68.
174. *Linz information about tides around New Zealand*. [cited 2021 4 February]; Available from: https://www.linz.govt.nz/sea/tides/introduction-tides/tides-around-new-zealand.
175. Walters, R.A., et al., *A study of tides and currents in Cook Strait, New Zealand.* Ocean dynamics, 2010. **60**(6): p. 1559-1580.
176. Hatziargyriou, N., *Microgrids: architectures and control*. 2014: John Wiley & Sons.
177. Roberts, D. and A. Chang, *Meet the Microgrid, the Technology Poised to Transform Electricity.* Vox. May, 2018. **24**: p. 2018.
178. Lambert, T., *Micropower System Modeling with Homer", in Integration of Alternative Sources of Energy by Felix A. Farret and M. Godoy Simoes.* 2006.
179. *Electricity Authority Information of New Zealand*. [cited 2021 25 July]; Available from: https://www.emi.ea.govt.nz/.
180. *Node load trends of New Zealand.* [cited 2020 12 January]; Available from: https://www.ems.co.nz/services/em6/.
181. Goring, D., *Computer models define tide variability.* The Industrial Physicist, 2001. **7**(5): p. 14-17.
182. Rakhshani, E., H. Mehrjerdi, and A. Iqbal, *Hybrid wind-diesel-battery system planning considering multiple different wind turbine technologies installation.* Journal of Cleaner Production, 2020. **247**: p. 119654.
183. Benato, A., et al., *TES-PD: A Fast and Reliable Numerical Model to Predict the Performance of Thermal Reservoir for Electricity Energy Storage Units.* Fluids, 2021. **6**(7): p. 256.

184. *Siemens Wind Turbine SWT-3.6-107*. Available from: https://www.renugen.co.uk/content/large_wind_turbine_brochures/large_wind_turbine_brochures/siemens_swt-3.6-107.pdf.
185. Symeonidou, M.M., C. Zioga, and A.M. Papadopoulos, *Life cycle cost optimization analysis of battery storage system for residential photovoltaic panels.* Journal of Cleaner Production, 2021. **309**: p. 127234.
186. El-Bidairi, K.S., et al., *Optimal sizing of Battery Energy Storage Systems for dynamic frequency control in an islanded microgrid: A case study of Flinders Island, Australia.* Energy, 2020. **195**: p. 117059.
187. Recordon, E., *Siemens Energías Renovables.* 2009.
188. Mitchell, S., I. Ogbonna, and K. Volkov, *Aerodynamic characteristics of a single airfoil for vertical axis wind turbine blades and performance prediction of wind turbines.* Fluids, 2021. **6**(7): p. 257.
189. Sinha, S. and S. Chandel, *Review of software tools for hybrid renewable energy systems.* Renewable and Sustainable Energy Reviews, 2014. **32**: p. 192-205.
190. Babcock, B.A. and K.E. Conover, *Design of cost-effective towers for an advanced wind turbine.* ASME SOL ENERGY DIV PUBL SED, ASME, NEW YORK, NY,(USA), 1994, 1994. **15**: p. 261-268.
191. Lombardi, D., S. Bhattacharya, and D.M. Wood, *Dynamic soil–structure interaction of monopile supported wind turbines in cohesive soil*. Soil Dynamics and Earthquake Engineering, 2013. **49**: p. 165-180.
192. *BS EN IEC 61400-3-1:2019 Wind energy generation systems. Design requirements for fixed offshore wind turbines*. 2019: BSI Standards Limited.
193. DNV, G., *Environmental conditions and environmental loads.* Recommend Practice DNV-RP-C205, 2014.
194. *NIWA Tide Forecaster*. Available from: https://tides.niwa.co.nz/.
195. *The KNMI/ERA-40 Wave Atlas*. Available from: http://projects.knmi.nl/wave_atlas/atlas_book.html#c57a.
196. *UoA wave tool*. Available from: https://coastalhub.science/data.
197. *Crest Energy*. Available from: http://www.crest-energy.com/faq.htm.
198. *Weibull Calculator*. Available from: https://wind-data.ch/tools/weibull.php.
199. *IEC 61400*. Available from: https://en.wikipedia.org/wiki/IEC_61400.
200. Gupta, R. and A. Biswas, *Wind data analysis of silchar (assam, india) by rayleighs and weibull methods.* Journal of Mechanical Engineering Research, 2010. **2**(1): p. 010-024.
201. Ayodele, T.R., et al., *Statistical analysis of wind speed and wind power potential of Port Elizabeth using Weibull parameters.* Journal of Energy in Southern Africa, 2012. **23**(2): p. 30-38.
202. *OPTUM CE*. Available from: https://optumce.com/.
203. Jose, N.M. and A. Mathai, *A study on lateral deformation of monopile of offshore wind turbine due to environmental loads.* Procedia technology, 2016. **24**: p. 287-294.
204. Bowles, L., *Foundation analysis and design*. 1996: McGraw-hill.
205. Bhattacharya, S. and K. Goda, *Use of offshore wind farms to increase seismic resilience of Nuclear Power Plants.* Soil Dynamics and Earthquake Engineering, 2016. **80**: p. 65-68.
206. Arany, L., et al., *An analytical model to predict the natural frequency of offshore wind turbines on three-spring flexible foundations using two different beam models.* Soil Dynamics and Earthquake Engineering, 2015. **74**: p. 40-45.

207. Camp, T., et al., *Design methods for offshore wind turbines at exposed sites (final report of the OWTES project EU Joule III project JOR3-CT98-0284).* Bristol United Kingdom, 2004.
208. RP2A-WSD, A., *Recommended practice for planning, designing and constructing fixed offshore platforms–working stress design–*. American Petroleum Institute, Washington Dc, 2000.
209. Poulos, H.G. and E.H. Davis, *Pile foundation analysis and design*. 1980.
210. Lin, Y.-H., S.-H. Kao, and C.-H. Yang, *Investigation of hydrodynamic forces for floating offshore wind turbines on spar buoys and tension leg platforms with the mooring systems in waves.* Applied Sciences, 2019. **9**(3): p. 608.
211. Arany, L. and S. Bhattacharya, *Simplified load estimation and sizing of suction anchors for spar buoy type floating offshore wind turbines.* Ocean Engineering, 2018. **159**: p. 348-357.
212. Mirzaei, F., A. Tavakoli, and Z. Tashakori, *Stability Analysis of TLP Floating Wind Turbine Under Severe Environmental Loading Condition.* 2018.
213. Chen, C., Y. Ma, and T. Fan, *Review of model experimental methods focusing on aerodynamic simulation of floating offshore wind turbines.* Renewable and Sustainable Energy Reviews, 2022. **157**: p. 112036.
214. Farr, H., et al., *Potential environmental effects of deepwater floating offshore wind energy facilities.* Ocean & Coastal Management, 2021. **207**: p. 105611.
215. *ballast in spar buoy*. Available from: https://www.theguardian.com/environment/2014/jun/23/drifting-off-the-coast-of-portugal-the-frontrunner-in-the-global-race-for-floating-windfarms.
216. Bortolotti, P., et al., *IEA Wind TCP Task 37: Systems Engineering in Wind Energy-WP2. 1 Reference Wind Turbines*. 2019, National Renewable Energy Lab.(NREL), Golden, CO (United States).
217. Statoil, *Hywind Scotland pilot park environmental statement.* 2015.
218. Arany, L., et al., *Design of monopiles for offshore wind turbines in 10 steps.* Soil Dynamics and Earthquake Engineering, 2017. **92**: p. 126-152.
219. Frohboese, P., C. Schmuck, and G.G. Hassan. *Thrust coefficients used for estimation of wake effects for fatigue load calculation*. in *European Wind Energy Conference*. 2010.
220. *Wave climate around New Zealand*. Available from: https://niwa.co.nz/our-science/coasts/research-projects/all/physical-hazards-affecting-coastal-margins-and-the-continental-shelf/news/waves#climate.
221. Fraenkel, P. *Development and testing of Marine Current Turbine's SeaGen 1.2 MW tidal stream turbine*. in *Proc. 3rd International Conference on Ocean Energy*. 2010.
222. McNaughton, J., et al. *Measuring and modelling the power curve of a commercial-scale tidal turbine*. in *Proceedings of the 11th European Wave and Tidal Energy Conference (EWTEC), Nantes, France*. 2015.
223. Haverson, D., et al., *Modelling the hydrodynamic and morphological impacts of a tidal stream development in Ramsey Sound.* Renewable Energy, 2018. **126**: p. 876-887.
224. Sudall, D., P. Stansby, and T. Stallard. *Energy yield for collocated offshore wind and tidal stream farms*. in *Proceedings of EWEA Offshore Conference, Denmark*. 2015.

225. McNaughton, J., *Turbulence modelling in the near-field of an axial flow tidal turbine in code_saturne*. 2013, The University of Manchester (United Kingdom).
226. Boukis, N., et al. *Corrosion Resistant Materials for SCWO-Applications: Experimental Results From Long Time Experiments*. in *CORROSION 2001*. 2001. NACE International.
227. Montllonch Araquistain, T., *TIDAL POWER: Economic and Technological assessment.* 2010.
228. Giordano, A.A. and A.H. Levesque, *Getting started with Simulink.* 2015.
229. Gasch, R. and J. Twele, *Wind power plants: fundamentals, design, construction and operation*. 2011: Springer Science & Business Media.
230. Mathew, S., *Wind energy: fundamentals, resource analysis and economics*. Vol. 1. 2006: Springer.
231. Vanapalli, V.T., *Modelling & Dynamic Analysis of Wind Turbine Blades*. 2015, National Institute of Technology: Odisha, India.
232. Mohamed, M., *Performance investigation of H-rotor Darrieus turbine with new airfoil shapes.* Energy, 2012. **47**(1): p. 522-530.
233. Danish Wind Industry Association. *Wind Energy Reference Manual Part 1: Wind Energy Concepts* 2003; Available from: http://xn--drmstrre-64ad.dk/wp-content/wind/miller/windpower%20web/en/stat/unitsw.htm#roughness.
234. Troen, L.B. and E.L. Petersen, *European wind atlas*. 1989: Risø National Laboratory.
235. Britwind. *Our windmills: The R9000*. 2019; Available from: http://www.britwind.co.uk/our-windmills/the-r9000.
236. Windpower Program. *WindPower program software*. 2019; Available from: http://www.wind-power-program.com/download.htm.
237. Eleni, D.C., T.I. Athanasios, and M.P. Dionissios, *Evaluation of the turbulence models for the simulation of the flow over a National Advisory Committee for Aeronautics (NACA) 0012 airfoil.* Journal of Mechanical Engineering Research, 2012. **4**(3): p. 100-111.
238. Izli, N., A. Vardar, and F. Kurtulmu, *A study on aerodynamic properties of some NACA profiles used on wind turbine blades.* Applied Sci, 2007. **7**: p. 426-433.
239. Marten, D., et al. *Development and application of a simulation tool for vertical and horizontal axis wind turbines*. in *ASME Turbo Expo 2013: Turbine Technical Conference and Exposition*. 2013. American Society of Mechanical Engineers.
240. Dhanak, M.R. and N.I. Xiros, *Springer handbook of ocean engineering*. 2016: Springer.
241. *SeaGen-S 2MW - SIMEC Atlantis Energy*. Available from: https://www.atlantisresourcesltd.com/wp/wp-content/uploads/2016/08/SeaGen-Brochure.pdf.
242. *Coefficient of Power vs Tip Speed Ratio*. Available from: http://people.bu.edu/dew11/turbineperformance.html.
243. Shapiro, G., *Effect of tidal stream power generation on the region-wide circulation in a shallow sea.* Ocean Science, 2011. **7**(1): p. 165.
244. Touma, J.S., *Dependence of the wind profile power law on stability for various locations.* Journal of the Air Pollution Control Association, 1977. **27**(9): p. 863-866.

245. *Water depth*. Available from: https://wetmaps.co.nz/#13/-36.3944/173.9510.
246. Morison, J., J. Johnson, and S. Schaaf, *The force exerted by surface waves on piles.* Journal of Petroleum Technology, 1950. **2**(05): p. 149-154.
247. Hald, T., et al. *Revisiting monopile design using py curves. Results from full scale measurements on Horns Rev*. in *Proceedings of European Offshore Wind 2009 Conference*. 2009.
248. Rong, X.-N., et al., *Analytical solution for natural frequency of monopile.* Wind and Structures, 2017. **25**(5): p. 459-474.
249. Arany, L., et al., *Closed form solution of Eigen frequency of monopile supported offshore wind turbines in deeper waters incorporating stiffness of substructure and SSI.* Soil Dynamics and Earthquake Engineering, 2016. **83**: p. 18-32.
250. Bhattacharya, S. and K. Goda, *Probabilistic buckling analysis of axially loaded piles in liquefiable soils.* Soil Dynamics and Earthquake Engineering, 2013. **45**: p. 13-24.
251. *Unit Weight of Soil*. Available from: http://www.geotechnicalinfo.com/soil_unit_weight.html.
252. Das, B.M., *Principles of Geotechnical Engineering 7th Edition. pdf.* 2002.
253. Coduto, D.P., *Foundation design: principles and practices*. 2001: Prentice Hall.
254. *geotech data*. Available from: http://geotechdata.info/parameter.

Appendix A Tidal Energy

Tidal energy is the energy dissipated by tidal movements in the oceans. A tide is a regular rise and fall of the surface of the ocean due to the gravitational force of the sun and moon on the earth and the centrifugal force produced by the rotation of the earth. The gravitational force that mutually attracts any two bodies is directly proportional to the product of their masses and is inversely proportional to the square of the distance that separates the masses. The gravitational force exerted by the sun or moon on a molecule of water can be calculated by A-1:

$$\boldsymbol{F = \frac{KMm}{d^2}} \qquad \text{(A-1)}$$

F: gravitational Force (N)

K: universal constant of gravity

M: the mass of the moon or sun (kg)

m: the mass of a water molecule (kg)

d: the distance from a water molecule to the moon/sun (m)

The gravitational force exerted by the moon on the earth is 2.17 times larger than exerted by the sun, due to the smaller distance between the earth and the moon. A bulge of water is created in the oceans, on the earth side nearest to the moon. Simultaneously, another bulge of water is created by the centrifugal pull due to the rotation of the earth, but in this case, the water bulge is created on the side of the earth farthest from the moon and is quite small (see Figure A-1).

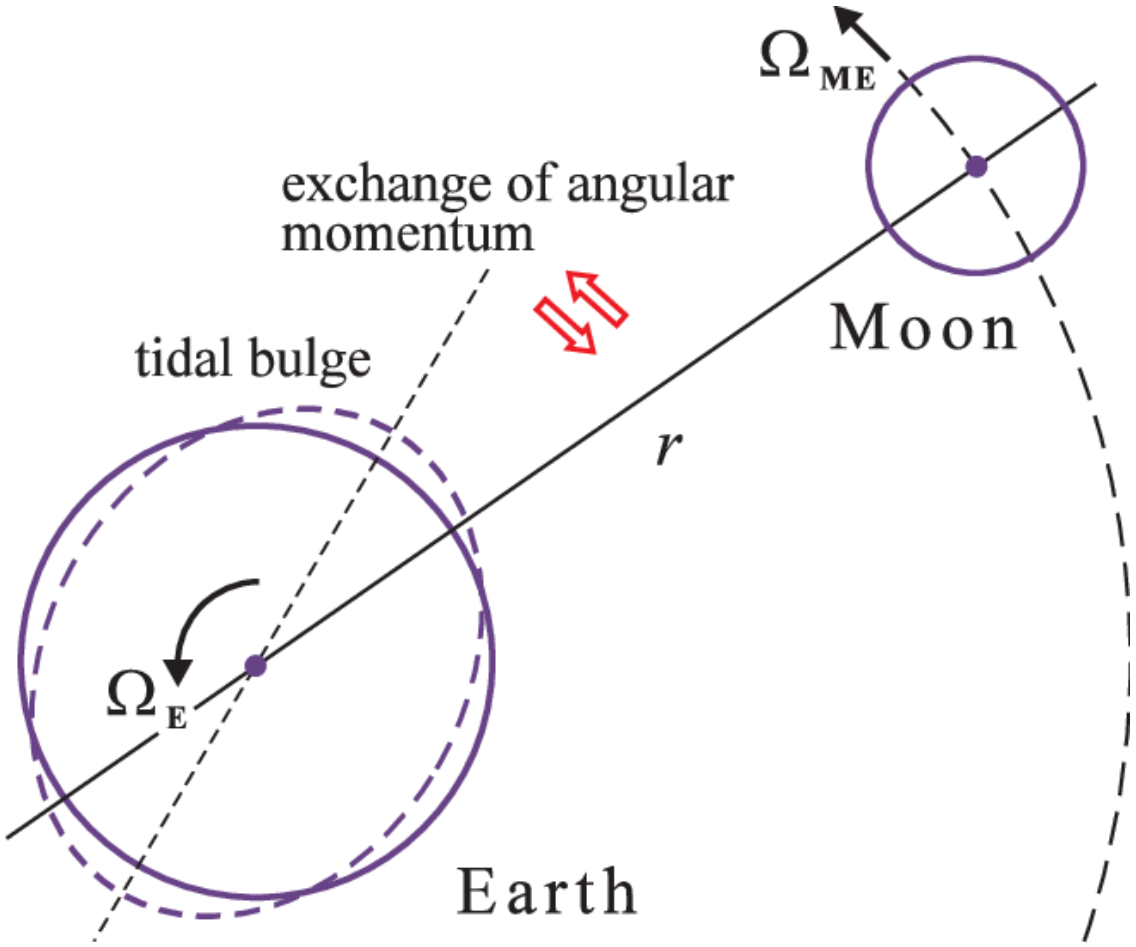

Figure A-1: Tidal interaction between earth and moon[226].

When the sun and moon are in line whether pulling on the same side or the opposite side (full or new moons), the combined gravitational attraction causes high tides, known as spring tides. Conversely, when the sun and moon are out of line, their gravitational forces pull water in different directions causing the bulges to cancel each other, giving place to low tides, known as neap tides. So a tidal turbine`s potential is maximum during spring tides and minimum during neap tides (see Figure A-2 for an example) [227].

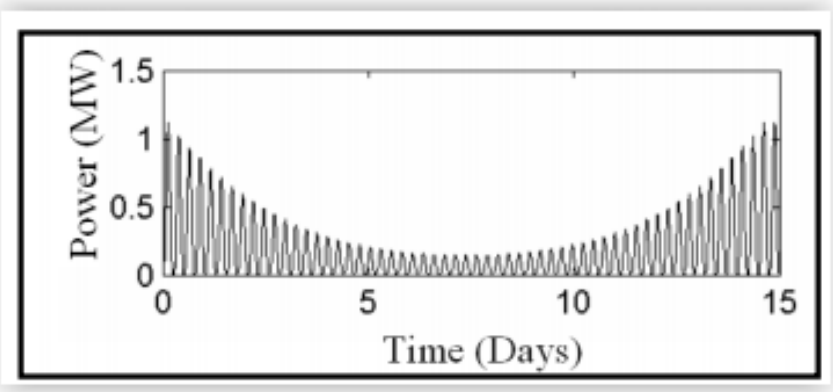

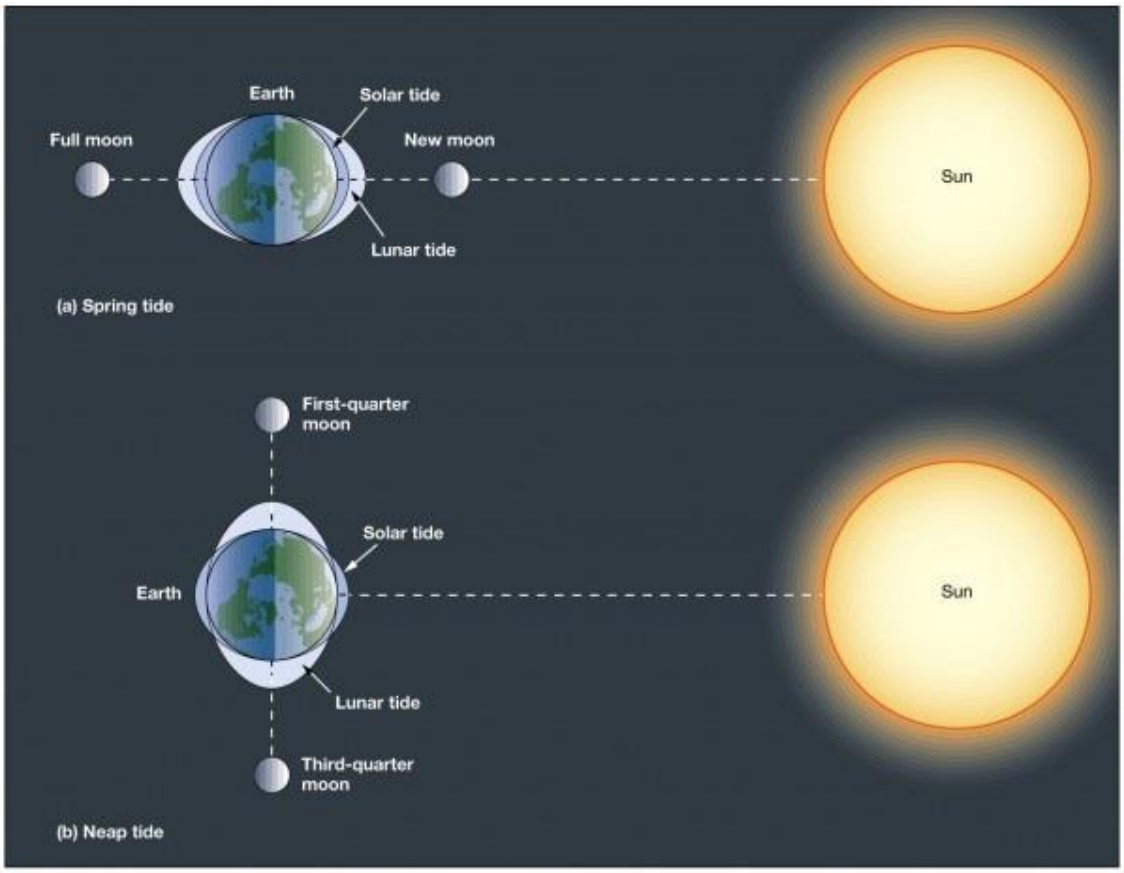

Figure A-2:How a tidal turbine`s energy potential fluctuates during a tidal cycle [227, 228].

Appendix B Criteria for Evaluation Turbins

B.1 Tip Speed Ratio

Equation B-1 is used for calculating tip speed ratio:

$$\lambda = \sqrt{\frac{80}{B}} \tag{B-1}$$

This equation is a rule of thumb for guessing the optimum tip speed ratio (Equation B-2) of a set of blades. So, if

$$C = \frac{16\pi R}{9\lambda^2 B}, \tag{B-2}$$

, at the tip speed $C = \left(\frac{7}{100}\right) R$, as shown in Figure B-3, B will be:

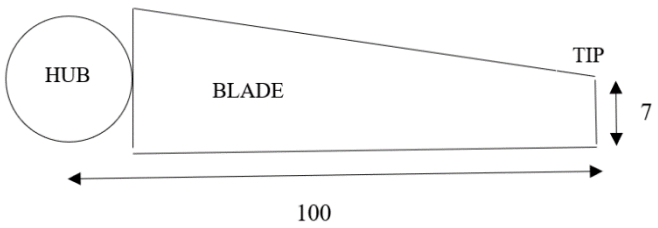

Figure B-3:The rule of thumb for tip speed ratio [229].

$$B = \frac{16\pi R}{9\lambda^2 \frac{7}{100} R} = \frac{80}{\lambda^2} \tag{B-3}$$

Proof of $C = \frac{16\pi R}{9\lambda^2 B}$: The maximum power generated from a wind turbine can be found by putting 0.593 or 16/27 as Betz limit value:

$$P_{max} = \dot{E}_{Betz} = C_p \frac{\rho}{2} v_1^3 (\pi r^2) = \frac{16}{27} \frac{\rho}{2} v_1^3 (\pi r^2) \tag{B-4}$$

So,

$$d\dot{E}_{Betz} = \frac{16}{27}\frac{\rho}{2}v_1^3(2\pi r dr) \tag{B-5}$$

The resultant mechanical power from a turbine with B blades with just considering lift as drag coefficient is very small:

$$dP = number\ of\ blades \times tangential\ component\ of\ the\ aerodynamic\ force \times local\ circumferential\ velocity = B.dU.\omega r = B.dL\ sin\phi.\omega r = B.\frac{\rho}{2}c_L w^2 c(r)dr\ sin\phi.\omega r = B\omega r\frac{\rho}{2}c_L w^2 c(r)dr\ sin\phi$$

(B-6)

With equating $dP = d\dot{E}_{Betz}$, in equations (B-6) and (B-7) the chord length yields:

$$c(r) = \frac{1}{B}\frac{16}{27}\frac{2\pi r}{c_L}\frac{v_1^3}{w^2\omega r\ sin\phi} \tag{B-2}$$

Using equations $v_1 = \frac{3}{2}w\ sin\phi$ and $u = \omega r = w\ cos\phi$, shown in Figure B-4 and rewriting above equation [229]:

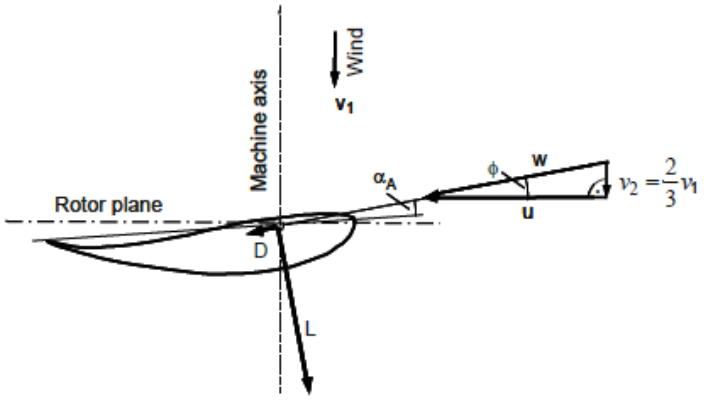

Figure B-4: Velocity Components in blade [229].

$$c(r) = 2\pi R \frac{1}{B} \frac{8}{9c_L} \frac{1}{\lambda \sqrt{\lambda^2 \left(\frac{r}{R}\right)^2 + \frac{4}{9}}} \quad \text{(B-3)}$$

For high tip speed ratio turbines with $\lambda > 3$, it can be simplified to

$$c(r) = 2\pi R. \frac{1}{B} \frac{8}{9c_L} \frac{1}{\lambda^2 (\frac{r}{R})} \quad \text{(B-4)}$$

A tip speed ratio around 5 is ideal which is for B=3. For B=1, $\lambda = 9$, for B=2, $\lambda = 6$ and for B=10, $\lambda = 3$ can be used.

B.2 Angle of attack

When the airfoil is exposed to a wind stream, pressure difference between upper and lower surfaces of airfoil results a force F, which its component is perpendicular in direction is called lift force L and in undisturbed direction is called drag force D as shown in Figure B-5.

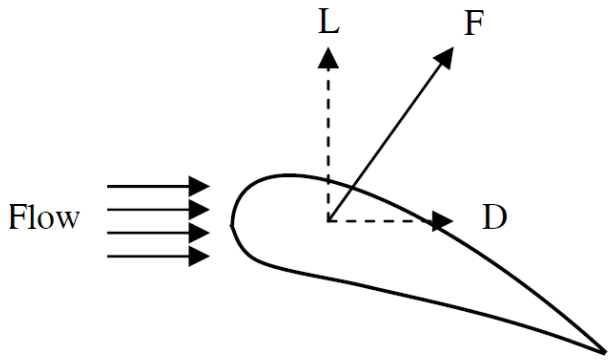

Figure B-5: Lift and drag [230].

The lift and drag forces are given by equations (B-11) and (B-12):

$$L = C_L \frac{1}{2} \rho_a A V^2 \quad \text{(B-5)}$$

$$D = C_D \frac{1}{2} \rho_a A V^2 \quad \text{0(B-6)}$$

where C_L and C_D are their coefficients respectively. So there is a need to identify α when C_D/C_L amount is minimum by plotting a tangent curve of them, as shown in Figure B-6 [231]. To maintain this minimum value and reach the optimum angle, the blade needs to be twisted along its length. Another factor affects lift and drag forces is Reynolds number[15] is given by equation (B-7:

$$Re = \frac{VC}{\gamma} \tag{B-7}$$

Where C is chord length, V is wind velocity, and γ is the kinematic viscosity for air is 15×10^{-6} m^2/s at 20° C. So, if there was a change in chord length or wind velocity, the Reynolds number will be changed. For instance, for a chord with 0.33 length exposed in a flow of 7 m/s, the changed Re number is 15×10^5 [230].

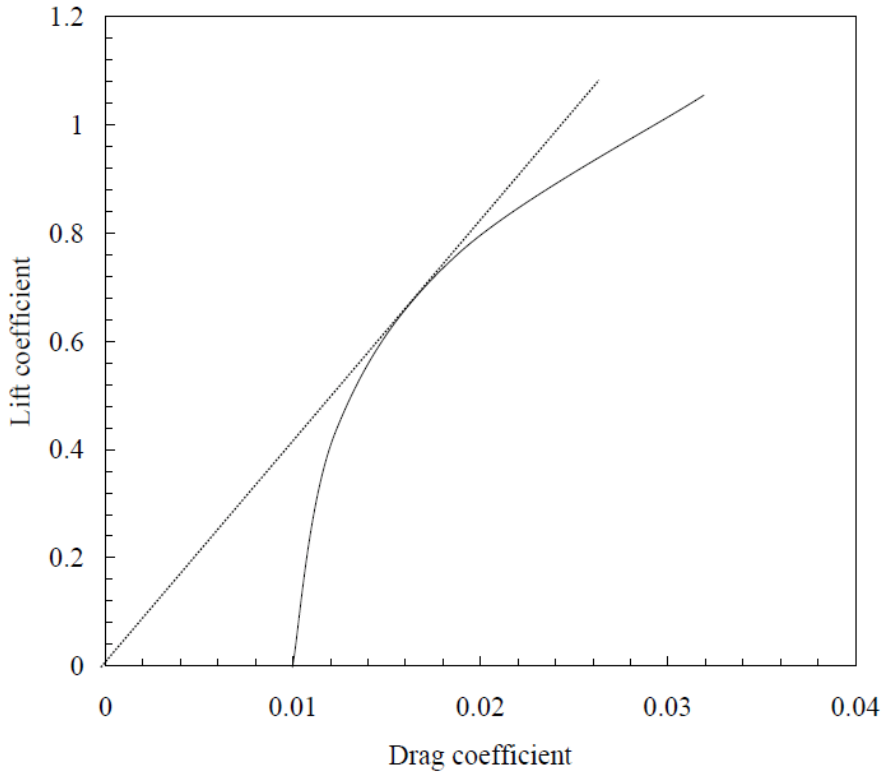

Figure B-6: Relationship of Lift and drag coefficients [230].

[15] The Reynolds number (Re) is an important dimensionless quantity in fluid mechanics used to help predict flow patterns in different fluid flow situations. At low Reynolds numbers, flows tend to be dominated by laminar (sheet-like) flow, while at high Reynolds numbers turbulence results from differences in the fluid's speed and direction, which may sometimes intersect or even move counter to the overall direction of the flow (eddy currents).

B.3 Airfoil Camber of Blade

Some manufacturers camber the airfoils in order to capture more energy at either side of the rotor. However, no significant difference in the performance has been reported as compared to the Darrieus VAWT with symmetrical airfoil, since cambering the airfoil causes an increase of tangential force in one half, but decreases the energy in the other half of the swept region, as given in Table B-1 [232].

Table B-1: List of airfoils simulated with the corresponding C_P [232].

Airfoil	C_P max
NACA 0010	0.2345
NACA 0015	0.2947
NACA 0018	0.2964
NACA 0021	0.2679
NACA 6312	0.1290
NACA 63415	0.1711
NACA 63418	0.2772
AH93W174	0.2469
AH93W215	0.2541
AH94W301	0.2130
AG18	0.0123
S 809	0.3428
S 9000	0.1696
S 1046	0.4051
S 1014	0.2769
FX66S196	0.2074
FX77W256	0.1639
FX71L150	0.2961
FXL142	0.3311
FXLV152	0.3576

B.4 The Effect of Hub Height in Wind Turbines

The height of the tower is the most essential criteria to be considered while designing the tower. Height of the tower is generally the height at which the nacelle and rotor-hub are from the ground (also called hub height). The height should be enough so that the rotor blades can rotate comfortably without encountering any hindrances. Another implication of the height of the tower is to access the fastest wind speeds. Since the higher the altitude, the faster and less turbulent the wind is. Ultimately, the optimum height of the tower is where the two growth functions of the cost and energy production intersect.

Knowing roughness height at this stage is necessary. The roughness z_0 class is defined in the European Wind Atlas on the basis of the roughness length in metres [233].For class 0(water areas) z_0=0.0002 m, class 1(open areas with few windbreaks) z_0 = 0.03 m, class 2(farmlands with windbreaks) z_0=0.1 m, class 3(urban districts, forests and farmland with many windbreaks) z_0 = 0.4 m [234].

For this simulation, a wind turbine with model Britwand (Formerly Evance) R9000 5kW Class 2 is chosen [235]. Its specification is:

Rotor diameter= 5.5 m

Tower Height= 15,18,20.5 m

Measurement Height= 12,15,18.3 m

TI(turbulence intensity) and mean wind speed values are imported to QBlade by installing and using WindPower program software [236].

Case (1)

- Rotor diameter= 5.5 m
- Tower Height= 15 m
- Measurement Height= 12 m

The results are given in Table B-2.

Table B-2:Vmax Simulation of Turbine Evance R9000 in Case of Tower Height 15 m.

Rotor Radius (m)	Tower Height(m)	Mean Wind Speed(m/s)	Measurement Height (m)	TI	roughness length(m)	Simulated V_{max} (m/s)
2.75	15	5	12	0.52	0.1	5.48
2.75	15	5.2	12	0.52	0.1	5.69
2.75	15	5.4	12	0.52	0.1	5.90
2.75	15	5.6	12	0.52	0.1	6.14
2.75	15	5.8	12	0.52	0.1	6.35
2.75	15	6	12	0.52	0.1	6.57
2.75	15	6.2	12	0.52	0.1	6.78
2.75	15	6.4	12	0.52	0.1	7.01
2.75	15	6.6	12	0.52	0.1	7.21
2.75	15	6.8	12	0.52	0.1	7.45
2.75	15	7	12	0.52	0.1	7.67
2.75	15	7.2	12	0.52	0.1	7.88
2.75	15	7.4	12	0.52	0.1	8.11
2.75	15	7.6	12	0.52	0.1	8.30
2.75	15	7.8	12	0.52	0.1	8.57
2.75	15	8	12	0.52	0.1	8.74
2.75	15	8.2	12	0.52	0.1	8.99
2.75	15	8.4	12	0.52	0.1	9.20
2.75	15	8.6	12	0.52	0.1	9.42
2.75	15	8.8	12	0.52	0.1	9.62
2.75	15	9	12	0.52	0.1	9.83
2.75	15	9.2	12	0.52	0.1	10.07
2.75	15	9.4	12	0.52	0.1	10.29
2.75	15	9.6	12	0.52	0.1	10.51
2.75	15	9.8	12	0.52	0.1	10.72
2.75	15	10	12	0.52	0.1	10.97

Case (2)

- Rotor diameter= 5.5 m
- Tower Height= 18 m
- Measurement Height= 15 m

The results are given in Table B-3.

Table B-3: Vmax Simulation of Turbine Evance R9000 in Case of Tower Height 18 m.

Rotor Radius (m)	Tower Height(m)	Mean Wind Speed(m/s)	Measurement Height (m)	TI	roughness length(m)	Simulated V_{max} (m/s)
2.75	18	5	15	0.52	0.1	5.35
2.75	18	5.2	15	0.52	0.1	5.60
2.75	18	5.4	15	0.52	0.1	5.81
2.75	18	5.6	15	0.52	0.1	6.03
2.75	18	5.8	15	0.52	0.1	6.25
2.75	18	6	15	0.52	0.1	6.44
2.75	18	6.2	15	0.52	0.1	6.68
2.75	18	6.4	15	0.52	0.1	6.90
2.75	18	6.6	15	0.52	0.1	7.15
2.75	18	6.8	15	0.52	0.1	7.34
2.75	18	7	15	0.52	0.1	7.53
2.75	18	7.2	15	0.52	0.1	7.78
2.75	18	7.4	15	0.52	0.1	7.97
2.75	18	7.6	15	0.52	0.1	8.20
2.75	18	7.8	15	0.52	0.1	8.40
2.75	18	8	15	0.52	0.1	8.63
2.75	18	8.2	15	0.52	0.1	8.84
2.75	18	8.4	15	0.52	0.1	9.07
2.75	18	8.6	15	0.52	0.1	9.26
2.75	18	8.8	15	0.52	0.1	9.52
2.75	18	9	15	0.52	0.1	9.70
2.75	18	9.2	15	0.52	0.1	9.92
2.75	18	9.4	15	0.52	0.1	10.15
2.75	18	9.6	15	0.52	0.1	10.34
2.75	18	9.8	15	0.52	0.1	10.53
2.75	18	10	15	0.52	0.1	10.77

Case (3)

- Rotor diameter= 5.5 m
- Tower Height= 20.5 m
- Measurement Height= 18.3 m

The results are given in Table B-4.

Table B-4: Vmax Simulation of Turbine Evance R9000 in Case of Tower Height 20.5 m.

Rotor Radius (m)	Tower Height(m)	Mean Wind Speed(m/s)	Measurement Height (m)	TI	roughness length(m)	Simulated V_{max} (m/s)
2.75	20.5	5	18.3	0.52	0.1	5.29
2.75	20.5	5.2	18.3	0.52	0.1	5.50
2.75	20.5	5.4	18.3	0.52	0.1	5.70
2.75	20.5	5.6	18.3	0.52	0.1	5.92
2.75	20.5	5.8	18.3	0.52	0.1	6.13
2.75	20.5	6	18.3	0.52	0.1	6.35
2.75	20.5	6.2	18.3	0.52	0.1	6.55
2.75	20.5	6.4	18.3	0.52	0.1	6.77
2.75	20.5	6.6	18.3	0.52	0.1	6.98
2.75	20.5	6.8	18.3	0.52	0.1	7.19
2.75	20.5	7	18.3	0.52	0.1	7.39
2.75	20.5	7.2	18.3	0.52	0.1	7.61
2.75	20.5	7.4	18.3	0.52	0.1	7.82
2.75	20.5	7.6	18.3	0.52	0.1	8.04
2.75	20.5	7.8	18.3	0.52	0.1	8.27
2.75	20.5	8	18.3	0.52	0.1	8.47
2.75	20.5	8.2	18.3	0.52	0.1	8.65
2.75	20.5	8.4	18.3	0.52	0.1	8.87
2.75	20.5	8.6	18.3	0.52	0.1	9.08
2.75	20.5	8.8	18.3	0.52	0.1	9.31
2.75	20.5	9	18.3	0.52	0.1	9.56
2.75	20.5	9.2	18.3	0.52	0.1	9.74
2.75	20.5	9.4	18.3	0.52	0.1	9.94
2.75	20.5	9.6	18.3	0.52	0.1	10.14
2.75	20.5	9.8	18.3	0.52	0.1	10.37
2.75	20.5	10	18.3	0.52	0.1	10.61

With respect to Figure B-7, It can be concluded; the best case is case 1 or TH=15.

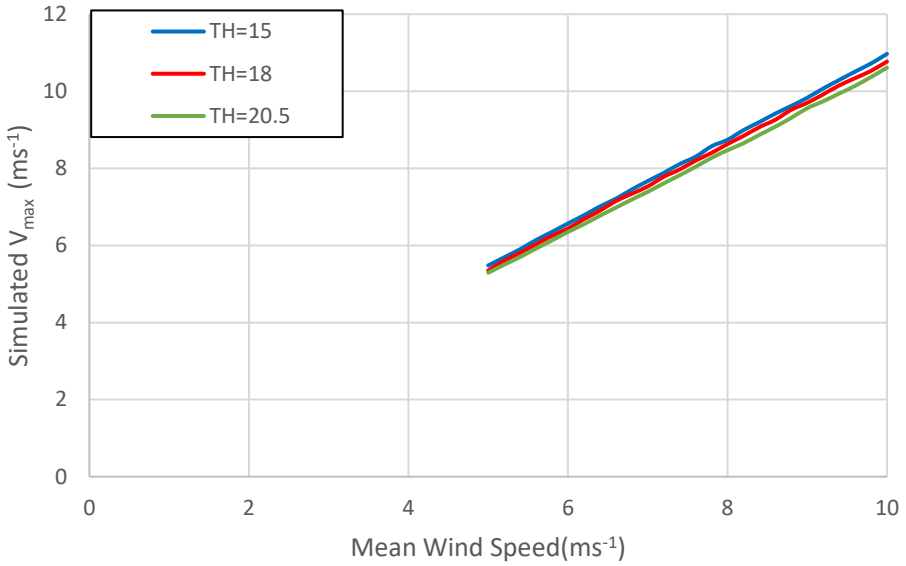

Figure B-7:Optimized Hub Height in R9000 Turbine

B.5 The effect of rotor radius on output power

The power generated in the rotor radius range of 3.5 to 6.5m is calculated here. Here different rotor radiuses result in different TSA or πR^2. Wind speed is assumed 15 m/s and rotational speed is 150 rpm. So, calculating λ yields CP and after that, power can be calculated for any rotor radius, shown in Figure B-8.

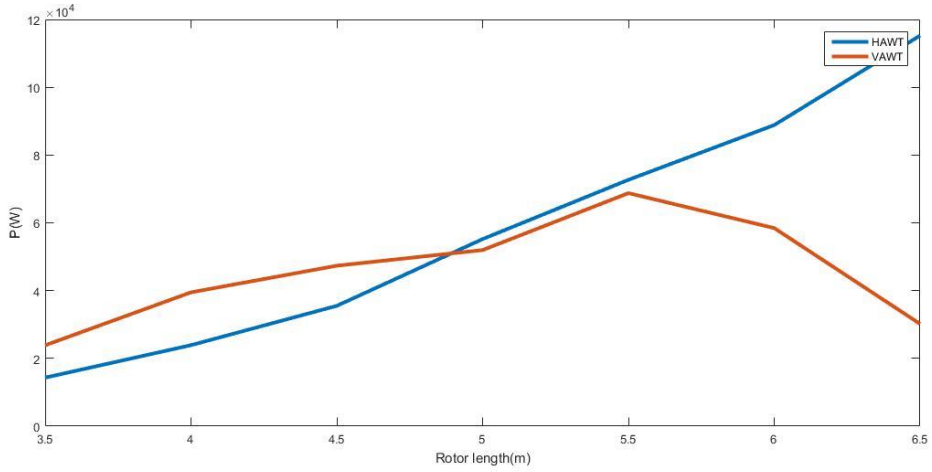

Figure B-8: The effect of rotor radius on the output power of wind turbines

In rotor radius range of 3.5 m to 4.88 m VAWT produces more power. After, the turning point of 4.88 m and onwards, HWAT power is higher than VAWT. However, if rotor radius increases from 5.5m in VAWT, there is a reduction in power generation in this type. The Maximum power for HAWT is for rotor radius 6.5 m and is $1.15x10^5$ W while it happens for VAWT at 5.5 m radius with power 6.87×10^4.

B.6 Effect of rotor length on generating power in horizontal axis wind turbines

The selected airfoil for simulation with Qblade of HAWT is the NACA (National Advisory Committee for Aeronautics) 0012. This airfoil was chosen because it has been used in many constructions. Typical examples of such use of the airfoil are the B-17 Flying Fortress and Cessna 152, the helicopter Sikorsky S-61 SH-3 Sea King as well as horizontal and vertical axis wind turbines [237]. A Reynolds value of 100000 was used. As B (number of blades) is 3, the tip speed ratio will be 5.1 according to equation (1). The chord length is calculated with respect to equation (2) [238].

As maximum rotor diameter in HAWT is 170 m, turbines from 10 m to 170 m diameters is modelled, and for them chord length separately is calculated. If we assume wind speed is at least 3 m/s, we can find the minimum required rpm for different kind of turbine diameters. The chord length and optimized rpm in each case are tabulated in Table B-5 and are plotted in Figure B-9.

Table B-5: Minimum rpms for different rotor diameters

Diameter(m)	Chord length (m)	rpm
7	0.35	60
10	0.5	36
20	1	26
30	1.5	21
40	2	13
50	2.5	11
60	3	9
70	3.5	7
80	4	6
90	4.5	5
100	5	5
110	5.5	5
120	6	4
130	6.5	4
140	7	3.5
150	7.5	3.5
160	8	3
170	8.5	3

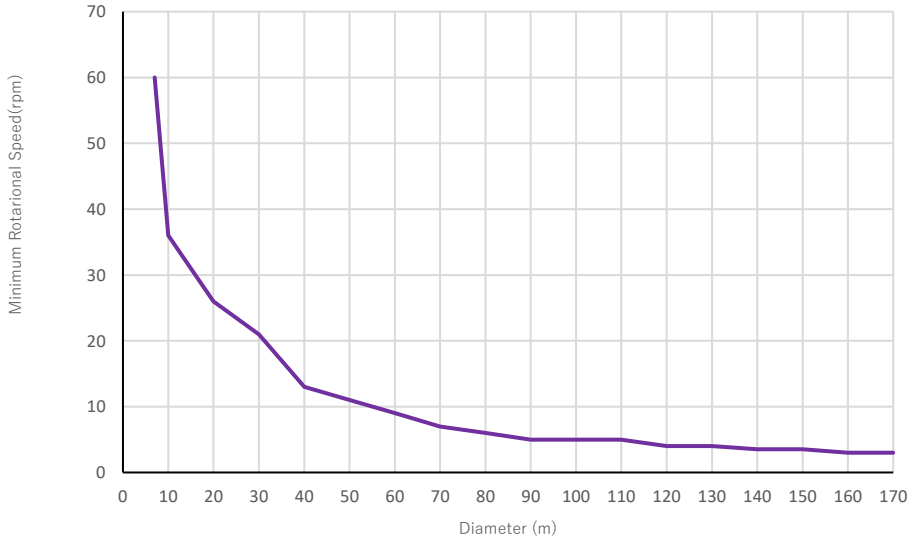

Figure B-9:Minimum Required rpm for different rotor lengths

The model in case of 10m diameter is shown in Figure B-10.

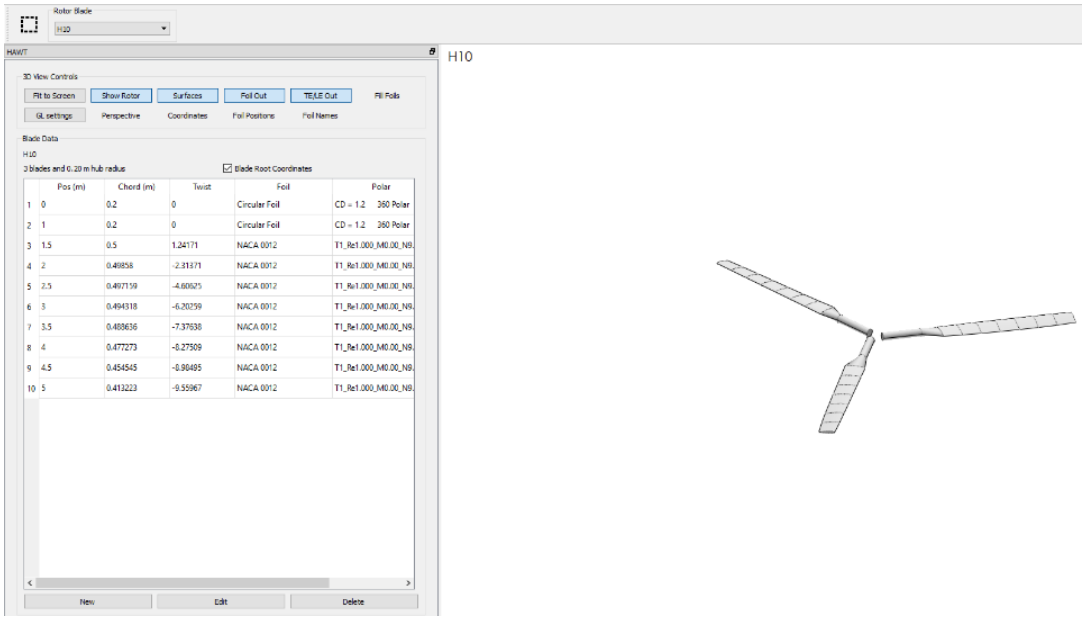

Figure B-10: Three- bladed Horizontal Axis Wind Turbine design module

Rotor blades have an optimal tip speed ratio designed, at which they will produce maximum power. The power generated by a wind turbine is proportional to the air mass lifted/ raised by the rotor blades in a given time. An increase in tip speed ratio results in decrease in the mass being lifted and affects the power output. The power curve in Figure B-11 shows the correlation between power output and TSR and power output reaches its maximum values for tip speed ratios of 4 to 7. It is intended that wind turbine be operated in that range of tip speed ratios for maintaining high power output. The corresponding results of tip speed ratio for maximum powers verify it as tabulated in Table B-6.

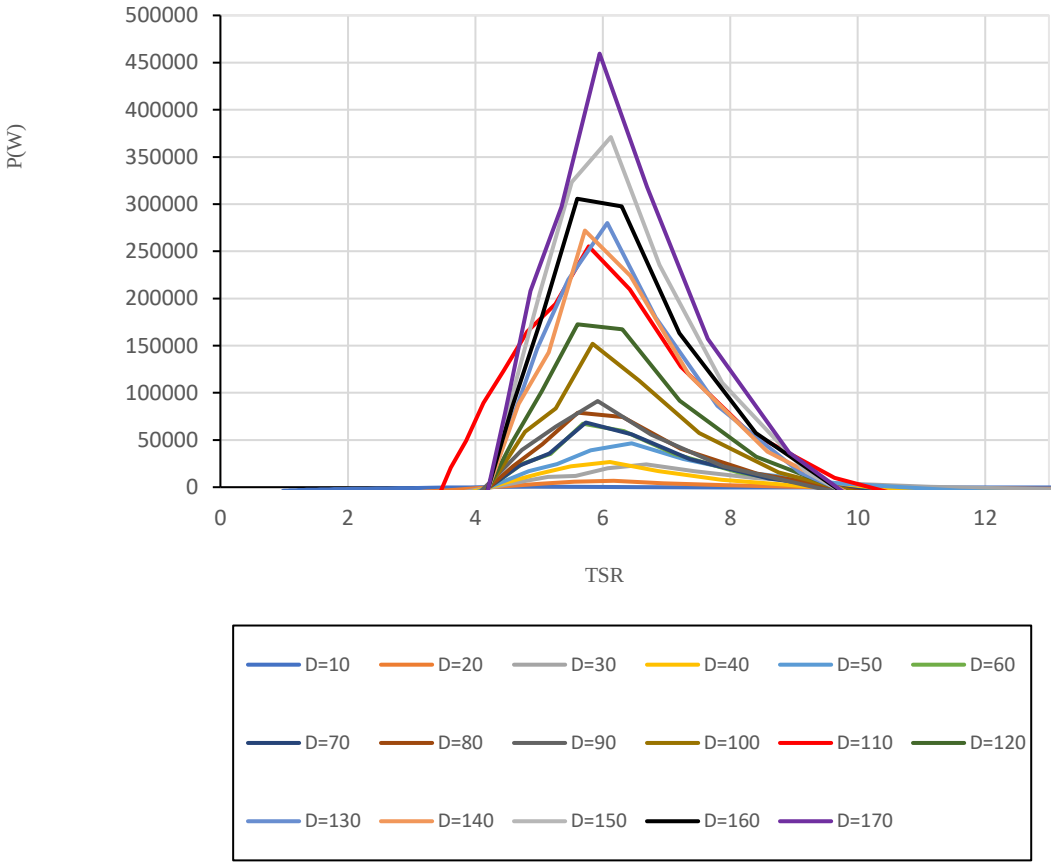

Figure B-11: Power Vs Tip Speed Ratio in HAWTs

Table B-6: Corresponding tip speed ratios for maximum powers

Diameter(m)	Pmax(W)	TSR
10	660.789	4.90088
20	6800.67	6.17148
30	24170.6	6.68531
40	26687	6.11098
50	46500	6.45
60	67300	5.69
70	68528.2	5.73399
80	79000	5.61
90	91300	5.92
100	152000	5.84
110	255247	5.78053
120	172598	5.60367
130	280000	6.07
140	272000	5.72
150	371064	6.12494
160	305689	5.59902
170	459483	5.94808

The maximum power coefficient can be found 0.43 for a 3 blade HAWT with D=30 m for a tip speed ratio of 6.69, as shown in Figure B-12.

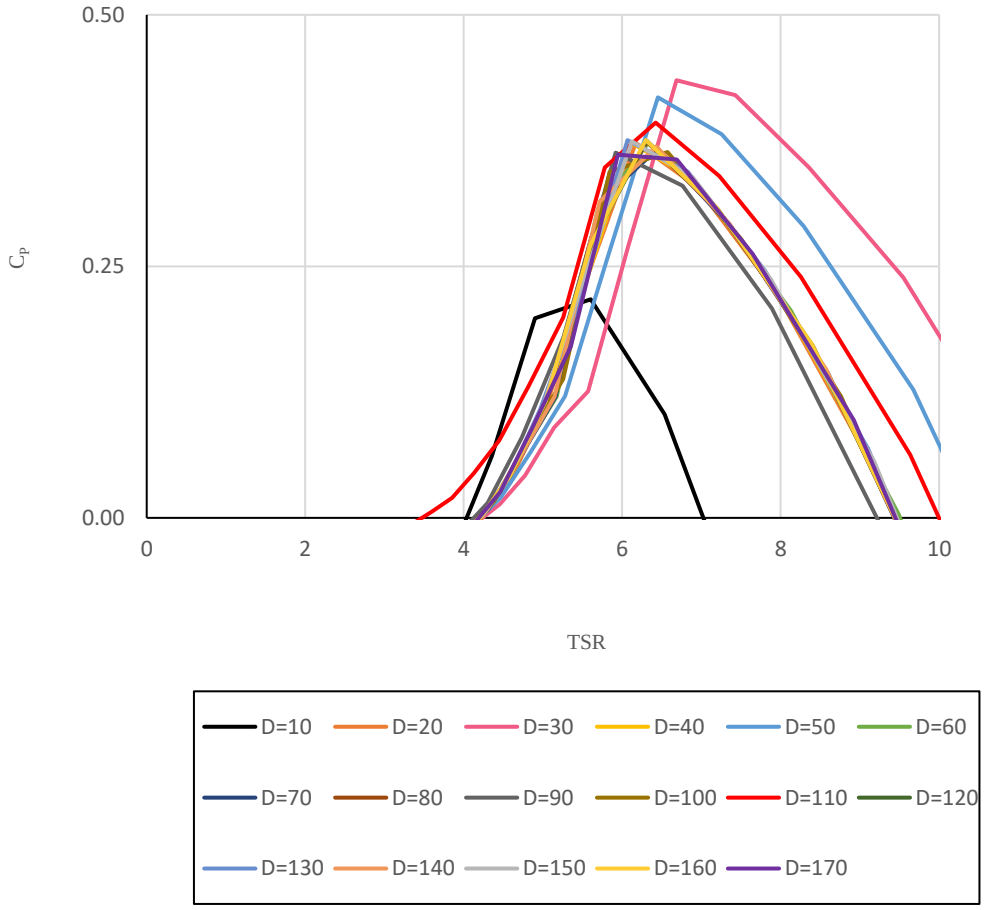

Figure B-12: Power Coefficient Vs Tip Speed Ratio in HAWTs

The power generated for different configuration of HAWT is shown in Figure B-13. From Figure B.12 can be understood that in all cases (D=10 to 170 m) maximum power generates in wind speed range of 4 to 5 m/s. To make trend clearer, maximum power values for each diameter imported and shown in Figure B-14.

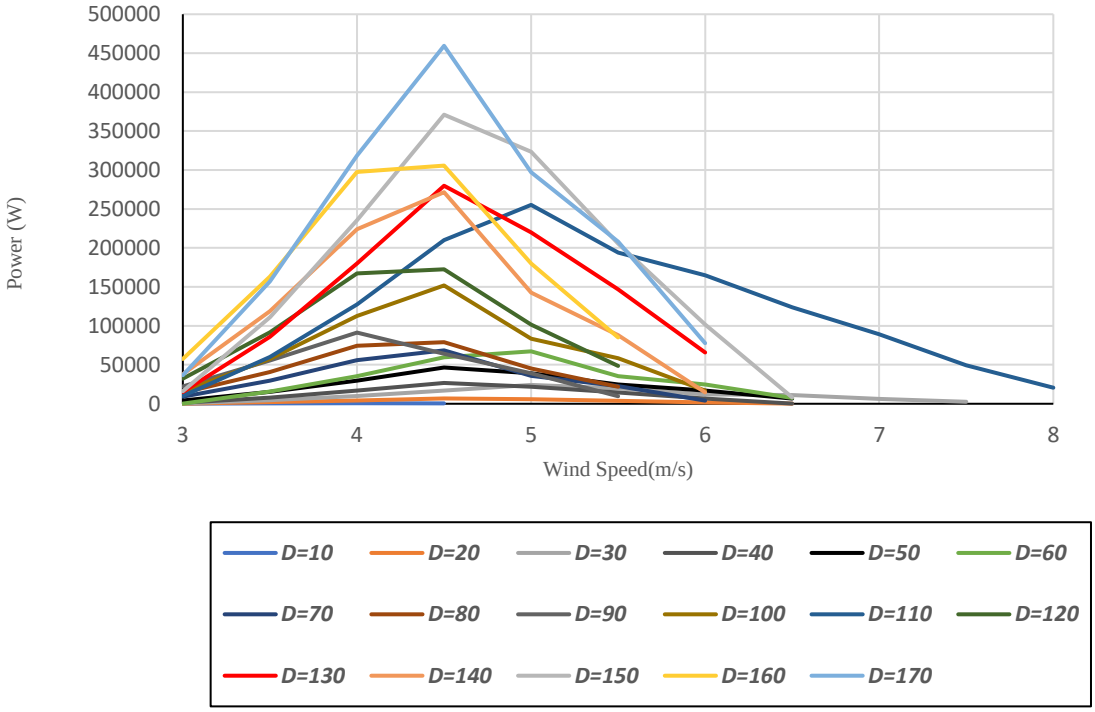

Figure B-13: Output power Vs Wind Speed in HAWTs

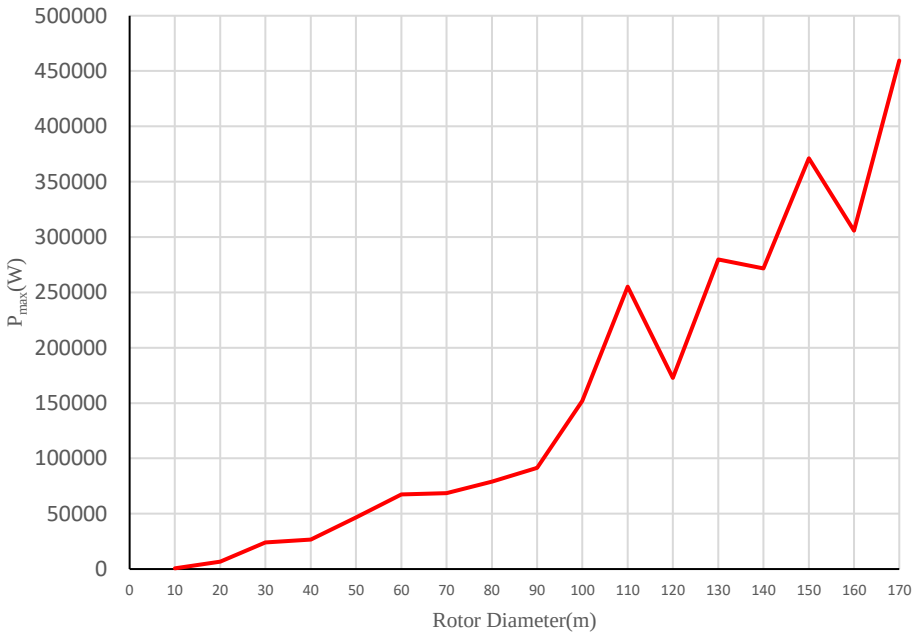

Figure B-14: Maximum power Vs Rotor Diameter in HAWTs

From Figure B-12, the trend is rising except rotor diameters 120,140 and 160 m which in case of D = 140 m is a slight fall.

In this part, different turbines in terms of rotor diameter are compared. Choosing a proper length for rotors is essential for two aspects; cost-effectiveness and power

generation. In terms of power generation, the maximum power achieves respectively from diameter: 170, 150, 160, 130,140, 110, 120, 100, …10. However, the maximum power coefficient of 0.43 achieves for D=30 m and in this case also highest tip speed ratio of 6.68 happens. Changing rotor diameter from 10 m to 20m increases power generation 10 times. Generated power of diameter 170 is 1.5 times of 160 m. Changing diameter from 90 to 110 m increases power 164 kW. Also, it can be concluded if we want to design a turbine in range of rotor diameters 90 to 140 m (in term of cost-effectiveness), the best options are 130 and 110 m respectively and again for range of 130 to 160 m, the best options are 150 and 130 m respectively.

B.7 Effect of number of blades on output power

To find which type of HAWT/VAWT in terms of the number of blades provides higher efficiency, a comparison is presented among 2 and 3 blade turbines here. Q-Blade is open-source wind turbine rotor blade calculation and design software [27]. Q-Blade software allows us to define an airfoil, compute its extreme performance and directly integrates with the wind turbine rotor design and simulation. The blade design module in QBlade allows the efficient and intuitive design of HAWT or VAWT rotor geometries. Blade geometry is defined by a distribution of airfoil geometries at selected sections over the length of the blade [239]. The design module for a three-blade VAWT is shown in Figure B-15, and with changing the number of blades 3 analysis will be done.

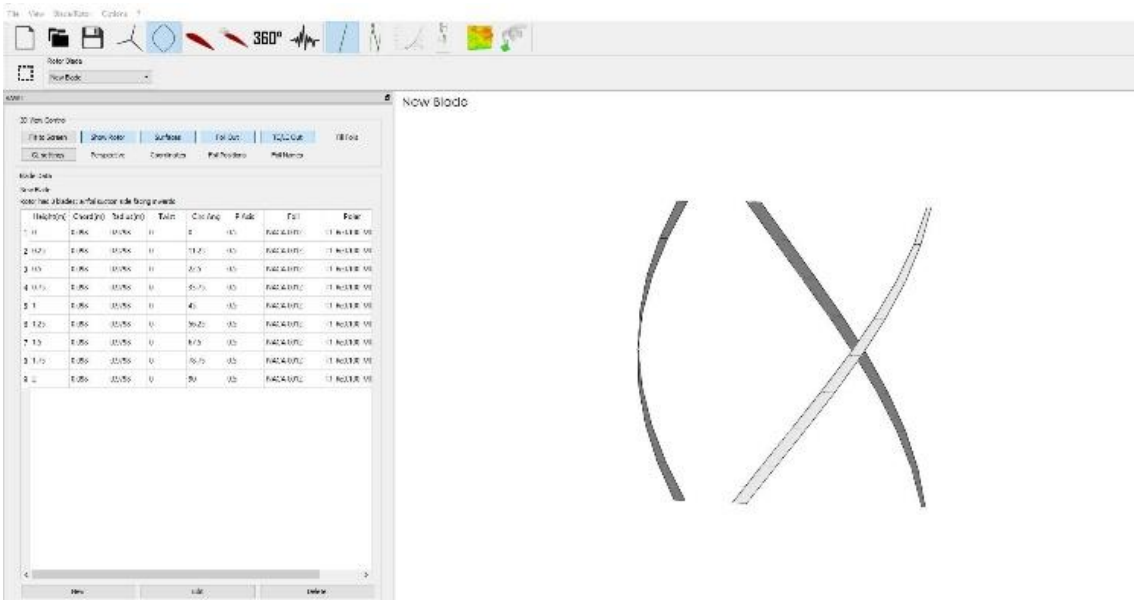

Figure B-15: Three-Bladed Vertical Axis Wind Turbine design module

The design module for a three-blade HAWT is shown in Figure B-16 and like VAWT with changing the number of blades 3 analysis will be done.

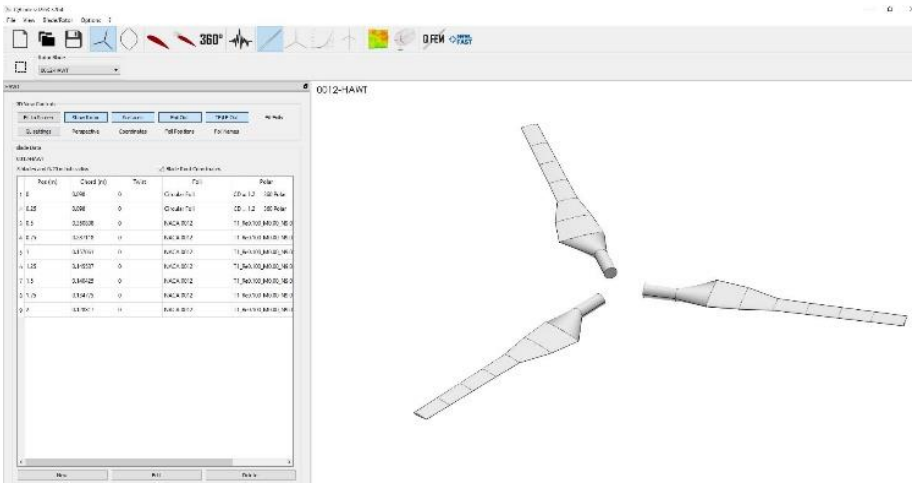

Figure B-16: 3- bladed Horizontal Axis Wind Turbine design module

Rotor blades have an optimal tip speed ratio designed, at which they will produce maximum power. The power generated by a wind turbine is proportional to the air mass lifted/ raised by the rotor blades in a given time. An increase in tip speed ratio results in decrease in the mass being lifted and affects the power output. The power curve in Figure 15 shows the correlation between power output and TSR and power output reaches its maximum values for tip speed ratios of 4 to 7. It is intended that

wind turbine be operated in that range of tip speed ratios for maintaining high power output. In optimal tip speed ratio of 6.91, the maximum out power in HAWTs can be achieved which as tabulated in Table B.7 is respectively 234, 329 for 2 and 3 blade HAWT as shown in Figure B-17.

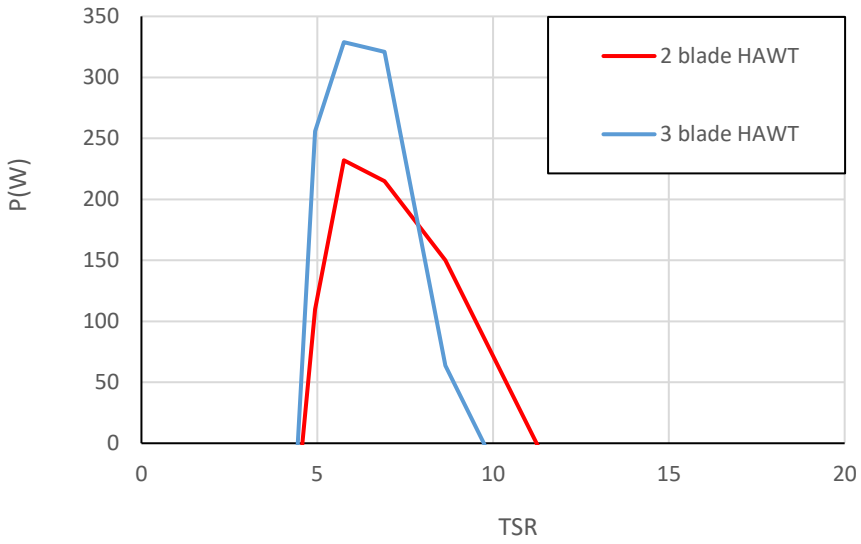

Figure B-17: Power Vs Tip Speed Ratio in HAWTs

In VAWTs with the different number of blades optimal tip speed ratio is not the same. From Figure B-15, it can be seen that the optimal TSR for 2 and 3 blade VAWT is 3.84 which in this value the maximum power in 2 blades is 46.07 W and in 3 blade is 59.51 W as shown in Figure B-18.

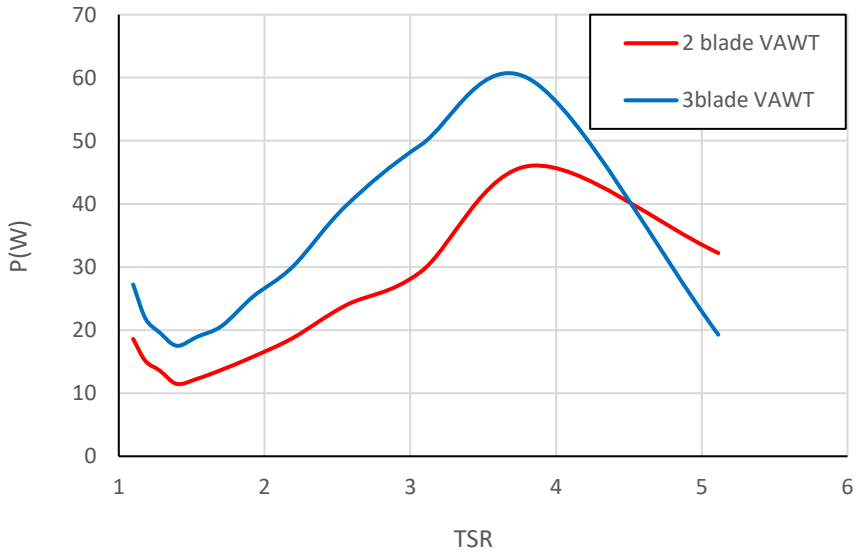

Figure B-18: Power Vs Tip Speed Ratio in VAWTs

The maximum power coefficient can be found 0.28 for a 3 blade HAWT for a tip speed ratio of 6.91, shown in Figure B-19.

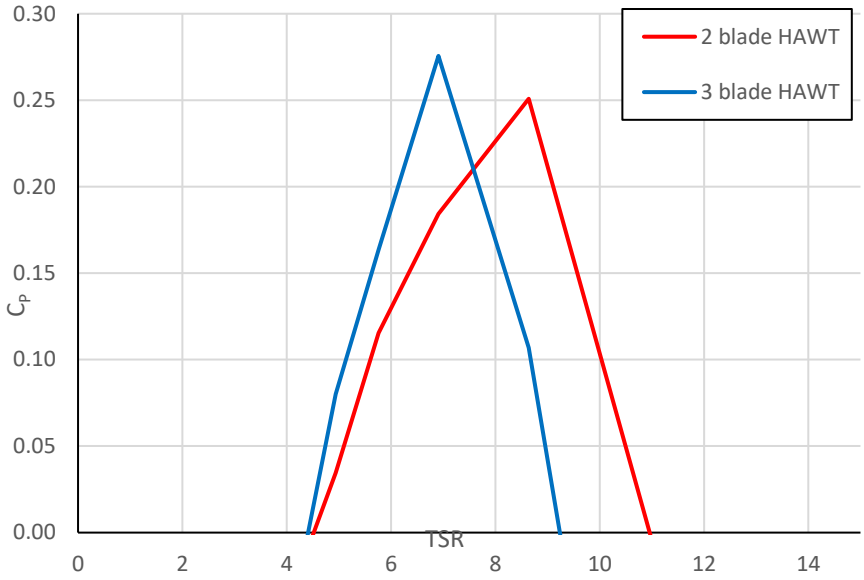

Figure B-19: Power Coefficient Vs Tip Speed Ratio in HAWTs

The maximum power coefficient can be found 0.49 for a 2 blade VAWT for a tip speed ratio of 5.11, shown in Figure B-20.

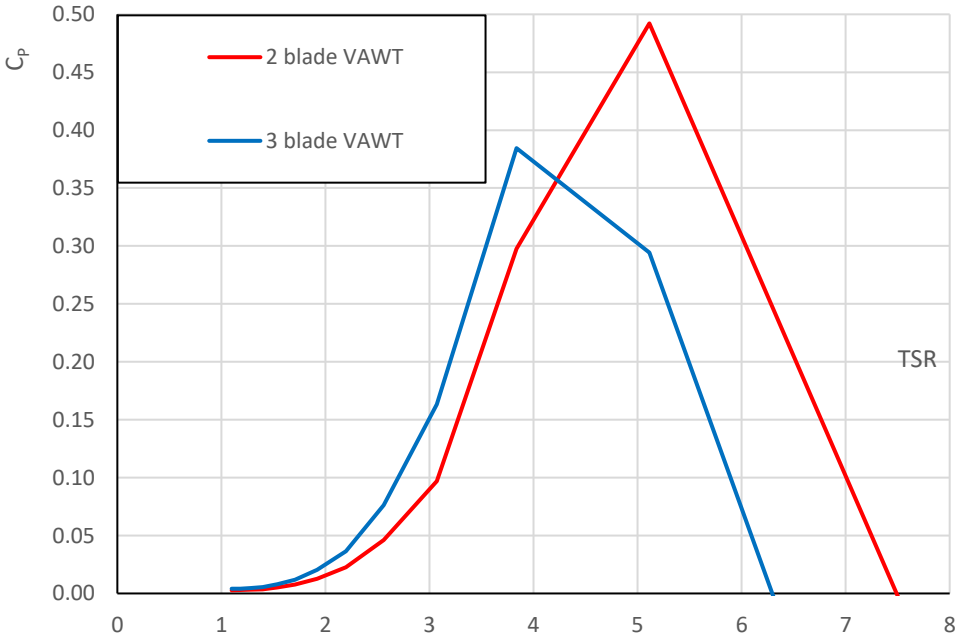

Figure B-20: Power Coefficient Vs Tip Speed Ratio in VAWTs

The power generated for different configuration of HAWT and VAWT is shown respectively in Figure B-21 and Figure B-22.

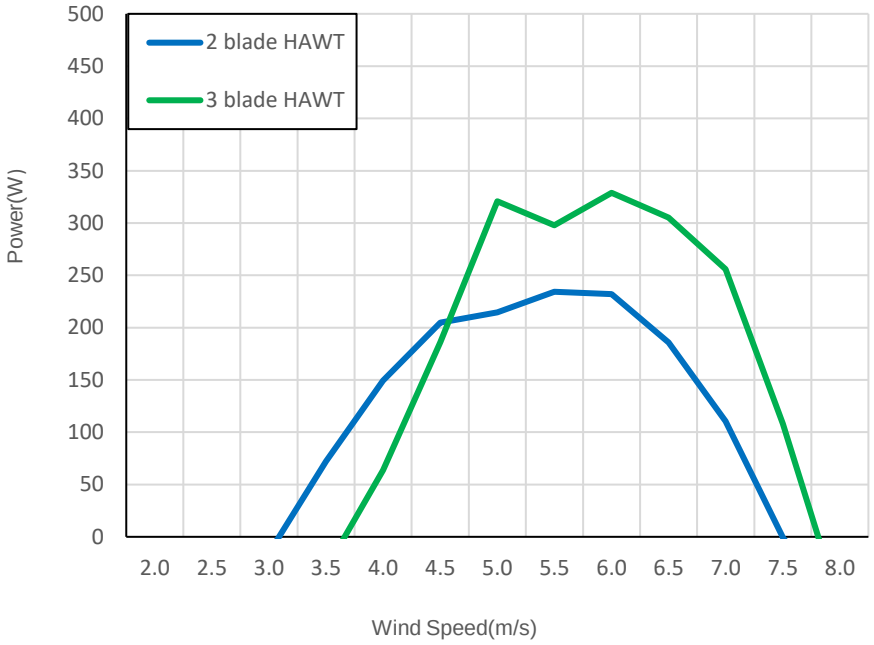

Figure B-21: Output power for 2,3 and 4 blade HAWTs Axis

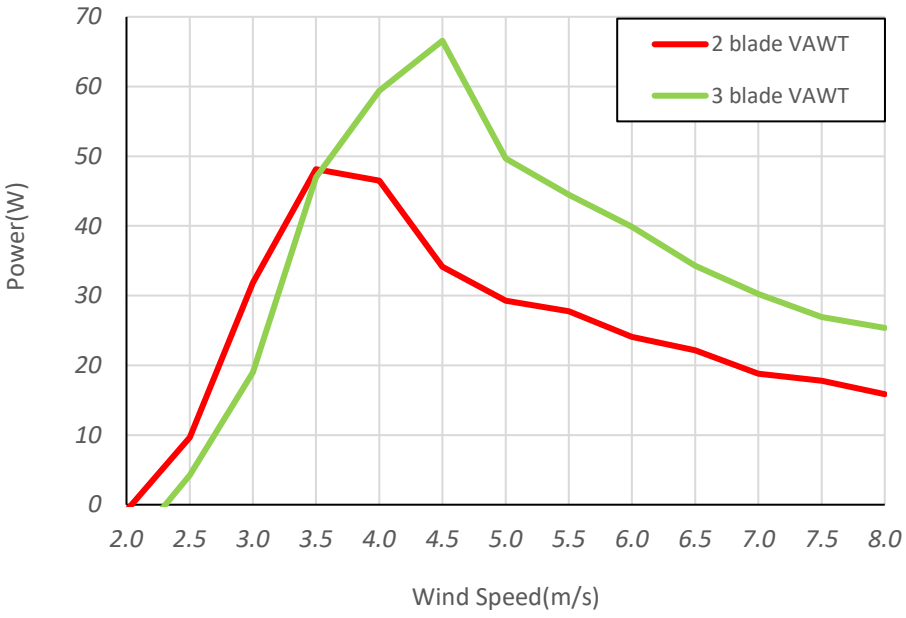

Figure B-22: Output power for 2,3 and 4 blade VAWTs Axis

The results of Figure B-21 and Figure B-22 tabulated in Table B-7.

Table B-7: Maximum power coefficient in Wind turbines

Turbine Type	C_{Pmax}
2 blade HAWT	0.25 @ TSR=8.64
3 blade HAWT	0.28 @ TSR=6.91
2 blade VAWT	0.49 @ TSR=5.11
3 blade VAWT	0.38 @ TSR=3.84

From the results it shows that HAWTs with the same number of blades can generate more than 4 times than the corresponding VAWT. However, maximum power appears in lower wind speeds for VAWTs in comparison to HAWTs. In VAWT, the optimal TSR happens in less than 4 and with adding another blade to design it decreases from 5.11 to 3.84. The blade profile is optimised to increase the power coefficient. Power coefficient is maximised to value 0.49 for a 2 blade VAWT for a tip speed ratio of 5.11 and 0.28 for a 3 blade HAWT for a tip speed ratio of 6.91.

B.8 Effect of rotational speed on output power

The selected airfoil for simulation with QBlade of VAWT and HAWT is the NACA 0012. A Reynolds value of 100000 was used for a rotor diameter (D) of 7 m with rotational speed is 150 rpm with is the optimized rotational speed for normal wind speed conditions (5-6 m/s) according to simulations done in different rpms with QBlade. The results of simulations in different rpms are given in Table Table B-8 and Table B-9.

Table B-8: P_{max} for different rpms for NASA 0012-HAWT

RPM	Pmax
100	97.5 W @ V=4 m/s
150	329 W @ V=6 m/s
200	779.5 W @ V=8 m/s
300	2646.8 W @ V=12.5 m/s
400	6328.8 W @ V=13.5 m/s
500	12180 W @ V=20 m/s

Table B-9: P_{max} for different rpms for NASA 0012-VAWT

RPM	Pmax
100	19.7 W @ V=3 m/s
150	66.5 W @ V=4.5 m/s
200	157.6 W @ V=6 m/s
300	532.5 W @ V=9 m/s
400	1262.3 W @ V=12 m/s
500	2464 W @ V=15 m/s

As B (number of blades) in both calculations are 3, tip speed ratio will be 5.1 according to equation **Error! Reference source not found.**. So, the chord length i s 0.35 m with respect to below formula [238]:

$$C = \frac{4D}{\lambda^2 B} \quad \text{0-8)}$$

The maximum power for VAWT is reached at wind speed 4.5 m/s which is P=66.5 W. While it is 329 W for HWAT at wind speed 6 m/s, shown in Figure B-23

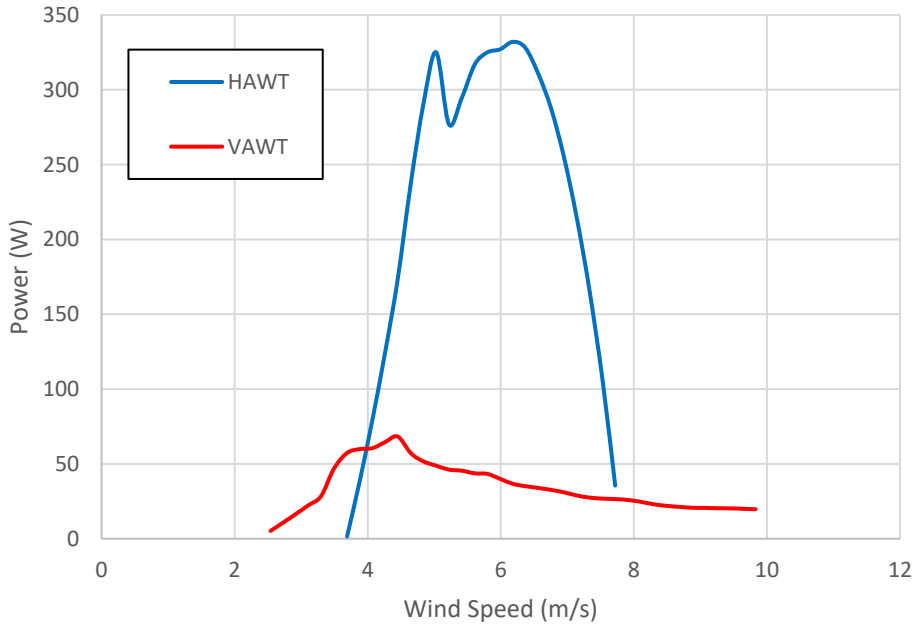

Figure B-23: Power versus wind velocity

In both cases, the blade has a C_l/C_d maximum at the angle of attack 5 or the optimized angle of attack is 5, shown in Figure B-24.

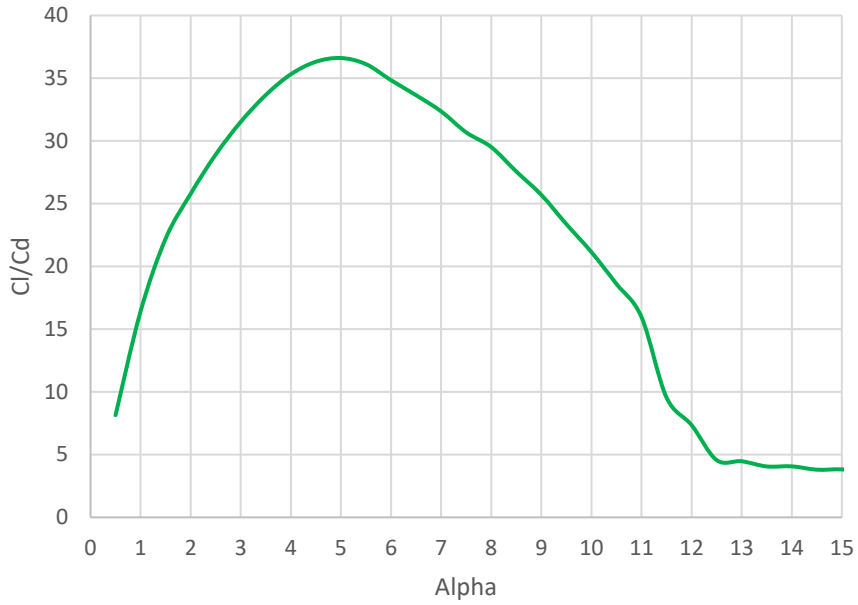

Figure B-24: C_l/C_d for different angle of attacks (a)VAWT (b)HAWT

The maximum power coefficient for VAWT was found 0.44 and for HAWT 0.25, shown in Figure B-25.

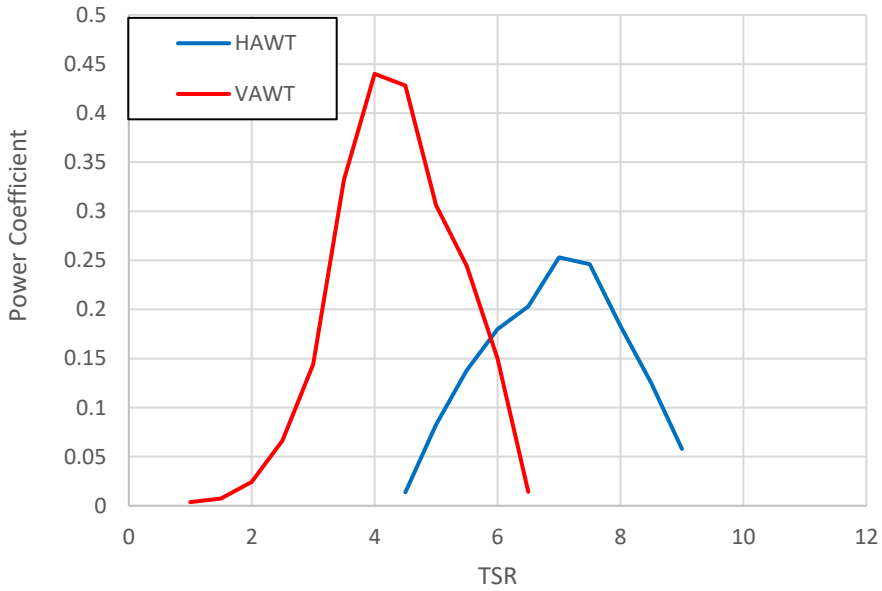

Figure B-25: Power Coefficient vs TSR

Simulation models for HAWT and VAWT are shown in Figure B-26.

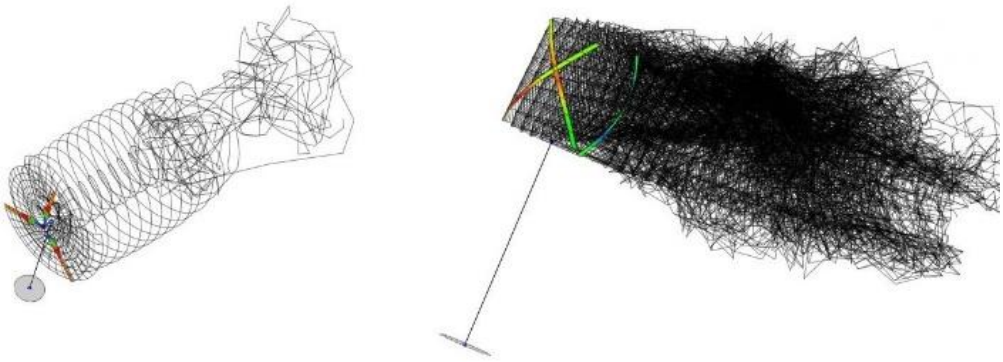

Figure B-26: Simulation of VAWT (left) and HAWT (right)

With respect to considering all parameters involved in this research, it can be recommended that using HAWT can gets much more electricity to VAWT. To reach this conclusion, the power generation of both turbines in different wind speeds calculated and QBlade results also showed higher power for HAWT. Changing rotor radiuses also verify that in the same rotor radiuses, HAWT can get more power rather VAWT.

The optimized angle of attack for both cases is 5, and best performance for HAWT is in wind speed of 15 m/s while it is for VAWT in 11 m/s.

B.9 Air/water density

The density of air at standard conditions is $\rho = 1.293$ kg/m^3. But, if elevation and temperature increase, it decreases, as shown in Figure B-27.

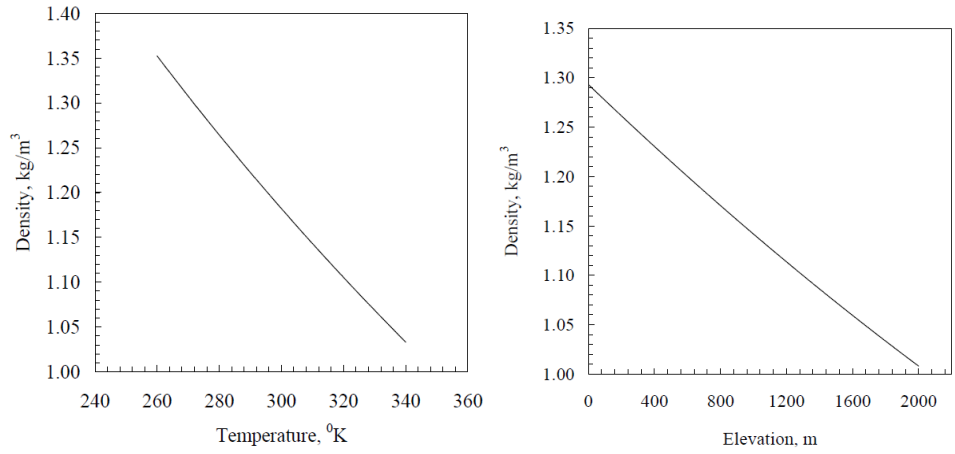

Figure B-27:Effect of elevation and temperature on air density [230].

By knowing temperature and elevation, the density can be calculated using equation (B-9 [230].

$$\rho = \frac{353.049}{T} e^{(-0.034\frac{Z}{T})} \quad \text{(B-9)}$$

So, according to power equation (equation B-4), the higher the temperature/elevation, the lower output power.

In case of effect of water depth on output power, relying to Bernoulli `s principle is helpful:

$$\frac{\boldsymbol{V_0^2}}{\boldsymbol{2g}} + \frac{\boldsymbol{p_0}}{\boldsymbol{\rho_a g}} + \boldsymbol{z_0} = \frac{\boldsymbol{V_1^2}}{\boldsymbol{2g}} + \frac{\boldsymbol{p_1}}{\boldsymbol{\rho_e g}} + \boldsymbol{z_1} + \sum \boldsymbol{H_{L(0\rightarrow 1)}} \quad \text{(B-10)}$$

where V is the velocity [m/s], p is the pressure [Pa], z is the elevation above an arbitrary datum [m], $\_\sum H_{L(0\rightarrow 1)}/$ is the total head loss between locations (0) and (1) [m], ρ_e is the density of effluent [kg/m^3], ρ_a is the density of ambient seawater [kg/m^3].

Density differences tend to be of the order of $(|\rho_e - \rho_a|/\rho_a) \times 100 \approx$ 3% for most sewage and desalination applications. Although this difference corresponds to a relatively small change to outfall shaft level when discharging into shallow waters, equation (B-10 shows that the density ratio effect is amplified for deeper outfall discharges. In addition to changes in plant operating conditions which could increase or decrease outlet flows, changes in sea level will also cause the outfall shaft effluent level to vary. The outfall system design should therefore consider the entire range of sea levels that could occur over the project design life, accounting for tidal fluctuations as well as storm surge. Statistical methods can be applied to sea level time series at the project location in order to determine exceedance probabilities and recurrence intervals. Using sound engineering judgment in conjunction with project requirements and/or local design standards for infrastructure design life, the results of the statistical analysis can be used to select design values for minimum and maximum sea level. To capture any seasonal trends

which could include wind and barometric effects, sea level data used in the statistical analysis should include field measurements taken regularly throughout the year. It is imperative that data specific to the project location is used because sea level characteristics can vary greatly from one locale to another, regardless of the distance between them. An allowance for sea level rises due to the effects of climate change should also be included because it could have a significant impact on maximum outfall shaft fluid level. Some statistical models estimate that the sea level will rise more than 1m by the year 2100 [240].

B.10 Air/water temperature

As explained before and according to equation (B.14), temperature change affects air density, and as a result, it changes output power expected from the turbine. To find its effect, generated electricity from using HAWT and VAWT in a moderate climate city (Auckland-New Zealand) is compared with a warm town (Ahvaz-Iran) and a cold city (Winnipeg-Canada). The Qblade results are shown in Figure B-28 and Figure B-29.

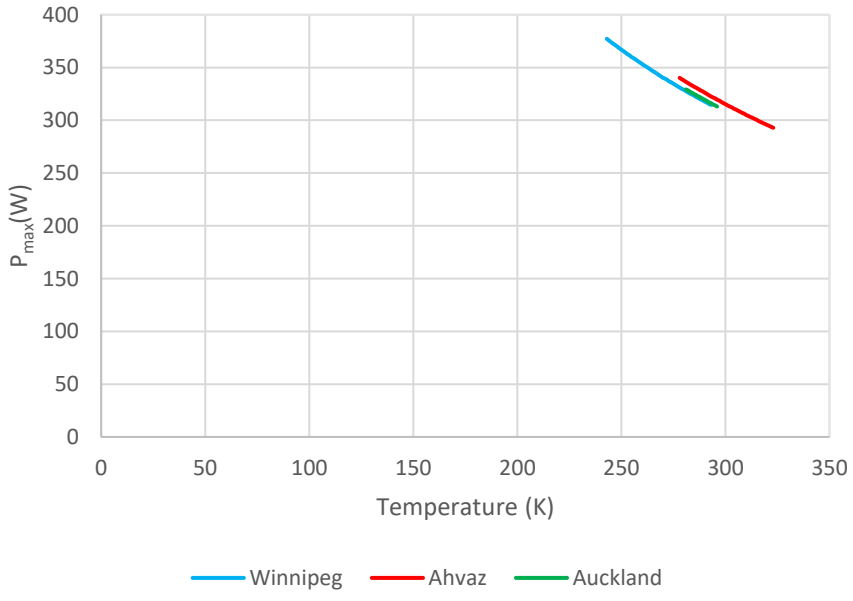

Figure B-28:Change of HAWT with temperature

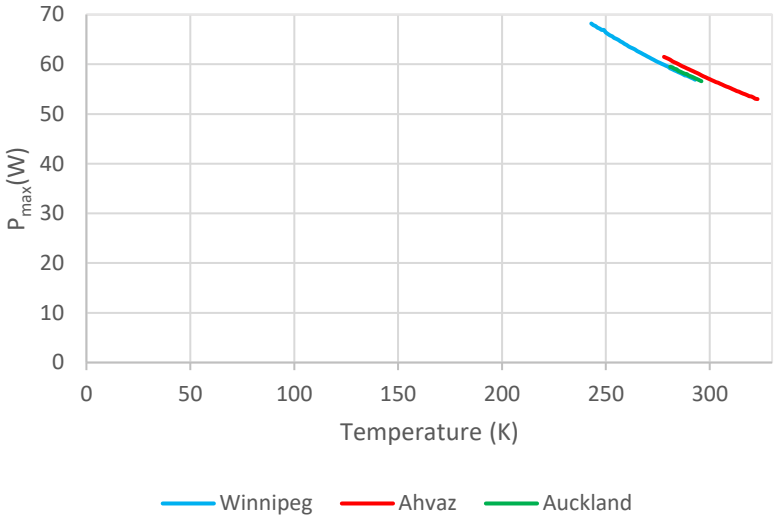

Figure B-29: Change of VAWT with temperature

From both figures, it can be concluded that:

1-Increasing temperature decreases generated power in wind turbines. However, generated power in horizontal type is 5 to 6 times more than vertical type.

2-In cold conditions, air density increases and as a result, output power is more than warm conditions.

Isle of Islay is a coastal city in United Kingdom. It is a quite dense city close to the water with a population of 3457 people. The water temperature around Isle of Islay changes moderately throughout the year. The temperature range varies throughout the year from 7°C (44.5°F) up to 13.2°C (55.7°F). To find effect of temperature on performance this turbine, density and viscosity of water in the temperature range of 7°C to 13 °C calculated for a 3 bladed tidal turbine. The hydrofoil NACA 4412 is used for this case for a range of -15° to 18° at Reynolds number of 250,000 to match an experiment by Pinkerton [146]. Rotor diameter and speed is considered respectively 20m and 11.5 rpm. NACA 4412 was chosen because of its good lift performance and good lift to drag ratio even at post stall. [85]. Assuming 10 °C the temperature of sea, water density and viscosity for simulation be 999.65 kg/m3 and 0.0000013081 m^2/s. The swept area using two rotors is 628m^2. The SeaGen-S model [241] was ran in Strangford Lough from 2008 to 2016.

Airfoil : NACA 4412

Speed Range: 1-2.5 m/s

Rotor Diameter: 20m

Hub Diameter: 0.4m

Reynolds: 250,000

Rotational Speed: 4-11.5 rpm

$\rho = 999.65\ kg/m^3$

$\vartheta = 0.0000013081\ m^2/s$

The simulation results show that changing temperature does not affect power coefficient and in all this range, it is 0.48 at tip speed ratio of 6.14. However, with increasing temperature generated power decreases and for velocity speed of 3 m/s, this drop from 7°C to 13 °C is 600 W as shown in Figure B-30.

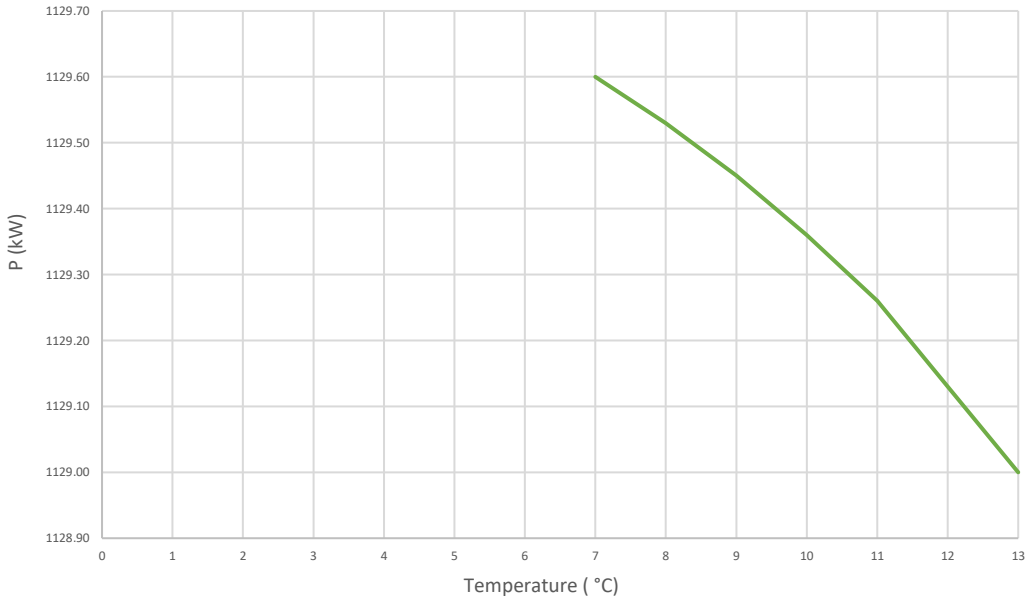

Figure B-30:Effect of Temperature on Output Power

B.11 Air/water Velocity

To find, which type of mentioned turbines have a better performance, power generated in the wind range of 5 to 15 is calculated. Here, ρ is the density (kg/m^3) of air which is 1.225 kg/m^3, and TSA is πR^2. For R=3.5m, TSA will be 38.451001 m^2. Just C_P remained which is dependent on λ or tip speed ratio, and it changes with changing λ. λ Can be calculated for any of wind speeds with:

$$\lambda = \frac{blade\ tip\ speed}{wind\ speed} = \frac{\frac{rpm \times \pi \times D}{60}}{wind\ speed} \quad \text{(B-11)}$$

After calculating λ , from C_P- λ diagram as shown in Figure B-31, C_P can be achieved and by putting it in equation (B-4), the output power results as shown in Figure B-32.

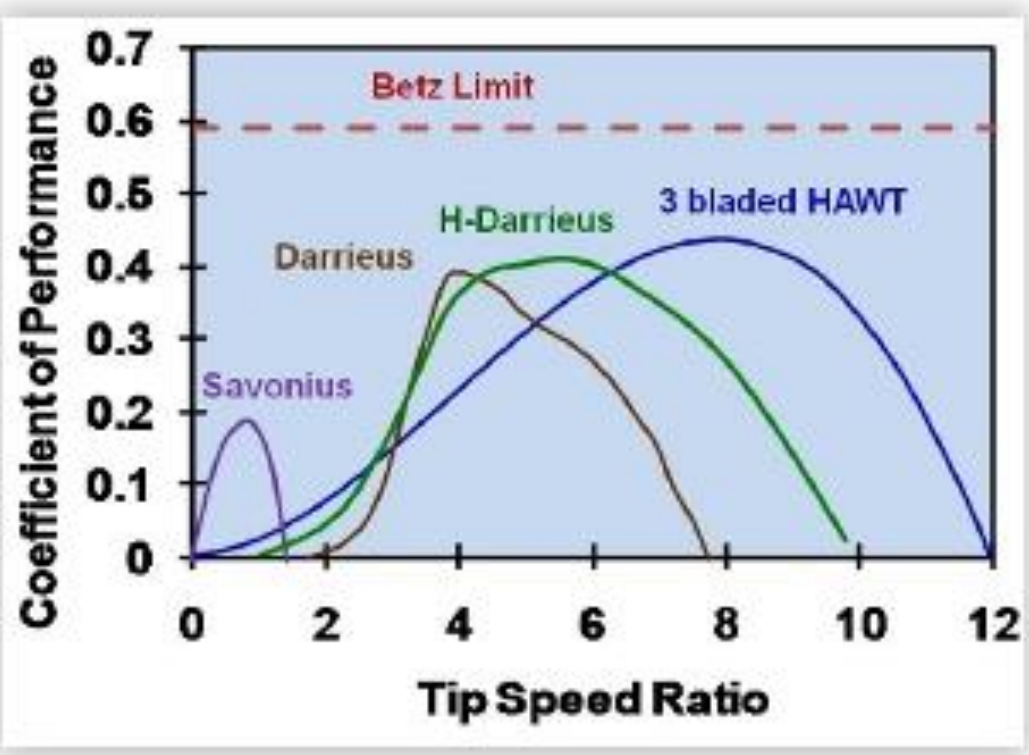

Figure B-31: C_P- λ diagram [242].

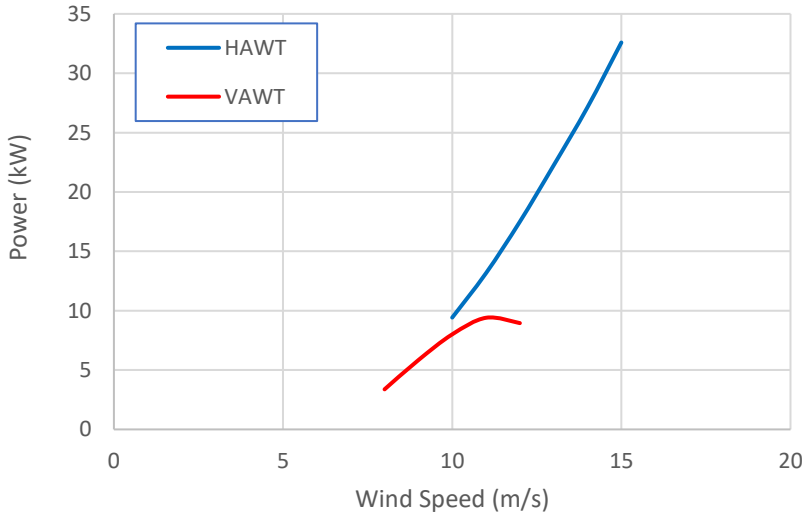

Figure B-32:The effect of wind speed on the output power of wind turbines

From Figure B-32, shows that VAWT type (i.e. Darrieus) cannot work in the wind speeds less than 8 m/s. However, its generated power in wind speeds 10.5 m/s and onwards is much better in comparison to HAWT. The Maximum power for both kinds of turbines generate in 14 m/s wind speed which is $1.42x10^4$ W for HAWT and $2.52x10^4$ W for VAWT.

Tidal current technology extracts the kinetic energy in a similar way to harvest wind energy from air. However, there are several differences in the operating conditions. Operating under similar conditions, water is 832 times denser than air, and the water flow speed generally is much smaller. Due to the difference in density between both fluids, the power intensity in water currents is significantly higher than air streams. Consequently, water current turbine can be built considerably smaller than an equivalent powered turbine. In contrast to atmospheric air flows, the availability of tidal currents can be predicted very accurately [227].

Appendix C Python Codes for Microgrid Design

C.1 RMS Tidal Currents


```
{
 "cells": [
  {
   "cell_type": "code",
   "execution_count": 1,
   "metadata": {},
   "outputs": [],
   "source": [
    "# import necessary python packages\n",
    "# note: for this particular code to\n",
    "# work, you need these to be installed\n",
    "# in python.  I recommend installing \n",
    "# python using anaconda, since it is \n",
    "# often easier to get dask to work\n",
    "# with conda instead of pip\n",
    "\n",
    "#THe first two lines should\n",
    "# already be included in your base python package,\n",
    "# so no need to install:\n",
    "import sys,os\n",
    "from collections import namedtuple\n",
    "\n",
    "# These you need to install with conda or pip\n",
    "# For example: conda install numpy\n",
    "# Glob will probably be conda install glob2\n",
    "# The full list will look something like\n",
    "# conda install numpy, pandas, netcdf4, xarray, glob2, datetime, dask\n",
    "import numpy as np\n",
    "import pandas as pd\n",
    "import netCDF4\n",
```

```
   "import xarray as xr\n",
   "import glob\n",
   "from datetime import datetime\n",
   "import datetime as dt\n",
   "import dask"
  ]
 },
 {
  "cell_type": "code",
  "execution_count": 2,
  "metadata": {},
  "outputs": [],
  "source": [
   "# Choose start and end date, within Moana model time range:\n",
   "start_date = '2017-01-01'\n",
   "end_date = '2017-12-01'\n",
   "\n",
   "# this is where to find the data (note: this is the old version of the backbone model)\n",
   "base_url =
'http://thredds.moanaproject.org:8080/thredds/dodsC/moana/ocean/NZB/v1.9/processed_3D/nz5km
%Y%m%d_00z_3D.nc'\n",
   "\n",
   "# Create list of files to be downloaded between start_date and end_date\n",
   "dates= pd.date_range(start_date, end_date, freq='1M')-pd.offsets.MonthBegin(1)\n",
   "files = [day.strftime(base_url) for day in dates]\n",
   "\n",
   "# Open list of files as single dataset as variable ds\n",
   "ds = xr.open_mfdataset(files, chunks={'time':1}, combine='by_coords', drop_variables =
['dep','temp','salt'])"
  ]
 },
 {
  "cell_type": "code",
  "execution_count": 3,
  "metadata": {},
```

```
 "outputs": [],
 "source": [
  "# create lists of coordinate pairs \n",
  "# in this example, we'll extract data at \n",
  "# three locations.  The first is at\n",
  "# -47.5deg latitude, 167deg longitude\n",
  "\n",
  "lats = [-47.5]\n",
  "lons = [167]\n",
  "\n",
  "# zip together for use later\n",
  "locations = zip(lats,lons)"
 ]
},
{
 "cell_type": "code",
 "execution_count": 5,
 "metadata": {},
 "outputs": [],
 "source": [
  "file_dir = r'C:\\Users\\Windows\\Desktop'\n",
  "\n",
  "# This block of code iterates through all the lat/lon\n",
  "# coordinate pairs in locations.  For each location,\n",
  "# it calculates the depth-average current speed and direction\n",
  "# over all depths at that location.  The result\n",
  "# is a pandas dataframe with arrays size 1xtime for\n",
  "# current speed and current direction.\n",
  "for latv,lonv in locations:\n",
  "    # get the model data, u and v current speeds, takes the depth-average:\n",
  "    da = ds.sel(dict(lat=latv,lon=lonv),method='nearest').mean(dim='lev', skipna=True)\n",
  "    # values are stored in an xarray dataset, just pull out the actual values\n",
  "    # so we can work with them more easily\n",
  "    u = da['u'].values\n",
  "    # only bother going ahead if all u values aren't nan:\n",
```

```
"    if not np.isnan(u).all():\n",
    "        # get the v values too\n",
    "        v = da['v'].values\n",
    "        # calculate current speed and direction from u and v\n",
    "        speed = np.sqrt(u**2+v**2)\n",
    "        direction = np.mod(np.rad2deg(np.arctan2(u, v)),360)\n",
    "        # convert time to something that python understands\n",
    "        time = pd.to_datetime(da['time'].values)\n",
    "        # create a pandas dataframe, which is useful for saving as csv format\n",
    "                    data = {'year':time.year, 'month':time.month, 'day':time.day, 'speed':speed,
'direction':direction} \n",
    "        df = pd.DataFrame(data)\n",
    "        # save output as csv\n",
    "        file_name = f'moana_current_2017_{lonv}_{latv}.csv'\n",
    "        file_path = os.path.join(file_dir,file_name)\n",
    "        df.to_csv(file_path)"
   ]
  },
  {
   "cell_type": "code",
   "execution_count": null,
   "metadata": {},
   "outputs": [],
   "source": [
    "[]"
   ]
  }
 ],
 "metadata": {
  "hide_input": false,
  "kernelspec": {
   "display_name": "Python 3",
   "language": "python",
   "name": "python3"
  },
```

C.2 Tidal Currents in Different Heights


```
{
 "cells": [
  {
   "cell_type": "code",
   "execution_count": 1,
   "metadata": {},
   "outputs": [],
   "source": [
    "#THe first two lines should\n",
    "# already be included in your base python package,\n",
    "# so no need to install:\n",
    "import sys,os\n",
    "from collections import namedtuple\n",
    "\n",
    "# These you need to install with conda or pip\n",
    "# For example: conda install numpy\n",
    "# Glob will probably be conda install glob2\n",
    "# The full list will look something like\n",
    "# conda install numpy, pandas, netcdf4, xarray, glob2, datetime, dask\n",
    "import numpy as np\n",
    "import pandas as pd\n",
    "import netCDF4\n",
    "import xarray as xr\n",
    "import glob\n",
    "from datetime import datetime\n",
    "import datetime as dt\n",
    "import dask"
   ]
  },
  {
   "cell_type": "markdown",
   "metadata": {},
```

```
  "source": [
   "# Processed Model Data Setup"
  ]
 },
 {
  "cell_type": "code",
  "execution_count": 32,
  "metadata": {},
  "outputs": [],
  "source": [
   "# Choose start and end date, within Moana model time range:\n",
   "start_date = '2017-01-01'\n",
   "end_date = '2017-12-01'\n",
   "'\n",
   "# this is where to find the data (note: this is the old version of the backbone model)\n",
   "#base_url =
'http://thredds.moanaproject.org:8080/thredds/dodsC/moana/ocean/NZB/v1.9/processed_3D/nz5km
%Y%m%d_00z_3D.nc'\n",
   "base_url = '/net/datastor1/data/ocean/nz/backbone-v2/nz5km%Y%m%d_00z_3D.nc'\n",
   "'\n",
   "# Create list of files to be downloaded between start_date and end_date\n",
   "dates= pd.date_range(start_date, end_date, freq='1M')-pd.offsets.MonthBegin(1)\n",
   "files = [day.strftime(base_url) for day in dates]\n",
   "#files = [files[i::12] for i in range(12)]\n",
   "files = [files[i:i + 12] for i in range(0, len(files), 12)]"
  ]
 },
 {
  "cell_type": "code",
  "execution_count": 3,
  "metadata": {},
  "outputs": [],
  "source": [
   "# choose lat and lon value\n",
   "'\n",
```

```
 "lon_value = [174.524249]\n",
 "lat_value = [-41.279497]\n",
 "locations = zip(lat_value,lon_value)"
 ]
},
{
 "cell_type": "markdown",
 "metadata": {},
 "source": [
 "# Calculate max depth and specify desired depth"
 ]
},
{
 "cell_type": "code",
 "execution_count": 34,
 "metadata": {},
 "outputs": [
  {
   "name": "stdout",
   "output_type": "stream",
   "text": [
    "Max depth at this point: 250\n",
    "All depths at this point: [  0   5  10  15  20  25  30  50  75 100 125 150 200 250]\n"
   ]
  }
 ],
 "source": [
 "# get the model data, u and v current speeds:\n",
 "da = ds.sel(dict(lat=lat_value,lon=lon_value),method='nearest')\n",
 "\n",
 "# calculate max depth and print below\n",
 "depths = da.isel(time=0).dropna(dim='lev',how='any')['lev'].values\n",
 "\n",
 "lat = da.isel(time=0).dropna(dim='lev',how='any')['lat'].values\n",
 "lon = da.isel(time=0).dropna(dim='lev',how='any')['lon'].values\n",
```

```
 "\n",
 "print(f'Max depth at this point: {np.nanmax(depths)}')\n",
 "print(f'All depths at this point: {depths}')"
]
},
{
"cell_type": "code",
"execution_count": 6,
"metadata": {},
"outputs": [],
"source": [
 "# choose depth (in meters), must be less than or equal to above value, input desired depth here:\n",
 "choose_depth = 45"
]
},
{
"cell_type": "markdown",
"metadata": {},
"source": [
 "# Export currents at chosen depth as csv"
]
},
{
"cell_type": "code",
"execution_count": 33,
"metadata": {},
"outputs": [
 {
  "name": "stdout",
  "output_type": "stream",
  "text": [
   "/net/datastor1/data/ocean/nz/backbone-v2/nz5km20150101_00z_3D.nc\n",
   "/net/datastor1/data/ocean/nz/backbone-v2/nz5km20150201_00z_3D.nc\n",
   "/net/datastor1/data/ocean/nz/backbone-v2/nz5km20150301_00z_3D.nc\n",
   "/net/datastor1/data/ocean/nz/backbone-v2/nz5km20150401_00z_3D.nc\n",
```

```
  "/net/datastor1/data/ocean/nz/backbone-v2/nz5km20150501_00z_3D.nc\n",
  "/net/datastor1/data/ocean/nz/backbone-v2/nz5km20150601_00z_3D.nc\n",
  "/net/datastor1/data/ocean/nz/backbone-v2/nz5km20150701_00z_3D.nc\n",
  "/net/datastor1/data/ocean/nz/backbone-v2/nz5km20150801_00z_3D.nc\n",
  "/net/datastor1/data/ocean/nz/backbone-v2/nz5km20150901_00z_3D.nc\n",
  "/net/datastor1/data/ocean/nz/backbone-v2/nz5km20151001_00z_3D.nc\n",
  "/net/datastor1/data/ocean/nz/backbone-v2/nz5km20151101_00z_3D.nc\n",
  "/net/datastor1/data/ocean/nz/backbone-v2/nz5km20151201_00z_3D.nc\n",
  "/net/datastor1/data/ocean/nz/backbone-v2/nz5km20160101_00z_3D.nc\n",
  "/net/datastor1/data/ocean/nz/backbone-v2/nz5km20160201_00z_3D.nc\n",
  "/net/datastor1/data/ocean/nz/backbone-v2/nz5km20160301_00z_3D.nc\n",
  "/net/datastor1/data/ocean/nz/backbone-v2/nz5km20160401_00z_3D.nc\n",
  "/net/datastor1/data/ocean/nz/backbone-v2/nz5km20160501_00z_3D.nc\n",
  "/net/datastor1/data/ocean/nz/backbone-v2/nz5km20160601_00z_3D.nc\n",
  "/net/datastor1/data/ocean/nz/backbone-v2/nz5km20160701_00z_3D.nc\n",
  "/net/datastor1/data/ocean/nz/backbone-v2/nz5km20160801_00z_3D.nc\n",
  "/net/datastor1/data/ocean/nz/backbone-v2/nz5km20160901_00z_3D.nc\n",
  "/net/datastor1/data/ocean/nz/backbone-v2/nz5km20161001_00z_3D.nc\n",
  "/net/datastor1/data/ocean/nz/backbone-v2/nz5km20161101_00z_3D.nc\n",
  "/net/datastor1/data/ocean/nz/backbone-v2/nz5km20161201_00z_3D.nc\n",
  "/net/datastor1/data/ocean/nz/backbone-v2/nz5km20170101_00z_3D.nc\n",
  "/net/datastor1/data/ocean/nz/backbone-v2/nz5km20170201_00z_3D.nc\n",
  "/net/datastor1/data/ocean/nz/backbone-v2/nz5km20170301_00z_3D.nc\n",
  "/net/datastor1/data/ocean/nz/backbone-v2/nz5km20170401_00z_3D.nc\n",
  "/net/datastor1/data/ocean/nz/backbone-v2/nz5km20170501_00z_3D.nc\n",
  "/net/datastor1/data/ocean/nz/backbone-v2/nz5km20170601_00z_3D.nc\n",
  "/net/datastor1/data/ocean/nz/backbone-v2/nz5km20170701_00z_3D.nc\n",
  "/net/datastor1/data/ocean/nz/backbone-v2/nz5km20170801_00z_3D.nc\n",
  "/net/datastor1/data/ocean/nz/backbone-v2/nz5km20170901_00z_3D.nc\n",
  "/net/datastor1/data/ocean/nz/backbone-v2/nz5km20171001_00z_3D.nc\n",
  "/net/datastor1/data/ocean/nz/backbone-v2/nz5km20171101_00z_3D.nc\n"
 ]
 }
],
"source": [
```

```
"# This block of code iterates through all the lat/lon\n",
"# coordinate pairs in locations.  For each location,\n",
"# it calculates the depth-average current speed and direction\n",
"# over all depths at that location.  The result\n",
"# is a pandas dataframe with arrays size 1xtime for\n",
"# current speed and current direction.\n",
"\n",
"\n",
"# values are stored in an xarray dataset, just pull out the actual values\n",
"# so we can work with them more easily\n",
"#for latv,lonv in locations:\n",
"latv = lat_value[0]\n",
"lonv = lon_value[0]\n",
"speed = []\n",
"direction = []\n",
"time = []\n",
"for filelist in files:\n",
"    for file in filelist:\n",
"        print(file)\n",
"        # Open list of files as single dataset as variable ds\n",
"        ds = xr.open_dataset(file, drop_variables = ['dep','temp','salt'])\n",
"        # get the model data, u and v current speeds, takes the depth-average:\n",
"        da = ds.sel(dict(lat=latv,lon=lonv,lev=choose_depth),method='nearest')\n",
"        # values are stored in an xarray dataset, just pull out the actual values\n",
"        # so we can work with them more easily\n",
"        if np.isnan(da['u'][0].values):\n",
"            continue\n",
"        u = da['u'].values\n",
"        v = da['v'].values\n",
"        # calculate closest model depth to chosen depth\n",
"        model_depth = da['lev'].values\n",
"        # calculate current speed and direction from u and v\n",
"        speed.extend((np.sqrt(u**2+v**2)).tolist())\n",
"        direction.extend((np.mod(np.rad2deg(np.arctan2(u, v)),360)).tolist())\n",
"        # convert time to something that python understands\n",
```

```
   "        time.extend((da['time'].values).tolist()) \n",
   "\n",
   "time = [pd.to_datetime(time_val) for time_val in time]\n",
   "year = [t.year for t in time]\n",
   "month = [t.month for t in time]\n",
   "day = [t.day for t in time]\n",
   "# create a pandas dataframe, which is useful for saving as csv format\n",
   "data = {'year':year, 'month':month, 'day':day, 'speed':speed, 'direction':direction} \n",
   "df = pd.DataFrame(data)\n",
   "# save output as csv\n",
   "model_lat = da['lat'].values\n",
   "model_lon = da['lon'].values\n",

"df.to_csv(f'/source/Data/Navid/moana_current_v1_{np.min(time)}_{np.max(time)}_{model_lat}
_{model_lon}_{model_depth}m.csv')"
   ]
  },
  {
   "cell_type": "code",
   "execution_count": null,
   "metadata": {},
   "outputs": [],
   "source": []
  }
 ],
 "metadata": {
  "hide_input": false,
  "kernelspec": {
   "display_name": "Python 3",
   "language": "python",
   "name": "python3"
  },
  "language_info": {
   "codemirror_mode": {
    "name": "ipython",
```

```
  "version": 3
 },
 "file_extension": ".py",
 "mimetype": "text/x-python",
 "name": "python",
 "nbconvert_exporter": "python",
 "pygments_lexer": "ipython3",
 "version": "3.6.9"
},
"toc": {
 "base_numbering": 1,
 "nav_menu": {},
 "number_sections": true,
 "sideBar": true,
 "skip_h1_title": false,
 "title_cell": "Table of Contents",
 "title_sidebar": "Contents",
 "toc_cell": false,
 "toc_position": {},
 "toc_section_display": true,
 "toc_window_display": true
},
"varInspector": {
 "cols": {
  "lenName": 16,
  "lenType": 16,
  "lenVar": 40
 },
 "kernels_config": {
  "python": {
   "delete_cmd_postfix": "",
   "delete_cmd_prefix": "del ",
   "library": "var_list.py",
   "varRefreshCmd": "print(var_dic_list())"
  },
```

```
   "r": {
    "delete_cmd_postfix": ") ",
    "delete_cmd_prefix": "rm(",
    "library": "var_list.r",
    "varRefreshCmd": "cat(var_dic_list()) "
   }
  },
  "types_to_exclude": [
   "module",
   "function",
   "builtin_function_or_method",
   "instance",
   "_Feature"
  ],
  "window_display": false
 }
},
"nbformat": 4,
"nbformat_minor": 2
}
```

Appendix D Calculation Details for Foundation Design

D.1 Aerodynamic and Hydrodynamic Loads on the Structure

The thrust force (Th) on a wind turbine rotor due to wind can be estimated by assumption wind load can be separated into a mean thrust force (or static force) and a turbulent thrust force (or dynamic force) as recommended by Bhattacharya [160].

$$Th = Th_{stat} + Th_{dyn} = \frac{1}{2}\rho_a A_R C_T \bar{u}^2 + \frac{1}{2}\rho_a A_R C_T (2\bar{u}u + u^2) \qquad \text{(D-1)}$$

where ρ_a is the density of air (1.225 kg/m^3), A_R is the rotor swept area, C_T is the thrust coefficient, $\bar{u}$ is mean wind speed, and u is variable wind speed. The equation must be solved for the turbine cut-in and cut-out speeds, with the appropriate thrust coefficients. The thrust coefficient can be approximated for operational range of the turbine using three different sections as shown in Figure D-33.

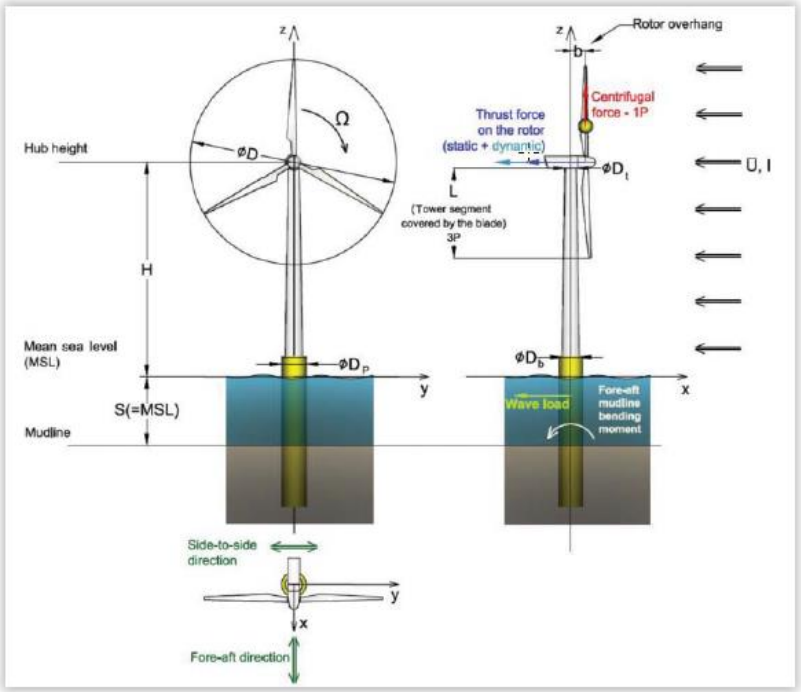

Figure D-33: Definition of the geometry, axes, loads, and directions of the offshore wind turbine structure[160].

The first step is to calculate static force Thstat. Next, dynamic thrust Th_{dyn}. Finally, calculate static and dynamic components of the moment at mudline ($M_{wind,stat}$ and $M_{wind,dyn}$):

$$Th_{stat} = \frac{1}{2}\rho_a A_R C_T \bar{u}^2 \tag{D-2}$$

$$Th_{dyn} = 0.345821 Th_{stat} \tag{D-3}$$

$$M_{wind,stat} = 105 Th_{stat} \tag{D-4}$$

$$M_{wind,dyn} = 105 Th_{dyn} \tag{D-5}$$

$$M = M_{wind,stat} + M_{wind,dyn} \tag{D-6}$$

The empirical coefficients in equations (D-2) to (D-6) are derived base on numerical analysis of results presented by Bhattacharya[160].

The mean wind speed is taken as the yearly mean wind speed at the site (Annual wind speed of Terawhiti) $\overline{u}$ = 7.10 [m / s]. So, the thrust coefficient C_T = 7 / $\overline{u}$ = 7/7.10=0.98.

$Th_{stat} = \frac{1}{2}\rho_a A_R C_T \bar{u}^2 = \frac{1}{2} \times 1.225 \times \frac{\pi}{4}(107)^2 \times \frac{7}{7.1} \times 7.1^2 = 273728.43\ N = 0.27\ MN$

$M_{wind,stat} = 105 Th_{stat} = 28.35\ MNm$

$Th_{dyn} = 0.345821 Th_{stat} = 0.345821 \times 0.27 \ = 0.09\ MN$

$M_{wind,dyn} = 105 Th_{dyn} = 9.45\ MNm$

$Th = Th_{stat} + Th_{dyn} = 0.36\ MN$

$M = M_{wind,stat} + M_{wind,dyn} = 37.8\ MNm$

For wind speeds between cut-in and cut-out, thrust coefficient is estimated as recommended by Arany et al.[218]:

$$C_T \approx \frac{7}{\bar{u}} \tag{D-7}$$

where $\overline{u}$ is mean wind speed. Equation (D.7) can be used as well for tidal turbines as recommended by Shapiro [243]. In this case ρ_w = 1030 [kg / m^3] and $A_R = \frac{\pi}{4}(20)^2 = 314.159$ m^2.

The wind produces drag force on the tower, which can be considered constant at given mean wind speed, ignoring buffeting and vortex shedding on the tower and without the effect of the rotating. In a simplified method, the magnitude is estimated by a simple geometric consideration: the upper part of the face area of the tower is partly covered by the blade when the blade is in a downward pointing position ($\varphi = \pi$). The drag force on the covered part of the tower is taken to be zero and the blade causes a load loss on the tower. When the blade is in the downward direction, it covers the tower from z = H − L to z = H. The total moment of drag force on this

upper section without the effect of blade passage and $D_T(z)$ and u(z) can be written by equations D-8 to D-10 sourced from Bhattacharya [160]:

$$M_{drag} = M_{towertop} = \int_{H-L}^{H} \frac{1}{2} \times \rho_a \times C_D D_T(z) u^2(z)(z+S)dz \quad \text{(D-8)}$$

$$D_T(z)=D_b-(D_b-D_t).\frac{z}{H} \quad \text{(D-9)}$$

$$u(z) = \bar{u}(\frac{z}{H})^{\beta} \quad \text{(D-10)}$$

where H is the hub height from mean sea level, L is the length of the blades, ρ_a is the density of air, C_D is the drag coefficient, $D_T(z)$ is the diameter of the tower at z (assuming the diameter linearly decreases between the bottom and top diameters), z is the vertical coordinate (zero at mean sea level), S is the mean sea depth, and U(z) is the power law velocity profile using the exponential wind profile with β = 1 / 7 ≈ 0.143.

The wind profile power law relationship is:

$$\frac{u}{u_r} = (\frac{z}{z_r})^{\alpha} \quad \text{(D-11)}$$

where u is the wind speed (in metres per second) at height z (in metres), and u_r is the known wind speed at a reference height z_r. The exponent (α) is an empirically derived coefficient that varies dependent upon the stability of the atmosphere. For neutral stability conditions, α is approximately 1/7, or 0.143 [244].

The drag load on the tower is calculated by integrating along with the whole tower [160]:

$$F_{drag} = \int_0^H \frac{1}{2} \rho_a C_D D(z) u(z)^2 dz \quad \text{(D-12)}$$

The following dimensions have been assumed for drag in Terawhiti site:

- tower bottom diameter D_b =5 m
- tower top diameter D_t =3 m
- β = 1⁄7 ≈ 0.143
- The drag coefficient of the tubular tower at high Reynolds number is $C_D \approx 0.5$
- The density of air is ρ_a = 1.225 [kg⁄m^3]
- H= 87 m hub height from mean sea level
- L= 52 m blade length
- The water depth of Terawhiti [245] suitable for monopile S= 30 m.

For $\bar{u}$ = 7.1, the moment can be written as:

$$M_{drag} = M_{towertop} = \int_{87-52}^{87} \frac{1}{2} \times 1.225 \times 0.5 \left(5 - 2.\frac{z}{87}\right) \bar{u}^2 \left(\frac{z}{87}\right)^{\frac{2}{7}} (z + 30) dz = 3444.46\, \bar{u}^2 = 3444.46 \times 7.1^2 = 173635.2\, Nm = 0.17\, MNm$$

The drag load is calculated as:

$$F_{drag} = \int_0^{87} \frac{1}{2} 1.225 \times 0.5 \times \left(5 - 2.\frac{z}{87}\right) \left(\bar{u}^2 \left(\frac{z}{87}\right)^{\frac{2}{7}} \right) dz = 6627.73\, \bar{u}^2\, N$$
$$= 0.0066\, \bar{u}^2\, MN$$

For calculating drag in tidal turbines, the following dimensions have been assumed:

- ρ_w = 1030 [kg⁄m3]
- A=$\frac{\pi}{4}(20)^2 = 314.159$ m2
- The drag coefficient of the tubular tower at high Reynolds number is $C_D \approx 0.5$
- U=velocity of water related to blades

The height from the seabed for tidal turbines are 25 m and rotor diameters are 20 m. So, the distance for drag momentum is 15 m which multiplies at drag forces to result drag momentums.

D.2 Scenarios of Wind Loads

Wind scenario U-1: Normal Turbulence (NTM) at Rated Wind Speed (U_R)

The mean wind speed is the rated wind speed (U_R) where the highest thrust force (Th) is expected, and the wind turbulence is modelled by the Normal Turbulence Model (NTM). This scenario is typical for normal operation of the turbine. The standard deviation of wind speed in normal turbulence following IEC (2005) can be written as

$$\sigma_{u,NTM} = I_{ref}(0.75u + b) \quad with \quad b = 5.6\ m/s \tag{D-13}$$

where I_{ref} is the reference turbulence intensity (expected value at u = 15[m ⁄ s]), $\sigma_{u,NTM}$ is the standard deviation of wind speed in normal turbulence model (NTM) and b is model parameter which is defined 5.6 according to IEC 2005. For the calculation of the maximum turbulent wind speed component (u_{NTM}), the time constant of the pitch control is assumed to be the same as the time period of the rotation of the rotor. In other words, it is assumed that the pitch control can follow changes in the wind speed that occur at a lower frequency than the rotational speed of the turbine. Then maximum turbulent wind speed component (u_{NTM}) may be determined by calculating the contribution of variations in the wind speed with a higher frequency than f_{1P}, max to the total standard deviation of wind speed. From the Kaimal spectrum used for the wind turbulence process, its standard derivation can be calculated using equation (D-:

$$\sigma_{u,NTM,f>f_{1P}} = \sigma_{u,NTM}\sqrt{\frac{1}{(\frac{6L_k}{u_R}f_{1P,max}+1)^{\frac{2}{3}}}} \tag{D-14}$$

where $\sigma_{u,NTM,f>f_{1P}}$ is the variations in the wind speed with a higher frequency than $f_{1P,}$ $\sigma_{u,NTM}$ is the standard deviation of wind speed in normal turbulence, L_k being the integral length scale, u_R is rated wind speed, f_{1P} is the frequency of rotation of the rotor (1P).

The turbulent wind speed encountered in normal operation in normal turbulence conditions is found by assuming normal distribution of the turbulent wind speed component and taking the 90% confidence level value. This is substituted into the quasi-static equation used in equation D-15. Equation D-16 shows expressions for the corresponding wind moment at the mudline [160].

$$u_{NTM} = 1.28\sigma_{u,NTM,f>f_{1P}} \quad \text{(D-15)}$$

$$F_{wind,NTM} = \frac{1}{2}\rho_a A_R C_T (u_R + u_{NTM})^2 \quad \text{(D-16)}$$

$$M_{wind,NTM} = F_{wind,NTM}(S + z_{hub}) \quad \text{(D-17)}$$

where u_{NTM} is the maximum turbulent wind speed component, $\sigma_{u,NTM,f>f_{1P}}$ is the variations in the wind speed with a higher frequency than $f_{1P,}$ ρ_a is air density, A_R is rotor swept area, C_T is the thrust coefficient, u_R is rated wind speed, $F_{wind,NTM}$ and $M_{wind,NTM}$ are mudline load and moment in normal turbulence, S is water depth and z_{hub} is hub height.

I_{ref} is assumed to be 16% from Table 6-4. Thus, $\sigma_{u,NTM} = 0.16(0.75 \times 15 + 5.6) = 2.69\, m/s$. $1.1f_{1P,\,max}$ is assumed to be 0.24 Hz or $f_{1P,\,max}$= 0.218 Hz from Table 5.6. L_K is assumed to be 340.2 m from Table 5.5 and u_R= 16.5 m/s from Table 5.7. So, $\sigma_{u,NTM,f>f_{1P}}$ (Equation (D-) will be 0.89 m/s. This value in equation ((D-) results, $u_{NTM} = 1.28 \times 0.89 = 1.13\, m/s$. Using this, the total wind load and moment for the Terawhiti are estimated as

$F_{wind,\,NTM} = \frac{1}{2} \times 1.225 \times \frac{\pi}{4}(107)^2 \times \frac{7}{7.1} \times (16.5 + 1.13)^2 = 1.68$ [MN]

$M_{wind,NTM} = 1.68\ (30\ +\ 87) = 196.5$ [MNm]

Wind scenario U-2: Extreme Turbulence (ETM) at Rated Wind Speed (U_R)

The ETM is used to calculate the standard deviation of wind speed at the rated wind speed, and from that the maximum wind load under normal operation in extreme turbulence conditions. The standard deviation of wind speed in ETM is given in IEC (2005) as

$$\sigma_{u,ETM} = cI_{ref}\left[0.072(\frac{u_{avg}}{c}+3)(\frac{u_R}{c}-4)+10\right] \quad with \quad c = 2\ [m/s] \tag{D-18}$$

where equation(D- terms are already defined (same as equation-19), but U_{avg} is the long-term average wind speed at the site. The maximum turbulent wind speed component u_{ETM} is determined similarly to the previous case.

$$\sigma_{u,ETM,f>f_{1P}} = \sigma_{u,ETM}\sqrt{\frac{1}{(\frac{6L_k}{u_R}f_{1P,max}+1)^{\frac{2}{3}}}} \tag{D-19}$$

The turbulent wind speed encountered in normal operation in extreme turbulence conditions, which is used for cyclic/dynamic load analysis, is found by assuming normal distribution of the turbulent wind speed component. As opposed to the normal turbulence situations, the 95% confidence level value is taken. This is substituted into the quasi-static equation used in equation D-16. Equation D-22 shows the expression for wind moments at the mudline [160].

$$u_{ETM} = 2\sigma_{u,ETM,f>f_{1P}} \tag{D-20}$$

$$F_{wind,ETM} = \frac{1}{2}\rho_a A_R C_T (u_R + u_{ETM})^2 \tag{D-21}$$

$$M_{wind,ETM} = F_{wind,ETM}(S + z_{hub}) \tag{D-22}$$

where equations (D-20 to D-22) terms are already defined (same as equations D-15 to D-17), but U_{avg} from Table 6-1 is 7.10 m/s for Terawhiti. So, results are estimated as:

$\sigma_{u,ETM} = 3.1\ m/s, \quad \sigma_{u,ETM,f>f_{1P}} = 1.01\ m/s, \quad u_{ETM} = 2.02\ m/s,$

$F_{wind,ETM} = 1.86\ MN, \quad M_{wind,ETM} = 217.62\ MNm$

Wind scenario U-3: Extreme operating Gust (EOG) at Rated Wind Speed (U_R)

The EOG is a sudden change in the wind speed and if it hits the rotor when it is operating at the rated wind speed of the turbine, the pitch control of the wind turbine has no time to alleviate the loading. IEC (2005) suggests that for simplified foundation design 50-year extreme operating gust (EOG) is assumed to estimate the highest single occurrence wind load. The 50-year extreme wind speed, which is typically used in wind turbine design for extreme wind conditions, can be determined by standard equations D-23 to D-26 sourced from Bhattacharya [160].

$$U_{10,50-year} = K[-ln\,(1 - 0.98^{\frac{1}{52596}})]^{\frac{1}{s}} \tag{D-23}$$

where the number 52596 = 365.25[days ⁄ year] · 24[hours ⁄ day] · 6[10 min intervals ⁄ hour] represents the number of 10-minutes intervals in a year. The 10-year extreme wind speed is represented by[16]

$$\mathrm{u}_{10,1-\mathrm{year}} = 0.8\mathrm{U}_{10,50-\mathrm{year}} \tag{D-24}$$

The characteristic standard deviation of wind speed can be calculated by

$$\sigma_{U,c} = 0.11\mathrm{U}_{10,1-\mathrm{year}} \tag{D-25}$$

Which c is the return period of EOG.

The extreme gust speed is then calculated at the rated wind speed from

$$u_{EOG} = min\left\{1.35\left(u_{10,1-\mathrm{year}} - u_R\right); \frac{3.3\sigma_{u,c}}{1+\frac{0.1D}{\Lambda_1}}\right\} \tag{D-12}$$

where D is the rotor diameter= 107 m, $\Lambda_1 = L_k / 8$ with L_k being the integral length scale (L_k =340.2 m). Using this, the total wind load is estimated as

$$\mathrm{F}_{\mathrm{wind,EOG}} = \mathrm{Th}_{\mathrm{EOG}} = \frac{1}{2}\rho_a \mathrm{A}_\mathrm{R}\mathrm{C}_\mathrm{T}(\mathrm{u}_\mathrm{R} + \mathrm{u}_{\mathrm{EOG}})^2 \tag{D-27}$$

[16] The methodology for the calculation of the magnitude of the 50-year extreme gust is described in DNV (2014). This methodology builds on the long-term distribution of 10-minutes mean wind speeds at the site, which is typically represented by a Weibull distribution.

where equation D-27 terms are already defined (same as equation D-21). For wind speeds between cut-in and cut-out, thrust coefficient is estimated as recommended by Arany et al.[218]:

$$C_T \approx \frac{7}{\bar{u}} \tag{D-28}$$

Using equation (D-, $C_T = 7 \,/\, \bar{u} = 7 \,/\, 7.1 = 0.98$ and rated wind speed $u_R = 16.5$ m/s. Using the water depth S and the hub height above sea level z_{hub}, the mudline bending
moment (without the load factor γ_L) can be estimated using equation D-29 sourced from [160].

$$M_{wind,\,EOG} = F_{wind,\,EOG}\,(S + z_{hub}) \tag{D-29}$$

The EOG wind speed is calculated using data from Table 6-4 and Equations D-23 to D-26

$$U_{10,50-year} = 31.1\ m/s, \mathrm{u}_{10,1-\mathrm{year}} = \ 24.8\ m/s, \sigma_{U,c} = 2.7\ m/s,\ u_{EOG} = 7.1\ m/s$$

Using this, the total wind load is estimated as

$$\mathrm{Th}_{wind,\,EOG} = \frac{1}{2} \times 1.225 \times \frac{\pi}{4}(107)^2 \times \frac{7}{7.1} \times (16.5 + 7.1)^2 \approx 3[\mathrm{MN}]$$

and using the water depth S = 30 [m] and the hub height above mean sea level z_{hub} = 87 [m]

$M_{wind,\,EOG} = 3\,(30 + 87) = 351[\mathrm{MNm}]$

Wind scenario U-4: Extreme operating Gust (EOG) at the Cut-Out Wind Speed (U_{out}) If the 50-year EOG hits the rotor slightly below the cut-out speed of the turbine, due to the sudden change in wind speed the turbine cannot shut down. Note that the EOG calculated at the cut-out wind speed is different from that evaluated at the rated wind speed (IEC 2005).

Wind load caused by the EOG at the cut-out wind speed U_{out} is calculated taking into consideration that according thrust coefficient expression of Frohboese and Schmuck 2010 (equation (D-D-28) [219] is no longer valid, and instead should be

determined by assuming that the pitch control keeps the power constant. This means that the thrust force is inversely proportional to the wind speed above rated wind speed U_R and the thrust coefficient is inversely proportional to the cube of the wind speed. So, between cut-in (U_{in}) and rated wind speed (U_R), equation (D-28 is used for calculating thrust coefficient and after rated wind speed, equation (D-30 is used for calculating thrust coefficient.

$$C_T = \frac{7u_R^2}{u^3} \tag{D-30}$$

The EOG speed at cut-out wind speed $u_{EOG,Uout}$ is determined from equations D-23 to D-26 by substituting a value for U_{out} (which is not the same at U_R). The thrust force and moment can be estimated using equations (D--32 and D-33 sourced from [160].

$$T_{wind,\, u_{out}} = \frac{1}{2}\rho_a A_R C_T (u_{out} + u_{EOG,u_{out}})^2 \tag{D-32}$$

$$M_{wind,\, u_{out}} = (S + z_{hub})\, T_{wind,\, u_{out}} \tag{D-33}$$

where equations (D-& (D- terms are already defined (same as equations (D- & (D-). So, using equation (D-12 $u_{EOG,u_{out}} = 7.1\ m/s$ and as a result:

$T_{wind,\, u_{out}} = \frac{1}{2} \times 1.225 \times \frac{\pi}{4}(107)^2 \times \frac{7 \times 16.5^2}{25^3} \times (25 + 7.1)^2 = 0.69$ [MN]

$M_{wind,\, EOG} = 0.69\,(30 + 87) = 80.7$ [MNm]

D.3 Scenarios of Wave Loads

The wave conditions recommended by Bhattacharya [160] for calculating critical wave loads acting on the substructure are:

(W-1) One-year extreme sea state (ESS). A wave with height equal to the 1-year significant wave height $H_{S,\,1}$.

(W-2) One-year extreme wave height (EWH). A wave with height equal to the 1-year maximum wave height $H_{m,\,1}$.

(W-3) 50-year ESS. A wave with height equal to the 50-year significant wave height $H_{S,\,50}$.

(W-4) 50-year EWH. A wave with height equal to the 50-year maximum wave height $H_{m,\,50}$.

Bhattacharya [160] states that the one-year ESS and EWH are used as a conservative overestimation of the normal wave height (NWH) prescribed in IEC 2019[192]. It is important to note here in relation to the ESS that the significant wave height and the maximum wave height have different meanings. The significant wave height HS is the average of the highest one-third of all waves in the three-hour sea state, while the maximum wave height Hm is the single highest wave in the same three-hour sea state.)

The highest wind load is expected to be caused by scenario U-3 and the highest wave load is due to scenario W-4. In practice, the 50-year extreme wind load and the 50-year extreme wave load have a negligible probability to occur at the same time, and the DNV 2014 code [193] also doesn't require these extreme load cases to be evaluated together. The designer has to find the most severe event with a 50-year return period based on the joint probability of wind and wave loading. Therefore, for the ULS analysis, two combinations are suggested by Arany et al. 2017[218]:

(1) The ETM wind load at rated wind speed combined with the 50-year EWH – the

combination of wind scenario U-2 and wave scenario W-4. This will provide higher loads in deeper water with higher waves.

(2) The 50-year EOG wind load combined with the one-year maximum wave height.

This will provide higher loads in shallow water in sheltered locations where wind load dominates.

These scenarios are somewhat more conservative than those required by standards, and can be adopted for simplified analysis. From the point of view of SLS and FLS, the single largest loading on the foundation is not representative, because the structure is expected to experience this level of loading only once throughout the lifetime.

In simplified load calculation methodologies, to determine the wave loading, simple linear waves are assumed. Higher-order theories like Stokes waves or Dean's

stream function theory would provide better estimates, especially in shallow waters. However, the linear theory allows for simpler load calculation and its application is justified for foundation design loads.

Bhattacharya [160] also stats that a simplified approach to wave load estimation is Morison's (or MOJS) equation Morison et al. 1950 [246]. In these equations, the diameter of the substructure is taken as $D_S = D_P + 2t_{TP} + 2t_G$[m] to account for the transition piece (TP) and the grout (t_G) thickness. The circular substructure area A_S is also calculated from this diameter. The methodology used here builds on linear (Airy) wave theory, which gives the surface elevation η, horizontal particle velocity w, and the horizontal particle acceleration $\dot{w}$ as

$$\eta(x,t) = \frac{H_m}{2}\ cos\ (\frac{2\pi t}{T_S} - kx) \tag{D-34}$$

$$w(x,z,t) = \frac{\pi H_m\ cosh\ (k(S+z))}{T_S\ sinh(KS)}\ cos(\frac{2\pi t}{T_S} - kx) \tag{D-35}$$

$$\dot{w}(x,z,t) = \frac{-2\pi^2 H_m cosh(k(S+z))}{T_S^2\ sinh(kS)}\ sin(\frac{2\pi t}{T_S} - kx) \tag{D-36}$$

where H_m is maximum wave height, T_s is peak wave period, S is mean water depth, t is time, x is the horizontal coordinate in the along-wind direction (x = 0 at the turbine, see Figure D-34). The wave number k is obtained from the dispersion relation

$$\omega^2 = gk\ tanh(kS)\ \ with\ \ \omega = \frac{2\pi}{T_S} \tag{D-37}$$

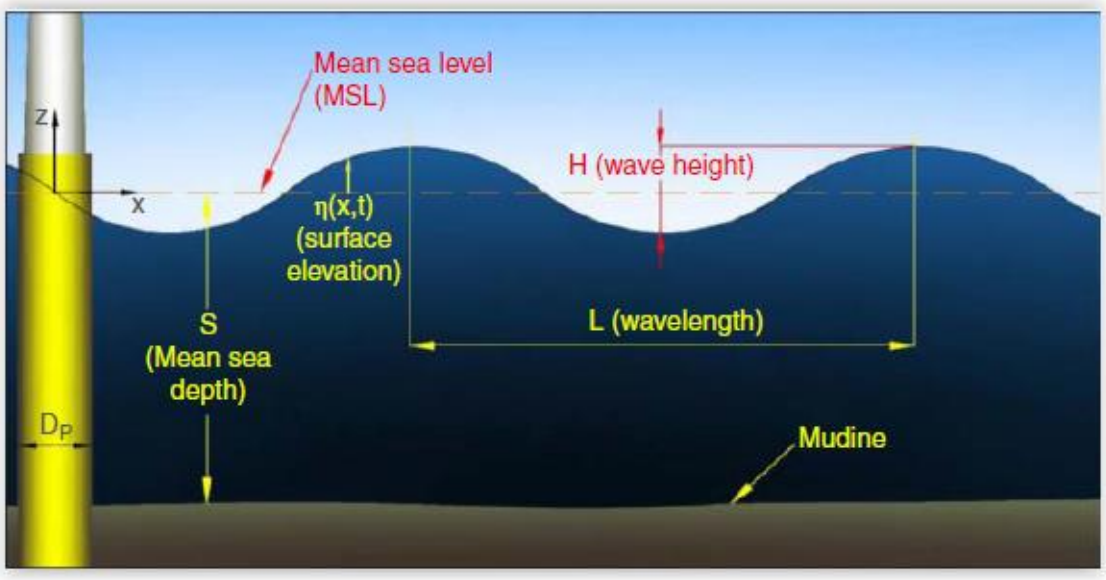

Figure D-34: Definition of wave terminology [247].

The force on a unit length strip of the substructure is the sum of the drag force F_D and
the inertia force F_I:

$$dF_{wave}(z,t) = dF_D(z,t) + dF_I(z,t) = \frac{1}{2}\rho_w D_S C_D w(z,t)|w(z,t)| + C_m \rho_w A_S \dot{w}(z,t) \quad \text{(D-38)}$$

where w horizontal particle velocity as a function of z coordinate and t time, C_D is the drag coefficient, C_m is the inertia coefficient, and ρ_w is the density of seawater, D_S and A_S are the diameter and circular substructure area. The total horizontal force and bending moment at the mudline is then given by integration as

$$F_{wave}(t) = \int_{-S}^{\eta} dF_D \, dz + \int_{-S}^{\eta} dF_I \, dz \quad \text{(D-39)}$$

$$M_{wave}(t) = \int_{-S}^{\eta} dF_D(S + z_{hub}) \, dz + \int_{-S}^{\eta} dF_I(S + z_{hub}) \, dz \quad \text{(D-40)}$$

The peak load of the drag and inertia loads occur at different time instants, and therefore the maxima are evaluated separately. The maximum of the inertia load

occurs at the time instant t = 0 when η = 0 and the maximum of the drag load occurs when t = T_S/4 and η = H_m / 2.

The maximum drag load & moment $F_{D,max}$ & $M_{D,max}$ is then obtained by carrying out the integrations:

$$F_{D,max} = \frac{1}{2}\rho_w D_S C_D \frac{\pi^2 H_m^2}{T_S^2 sinh^2(kS)} P_D(k,S,\eta) \quad \text{(D-41)}$$

$$M_{D,max} = \frac{1}{2}\rho_w D_S C_D \frac{\pi^2 H_m^2}{T_S^2 sinh(kS)} Q_D(k,S,\eta \quad \text{(D-42)}$$

$$P_D(k,S,\eta) = \frac{e^{2k(S+\eta)} - e^{-2k(S+\eta)}}{8k} + \frac{S+\eta}{2} \quad \text{(D-43)}$$

$$Q_D(k,S,\eta) = (\frac{S+\eta}{8k} - \frac{1}{16k^2})e^{2k(S+\eta)} - (\frac{S+\eta}{8k} + \frac{1}{16k^2})e^{-2k(S+\eta)} + (\frac{S+\eta}{2})^2 + \frac{1}{8k^2} \quad \text{(D-44)}$$

The maximum inertia load & moment $F_{I,max}$ & $M_{I,max}$ are obtained by:

$$F_{I,max} = \frac{1}{2}\rho_w C_m D_S^2 \frac{\pi^3 H_m}{T_S^2 sinh(kS)} P_I(k,S,\eta) \quad \text{(D-45)}$$

$$M_{I,max} = \frac{1}{2}\rho_w C_m D_S^2 \frac{\pi^3 H_m}{T_S^2 sinh(kS)} Q_I(k,S,\eta) \quad \text{(D-46)}$$

$$P_I(k,S,\eta) = \frac{sinh(k(S+\eta))}{k} \quad \text{(D-47)}$$

$$Q_I(k,S,\eta) = (\frac{S+\eta}{2k} - \frac{1}{2k^2})e^{k(S+\eta)} - (\frac{S+\eta}{2k} + \frac{1}{2k^2})e^{-k(S+\eta)} + \frac{1}{k^2} \quad \text{(D-48)}$$

In the simplified method for obtaining foundation loads, it can be conservatively assumed that the sum of the maxima of drag and inertia loads is the design wave load. This assumption is conservative, because the maxima of the drag load and

inertia load occur at different time instants. All wave scenarios (W-1)–(W-4) are evaluated with the same procedure, using different values of wave height H and wave period T [160].

In this step, a simplified estimation of the extreme wave height and the corresponding wave period for a given site is explained which involves the following sub-steps:

6. Obtain the relevant **significant wave height Hs** from a reliable source. The 1-year equivalents are calculated following DNV 2014 [193] from the 50-year significant wave height according to

$$H_{S,1} = 0.8H_{S,50} \tag{D-49}$$

7. Calculate the **peak wave period corresponding to the significance wave height, Ts** using:

$$T_S = 11.1\sqrt{\frac{H_S}{g}} \tag{D-50}$$

8. Calculate **the number of waves in a 3-hour period, N**: Typically, significant wave heights are given for a 3-hour period. In other words, this means that the significant wave height is calculated as the mean of the highest 1/3 of all waves. Therefore, many different wave heights occur within this 3-hour period, and the highest occurring wave height is called the maximum wave height H_m. To find this, one needs to know the number of waves in the 3-hour period, because the more waves there are, the higher the chance of higher waves occurring.

$$N = \frac{3hours}{T_S} = \frac{10800s}{T_S} \tag{D-51}$$

9. Calculate the **maximum wave height, H_m** by

$$H_m = H_S \sqrt{\frac{1}{2} ln(N)} \quad \text{(D-52)}$$

10. Calculate the **peak wave period corresponding to the maximum wave height, T_m.** The same formulae can be used as in step 2.

$$T_m = 11.1 \sqrt{\frac{H_m}{g}} \quad \text{(D-53)}$$

The 50-year significant wave height, $H_{S,50}$ at Terawhiti can be found from NIWA [220]. Alternatively, ERA-40 Wave Atlas [195] provides an approximate value of 15m which was shown in Table 6-2. So, according to equation (D-, $H_{S,1}$ is 12m. Going to step 2, $T_{S,1}$ can be 12.2s. Equation (D- gives N=885.24 and as a result $H_{m,1}$=22.10m and $T_{m,1}$=16.66 s. Also, $H_{m,50}$ is 27.62m according to equation (D-. The wave periods for 4 scenarios are:

(W-1): $T_{S,1} = 11.1\sqrt{\frac{H_{S,1}}{g}}$ =$11.1\sqrt{\frac{12}{9.8}}$ =12.2 s

(W-2): $T_{m,1} = 11.1\sqrt{\frac{H_{m,1}}{g}}$ =$11.1\sqrt{\frac{22.10}{9.8}}$ =16.66 s

(W-3): $T_{S,50} = 11.1\sqrt{\frac{H_{S,50}}{g}}$ =$11.1\sqrt{\frac{15}{9.8}}$ =13.73 s

(W-4): $T_{m,50} = 11.1\sqrt{\frac{H_{m,50}}{g}}$ =$11.1\sqrt{\frac{27.62}{9.8}}$ =18.63 s

The wave heights and wave periods are summarised for all wave scenarios (W-1) to (W-4) in Table 6-2 according to the explanations presented at the beginning of section 6.3.3.2.

Table D-10: Wave heights and wave periods for different wave scenarios for Terawhiti.

Parameters	Wave scenario (W-1)	Wave scenario (W-2)	Wave scenario (W-3)	Wave scenario (W-4)
Wave height H[m]	$H_{S,1}$=12	$H_{m,1}$=22.10	$H_{S,50}$=15	$H_{m,50}$=27.62
Wave period T[s]	$T_{S,1}$=12.2	$T_{m,1}$=16.66	$T_{S,50}$=13.73	$T_{m,50}$=18.63

The wave loads (equations D-39 and D-40) are calculated only for the most severe wave scenarios used for Load Cases E-2 and E-3, i.e. wave scenario (W-2) and (W-4), the 1-year and 50-year extreme wave heights (EWHs), using the definitions presented in Table 6-2 where $\rho_w = 1030$ kg/m^3 and S=30 m (from Table 6-2)

$D_S = D_P + 2t_{TP} + 2t_G$=6.3m (knowing D_P=6m from and $t_{TP} + t_G$ =0.15m from Table 6-6)

C_D=0.5 and C_m=2 (based on DNV [193])

Hm, Ts, η, k for W-1 scenario: H_m =12m, T_s =12.2s, η = 0 for inertia loads and η = 6m for drag loads, k=0.034m^{-1} (based on equation D-38)

Using equations (D- to(D- for W-1 scenario:

$$F_{D,max} = \frac{1}{2}\rho_w D_S C_D \frac{\pi^2 H_m^2}{T_S^2 sinh^2(kS)} \cdot \left(\frac{e^{2k(S+\eta)} - e^{-2k(S+\eta)}}{8k} + \frac{S+\eta}{2}\right) =$$

$$\frac{1}{2} \times 1030 \times 6.3 \times 0.5 \frac{\pi^2 12^2}{12.2^2 sinh^2(0.034 \times 30)} \left(\frac{e^{2\times0.034(30+6)} - e^{-2\times0.034(30+6)}}{8 \times 0.034} + \frac{30+6}{2}\right) = 1622.25 \times 7.9 \times (42.2 + 18) = 771509.65N$$

$$= 0.77MN$$

$$M_{D,max} = \frac{1}{2}\rho_w D_S C_D \frac{\pi^2 H_m^2}{T_S^2 sinh(kS)} \cdot \left[\left(\frac{S+\eta}{8k} - \frac{1}{16k^2}\right) e^{2k(S+\eta)} - \left(\frac{S+\eta}{8k} + \frac{1}{16k^2}\right) e^{-2k(S+\eta)} + \left(\frac{S+\eta}{2}\right)^2 + \frac{1}{8k^2}\right] = 1622.25 \times 7.9 \left[\left(\frac{30+6}{8\times0.034} - \frac{1}{16\times0.034^2}\right) e^{2\times0.034(30+6)} - \left(\frac{30+6}{8\times0.034} + \frac{1}{16\times0.034^2}\right) e^{-2\times0.034(30+6)} + \left(\frac{30+6}{2}\right)^2 + \frac{1}{8\times0.034^2}\right] = 1622.25 \times 7.9 \times (902.14 - 16.14 + 324) = 15507087.75Nm = 15.5MNm$$

$$F_{I,max} = \frac{1}{2}\rho_w C_m D_S^2 \frac{\pi^3 \times 12}{T_S^2 sinh(kS)} \cdot \frac{sinh(k(S+\eta))}{k} =$$

$$\frac{1}{2} \times 1030 \times 2 \times 6.3^2 \frac{\pi^3 \times 12}{12.2^2 sinh^2(0.034 \times 30)} \cdot \frac{sinh(0.034(30+0))}{0.034}$$

$$= 40880.7 \times 1.71 \times 35.47 = 2479565.71N = 2.4MN$$

$$M_{I,max} = \frac{1}{2}\rho_w C_m D_S^2 \frac{\pi^3 H_m}{T_S^2 sinh(kS)} \cdot \left[\left(\frac{S+\eta}{2k} - \frac{1}{2k^2}\right) e^{k(S+\eta)} - \left(\frac{S+\eta}{2k} + \frac{1}{2k^2}\right) e^{-k(S+\eta)} + \frac{1}{k^2}\right] = 40880.7 \cdot \frac{\pi^3 \times 12}{12.2^2 sinh(0.034\times30)} \cdot \left[\left(\frac{30+0}{2\times0.034} - \frac{1}{2\times0.034^2}\right) e^{0.034(30+0)} - \left(\frac{30+0}{2\times0.034} + \frac{1}{2\times0.034^2}\right) e^{-0.034(30+0)} + \frac{1}{0.034^2}\right] = 40880.7 \times 1.71 \times (23.81 - 315.05 + 865.05) = 40112760.1Nm = 40.1MNm$$

The results are:

$F_{wave,\ W\text{-}1}$= 3.1 MN

$M_{wave,\ W\text{-}1}$= 55.6 MNm

Hm, Ts, η, k for W-2 scenario: H_m =22.10m, T_s =12.2s, η = 0 for inertia loads and η = 11.05m for drag loads, k=0.034m^{-1}(based on equation D-38

Using equations (D- to(D- for for W-2 scenario:

$$F_{D,max} = \frac{1}{2}\rho_w D_S C_D \frac{\pi^2 H_m^2}{T_S^2 sinh^2(kS)}.\left(\frac{e^{2k(S+\eta)}-e^{-2k(S+\eta)}}{8k}+\frac{S+\eta}{2}\right) = \frac{1}{2}\times 1030\times 6.3\times 0.5\frac{\pi^2 22.10^2}{12.2^2 sinh^2(0.034\times 30)}\left(\frac{e^{2\times 0.034(30+11.05)}-e^{-2\times 0.034(30+11.05)}}{8\times 0.034}+\frac{30+11.05}{2}\right) = 1622.25\times 21.32\times 83.28 = 2893199.73N = 2.89MN$$

$$M_{D,max} = \frac{1}{2}\rho_w D_S C_D \frac{\pi^2 H_m^2}{T_S^2 sinh(kS)}.\left[\left(\frac{S+\eta}{8k}-\frac{1}{16k^2}\right)e^{2k(S+\eta)}-\left(\frac{S+\eta}{8k}+\frac{1}{16k^2}\right)e^{-2k(S+\eta)}+\left(\frac{S+\eta}{2}\right)^2+\frac{1}{8k^2}\right] = 1622.25\times 26.78\left[\left(\frac{30+11.05}{8\times 0.034}-\frac{1}{16\times 0.034^2}\right)e^{2\times 0.034(30+11.05)}-\left(\frac{30+11.05}{8\times 0.034}+\frac{1}{16\times 0.034^2}\right)e^{-2\times 0.035(30+11.05)}+\left(\frac{30+11.05}{2}\right)^2+\frac{1}{8\times 0.034^2}\right] = 1622.25\times 26.84\times 2071.53 = 90196881.32Nm = 90.2MNm$$

$$F_{I,max} = \frac{1}{2}\rho_w C_m D_S^2 \frac{\pi^3 22.10}{T_S^2 sinh(kS)}.\frac{sinh(k(S+\eta))}{k} = \frac{1}{2}\times 1030\times 2\times 6.3^2\frac{\pi^3 22.10}{12.2^2 sinh^2(0.034\times 30)}.\frac{sinh(0.034(30+0))}{0.034} = 40880.7\times 3.16\times 35.47 = 4582121.4N = 4.5MN$$

$$M_{I,max} = \frac{1}{2}\rho_w C_m D_S^2 \frac{\pi^3 H_m}{T_S^2 sinh(kS)}.\left[\left(\frac{S+\eta}{2k}-\frac{1}{2k^2}\right)e^{k(S+\eta)}-\left(\frac{S+\eta}{2k}+\frac{1}{2k^2}\right)e^{-k(S+\eta)}+\frac{1}{k^2}\right] = 40880.7.\frac{\pi^3 22.10}{12.2^2 sinh(0.034\times 30)}.\left[\left(\frac{30+0}{2\times 0.034}-\frac{1}{2\times 0.034^2}\right)e^{0.034(30+0)}-\left(\frac{30+0}{2\times 0.034}+\frac{1}{2\times 0.034^2}\right)e^{-0.034(30+0)}+\frac{1}{0.034^2}\right] = 40880.7\times 3.16\times(23.98-315.05+865.05) = 74148465.2Nm = 74.14MNm$$

The results are:

$F_{wave,\ W\text{-}2}$= 7.4 MN

$M_{wave,\ W\text{-}2}$= 164.3 MNm

Hm, Ts, η, k for W-3 scenario: H_m =15m, T_s =13.73s, η = 0 for inertia loads and η = 7.5m for drag loads, k=0.029m^{-1}(based on equation D-38

Using equations (D- to(D- for W-3 scenario:

$$F_{D,max} = 1622.25\frac{\pi^2 15^2}{13.73^2 sinh^2(0.87)}\left(\frac{e^{2\times0.029(30+7.5)} - e^{-2\times0.029(30+7.5)}}{8\times0.029} + \frac{30+7.5}{2}\right) = 1622.25 \times 12.16 \times 56.2 = 1108632.6N = 1.1MN$$

$$M_{D,max} = 1622.25\frac{\pi^2 15^2}{13.73^2 sinh(0.87)}.\left[\left(\frac{30+7.5}{8\times0.029} - \frac{1}{16\times0.029^2}\right)e^{2\times0.029(30+7.5)} - \left(\frac{30+7.5}{8\times0.029} + \frac{1}{16\times0.029^2}\right)e^{-2\times0.029(30+7.5)} + \left(\frac{30+7.5}{2}\right)^2 + \frac{1}{8\times0.029^2}\right] = 1622.25 \times 31.95 \times (745.6 - 27.1 + 351.5 + 148.6) = 63161119.5NM = 63.1MNM$$

$$F_{I,max} = 40880.7 \times \frac{\pi^3 15}{13.73^2 sinh^2(0.029\times30)}.\frac{sinh(0.029(30+0))}{0.029} = 40880.7 \times 2.54 \times 33.93 = 3523188.6N = 3.5MN$$

$$M_{I,max} = 40880.7.\frac{\pi^3 15}{13.73^2 sinh(0.029\times30)}.\left[\left(\frac{30+0}{2\times0.029} - \frac{1}{2\times0.029^2}\right)e^{0.029(30+0)} - \left(\frac{30+0}{2\times0.029} + \frac{1}{2\times0.029^2}\right)e^{-0.029(30+0)} + \frac{1}{0.029^2}\right] = 40880.7 \times 2.54 \times (-184.4 - 465.7 + 1189.06) = 55964044.3Nm = 55.9MNm$$

The results are:

$F_{wave,\ W\text{-}3}$= 4.6 MN

$M_{wave,\ W\text{-}3}$= 119 MNm

Hm, Ts, η, k for W-4 scenario: H_m =27.62m, T_s =13.73s, η = 0 for inertia loads and η = 13.81m for drag loads, k=0.029m^{-1}(based on equation D-38

Using equations (D- to(D- for W-4 scenario:

$$F_{D,max} = 1622.25\frac{\pi^2 27.62^2}{13.73^2 sinh^2(0.87)}\left(\frac{e^{2\times0.029(30+13.81)} - e^{-2\times0.029(30+13.81)}}{8\times0.029} + \frac{30+13.81}{2}\right) = 1622.25 \times 41.2 \times (54.3 + 21.9) = 5092956.5N = 5.1MN$$

$$M_{D,max} = 1622.25\frac{\pi^2 27.62^2}{13.73^2 sinh(0.87)}.\left[\left(\frac{30+13.81}{8\times0.029} - \frac{1}{16\times0.029^2}\right)e^{2\times0.029(30+13.81)} - \left(\frac{30+13.81}{8\times0.029} + \frac{1}{16\times0.029^2}\right)e^{-2\times0.029(30+13.81)} + \left(\frac{30+13.81}{2}\right)^2 + \frac{1}{8\times0.029^2}\right] = 1622.25 \times 41.2 \times (1419.02 - 20.9 + 479.8 + 148.6) = 135466782.4NM = 135.4MNM$$

$$F_{I,max} = 40880.7 \times \frac{\pi^3 27.62}{13.73^2 sinh^2(0.029\times30)}.\frac{sinh(0.029(30+0))}{0.029} = 40880.7 \times 2.89 \times 33.79 = 3992493.74N = 3.99MN$$

$M_{I,max} = 40880.7.\frac{\pi^3 27.62}{13.73^2 sinh(0.029\times30)}.\left[(\frac{30+0}{2\times0.029}-\frac{1}{2\times0.029^2})e^{0.029(30+0)}-(\frac{30+0}{2\times0.029}+\frac{1}{2\times0.029^2})e^{-0.029(30+0)}+\frac{1}{0.029^2}\right] = 40880.7\times4.63\times549.38 = 103985577.5Nm = 103.98MNm$

The results are:

$F_{wave,\ W\text{-}4}$= 8.04 MN

$M_{wave,\ W\text{-}4}$= 210.93 MNm

D.4 Estimate Geotechnical Load Carrying Capacity

According to Bhattacharya [160], for offshore foundations, the limiting case for maximum lateral load results from the yield strength of the pile. However, a check has to be performed to make sure that the seabed sediment does not fail at the ULS load. Based on the standard methods, the ultimate horizontal load bearing capacity and the ultimate moment capacity of the pile are established as F_R = 64.8 MN and M_R = 2475 MNm, respectively. These are well above the limit (10.4 MN and 515.3 MNm in Table 6-13).

In seabeds, where the sediment resistance increases linearly with depth e.g. cohesionless sand and lightly overconsolidated clay (see Figure D-35), the horizontal load bearing capacity F_R and moment capacity M_R of a piled foundation, assuming that the soil fails first (no plastic hinge is formed in the pile), is expressed using the following equations:

$$K_P = \frac{1+sin\,\phi'}{1-sin\,\phi'} \tag{D-54}$$

$$F_R = \frac{0.5\gamma D_P L_P^3 K_P}{e+L_P} \tag{D-55}$$

$$f = 0.82\sqrt{\frac{F_R}{D_P K_P \gamma}} \tag{D-13}$$

$$M_R = F_R(e+\frac{2}{3}f) \tag{D-57}$$

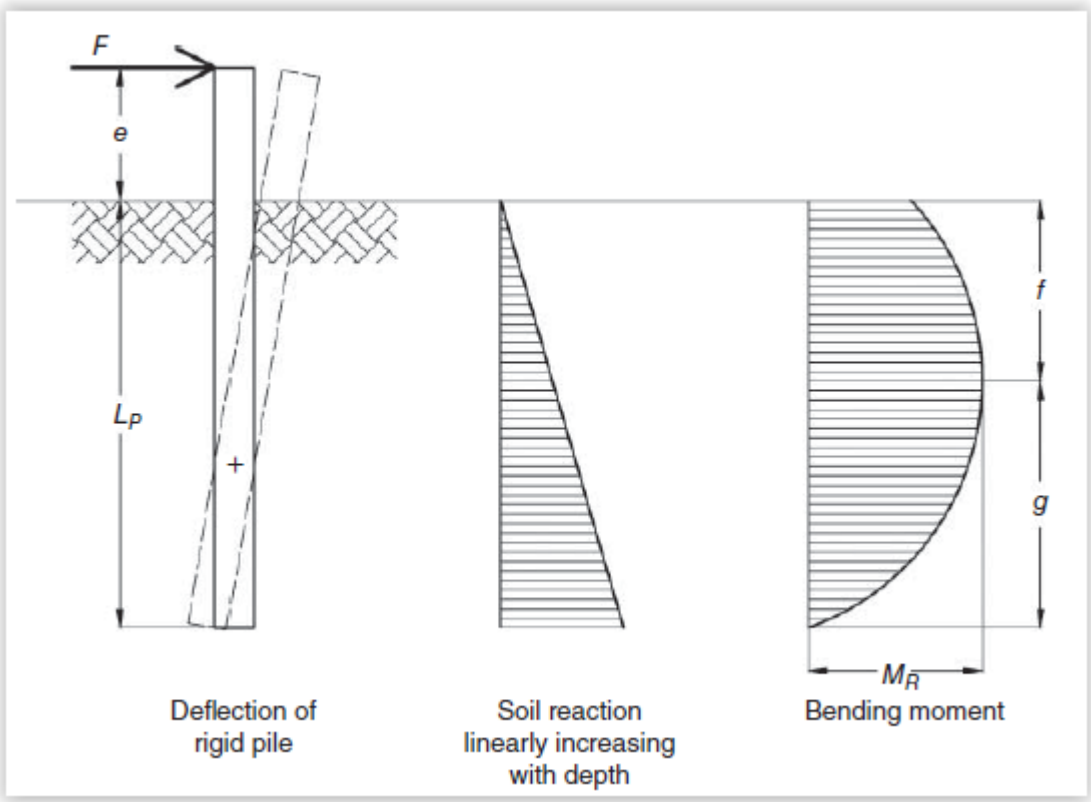

Figure D-35: Lateral pile capacity with ground stiffness increasing linearly with depth [209].

At Terawhiti where seabed ecology is cohesionless sand, $\gamma = 16\ kN/m^3$ is the soil 's unit weight assumed constant with depth (from Table 6-9), K_P[-] is coulomb coefficient of passive soil resistance, f [N] is Unit shaft friction, D_P = 6m is the pile diameter(from Table 6-6), L_P = 30m is embedded length and e=30m is assumed to be the load eccentricity. ϕ'=30° is assumed to be the effective angle of internal friction (from **Error! Reference source not found.**).

D.5 Natural Frequency

Based on a pile geometry and ground profile (i.e. changes in ground stiffness), one can obtain the initial stiffness of the foundation (i.e. K_L, K_R, and K_{LR}). K_L represents lateral stiffness i.e. force required for unit lateral displacement of the pile head (unit of MN m^{-1}), whereas K_R represents moment required for unit rotation of the pile head (GNmrad^{-1}). K_{LR} is the cross-coupling spring (foundation stiffness) dependent

on the soil stiffness (MN). Once K_L, K_R, and K_{LR} are known, one can predict the first natural frequency of the whole system for sway-bending modes. K_V is the vertical stiffness of the foundation (kNm^{-1}) and is necessary for axial vibration analysis [205]. Stiffness formulas are:

$$K_L = 2.65\left(\frac{L}{D_P}\right)^{1.07} f_{(vs)} E_{SO} D_P \quad \text{(D-58)}$$

$$K_{LR} = -1.8\left(\frac{L}{D_P}\right)^{2} f_{(vs)} E_{SO} D_P^2 \quad \text{(D-59)}$$

$$K_R = 1.63\left(\frac{L}{D_P}\right)^{3} f_{(vs)} E_{SO} D_P^3 \quad \text{(D-60)}$$

where L and D_P are length and diameter of monopile, f (υ_s) is the variation of Poisson `s ratio and E_{SO} is stiffness.

And their solutions are:

f (υ_s) = 1 + 0.6|υs $-$ 0.25|=1+0.6|0.2 – 0.25|=1.03

$K_L = 2.65(\frac{L}{D_P})^{1.07} f_{(vs)} E_{SO} D_P = 2.65(\frac{60}{6})^{1.07} \times 1.03 \times 20 \times 6 = 3848.25\ MN/m$=3848259451.4 N/m

$K_{LR} = -1.8\left(\frac{L}{D_P}\right)^{2} f_{(vs)} E_{SO} D_P^2 = -1.8\left(\frac{60}{6}\right)^{2} \times 1.03 \times 20 \times 6^2 = -133488\ MN$=-133488000000 N

$K_R = 1.63\left(\frac{L}{D_P}\right)^{3} f_{(vs)} E_{SO} D_P^3 = 1.63\left(\frac{60}{6}\right)^{3} \times 1.03 \times 20 \times 6^3 = 7252848 MNm/rad = 7252.84\ GNm/rad$=7252848000000 Nm/rad

These values will be used in section 5.3.6 for calculating of deflection under rotor mass imbalance loadings.

In order to avoid resonance, the natural frequency of the tower foundation should differ from the forcing frequencies due to wind turbulence, waves, the rotational frequency (1P) and the blade passing frequency (2P or 3P). If this is not done, the rotor may detach and topple from its foundation. Therefore, the estimation of the natural frequency of the whole system is essential in design calculation. This is a challenging task. Because the turbines installed are becoming higher and heavier, their intervals of target frequency are becoming narrower [248], so the risk that real natural frequency may deviate from the design is becoming greater.

The simple cantilever beam formula as recommended by Arany [206] will be used to estimate the natural frequency of the tower and then will be applied to modify coefficients to consider the flexibility of the foundation and the substructure. The formula is:

$$f_0 = C_L C_R C_S f_{FB} \tag{D-61}$$

Where f_0 the natural frequency of the tower , C_L and C_R are the lateral and rotational foundation flexibility coefficients, C_S is the substructure flexibility coefficient and f_{FB} is the fixed-base (cantilever) natural frequency of the tower.

The fixed-base natural frequency of the tower is expressed simply with the equivalent stiffness k_0 and equivalent mass m_0 of the first mode of vibration as

$$f_{FB} = \frac{1}{2\pi}\sqrt{\frac{k_0}{m_0}} = \frac{1}{2\pi}\sqrt{\frac{3E_T I_T}{L_T^3(m_{RNA} + \frac{33}{140}m_T)}} \tag{D-62}$$

where the average area moment of inertia is calculated as

$$I_T = \frac{1}{16} t_T \, \pi (D_b^3 + D_t^3) \tag{D-63}$$

In equation (D-, E_T is Young `s modulus of the tower, L_T is tower height, I_T is second moment of tower which is given by equation(D-, m_T is the mass of the tower and m_{RNA} is the mass of the rotor-nacelle assembly and tidal turbines. The average wall thickness and the average tower diameter given by

$$t_T = \frac{m_T}{\rho_T L_T D_T \pi}, \quad D_T = \frac{D_b + D_t}{2} \tag{D-64}$$

where D_b is tower bottom diameter and D_t is tower top diameter.
The equivalent bending stiffness of tower is calculated as

$$q = \frac{D_b}{D_t} \quad , \qquad f(q) = \frac{1}{3} \times \frac{2q^2(q-1)^3}{2q^2 lnq - 3q^2 + 4q - 1} \tag{D-65}$$

The nondimensional foundation stiffness parameters are:

$$\eta_L = \frac{K_L L_T^3}{EI_\eta} \tag{D-66}$$

$$\eta_{LR} = \frac{K_{LR} L_T^2}{EI_\eta} \tag{D-67}$$

$$\eta_R = \frac{K_R L_T}{EI_\eta} \tag{D-68}$$

Where EI_η is the equivalent bending stiffness of the tower calculated as

$$EI_\eta = E_T I_T . f(q) \tag{D-69}$$

For the Terawhiti site (from Table 6-6) t_T = 0.027 m,E_T=210 GPa, L_T=68 m, D_b=5 m, D_t= 3 m. m_T is the mass of the tower = 255000 kg and m_{RNA} is the mass of the rotor-nacelle assembly for one wind plus two tidal turbines = 100+125+2×150=525 t=525000 kg. So, f_{FB} and I_T using equations D-62 and D-63 will be:

$$I_T = \frac{1}{16} \times 0.027 \times \pi(5^3 + 3^3) = 0.80\, m^4$$

$$f_{FB} = \frac{1}{2\pi} \sqrt{\frac{3 \times 210 \times 10^9 \times 0.80}{68^3 (525000 + \frac{33}{140} \times 255000)}} = 2.59\, Hz$$

C_L and C_R are calculated by equations(D- and (D- where Nondimensional lateral stiffness $\eta_L = 7763$, Nondimensional rotational stiffness $\eta_R = 77.49$, Nondimensional cross stiffness $\eta_{LR} = -511.7$ and a = 0.5 and b = 0.6 are empirical coefficients sourced from Arany [206].

$$C_R = 1 - \frac{1}{1 + a(\eta_R - \frac{\eta_{LR}^2}{\eta_L})} \quad \text{(D-70)}$$

$$C_L = 1 - \frac{1}{1 + b(\eta_L - \frac{\eta_{LR}^2}{\eta_R})} \quad \text{(D-71)}$$

The solution for C_R is 0.09 and for C_L is 1.7. The substructure flexibility coefficient C_S is calculated by assuming that the monopile goes up to the bottom of the tower. The tower is 68 m tall, the hub height is 87 m, the nacelle is ~5 m tall, so the distance between the mudline and the bottom of the tower is about L_S = 41.5m (this is the platform height) [160]. The foundation flexibility is expressed in terms of two dimensionless parameters, the bending stiffness ratio of tower to the pile $\chi = \frac{E_T I_T}{E_P I_P} = 0.11$($E_P$=200 GPa and t_P=0.083 m from Table 6-6 and as a result I_P=7.04 m^4) and the length ratio $\psi = \frac{L_S}{L_T} = 0.6104$ which have been sourced from Arany et al.[249].

$$C_S = \sqrt{\frac{1}{1 + (1+\psi)^3 \chi - \chi}} = 0.86 \quad \text{(D-72)}$$

Natural frequency of the tower f_0 is estimated from equation (C.60) as 0.34 Hz. A natural frequency of 0.34 Hz is acceptable, as the condition is that the target frequency of the selected wind and tidal turbines is 0.24 Hz [160]. This can be explained; The target Eigen frequency (first natural frequency) is a frequency in the gap between 1P and 3P. For this wind turbine, the rotational speed range is 5–13 rpm, equivalent to 0.083–0.216 Hz, then the 3P frequency band is 0.25–0.65 Hz [248].

If the structural natural frequency is 0.24 Hz, then the pitch control may regulate the rotational speed such that the corresponding 3P frequency avoids ±10% of the structural natural frequency i.e. the frequency band 0.315–0.385 Hz to comply with the DNV code [249]. The structural natural frequency of the wind turbine-tower

substructure-foundation system has to avoid the frequency of rotation of the rotor (1P) by at least 10%. ($f_0 > 1.1f_{1P,\,max} = 0.24$ Hz) [160].

D.6 Plastic Moment of Pile (M_P) and Moment at First Yield (M_Y)

It is necessary to find the maximum moment that a pile section may withstand structurally. Two types of calculation can be carried out: moment at first yield (elastic) and fully plastic. There are two types of section:

1-Plastic Moment of a Solid Circular Section: The stress distribution for a solid section for the two conditions mentioned above (elastic and fully plastic) can be visualised in Figure D-36. The plastic moment is given by the following equation:

$$(\sigma_y \times \frac{\pi R^2}{2}) \times 2 \times \frac{4R}{3\pi} = \frac{4}{3}R^3\sigma_y = \frac{4}{3}\frac{D^3}{8}\sigma_y = \frac{1}{6}D^3\sigma_y \Rightarrow M_P = \frac{1}{6}D^3\sigma_y \quad \text{(D-73)}$$

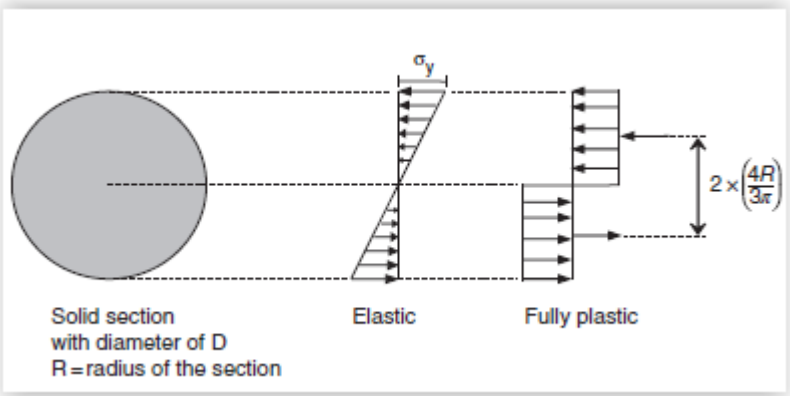

Figure D-36: Stress distribution for a solid section [160].

2-Plastic Moment of a Hollow Pile Section: Properties of a hollow section can be computed by subtraction, i.e. outer diameter minus inside diameter, as shown in Figure D-37. For a thin-walled section, it is assumed that thickness is much less as compared to the diameter. If d_o is the outer diameter and d_i is the inside diameter, the plastic moment capacity is given by:

$$M_P = \frac{\sigma_y}{6}(d_o^3 - d_i^3) \quad \text{(D-74)}$$

Figure D-37: Plastic moment of a hollow section estimation [160].

The shape factor is the ratio of plastic moment to the elastic moment is given by:

$$\text{Shape factor: } \frac{Z_p}{Z_e} = \frac{d^2 t}{\frac{\pi}{4} d^2 t} = \left(\frac{4}{\pi}\right) \tag{D-75}$$

For calculating moment capacity at first yield (M_y) of hybrid model, the inside diameter of pile is calculated as [160]:

Pile diameter (inside) = $\left(6 - \frac{2\times 83}{1000}\right) = 5.834\ m$

Taking $\sigma_y = 355$ MPa from Table 6-6 and putting it in equation D-74

$$M_P = \frac{355}{6}(6^3 - 5.834^3) = 1031.6\ MN.m$$

Using equation (C.74), M_y will be:

$$M_y = \frac{M_P}{\frac{4}{\pi}} = \frac{1031.6}{1.27} = 812.2\ MNm$$

This monopile will have very high geotechnical moment capacity i.e. the capacity at which the soil surrounding the pile will fail. It is highly likely that the monopile will fail by forming plastic hinge (structural failure) long before they will fail geotechnically i.e. soil fails first.

D.7 Seabed Type

For the current application, an advanced method of analysis represents a finite element, discrete element, or finite difference methods. Figure D-38 shows a model of the whole problem. [160]. OPTUM G3 is used considering the different soils for foundation and how type of the soil affects the stability of the hybrid system. Optum

CE develops fast, user-friendly software for the design of Geotech and Concrete structures. The software is developed with a focus on providing advanced FE analysis packages, but at the same time making the tools are accessible for engineering practitioners including structural engineers, contractors, and building companies [202].

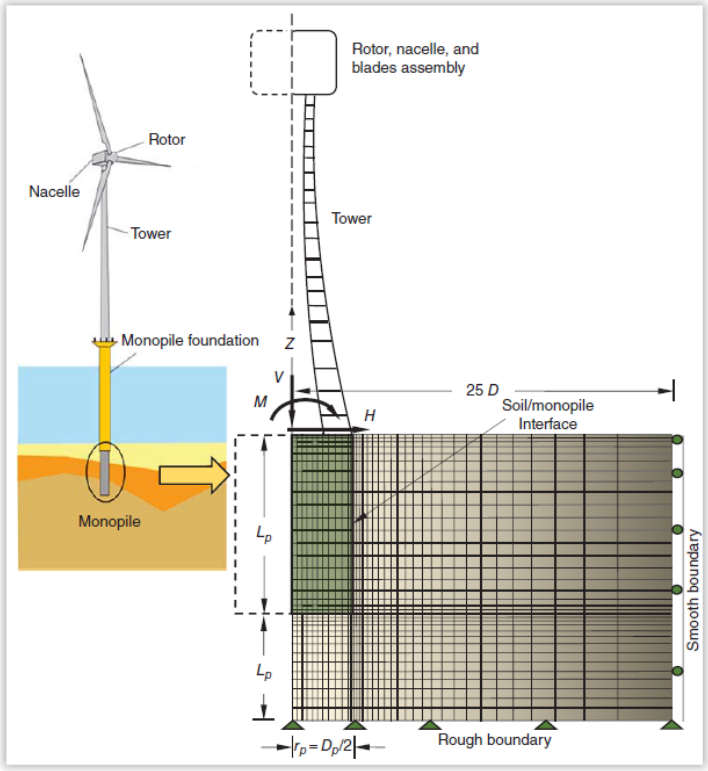

Figure D-38: Finite element of a monopile and surrounding elastic medium [160].

As explained in Chapter Five, the foundation loads can be static or dead load is due to the self-weight of the components or cyclic or dynamic loads due to the wind, wave, rotor frequency (1P), and blade-passing frequency (2P/3P). The total vertical (static or dead) load on the foundation is calculated as

$$V = mg \tag{D-76}$$

where m is the total mass of the structure

Table D-11: Component Weights of Hybrid System

Item	Value
Wind Turbine	
Model	Siemens SWT-3.6-107 Offshore 3.6 MW
Nacelle weight	125 t
Rotor+hub weight	100 t
Tower weight	255 t
Substructure	
Type	Monopile
Transition piece weight	300 t
Monopile weight	700 t
Tidal Turbines	
Model	AR 2000
Total weight for 2 turbines	300 t
Total weight of the structure	1780 t

So, V= 1780×1000×9.81=17461800 N=17461.8 kN as shown separately for each component in Table D-2. Pressure on the foundation is calculated by

$$P=F/A = 17461.8/\pi \times 3^2 = 617.58 \text{ kPa} \quad \text{(D-77)}$$

This load should be less than the allowable axial load. Basic Euler equation may be used [160]:

$$P_{all} = \frac{\pi^2 EI}{L_{eff}^2} \quad \text{(D-78)}$$

Where EP=200 GPa and I=2200 kg.m and Leff based on the explanations by Bhattacharya and Goda (2013) [250] assumed 3LP or 180 m. Using mentioned values, the results in allowable axial load of 134031664.7 kPa which satisfies the condition of P< Pall. **Error! Reference source not found.** shows the parameters u sed by OPTUM for simulations.

Table D-12: Geotechnical Parameters used by OPTUM software for simulations.

Item	Loose Sand-MC	Medium Sand-MC	Dense Sand-MC	Soft Clay-MC	Firm Clay-MC	Stiff Clay-MC
Cohesion c (kPa)	0	0	0	5	10	20
Friction angle ϕ (°)	30	35	40	18	20	22
Soil Unit Weight γ (kN/m^3)	16	18	20	19	20	21

Unit weight of a soil mass is the ratio of the total weight of soil to the total volume of soil. Unit Weight, g, is usually determined in the laboratory by measuring the weight and volume of a relatively undisturbed soil sample obtained from a brass ring. Measuring unit weight of soil in the field may consist of a sand cone test, rubber balloon or nuclear densometer [251].

In Table D-3, there are two parameters related to shear strength: c and ϕ. In other words, shear strength consists of two components: Cohesive and Frictional. The higher these values, higher the shear strength. According to Mohr- Mohr-Coulomb failure criteria ((D), there is a relationship between normal and shear stress on the failure plane:

$$\tau_f = c + \sigma \, tan\phi \tag{D-79}$$

Where τ_f is shear strength, c is cohesion, σ is normal stress and ϕ is friction angle. The graphical representation of this criteria and stress plane is shown in Figure D-39 [252, 253].

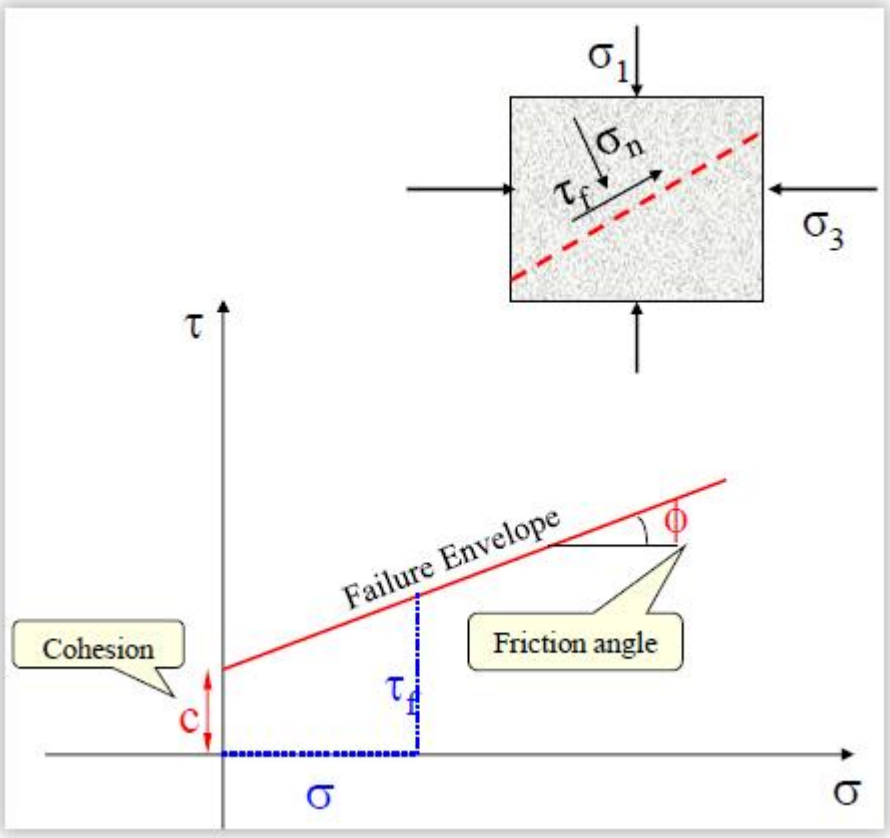

Figure D-39: Mohr-Coulomb Failure Criteria and normal and shear stress on the failure plane.

Soil friction angle (ϕ) is a shear strength parameter of soils. Its definition is derived from the Mohr-Coulomb failure criterion and it is used to describe the friction shear resistance of soils together with the normal effective stress. Soil friction angle is a shear strength parameter of soils. Its definition is derived from the Mohr-Coulomb failure criterion and it is used to describe the friction shear resistance of soils together with the normal effective stress. In the stress plane of Shear stress-effective normal stress, the soil friction angle is the angle of inclination with respect to the horizontal axis of the Mohr-Coulomb shear resistance line.

The cohesion is a term used in describing the shear strength soils. Its definition is mainly derived from the Mohr-Coulomb failure criterion and it is used to describe the non-frictional part of the shear resistance which is independent of the normal stress. In the stress plane of Shear stress-effective normal stress, the soil cohesion is the intercept on the shear axis of the Mohr-Coulomb shear resistance line [254].

The applied load to the monopile and reaction of different soil types explained in Chapter 6.